



Otto-von-Guericke Universität Magdeburg
Institut für Verfahrenstechnik
Lehrstuhl für Mechanische Verfahrenstechnik
Universitätsplatz 2
39106 Magdeburg, Germany



Delft University of Technology
DelftChemTech
NanoStructured Materials
Julianalaan 136
2628 BL Delft, the Netherlands

Influence of vibrations on particle flow behaviour

Jesper Knijnenburg

J.T.N.Knijnenburg@tnw.tudelft.nl

1148834

Chemical Engineering

TU Delft

Master final thesis

CH3901

February 2008 – September 2008

Supervised by:

Prof. Dr. A. Schmidt-Ott

Prof. Dr. S. Luding

Preface

This work is done in the scope of the Master Thesis (CH3901) of the Chemical Engineering master programme at Delft University of Technology in Delft, the Netherlands. The research is performed during February-August 2008 at the Otto-von-Guericke Universität in Magdeburg, Germany. During my time in Magdeburg I was under daily supervision of Dipl. Ing. Guido Kache and my supervisor from Delft University of Technology was Prof. Dr. Andreas Schmidt-Ott. Furthermore, I was supervised by Prof. Dr. Stefan Luding from the University of Twente.

In the Bachelor program of "Scheikundige Technologie & Biotechnologie", the course Particle Technology was given. This course gave an introduction to particle technology, and this immediately caught my interest. During my search for a master thesis, I contacted the teacher of Particle Technology, Dr. Stefan Luding, for a possibility to do my master thesis abroad. He contacted Prof. Tomas at the Otto-von-Guericke Universität in Magdeburg, if he would be able to host me for my master thesis. Prof. Tomas was very enthusiastic and invited me to come to Magdeburg for my thesis. Mr. Guido Kache would be available to be my daily supervisor in Magdeburg.

During the project I experienced that modelling is more difficult than expected, and that models hardly represent a real system. Setting the "right" parameters that agree with reality is hardly achieved and is still a challenge for researchers nowadays. On the experimental front I experienced that at first it seems difficult to do shear tests and wall shear tests, and when the technique is mastered, the process remains interesting as one should remain focused on carrying out the same procedure each test.

Concerning my personal skills, I have experienced several differences between Germany and the Netherlands. One experience is that German people in the city are in general not so friendly when they come to know that you do not speak German. Lectures at the university start very early compared to the Delft standard (first lecture at 07:30), and people also start working earlier than in the Netherlands. Fortunately I could adapt quite easily to this schedule. Some positive surprises were that German dishes were quite good and more varied than expected. On the other hand, it was also quite funny to see the general German stereotype to be confirmed (sausages and beer).

Abstract

Many ultrafine powders show cohesive behaviour, due to which often flow disturbances occur (e.g. arching, ratholing) when such powders are stored in a silo. The application of mechanical vibrations provides a means to promote powder flow. In this project research has been done to study the effect of vibrations on the flow behaviour of limestone. On one hand experiments have been performed using a vibrating Jenike shear cell, while also simulations have been done to model the material flow through a vibrating hopper using the 2D Discrete Element Method (DEM).

Bulk shear tests have been performed, which have shown that the unconfined yield strength and the major consolidation strength are reduced with increasing vibration. In the case of wall shear tests the wall friction angle drastically decreases with increasing vibration velocity. This offers interesting opportunities in increasing the hopper angle and decreasing the hopper outlet.

Multiple simulations of two colliding particles have been done, which have explained the behaviour of the tangential spring and normal and shear viscous damping. For local damping, no equations satisfying the results could be derived. This local damping however was found to be required in the silo simulations in order to simulate realistic behaviour. Vibrations have shown to hardly effect the hopper flow rate, mainly due to the simplified contact model (no cohesion). Vibrations show a promising discharge aid, as the shear test results have shown.

Key words: Vibrating hopper; DEM; modelling; PFC^{2D}; Jenike shear cell; discharge aids; cohesion; viscous damping; ultrafine powder

Kurzfassung

Viele hochdisperse Pulver zeigen kohäsives Verhalten. Aufgrund dieser kohäsiven Eigenschaften können Fließstörungen auftreten, wenn diese Pulver in einem Silo gelagert werden. Die Anwendung von mechanischen Schwingungen bietet ein Mittel den Schwerkraftfluss der Pulver zu unterstützen. In diesem Projekt werden die Auswirkungen von Schwingungen auf das Fließverhalten eines Kalksteinpulvers untersucht. Hierfür wurden Experimente an einer Vibrationsscherzellenapparatur durchgeführt. Außerdem erfolgten Simulationen um den Pulverfluss in einem Schwingtrichter mit der Diskrete-Elemente-Methode (DEM) zu modellieren.

Die Scherversuche zeigten, dass die einaxiale Druckfestigkeit und größte Hauptspannung beim Verfestigen durch die eingeleiteten Schwingungen reduziert werden. Aus dem Wandfließverhalten wird deutlich, dass der Wandreibungswinkel drastisch mit zunehmender maximaler Schwinggeschwindigkeit sinkt. Bei der Auslegung von Silotrichtern führt dies zu größeren maximalen Trichterwinkeln zur Gewährleistung von Massenfluss und zu kleineren minimalen Trichteröffnungsweiten zur Vermeidung von Brückenbildung. Dies ermöglicht eine günstiger Bauform.

Simulationen von zwei stoßenden Partikeln wurden durchgeführt, und können mit analytischen Berechnungen nachvollzogen werden. Die lokale Dämpfung (in PFC^{2D}) kann nicht zufriedenstellend durch analytische Gleichungen beschrieben werden. Allerdings ist dieser Parameter notwendig, um in den Simulationen realistisches Verhalten der Partikeln zu erzielen. Schwingungen bieten die Möglichkeit das Fließverhalten eines Pulvers zu verbessern, wie die Ergebnisse der Scherversuche zeigen.

Schlüsselwörter: Schwingtrichter; DEM; Modellierung; PFC^{2D}; Jenike Scherzelle; Austraghilfen; Kohäsion; viskose Dämpfung; hochdisperse Pulver

Table of contents

Preface	i
Abstract	ii
Table of contents	iii
1 Introduction	1
2 Background on particle technology	3
2.1 Limestone	3
2.2 Particle-particle adhesion	3
2.3 Mass and core flow	5
2.4 Vibratory discharge aids	7
2.5 Stresses in silos	9
2.6 Conclusions	11
3 Experimental part – shear tests	12
3.1 Standard shear test	12
3.1.1 <i>Principle of a shear test</i>	12
3.1.2 <i>Yield loci and Mohr's circles</i>	13
3.1.3 <i>Powder flowability</i>	16
3.2 Wall shear tests	17
3.2.1 <i>Principle of a wall shear test</i>	18
3.2.2 <i>Wall yield locus</i>	18
3.2.3 <i>Stick-slip phenomenon</i>	19
3.3 Additional factors of influence	19
3.4 Vibrational behaviour and shear cells	20
3.4.1 <i>Sinusoidal vibrations</i>	20
3.4.2 <i>Vibrating shear cell</i>	21
3.4.3 <i>Vibrating wall shear test</i>	25
3.5 Experimental setup	25
3.5.1 <i>Material properties</i>	25
3.5.2 <i>Experimental procedures</i>	26
3.6 Results and discussion	28
3.6.1 <i>Shear test results</i>	28
3.6.2 <i>Wall shear test results</i>	33
3.7 Conclusions	38
3.8 List of symbols and abbreviations	39
4 Discrete Element Model	40
4.1 Theoretical background	40
4.2 Calculation cycle	41
4.3 Integration time step.....	42
4.4 Law of motion.....	42
4.5 Force-displacement law	43
4.5.1 <i>Friction</i>	45
4.5.2 <i>Normal force-displacement model</i>	47
4.5.3 <i>Normal viscous damping</i>	49
4.5.4 <i>Classification of collisions</i>	57
4.5.5 <i>Tangential force-displacement model</i>	62
4.5.6 <i>Tangential viscous damping</i>	64
4.5.7 <i>Local damping</i>	66
4.6 DEM programming languages.....	70

4.7	Common mistakes.....	71
4.8	Conclusions	72
4.9	List of symbols and abbreviations	74
5	Silo simulations	75
5.1	Silo geometry	75
5.2	Particle generation	76
5.3	Simulation setup	78
5.3.1	<i>Hopper loading.....</i>	<i>78</i>
5.3.2	<i>Hopper discharge.....</i>	<i>80</i>
5.4	Simulation results and discussion.....	80
5.4.1	<i>Effect of damping.....</i>	<i>80</i>
5.4.2	<i>Effect of friction.....</i>	<i>84</i>
5.4.3	<i>Effect of vibrations</i>	<i>84</i>
5.4.4	<i>Effect of internals.....</i>	<i>85</i>
5.5	Conclusions	86
5.6	List of symbols and abbreviations	86
6	Summary, conclusions and recommendations	87
6.1	Review of obtained results	87
6.2	Summary and conclusions.....	88
6.3	Recommendations.....	89
	Acknowledgements	91
	References	92
	Appendices	97
	Appendix 1: Particle-particle contact models.....	- 1 -
	Appendix 2: User-defined contact model: hysteretic damping.....	- 5 -
	Appendix 3: Hysteretic damping model from ITASCA Manual.....	- 7 -
	Appendix 4: Limestone production and sources (German)	- 11 -
	Appendix 5: Silo design by Schäffer	- 15 -
	Appendix 6: Equations of calculation cycle	- 17 -
	Appendix 7: Results of shear tests	- 20 -
	Appendix 8: Results of wall shear tests.....	- 24 -
	Appendix 9: Results of e_n and t_c simulations	- 26 -
	Appendix 10: Results of Ψ_1-Ψ_2 simulations.....	- 28 -
	Appendix 11: Test charts of the vibrating shear cell	- 44 -
	Appendix 12: Used scripts for simulations	- 51 -

1 Introduction

Granular materials can be defined as composed of many individual solid particles, irrespective of the particle size. This thus includes the finest grains of sugar, talc and pigments, but also the coarsest blocks of rubble. Handling of granular material is of great importance in the chemical industry as they are widely manipulated in industry. Granular materials, or bulk solids, are generally stored in silos or bunkers. These can also largely vary in size, like the granular materials itself. Over the past ages, silos of various shapes and sizes have been designed and built by trial and error, to provide the optimal storage capacity and discharge properties ^[1,2].

When discharging granular material from a hopper, one aims to have a perfect residence time distribution of the material: what comes in first also comes out first. In reality, however, this is generally not the case, and flow disturbances occur. The main cause for this is the poor design of the silo, caused by the fact that buyers tend to save money and time. In reality, the contrary is true, as improper design gives an economic penalty and often asks for redesign. In these silos it is very likely that flow disturbances occur, especially for cohesive materials. The well-known but unsolved problems that occur with cohesive solids in silos and hoppers include arching, channelling, segregation and feeding and dosing problems.

It is often too expensive to remove the silo and rebuild it. A cheaper and easier solution might be to install discharge aids. One method of aiding the flow behaviour is by means of vibrations, where the discharge of a silo can be installed with a vibrating hopper. By applying horizontal harmonic vibrations to the hopper, the powder is activated, and the material flows out more easily.

A cheap and relatively quick method to investigate and visualise the effect of these vibrations is to perform a two-dimensional simulation of the vibrating hopper. In this project, a two-dimensional model of the vibrating hopper is modelled using the Discrete Element Method. In comparison, experiments are done with the vibrating Jenike shear cell using ultrafine limestone powder. Limestone is a cohesive powder and is likely to cause flow disturbances in silos. Conclusions are drawn with respect to industrial applicability of the vibrating hopper.

The project goals are summarized in Figure 1, where the focus will be on the two question marks. For the other issues a short literature review will be made. At the end of the report, Chapter 6.1 discusses the new results in a complete picture.

	Shear test	Silo
Experiments	?	
Simulations		?

Figure 1: Schematic display of the project goals

Experiments using the vibrating Jenike shear tester have been done by Roberts ^[3,4] and Arnold ^[5]. Their results show a decrease of shear stress and increase of flowability with increasing frequency. More recent results show similar results, however instead of the frequency, a better correlation with the vibration peak velocity was found ^[6,7]. Simulations of the Jenike shear tester using the same PFC^{2D} software ^[8-10] or even PFC^{3D} ^[1] have been performed before. These have shown good agreement with experimental results. However no reports of simulations considering the vibrating Jenike shear cell have been found.

Most likely Chladni ^[12] was the first to study the behaviour of vibrated beds of particles. In his experiment he found that when sand is scattered on a vibrating membrane, the particles move to the positions with the small vibration amplitude. Faraday ^[13] did similar experiments, and he found the same patterns. Bachmann ^[14] and later Kroll ^[15] did experiments on vibrated beds of granular material. Their observations were that when the bed is insufficiently deep, the particles bounce around as in a fluidized bed. When the depth is larger than about six particle diameters, the bed behaves as a single body. This has been confirmed by other researchers as well ^[16].

Perhaps the first experiments with vibrations in hoppers have been done by Takahashi et al. ^[17], who used vertically oscillating wedge hoppers and flat bottom bins. They found that the discharge rate from the hopper is decreased significantly at high oscillation accelerations. Wassgren et al. ^[18] examined the discharge rate from wedge-shaped hoppers as a function of vibration parameters ^[16]. They found that the discharge rate decreases with increasing vibration velocity. Silo experiments have been performed as well ^[19] using vertical vibrations ^[20-22]. The effect of vertical vibrations by means of simulations has been investigated as well, using the 2D DEM method ^[16,18]. These have shown a similar trend as experiments, although no absolute agreement was found.

This report comprises several modules, each of which focuses on a separate theme. At the end of each module, a small conclusion is made, and an outlook to the next chapter is given. First a short introduction to particle technology shall be given in Chapter 2. Chapter 3 contains the practical part of this project, where vibrating shear tests and wall shear tests have been done. In Chapter 4 the Discrete Element Method (DEM) is explained, supported by several two-particle simulations. Chapter 5 gives all information about the silo simulations, where the effect of e.g. vibrations on the flow rate has been evaluated. In Chapter 6 a review back to the project goals will be made, final conclusions are drawn and various recommendations for continued research are given. As each chapter uses its own symbols, a symbol list can be found after each chapter, whereas a general list of references is published at the end of the report.

2 Background on particle technology

This chapter contains a basic introduction to powder behaviour and flowability. First the used material will be described, and some theory of adhesion will be given. This is followed by a small overview of flow patterns of bulk materials in silos, as well as how the stress is developed in silos and hoppers.

2.1 Limestone

Limestone is one of the natural rocks that consist mostly of calcium carbonate (CaCO_3). It is formed by accumulation of secreted shells of marine organisms, which deposit on ocean floors. Secondary limestone may be formed by precipitation from groundwater in caves, to form stalagmites and stalactites. A third form of limestone occurs in granular form ^[23].

Limestone contains several natural impurities, mainly magnesium, silicates, aluminates and iron. It is commonly used for the production of quicklime and slaked lime, in the steel industry, agriculture, gas treatment, drinking water and wastewater treatment and in the glass industry. The limestone used in this project is supplied by "sh minerals", Heidenheim, Germany. They use their highest quality (finest and purest) limestone for plastic production (filler material).

The mean particle size of the used limestone is 1.6 μm , which means it is an ultrafine powder. Limestone itself acts rather cohesive and storage of ultrafine limestone powder in silos is likely to cause flow disturbances. Different reasons could be addressed to this cohesive behaviour. This will be evaluated more closely in the next chapter.

2.2 Particle-particle adhesion

Adhesion is the tendency of molecules to stick together due to intermolecular attraction forces. There is a difference in definition between cohesion and adhesion. Cohesion accounts for surfaces of the same material (such as particle-particle), whereas adhesion is for different surfaces (e.g. particle-wall). Here adhesion will be used as the more general definition. Figure 2 gives an overview of different adhesion forces between particles. Surface and field forces may be the cause for adhesion. These forces include van der Waals forces, electrostatic and magnetic forces.

Between all solids, there exist molecular based attractive and repulsive forces, which are known as van der Waals forces. The energy of these forces is in the range of 0.1 eV, and decreases with the sixth power of the distance between the molecules. Compared to chemical bonds, the range of van der Waals forces is quite large ^[24]. Van der Waals forces are more important for particles in the range of nanometers (nanoparticles) than for larger particles.

Electrostatic charging of particles and surfaces occurs due to friction and frequent rubbing of particles against equipment surfaces, where the charge is a result of electron transfer between particles. Electrostatic forces do not require the particles to be in contact, and these forces may be attractive or repulsive, and can act over a relatively long distance ^[21]. Electrostatic forces are present when surface charges exist, e.g. metal powders (conductive) and polymer powders (non-conductive).

Magnetic forces are present when the material exhibits magnetism (such as iron powder). Due to a magnetic field, magnetism is induced upon these particles, which causes them to attract each other, and thus stick together to form agglomerates.

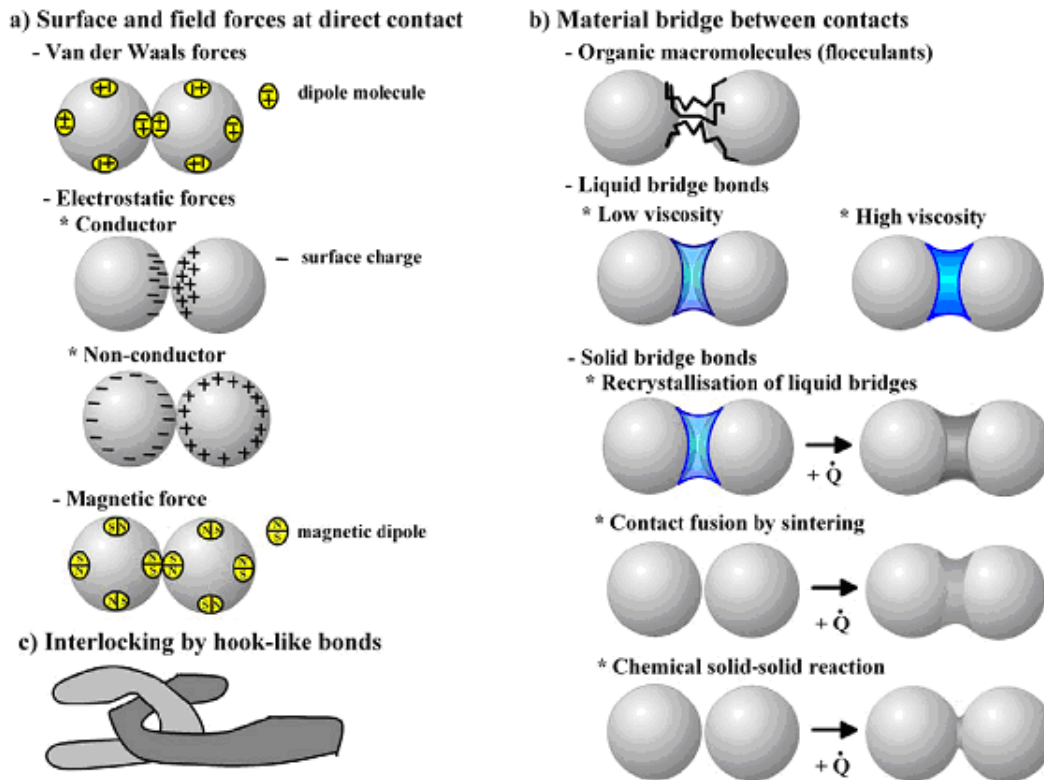


Figure 2: Particle adhesion and microprocesses of particle bond effects in contact ^[25]

Particles in the presence of a condensable vapour will have a layer of adsorbed vapour on their surface. Whenever these particles contact each other, attractive forces result from the overlap of the adsorbed vapour layers. The bond strength depends on the contact area between the particles and the tensile strength of the adsorbed layers, where the size and strength of the layers depends on the partial pressure of the vapour ^[24].

Material bridges between contacts are possible, due to organic macromolecules that adsorb on the outside of the particles, or in the case of hydrogen bonding between particle surfaces. Even in very small amounts, liquids can cause adhesion between particles, since it can reduce the interparticle distance and it increases the smoothness of rough surfaces. Liquid bridging between particles causes adhesion due to the capillary pressure and surface tension. There is a difference between low viscous (such as is the case with moist sand) and high viscous liquid bridges (such as resins).

In general, agglomeration caused by liquid bridges is not a permanent problem. More severe are solid bridges between particles. Solid bridges can be caused by recrystallization of liquid bridges, e.g. when a salt is dissolved in the liquid. Also fusion of the contacts by sintering can occur when high temperatures are present. Furthermore, a chemical solid-solid reaction can cause the particles to stick together. Other cases of solid bridging include freezing of liquid bridges, solidification of a high viscous liquid bond, and chemical reactions with adsorbed surface layers.

Apart from surface/field forces and material bridges, a third reason for particle adhesion may be interlocking of particles. This is highly dependent on the surface roughness and shape of the particles. Typical effects include interlocking of chain branches (as can be the case with proteins), hooking of particles by hook-like bonds (fibres), and interlocking caused by surface roughness. Without any possibility for liquid bridging, the van der Waals forces of a dry contact are dominating. These van der Waals forces are largely dependent on surface roughness ^[25,26].

The reason why ultrafine limestone particles are cohesive can be explained by their surface roughness. Limestone particles are far from spherical, as can be seen in Figure 3. Liquid bridges cannot occur, since the equilibrium moisture content of limestone is as low as 0.2% (see Appendix 4, room temperature, open lab). Also solid bridges are unlikely, since there is no possibility to form solid bridges. Surface charges are not applicable here, since limestone particle surfaces are in general free of charge. Due to their small size range (μm range) and in the absence of other mechanisms, van der Waals forces will play a dominant role between dry limestone particles.

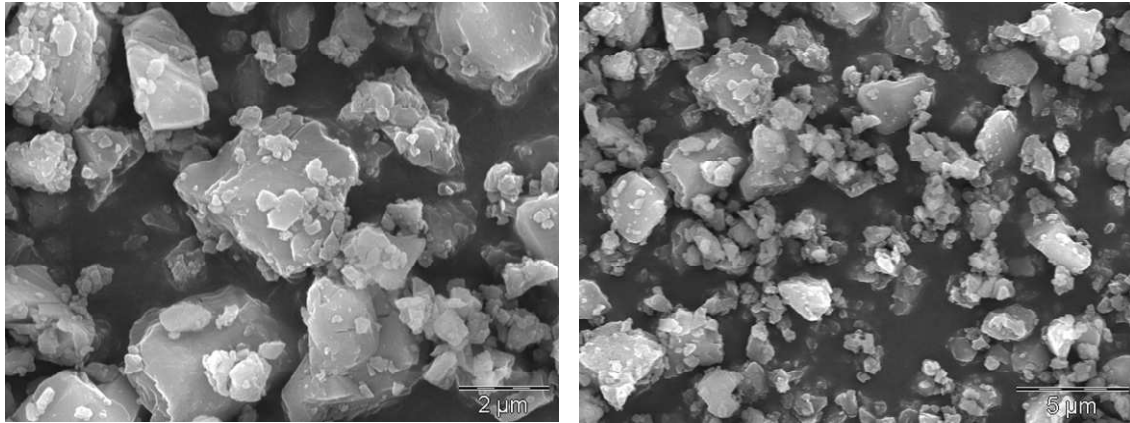


Figure 3: Scanning Electron Microscope photographs of limestone (CaCO_3). It can be seen that limestone particles are not spherical and the surfaces are far from smooth. Also the size distribution is already visible (clusters/agglomeration)

Due to this cohesive behaviour, limestone is likely to be prone to flow disturbances. In the next section, an overview of flow patterns and disturbances will be given.

2.3 Mass and core flow

Discharge of silos can occur in two patterns: mass flow and core flow (see Figure 4). In the case of mass flow, each particle moves as the silo bottom is opened; all the material inside the hopper is in motion. Mass flow is only possible when the hopper walls are sufficiently steep and/or smooth. If this is not the case, core or funnel flow will occur. The material will only flow through the centre of the silo and dead zones at the sides will emerge. A combination of both is called expanded flow, where mass flow is found at the outlets but higher regions consist of static zones ^[24,27,28].

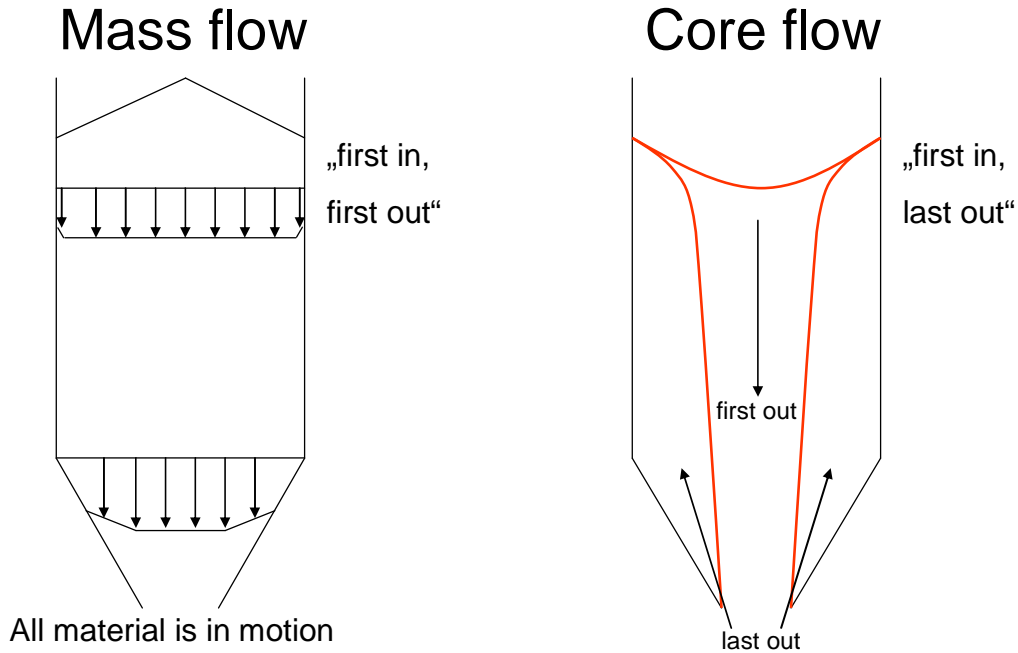


Figure 4: Discharge patterns of hoppers. Left: mass flow pattern. Right: core or funnel flow pattern ^[28]

The main advantages of mass flow are that a steady state mass flow can be closely approximated, also providing a narrow residence time distribution. The velocity of the material is constant and practically independent of height (until entering the hopper, see Chapter 2.5), so that a constant mass flow rate is obtained. Since there are no dead zones in the silo, the risk of product degradation is negligible compared to the case of core flow.

Another important advantage of mass flow is that the stress field in the storage tank is more predictable than in the case of core flow. Here, one can expect where the highest stresses are being formed. Also in the case of mass flow, the complete silo capacity is used, as there are no dead regions to be found.

One disadvantage of mass flow is that friction between the moving particles and the walls results in attrition of the wall. This gives rise to product contamination, as small particles of the silo and hopper walls will be present in the product.

Core flow has many disadvantages. The main disadvantage is that the material that enters first will go out last. This is a huge problem with storage of biological material because of the biological stability of the material.

Arching (or doming) can occur in both mass and core flow situations. In this case, the material has enough strength to support its own weight, causing an arch to form at the hopper outlet. This often occurs in the case of cohesive material.

A special case of arching is mechanical arching, which occurs due to interlocking of the particles (see Figure 2, Chapter 2.2). In this case, the hopper outlet is too small compared to the particle size, so that a "traffic jam" is formed; particles compete to get out through the small outlet, and get stuck ^[24,27,28]. A general rule of thumb is that the outlet diameter has to be five times the upper particle diameter to prevent mechanical arching.

Insufficient flow can occur when the material in the cylindrical section compresses the material in the conical section, which is required to dilate before it can flow out. This results in fluctuating flow, where only certain powder packages are released periodically.

Another problem would be flushing of the silo. In this case, uncontrolled flow from the hopper occurs due to the powder being in an aerated state. This can only occur with fine powders, and causes for this would be improper use of aeration equipment, or by the collapse of a rathole.

Many powders tend to consolidate after time, due to the humidity, pressure and temperature in the silo. Due to this material sticking together, it is difficult or impossible to discharge the material from the hopper. This is particularly a problem in the case of core flow, and especially for hoppers that are infrequently discharged.

One problem caused by the filling method is segregation. Finer particles remain in the centre of the silo, whereas larger particles roll away to the outside. The particle material will be separated by particle size, shape or density, which results in an uneven product distribution.

In some cases, core flow is desired over mass flow. Think of cases when powder deterioration does not take place over time, or when abrasive solids are stored, so that there is minimum hopper wall wear ^[29].

When the material in a silo flows out under the core flow profile, it is often too expensive to remove the silo and rebuild it to get a mass flow profile. It is also possible that a mass flow design leads to silo dimensions that cannot be realized, due to the connected conveying devices or simply due to space requirements. A common solution for flow disturbances is to apply one or multiple discharge aids.

2.4 Vibratory discharge aids

A discharge aid may be defined as a device that stimulates or improves bulk solids flow out of a silo ^[2]. Before considering installing a discharge aid, it may be practical to study the bulk material itself and its flow properties in relation to the present design. Hopper modifications might prove to be an economically more favourable solution. Here one could think of a steeper hopper, inside coatings, change of the hopper shape or use flow aids (e.g. anti-statics and lubricants). In situations where these modifications are insufficient to promote flow or are not possible at all, a discharge system must be used.

Many types of discharge aids are possible. Think of pneumatics, mechanical aids or vibrations, but also passive devices (e.g. inverted cone) to change the stress and flow patterns within a silo offer possibilities of flow improvement. In the research done in this project, the aim was on the use of a vibrating hopper, so discharge aids by means of vibrations will be explained here in more detail.

The technique of vibratory discharge aids is known for decades and has already been applied in the primitive forms of mallets and sledgehammers. Material deformations and 'hammer rashes' are often seen in plants where these barbaric techniques have been used. Even though the application is old, research on wave propagation in bulk material has been rather limited ^[30-36].

Vibratory aids can be (partly) installed internally, directly in the material flow, or attached to the outside of the shell, close to the hopper outlet. A classification is given in Figure 5. External vibrators include air driven or electric driven devices, either rotary or linear. Examples are turbines, pistons and electric motors. Internal dischargers include vibrating louvers (so-called "deflectors", collection of flat blades that are tilted over a certain angle) and cones.

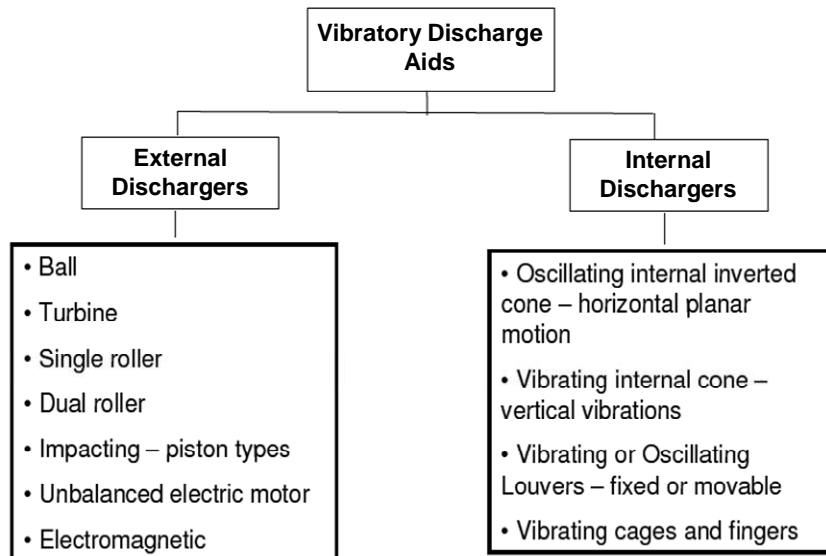


Figure 5: Classification of vibratory discharge aids ^[2]

The vibrating equipment as focused on in this project is within the group of internal dischargers. It falls in the category of vibrating cones; however it vibrates in horizontal instead of vertical direction.

The design of the hopper is displayed in Figure 6. The complete vibrating hopper design is outlined in Appendix 6. On the inverted cone, multiple baffles are placed to aid the powder flow. There is an annular space between the inverted cone and the hopper through which the material is able to flow out. The cone oscillates in horizontal direction at standard frequencies of 15 to 50 Hz and amplitudes up to 2 mm. If higher frequencies are required, one can use a frequency converter to drive the electric motor of the hopper. Additional baffles are placed below the vibrating cone to assist flow and to prevent material compaction.

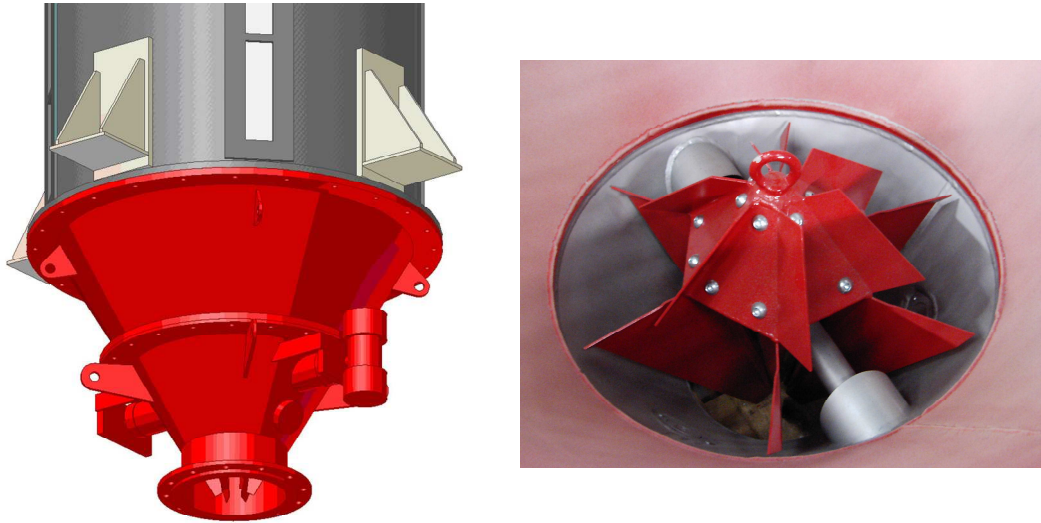


Figure 6: Left: 3D-model of the bottom view of the vibrating hopper. Right: inside photograph of the horizontally vibrating internal cone

The vibrating cone serves three purposes:

- to impart force into the bulk to break potential arches
- to reduce stresses in the outlet region by shielding flow over the outlet
- to provide a slot-like outlet and pseudo-flow, offering a favourable flow shape

Vibration intensity can be altered by moving eccentric weights on the drive motor. In practice, the vibrators are often not driven continuously but there are periods without any vibrations. Normally a period of 20 to 30 seconds of vibrations is followed by an idle time of 30 to 120 seconds (depending on the material). However such practical experiences are not provided by research yet.

According to ^[2], vibrating discharge aids are suitable for cohesive, caking and brittle materials, but unsuitable for powders that tend to consolidate with vibrations (e.g. spongy and soft powders). This makes the vibrating hopper an ideal tool for materials that behave as limestone.

2.5 Stresses in silos

When a powder is stored in a silo, stresses are developed. These stresses are in general very different from the stresses that are present in the case of a liquid. Bulk solids can transfer shear stresses under static conditions, which shows why liquids form level surfaces, whereas bulk solids form piles. Many solids can keep a certain shape when consolidated, while this is not possible with liquids. In a liquid, shear stresses are dependent on the shear rate and independent on the pressure; this is the other way around in solid flow. This is why flow criteria derived from fluid flow concepts are not successful when applied to bulk material ^[29].

In the case of a liquid, the pressure increases linearly with the filling height, the so-called hydrostatic pressure. For a bulk solid material, if the height is sufficiently large, the pressure does not increase anymore when adding more material, even for a much higher filling height. After some point, a constant vertical stress is created. The reason for this is the shear stresses acting between the material and the wall (friction). Due to these shear stresses, the wall carries a part of the material. One of the most fundamental publications about stress development along the height of a silo was written by Janssen ^[37,38], which is still widely used as reference material by engineers nowadays.

When starting to discharge the silo, the stress state of the material in the hopper changes from the filling state (major principal stress in vertical direction) to the discharge state (horizontal direction), as is shown in Figure 7 ^[19].

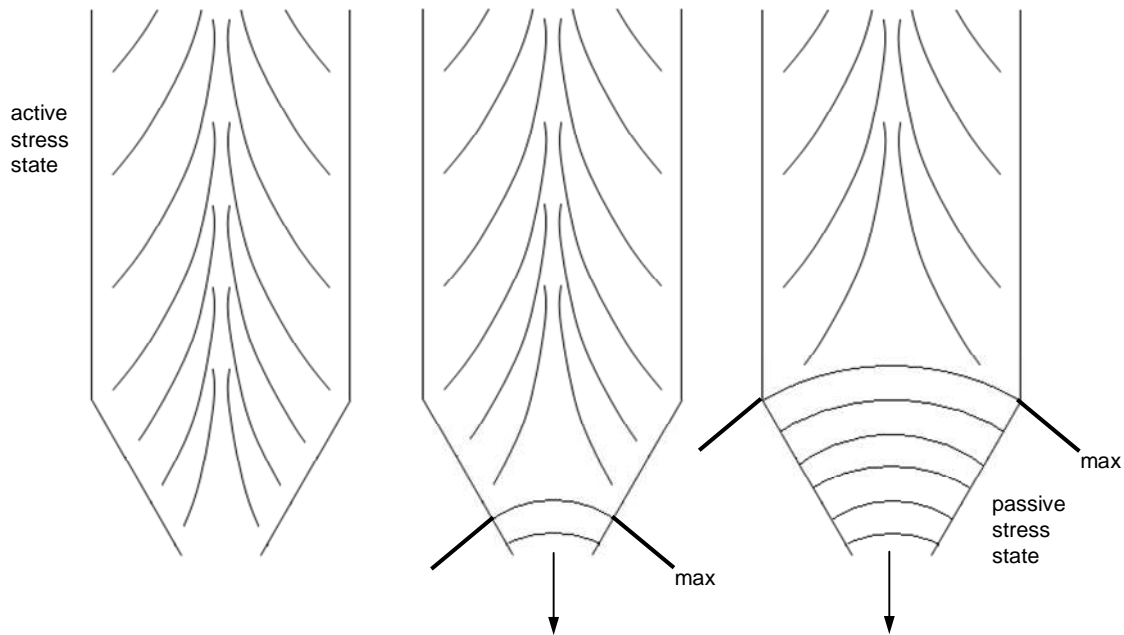


Figure 7: Principle stress trajectories and maximum normal wall stress, changing from active to passive stress state in the hopper and upward movement of the stress peak at the beginning of discharge ^[19]

This transition of stress direction is the so-called "switch". At this "switch", a peak in the wall normal stress occurs. This peak emerges because when starting to discharge, the lowest layer dilates first, whereas the higher layers in the hopper are still stagnant. Because of this dilation, the bulk solid density, the strength, and also the supporting stresses for the layers above decrease. This results in the fact that shear stresses on the wall must increase to keep force equilibrium with the layer above. The dilation continues in upward direction, which means the switch also moves upwards, and ends where the hopper ends and the silo begins. In the silo, the major principal stress dominates in vertical direction. When the discharge state is reached, the bulk flow is in steady state since the density and stresses do not change any further ^[19].

The stress as a function of height is shown in Figure 8. In some special cases it is possible for the peak pressure to be higher than the hydrostatic pressure. Note that there is low stress at the hopper outlet, which is good for discharge devices. The asymptotic pressure only depends on the silo diameter and not on the height. This is why silos are generally high and thin, rather than short and squat.

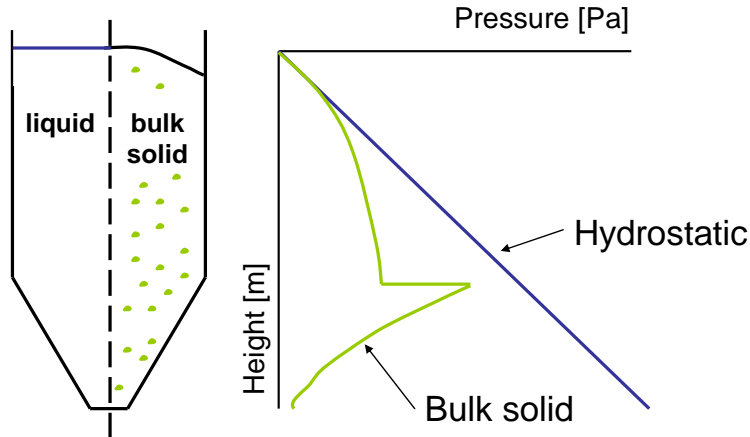


Figure 8: Pressure distribution as a function of height ^[28]

As was outlined in Chapter 2.4, the vibrating cone reduces stresses even further in the outlet region. Bulk flow is directed by the hopper outlet, where it will flow out through the annular region. Material compaction is not as much a problem anymore, since there is less stress developed in the powder, and in case of strong compaction, horizontal vibrations break the solid bulk structure.

2.6 Conclusions

In this chapter some general theory on particle-particle adhesion and silo flow has been given. Limestone is expected to give flow disturbances and core flow due to its cohesive properties, where surface roughness and van der Waals forces are thought to be the main causes.

Various problems can occur when paying insufficient attention to designing a silo. Core flow is generally the cause and unwanted powder flow behaviour arises. Instead of redesigning and rebuilding the complete silo, discharge aids can provide an economic solution. A range of discharge aids is available, where vibratory devices have proven to be suitable for the cohesive limestone material.

An introduction to stress development in silos is given, and it was found that in the case of a bulk solid, silo walls are subjected to stresses that are different than when the silo would be filled with a liquid. Furthermore, stresses in silos in the discharge state are different than that in the filling state. One should pay attention to this when choosing materials for silo wall.

3 Experimental part – shear tests

This chapter contains the theory and experimental work of the effect of vibrations on the performed shear tests. Bulk shear tests and wall shear tests have been done, both non-vibrated and vibrated. First an overview of the theory will be given, after which the experimental setup and results will be discussed.

3.1 Standard shear test

The goal of a shear test is to achieve material flow parameters, so that the flow behaviour of the powder can be classified. Globally, the normal stress on the material is varied, while the shear stress is measured. To perform shear tests, many devices are available, of which the Jenike shear cell and the uniaxial and biaxial shear cell are the most common ^[39]. In this research project the Jenike shear cell was used. First the standard method for shear testing will be explained ^[39,40].

3.1.1 Principle of a shear test

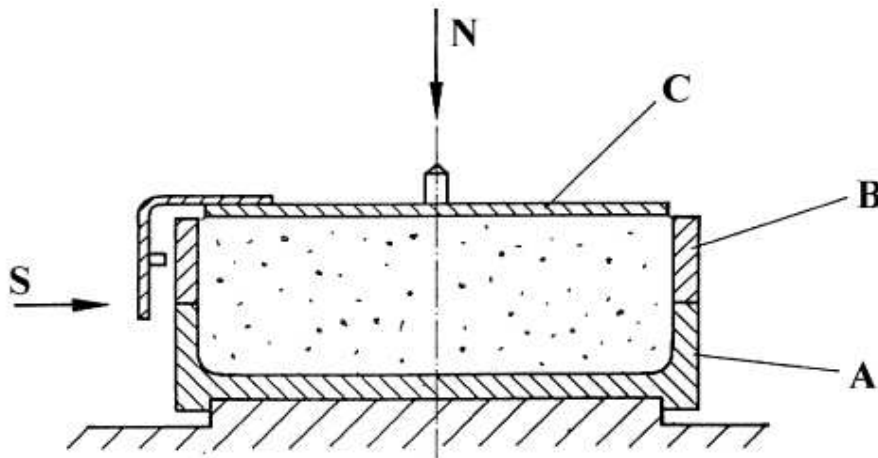


Figure 9: Jenike shear cell (A: shear base, B: shear ring, C: shear lid) ^[39]

Each shear tests consists of three steps: pre-consolidation, pre-shear and shear. With the first two steps a reproducible initial state is obtained for shear. The Jenike shear cell is displayed in Figure 9. The bottom ring is placed on the shear base, and the upper ring is placed on this bottom ring. The assembly is filled with the desired powder, the cell is closed with the consolidation lid, and the consolidation may be started. For this consolidation, the desired weight is hung on the yoke and the lid is twisted back and forth a number of times. After consolidation, the sample is closed with a different lid. The sample is now prepared for pre-shear.

The cell is loaded with a normal force on the shear lid. To create the shear deformation, the lid and upper ring are displaced in horizontal direction by pushing with the shear pen with constant velocity against the shear ring. With this movement, a shear force is induced to the cell, which is monitored during the test. After stationary flow is reached, the shear direction is inversed until the shear force is back to zero. This procedure is the so-called pre-shear.

Now the normal load is reduced and shear is induced again. The force is increased until the powder starts to flow. The required shear force increases until it reaches a peak, after which the shear force gradually decreases. This peak is a measure for the powder flowability. This procedure is called shear.

The relation between normal stress σ and shear stress τ is called a yield locus. Each pre-shear and shear measurements gives a point on such a yield locus. This is represented in Figure 10. A different point on the yield locus is obtained by having identical pre-consolidation and pre-shear conditions but a different normal load during shear.

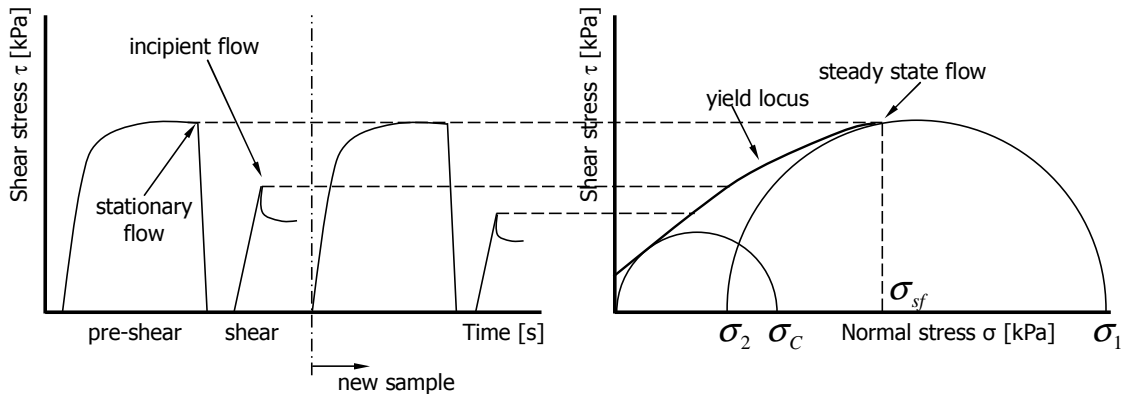


Figure 10: Procedure to get a point of a yield locus, using the Jenike shear tester ^[39]

The procedure is repeated but with a greater normal load on the yoke during pre-shear, causing a higher bulk density. For a higher bulk density, the yield locus moves upwards and extends further into the compressive regime. So for the same normal stress, a higher shear stress is required to reach the yield locus ^[41]. Each set of measurements therefore creates a set of values for normal load and shear stress for a powder with a certain bulk density. It is important to have a constant bulk density, meaning that for each test, the bulk density should be measured as well. The shear stresses are plotted to give a yield locus, where the end of the yield locus corresponds to critical flow conditions (constant shear stress), where the start of the flow is not accompanied by a change in bulk density.

3.1.2 Yield loci and Mohr's circles

The yield locus describes the powder strength at a certain bulk density as function of the confining stress. It represents the maximum shear stress a bulk solid can support under the current normal stress, and it indicates the onset of failure in the material. The results of the Jenike shear cell tests can be displayed in a shear stress versus normal stress diagram ^[41]. An example is shown in Figure 11.

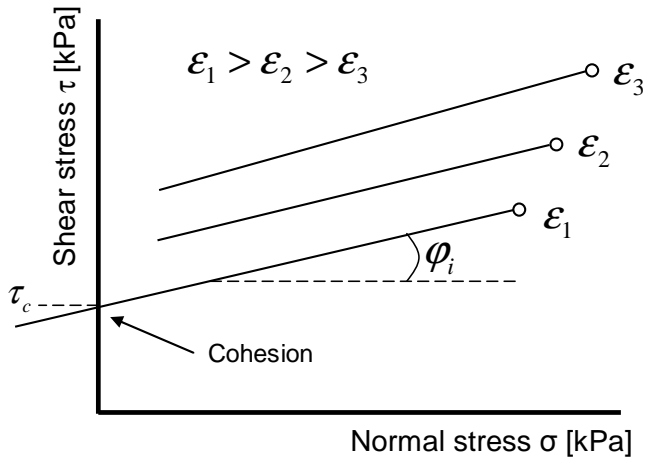


Figure 11: Typical result after shear tests: a family of yield loci, angle of internal friction φ_i and shear resistance τ_c . ε represents the porosity of the sample ^[24,42]

Ideally the yield locus is a straight line and the slope of a yield locus is the angle of internal friction φ_i , which is a measure for the contact failure at sliding. From this we can find the particle friction coefficient, defined as $\mu_p = \tan \varphi_i$ [-]. The intersection of the yield locus with the vertical axis is τ_c [Pa], which is the shear resistance present without any normal stress, caused by e.g. particle adhesion. Since the yield locus is generally slightly curved, the angle of internal friction slightly changes as a function of the normal stress.

Each point on a yield locus corresponds to that point on a certain Mohr’s circle, which is tangential to the yield locus. A Mohr’s circle gives a graphical representation of possible combinations of normal and shear stresses acting on a particular plane in a powder under stress. This means that a yield locus is a tangent of all possible Mohr’s circles that represent the stress systems under which the powder will flow. Mohr’s circles larger than the circle that would be tangential to the yield locus are not relevant since the system under consideration cannot support these stress combinations, whereas smaller circles contain stresses that are insufficient to cause flow. In this case, deformations are still in the elastic region and are therefore still reversible.

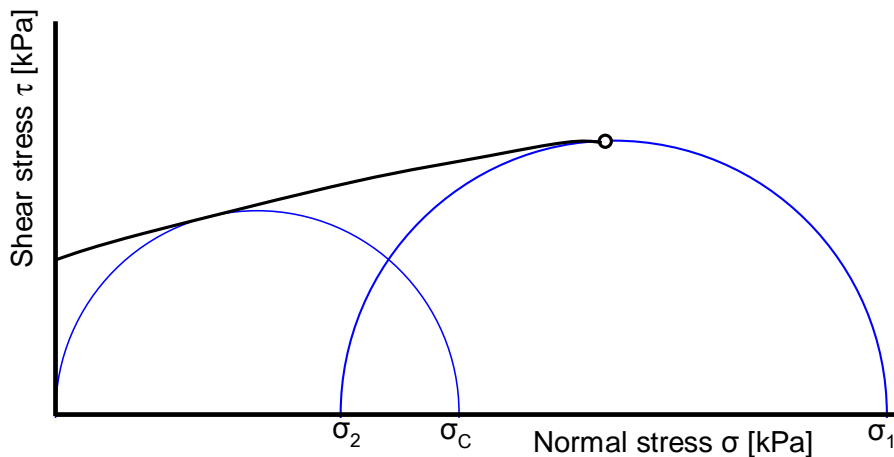


Figure 12: Determination of unconfined yield strength σ_c , and minor and major principal stress σ_2 and σ_1 , resp., found by Mohr’s circles ^[24]

In Figure 12, the two Mohr's circles are of particular interest. The smallest circle, tangential to the yield locus and the y-axis, represents conditions of the free surface of the material, where there is zero shear and zero normal stress. This circle provides us the unconfined yield strength σ_c . The larger Mohr's circle is tangential to the end point of the yield locus, and thus represents conditions for steady state flow under pre-shear. The major (minor) stress on this circle is taken to be the major (minor) consolidation stress σ_1 (σ_2). Each yield locus gives new values for σ_c , σ_1 and σ_2 . Figure 13 shows how a Mohr's circle is related to the stress system.

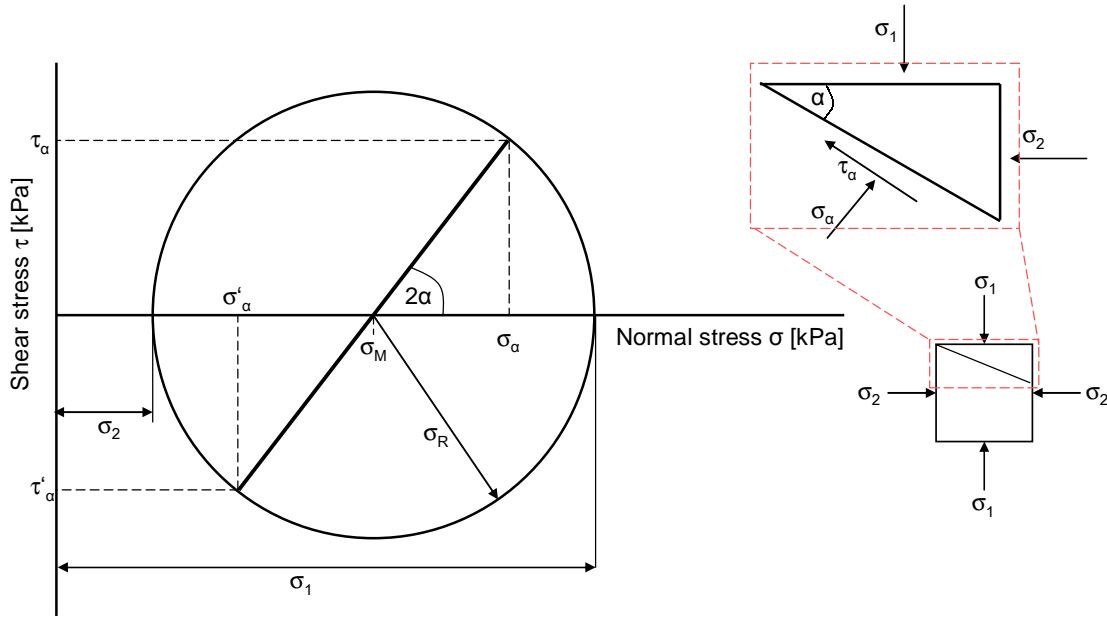


Figure 13: Construction of Mohr's circle in relation to the stress system ^[1,24]

Mohr's circle can be used to translate stresses into a new coordination system. The angle between the current axes (σ and τ) and the principal axes is defined as α , which is equal to half the angle between line $(\sigma'_\alpha, \tau'_\alpha) - (\sigma_\alpha, \tau_\alpha)$ and the horizontal. When shifting the line over angle 2α , the stresses in the new system can be read on the Mohr's circle.

The centre σ_M and the radius σ_R of the Mohr's circle can be obtained by

$$\sigma_M = \frac{\sigma_1 + \sigma_2}{2} \tag{3.1}$$

$$\sigma_R = \frac{\sigma_1 - \sigma_2}{2} \tag{3.2}$$

The radius is also equal to the maximum shear stress. A derivation of these equations can be found in literature ^[1,40].

A tangent line can be drawn along the Mohr's circles that are tangent to the end points of the yield loci, straight through the origin, as shown in Figure 14. This line is called the effective yield locus of the material. The angle between the horizontal axis and the effective yield locus is the effective friction angle φ_e , which is not really a physical angle within the material but merely the tangent of the ratio of shear stress to normal stress.

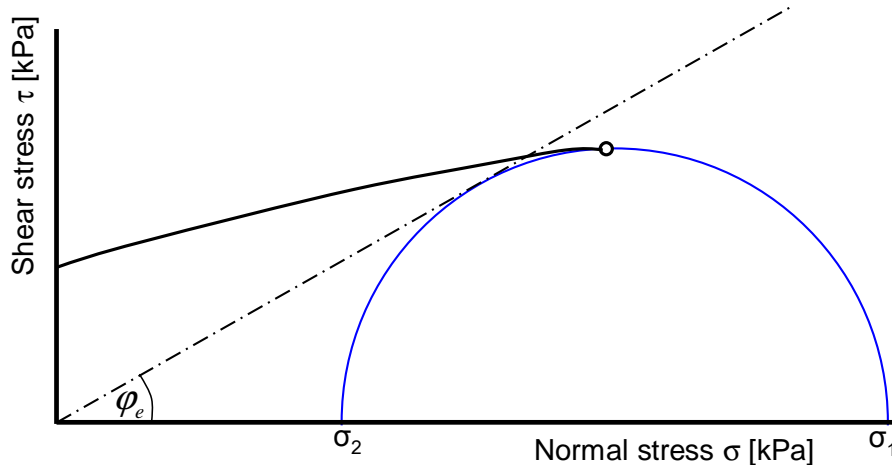


Figure 14: Determination of the effective friction angle φ_e ^[24]

For most bulk solids that have been tested, there was found to be a linear relation between σ_1 and σ_2 ^[24]:

$$\frac{\sigma_1}{\sigma_2} = \frac{1 + \sin \varphi_e}{1 - \sin \varphi_e} \quad (3.3)$$

If we solve Eq. (3.3) for φ_e , we get:

$$\sin \varphi_e = \frac{\sigma_1 - \sigma_2}{\sigma_1 + \sigma_2} \quad (3.4)$$

The effective friction angle φ_e is an essential parameter for the design of hoppers. For each yield locus a different value for φ_e is found, since φ_e is a function of the applied consolidation stress.

3.1.3 Powder flowability

People may have different perceptions on "easy flowing" and "non-flowing" powder, and one may find a certain powder to flow "easily" while others may find the same particular powder to flow "hardly". It is therefore convenient to have a quantitative description about the flowability of powders, so that there is agreement on the terms "easy flowing" and "non-flowing". The criteria that are important for this description are the major consolidation stress σ_1 and the unconfined yield strength σ_c . When σ_c is plotted against σ_1 , the flow function is found, which provides a measure for the powder strength. The flow index ff_c is defined as the inverse slope of the flow function:

$$ff_c = \frac{\sigma_1}{\sigma_c} \tag{3.5}$$

The flow function is a plot of the unconfined yield stress of the powder versus the major consolidating stress. $\sigma_c > \sigma_1$ means the powder will not flow, whereas a point below the line means that flow will occur. Powders are classified according to their flowability, which can be seen in Figure 15 and in Table 1.

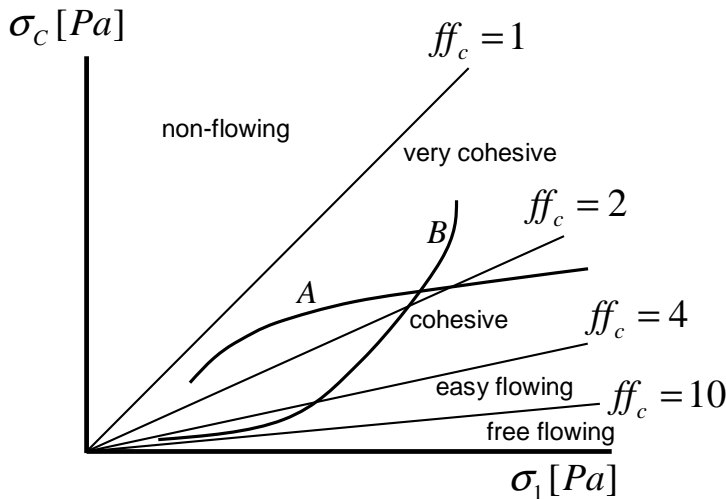


Figure 15: Classification of powder flowabilities by the flow function ff_c [16,30].

In most cases, the flow function increases with increasing major consolidation stress. A powder with flow function curve A will start to flow more easily under high major consolidation stresses, whereas the reverse is true for curve B: a higher major consolidation stress means more difficult flowability. Cohesionless powders do not have any compressive strength ($\sigma_c = 0$), so for these powders the flow index converges to infinity.

Table 1: Classification of powder flowabilities [29,42]

flow index ff_c	evaluation	examples
10-100	free flowing	dry fine sand
4-10	easy flowing	moist fine sand
2-4	cohesive	dry powder
1-2	very cohesive	moist powder
<1	non-flowing	hydrated cement

Each yield locus provides a single point on the consolidation function. Generally 3 or 4 different yield loci are measured to define the flow function.

3.2 Wall shear tests

Apart from the measurement of bulk yield loci, some wall shear tests have been performed as well. These tests are done in order to get the wall friction angle, which is essential to determine the hopper outlet diameter and the hopper angle.

3.2.1 Principle of a wall shear test

The experimental setup of a typical wall shear test is schematically shown in Figure 16.

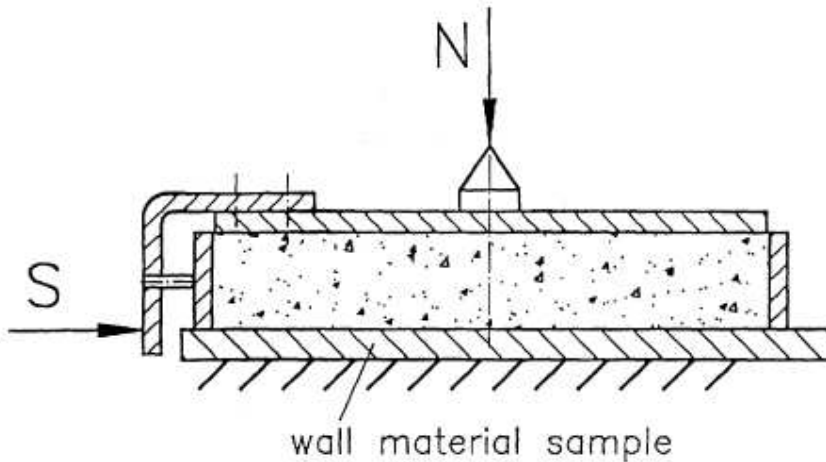


Figure 16: Determination of the wall friction with Jenike shear tester ^[39]

A sample of the wall material is placed on a base, so that the top surface of the sample is equal with the stem. The ring is then placed on the sample, filled with the material, and enclosed with the consolidation lid. The pre-consolidation is done in a similar way as the normal shear test, but with different normal loads. After pre-consolidation, the sample is closed with the wall shear lid, and the cell is loaded with a normal force. Pre-shear is now done, until the shear force levels off. The weight on the yoke is reduced and the sample is sheared over the wall material. After a stationary level is reached, the normal load is reduced and shear is continued. This procedure is repeated until the desired normal load has been reached.

To obtain a different wall yield locus, this procedure is repeated with a different mass for pre-shear. After all experiments have been done, the wall yield locus can be determined, from which the wall friction angle can be calculated.

3.2.2 Wall yield locus

From a wall shear test, a yield locus similar to the bulk yield locus is obtained.

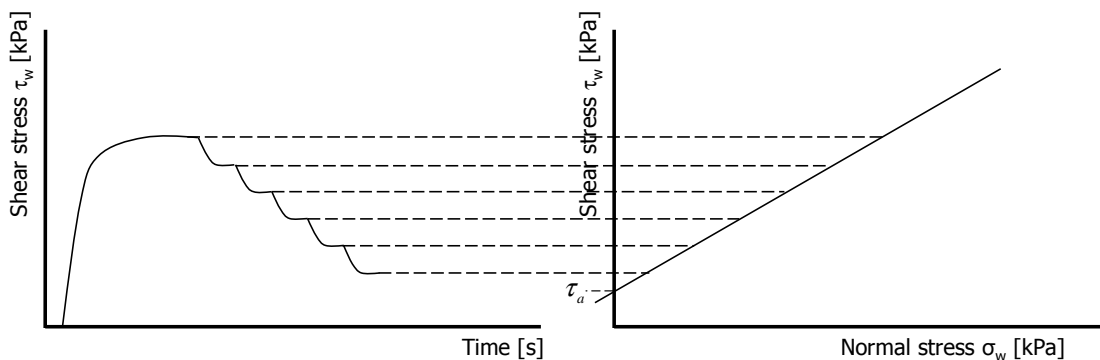


Figure 17: Procedure to get a point of a wall yield locus, using the Jenike shear tester ^[39]

The angle between the horizontal and the wall yield locus is the wall friction angle φ_w . The tangent of this value is better known as the particle-wall friction coefficient μ_{pw} . The wall yield locus is often a straight line for metallic surfaces. Very often, however, the yield locus does not go straight through the origin but there is an intersection with the τ_w -axis. This intersection represents the adhesion τ_a . Due to this offset, φ_w becomes a function of the normal stress σ_w . The wall friction angle can be obtained by

$$\tan \varphi_w = \frac{\tau_w}{\sigma_w} \quad (3.6)$$

The wall friction angle and the effective angle of internal friction are required for hopper design.

3.2.3 Stick-slip phenomenon

The stick-slip phenomenon is the effect caused by the fact that two surfaces alternately stick to and slide over each other, which corresponds to a change in friction force. The cause of this effect is explained by the fact that between two sliding surfaces, friction occurs. The force to overcome this friction is larger at static situations than at dynamic situations. If a force is large enough to overcome the static friction, the change of friction from static to dynamic may cause a sudden change of the velocity.

During shear tests, solids that exhibit stick-slip behaviour show oscillatory results in the shear force, and the shear force does not level off^[29]; there is no constant average shear stress, but rather a minimum and maximum peak value. To obtain the average shear stress at steady state, the mean value between the upper and lower peak is taken. Although this value might underestimate the true shear stress at steady-state flow, it gives a good approximation since the exact value cannot be measured^[39].

3.3 Additional factors of influence

Apart from the flow behaviour, three other factors are of importance for the flowability of a bulk material^[43]

- moisture content
- temperature
- storage time at rest

The moisture content increases a material's cohesive strength and arching tendency, and it will also influence the frictional properties of the material itself. Generally, increasing moisture means decreasing flowability. The equilibrium moisture content of the used limestone is around 0.2 wt%. In general this should not cause flow disturbances. The powder should not deviate from 'normal' behaviour if the moisture content is below 1%. Each measurement day, the moisture content of the material has been measured. In case inexplicable results have been found at the shear tests (e.g. unexpected high shear forces), this could be related to the moisture.

Extreme temperatures will affect flow properties of a material, especially freezing and thawing processes (at around 0°C). At high temperatures, material adhesion could increase due to the bulk solid becoming less free flowing. In the case of the tests done in this project, temperature should not cause any problems, as all experiments are executed at ambient conditions within a considerate time (no extreme weather condition changes). To be sure, the temperature is recorded each measurement day.

Storage time at rest may cause solids to compact or consolidate. Materials could lose or gain moisture, changing the adhesive properties of the material. In the case of limestone, if the material has not been used for a while, sieving is done to break the adhesive clumps and the moisture content is measured.

3.4 Vibrational behaviour and shear cells

Different setups of vibrating shear cells are available. Before these are discussed, an introduction to sinusoidal vibrations is given.

3.4.1 Sinusoidal vibrations

The vibrations during the tests are carried out with sinusoidal vibrations. The same vibrational behaviour is used in the simulations. Figure 18 displays the displacement (a), velocity (b) and acceleration (c) of the vibration signal.

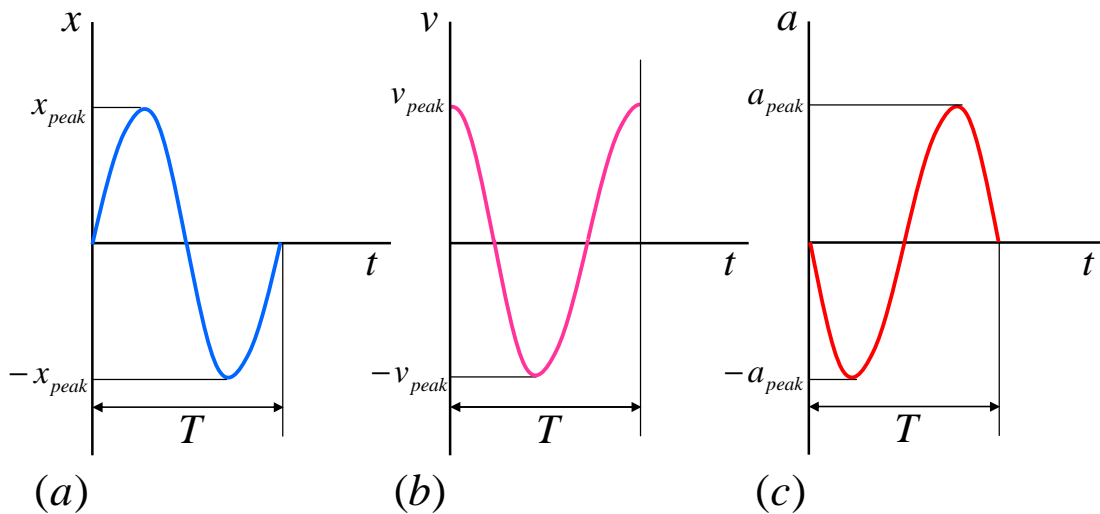


Figure 18: a) Vibration displacement x versus time t , b) Vibration velocity v versus time t , c) vibration acceleration a versus time t

The vibration displacement $x(t)$ [m] is a sinusoidal function that can be expressed by

$$x(t) = x_{peak} \sin(\omega t) \quad (3.7)$$

Here x_{peak} is the peak oscillation displacement [m], and ω is the angular frequency [1/s].

The angular frequency is related to the normal frequency f [Hz]:

$$\omega = 2\pi f = \frac{2\pi}{T} \quad (3.8)$$

Here T is the period of the vibration [s].

If we differentiate Eq. (3.7) to time, we get the vibration velocity v [m/s]:

$$v = \frac{dx}{dt} = x_{peak} \omega \cdot \cos(\omega t) \quad (3.9)$$

With the following definition for the peak velocity v_{peak} [m/s]:

$$v_{peak} = x_{peak} \omega \quad (3.10)$$

We can simplify Eq. (3.9) to

$$v = v_{peak} \cos(\omega t) \quad (3.11)$$

To find an equation for the vibration acceleration a [m/s²], Eq. (3.11) is differentiated with respect to time:

$$a = \frac{d^2x}{dt^2} = \frac{dv}{dt} = -v_{peak} \omega \sin(\omega t) \quad (3.12)$$

The peak acceleration a_{peak} [m/s²] is defined as

$$a_{peak} = v_{peak} \omega = x_{peak} \omega^2 \quad (3.13)$$

With this definition, Eq. (3.12) is reduced to

$$a = -a_{peak} \sin(\omega t) \quad (3.14)$$

Each sinusoidal function can be characterized by the frequency and amplitude. During previous research it has been found that the flow behaviour correlates best to the peak vibration velocity v_{peak} ^[6]. This velocity is therefore used to characterize a certain vibration.

3.4.2 Vibrating shear cell

In the case of the vibrating shear cell, horizontal vibrations are applied perpendicular to the direction of shearing. The vibrating shear cell has been constructed based on the test apparatus by Roberts^[3,4]. Two arrangements are possible when testing the effect of vibrations on the shear tests:

- the top half of the cell is vibrated (as shown in Figure 19 (a))
- the complete shear cell is vibrated (as shown in Figure 19 (b))

When vibrating only the top half of the shear cell, the base is fixed and the ring is vibrated in horizontal direction, perpendicular to the shear direction. This set-up provides measurement of parameters that are required for design of storage and handling equipment (e.g. wall friction angle).

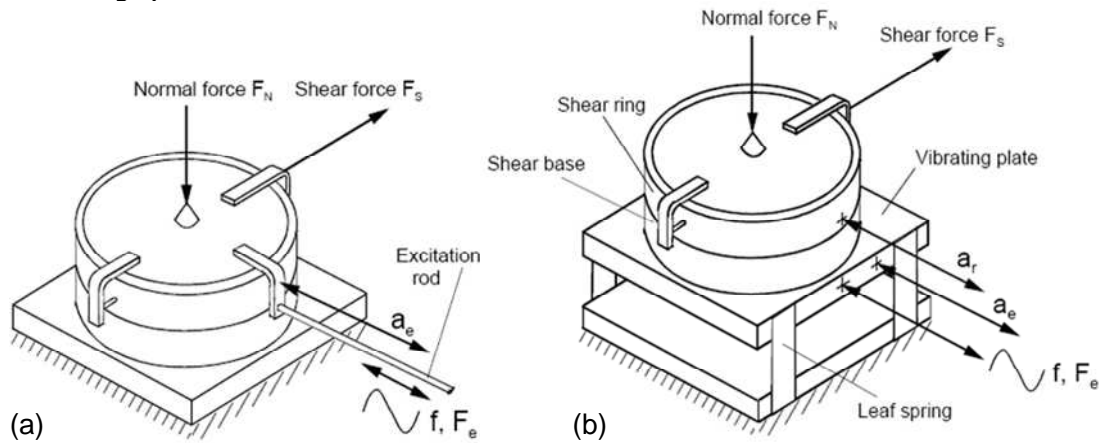


Figure 19: Vibrating Jenike shear cell, (a) with only vibrating top half, (b) complete vibrating shear cell [3-7]

In the second arrangement, the shear cell is mounted on a vibrating plate, which is connected to the horizontal base by means of vertical leaf springs. These leaf springs allow horizontal vibration in only one direction, so that the shear force measurements are not disturbed by the vibrations, as the springs are stiff in the shear direction but elastic in the oscillation direction. The accelerations are monitored on the shear base and the shear ring, to measure the base- and the response- vibration acceleration, respectively. Vibrations are applied by an electrodynamic vibrator, which is connected to the vibrating plate.

Several modes of operation can be applied, as shown in Table 2. These modes differ in the time span when vibrations are applied.

Table 2: Procedures for vibrated shear testing [6]

Method	Vibration Excitation	Application examples
A	during shear	pulsed vibration, e.g. for bridge breaking and discharging
B	during pre-shear and shear	continuous vibration during discharge, e.g. vibrating hopper
C	during pre-consolidation	undesirable vibration during silo filling and storage time without discharging
D	between pre-shear and shear	undesirable vibration during storage, e.g. transportation by truck and train (equivalent to "time consolidation")

The focus of this study is on method B, where vibrations are applied during both pre-shear and shear. The standard procedure of the shear tests is done as explained in Chapter 3.1. The arrangement as used in this project is the complete vibrating shear cell, as shown in Figure 19 (b). The complete experimental setup, which has been worked with in this project, is displayed in Figure 20.

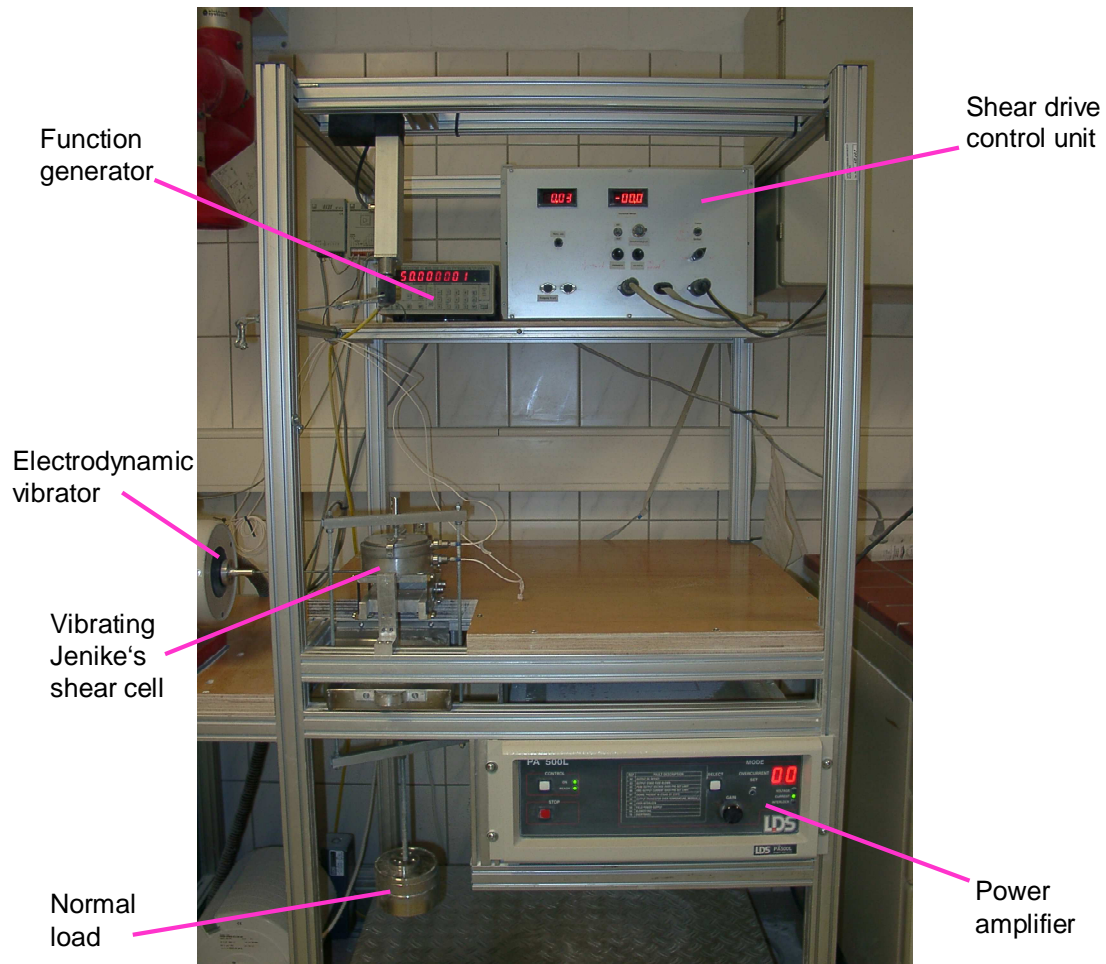


Figure 20: Complete setup of the vibrating Jenike shear cell

The function generator, which is coupled to the electrodynamic vibrator, is used to output a sinusoidal function. The vibrator transmits the sinusoidal vibrations to the shear cell, where the vibration velocity can be fine-tuned using the power amplifier. During the shear test, the shear rate is controlled with the control unit, which is connected to the shear sensor. This sensor and both acceleration sensors are connected to a computer, where the base vibration, response vibration and shear force are monitored using LabVIEW 7.1. The results are analysed using DIAdem 9.1. From Figure 20, if we zoom in on the shear cell, the result is Figure 21. The LabVIEW layout is displayed in Figure 22.

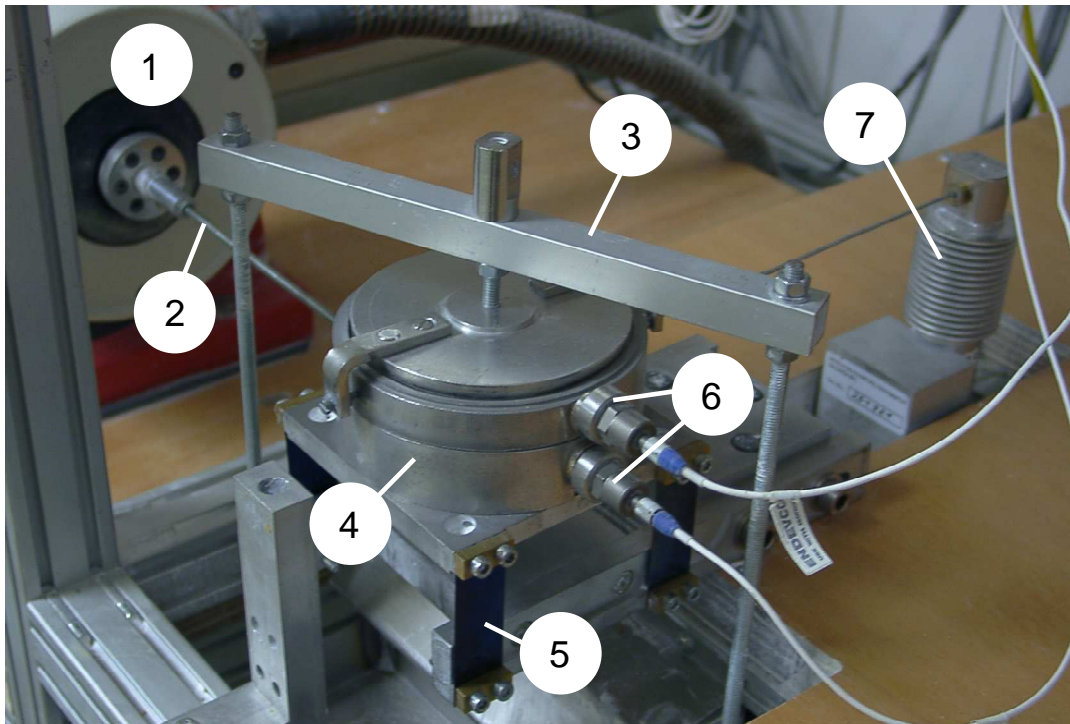


Figure 21: Vibrating Jenike shear cell, as used in the experiments: 1) electrodynamic vibrator, 2) excitation rod, 3) yoke for normal load, 4) shear cell, 5) leaf spring, 6) accelerometers, 7) shear force sensor

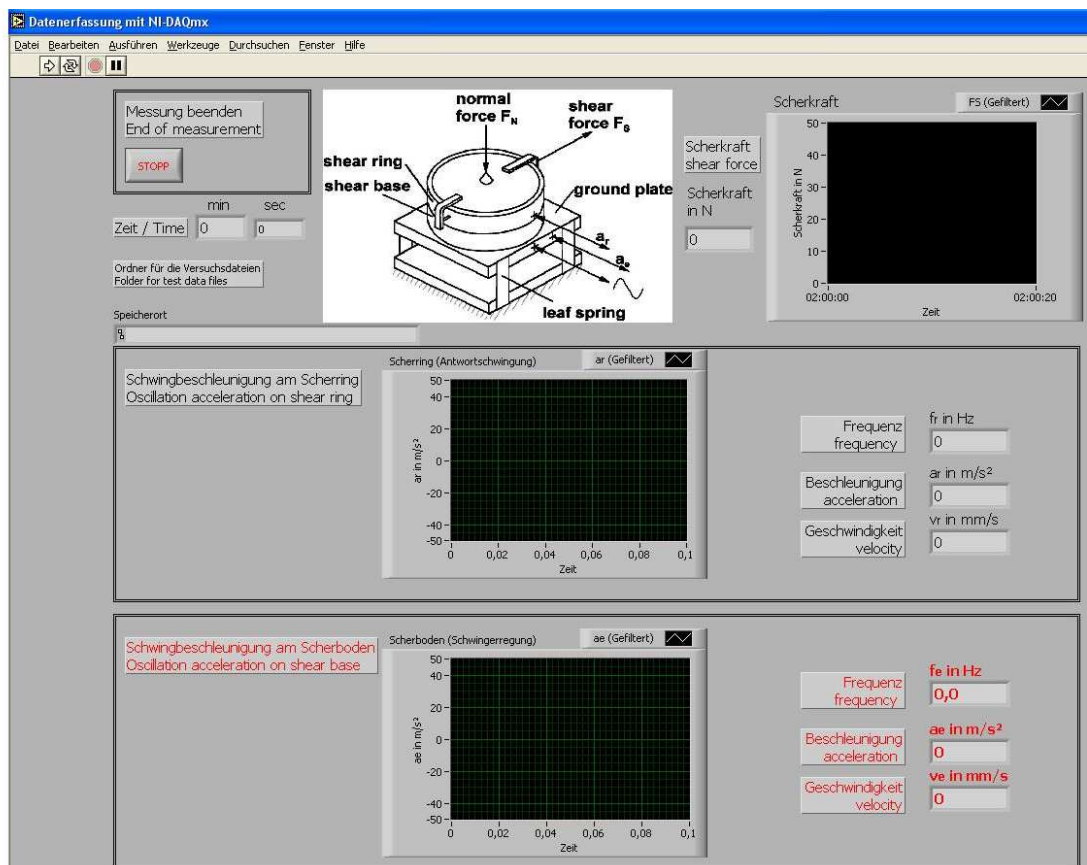


Figure 22: Layout of the LabVIEW program which has been used to monitor vibration accelerations and shear force.

3.4.3 Vibrating wall shear test

The principles of the vibrating wall shear tests are similar to that of the normal wall shear test (see Chapter 3.2.1). Vibrations are induced perpendicular to the shear direction, by fixing the shear ring to the exciter, while the wall material sample is kept non-vibrating. During shearing, the vibration velocity of the exciter is varied, and in times kept at a certain value until the shear force reaches a stationary level again. This procedure is repeated with the same pre-consolidation and pre-shearing load but with a different normal load during shearing. The procedure has been described by Roberts ^[3,4], who extended the work of Arnold ^[5].

3.5 Experimental setup

Now that the principles of the various tests have been reviewed, the material properties and experimental procedures will be outlined and explained.

3.5.1 Material properties

The material that is used for the shear tests is chosen to be limestone Calcit MX10 (CaCO₃, 99.5% pure). This powder originates from "sh minerals", Heidenheim, Germany. Information about Calcit MX10 production and sources can be found in Appendix 4.

Material properties are summarized in Table 3, whereas the particle size distribution is displayed in Figure 23. The average value from 18 measurements is taken; also the error bars are displayed.

Table 3: Calcit MX10 particle properties

d ₁₀	µm	0.5
d ₅₀	µm	1.6
d ₉₀	µm	4.0
Mean surface diameter	µm	0.507
Solid density	kg/m ³	2714
Bulk density	kg/m ³	579
Specific surface area	m ² /g	4.370
Moisture	%	0.22

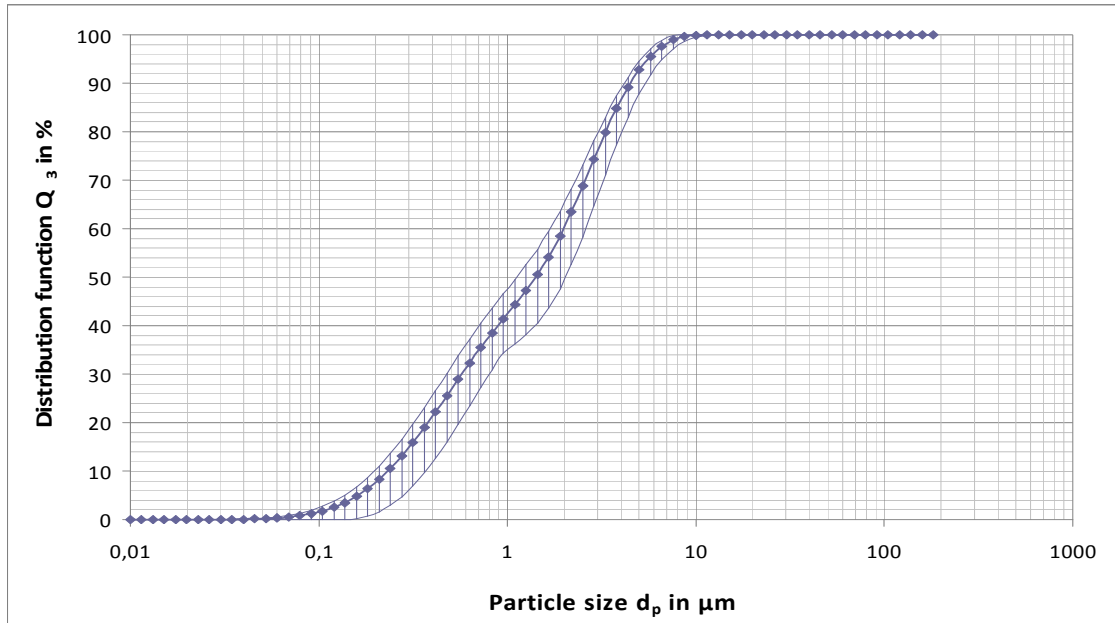


Figure 23: Particle size distribution of the used limestone Calcit MX10

For the wall shear tests, stainless steel X5CrNi 18.10 (cold rolled) is used. This material has roughness of $R_z = 59\mu m$ (largest peak-valley difference) and $R_a = 3.8\mu m$ (arithmetic average). This roughness is a medium roughness, as stainless steel with higher and lower roughness is available as well.

3.5.2 Experimental procedures

The experimental setup of the shear cell is described in Chapter 3.4. The shear cell masses and dimensions are summarized in Table 4.

Table 4: Masses and dimensions of the vibrating Jenike shear cell

Masses			Shear cell dimensions	
Yoke	m_y	0.4844 [kg]	Cell diameter	$9.5 \cdot 10^{-2}$ [m]
Shear lid	m_l	0.1287 [kg]	Height of base	$1.3 \cdot 10^{-2}$ [m]
Shear ring	m_r	0.0741 [kg]	Height of ring	$1.6 \cdot 10^{-2}$ [m]
Consolidation lid	m_{cl}	0.1565 [kg]	Cross sectional area	$7.088 \cdot 10^{-3}$ [m ²]
Empty shear cell	m_{sc}	0.3228 [kg]	Total volume	$2.056 \cdot 10^{-4}$ [m ³]

The applied shear rate is 2 mm/min, the frequency and amplitude of the vibration function generator are set to 50 Hz and 0.20 Vp-p (peak to peak voltage), respectively. For pre-consolidation, 20 twists have been performed. The test charts for the shear tests and wall shear tests are shown in Appendix 11. The normal load masses that have been applied for each yield locus are summarized in Table 5.

Apart from these listed values, shear tests with $v_{peak} = 0.07 \text{ m/s}$ have been performed as well, however it was found to be impossible to do shear tests at this high vibration intensity. The whole shear cell vibrates too heavy and powder escaped from under the shear ring and under the shear lid.

Each day, the temperature and relative humidity were written down, as well as the moisture content of the limestone was measured. This was done by putting a sample of $\sim 12 \text{ g}$ at 120°C in a Sartorius MA30 Moisture Analyzer. These results have shown no extremely high values (max. 0.81%).

Table 5: Applied masses for different yield loci

Yield locus	Pre-consolidation	Pre-shear	Shear						v_{peak}
			kg						
-	kg	kg	kg						m/s
1	3	1.1	0.8	0.5	0.2	0.0	0 - 0.02		
2	4	2.1	1.6	1.0	0.5	0.3	0 - 0.02		
Wall	13	13	9.0	7.0	4.0	2.0	1.0	0.3	0 - 0.06

To calculate the bulk density ρ_b [kg/m^3] of the material, the complete shear cell with powder is weighed on a balance to give weight m_T [kg]. The bulk density can be calculated by

$$\rho_b = \frac{m_T - m_{sc}}{V_{sc}} \quad (3.15)$$

Here m_{sc} is the mass of the empty cell [kg] and V_c is the inner powder volume of the cell [m^3].

A normal force is induced by hanging weights on a yoke. In order to obtain the applied normal stress σ_n [Pa] from the applied masses, one can use the following equation:

$$\sigma_n = \frac{(m_m + m_y + m_l + m_r + V_r \cdot \rho_b) \cdot g}{A} \quad (3.16)$$

Here m_m is the mass that is placed on the yoke [kg], V_r is the volume of the ring [m^3], g is the gravitational acceleration [m/s^2] and A is the cell cross sectional area [m^2].

To calculate the shear stress τ [Pa], merely divide the shear force by the cell cross sectional area:

$$\tau = \frac{F_s}{A} \quad (3.17)$$

3.6 Results and discussion

After the tests have been done, the results are analysed. In this chapter, the results of the tests are given and discussed. Examples of raw data will be given, which after treatment give the desired yield loci. Results regarding the effect of vibrations on the powder flowability and wall friction are discussed as well.

3.6.1 Shear test results

All shear test results have been summarized in Appendix 8. In Figure 24, a typical outcome of a shear test is displayed. On each horizontal axis the time [s] is displayed. The first graph shows the shear force [N], the second graph the base acceleration [m/s^2] and the last graph shows the response acceleration [m/s^2].

The test is divided into two parts, where first pre-shearing and then shearing is done. During pre-shearing, the shear force reaches a steady state value for a certain vibration intensity. For the shearing part, the shear force increases until a peak value is reached and then gradually decreases.

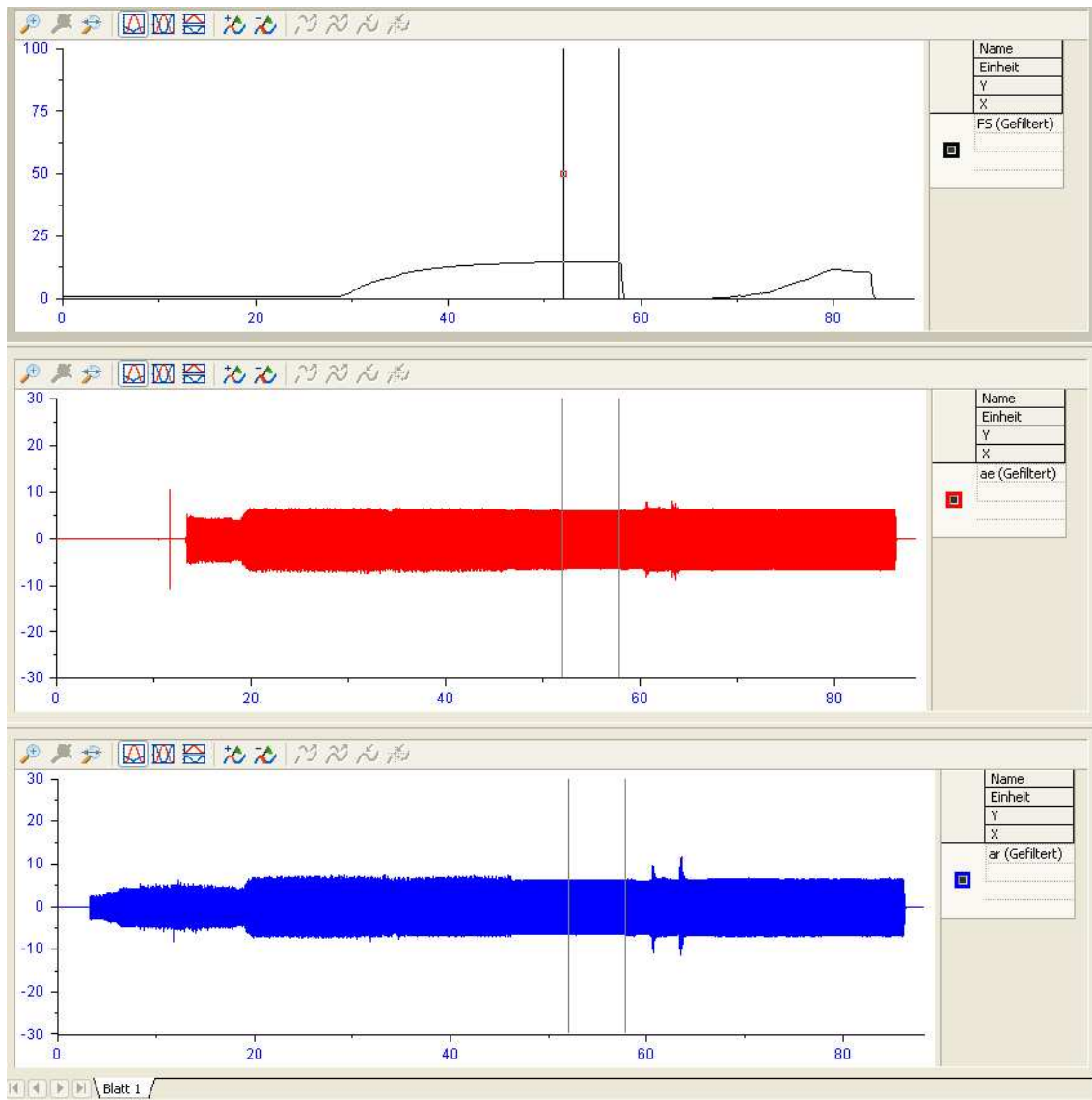


Figure 24: Example of a typical shear test outcome. Here $v_{peak} = 0.02m/s$, $m_{pre} = 1.1kg$ and $m_m = 0.2kg$ have been used. Top graph: shear force versus time. Middle graph: base acceleration versus time. Bottom graph: response acceleration versus time

If we zoom in we can see Figure 25. By using the DIAdem software, by zooming in we can find the steady state shear force and the corresponding acceleration, both base and response. The difference between the top and bottom peak is written down and taken to be the double peak acceleration.

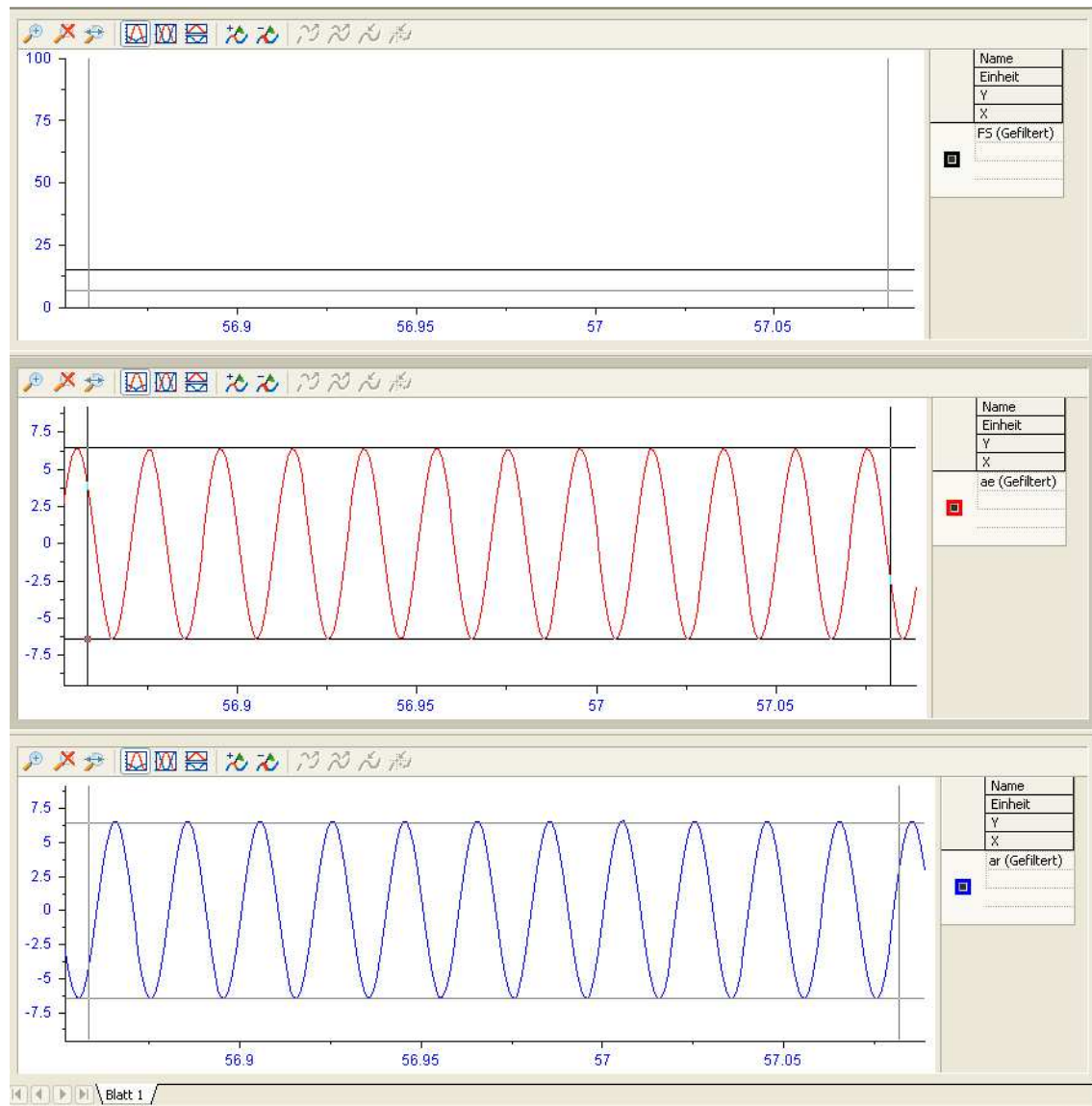


Figure 25: Example of a typical shear test outcome. Here $v_{peak} = 0.02m / s$, $m_{pre} = 1.1kg$ and $m_m = 0.2kg$ have been used. This sample is a magnification of Figure 24

Yield loci have been measured for different vibration velocities at fixed frequency $f = 50Hz$. These are summarized in Figure 26.

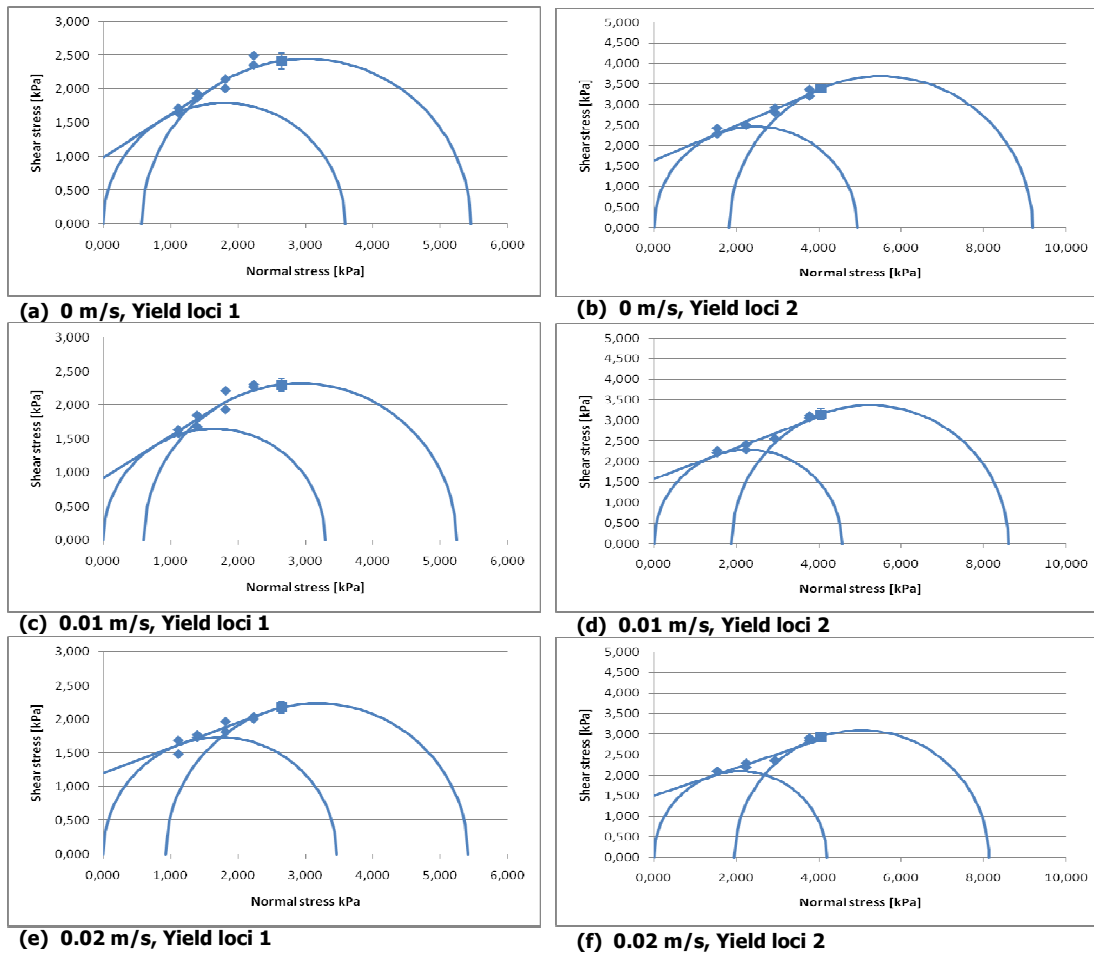


Figure 26: Yield loci 1 and 2 with corresponding Mohr's circles for peak vibrations $v_{peak} = 0 - 0.02 m/s$

It can be seen that, with increasing peak vibration, σ_c and σ_1 remain constant or only slightly decrease. This is shown more clearly in Figure 27. The effect is seen to be stronger for higher densities. Vibrations hardly seem to affect the cohesion τ_c . It may be concluded that vibrations do have a significant effect on the flow behaviour.

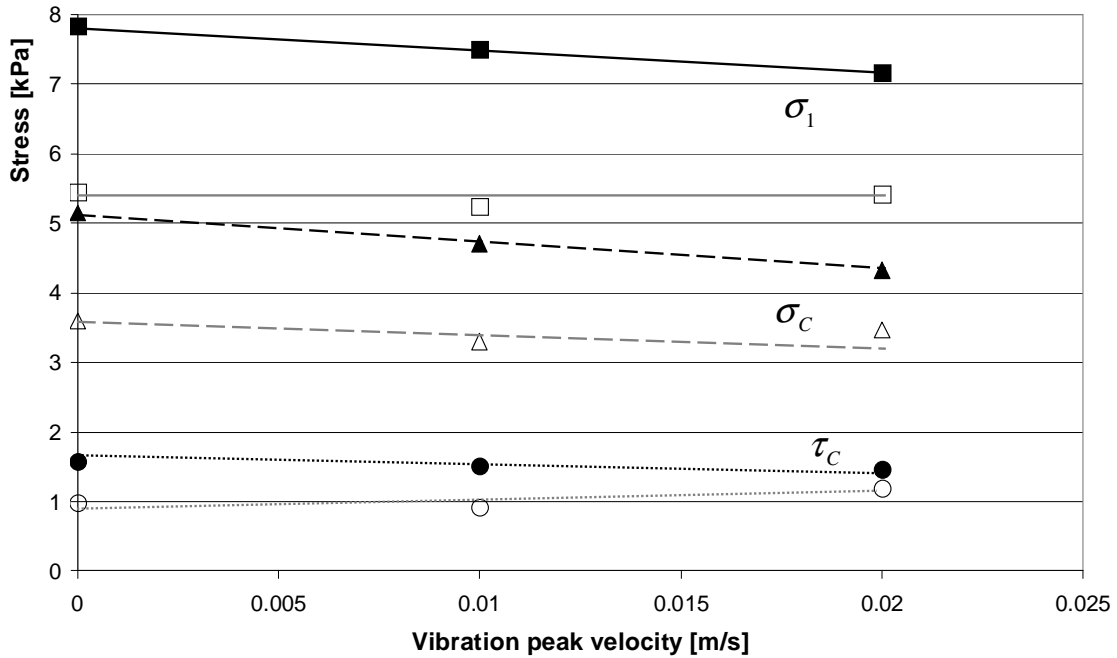


Figure 27: σ_1 , σ_c and τ_c as function of v_{peak} for both yield loci

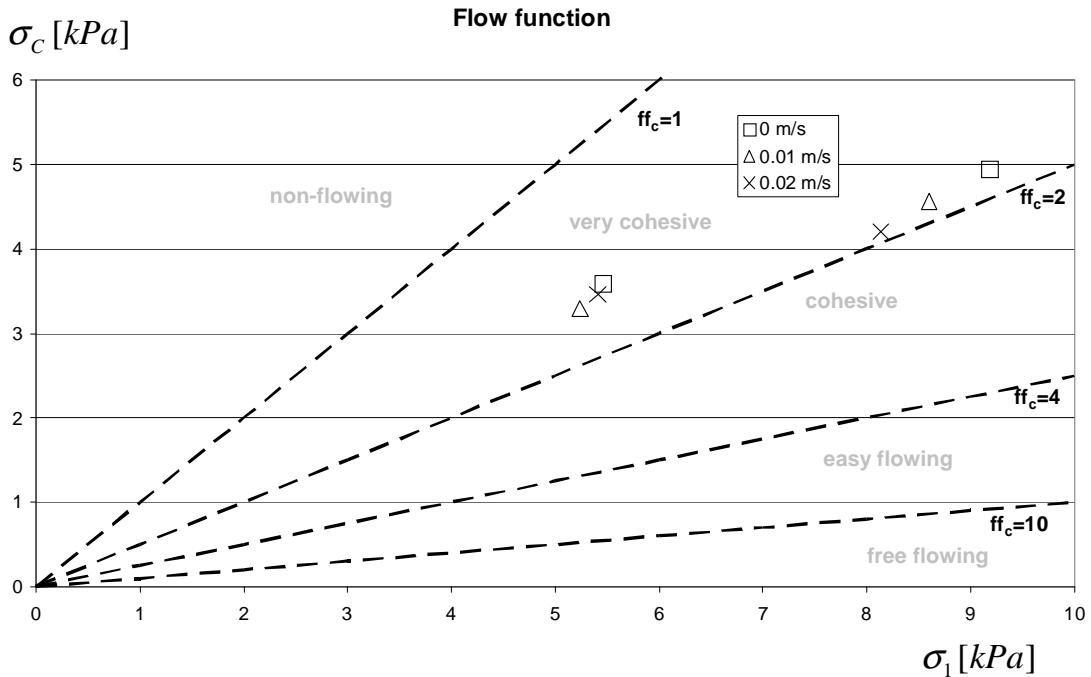


Figure 28: Flow function for the different vibration peak velocities

Each test represents a point on a flow function. For each peak vibration there are two points of the flow function. This is shown in Figure 28. Here it can be seen that the vibration slightly decreases the flow function, although no clear effect is observed. All points remain in the same (very cohesive) flow region. No clear conclusion can be drawn, as too few measurements have been performed to be able to say anything about the effect of vibrations on the flowability. Due to the low peak oscillation velocities the flow classification is apparently not changed.

We are also interested in the effect on the effective and internal friction angle, φ_i and φ_e , respectively. These results are displayed in Figure 29. Here a clear decrease of both friction angles is shown with respect to v_{peak} . Vibrations do have a significant effect on internal particle friction.

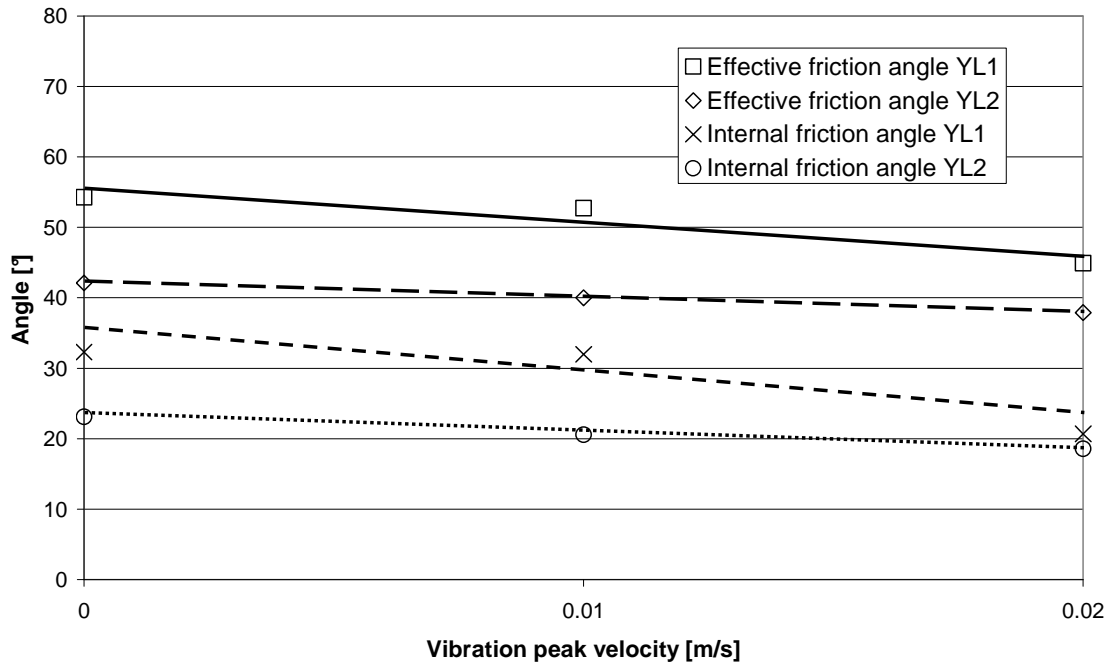


Figure 29: φ_i and φ_e as a function of the vibration peak velocity

3.6.2 Wall shear test results

All wall shear test results have been summarized in Appendix 8. A typical result of a wall shear test is shown in Figure 30. Here only one of the sensors was mounted on the shear ring so only the response is monitored.

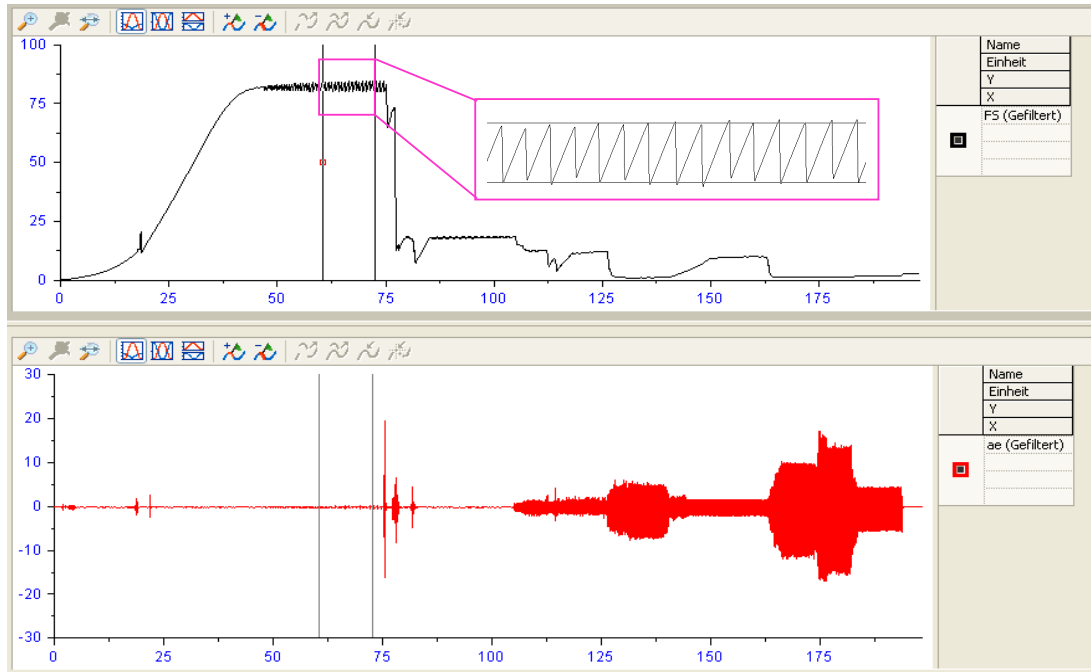


Figure 30: Example of a typical wall shear test result. Here $m_{pre} = 13kg$ and $m_m = 2.0kg$ have been used. The inlet clearly shows the zigzag pattern of the stick-slip effect

It can already be seen that the vibrations have an effect on the shear force. When we zoom in to the selected region, the stick-slip effect is visible by the zigzag pattern (see inlet). Both the upper and lower value of the shear force are recorded, where the average value is taken for the wall yield locus.

When vibrations were applied, the stick-slip behaviour was found to be decreased; the relative difference between upper and lower value was decreased or even disappeared.

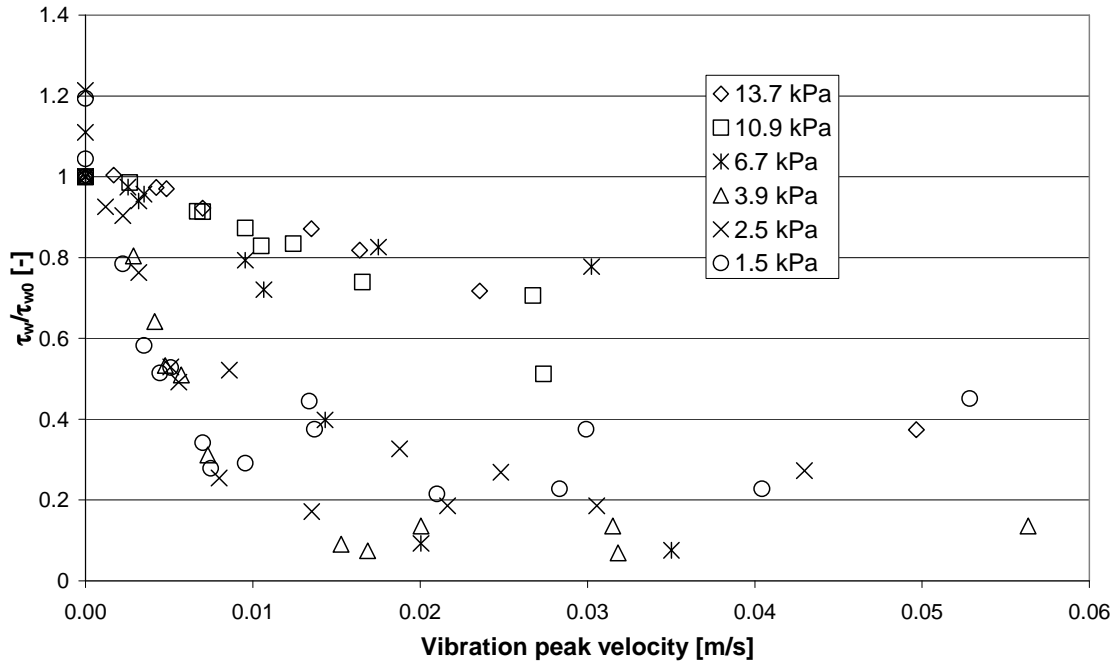


Figure 31: Wall shear stress ratio as a function of the peak vibration velocity

In this figure, no general relation can be seen between the wall shear stress ratio and v_{peak} , as the effect is different for each normal load. The relation between τ_w / τ_{w0} and v_{peak} has been modelled by Roberts [3], who introduced a failure criterion:

$$\frac{\tau_w}{\tau_{w0}} = 1 - \frac{\beta_w}{\tau_w} \left[1 - \exp\left(-\frac{v_{peak}}{\gamma_w}\right) \right] \tag{3.18}$$

In this model, β_w represents the maximum possible reduction in wall shear stress [kPa] and γ_w is the vibration velocity constant [m/s] which indicates the rate of decay of the shear stress. The meaning of these parameters is displayed more clearly in Figure 32. In this figure, $\tau_{w\infty}$ represents the limiting wall shear stress for high vibration peak velocities.

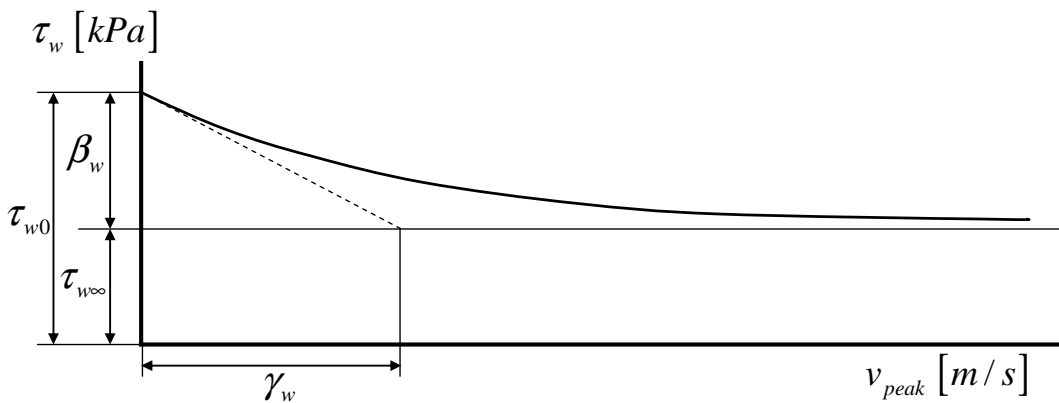


Figure 32: Wall shear stress failure criterion [3]

Using β_w and γ_w as regression parameters, the model was fitted through the experimental results. For low normal stresses (≤ 3.9 kPa), it was found that the experimental results can be predicted by the model. The results are displayed in Figure 33. The fit parameters are shown as inset.

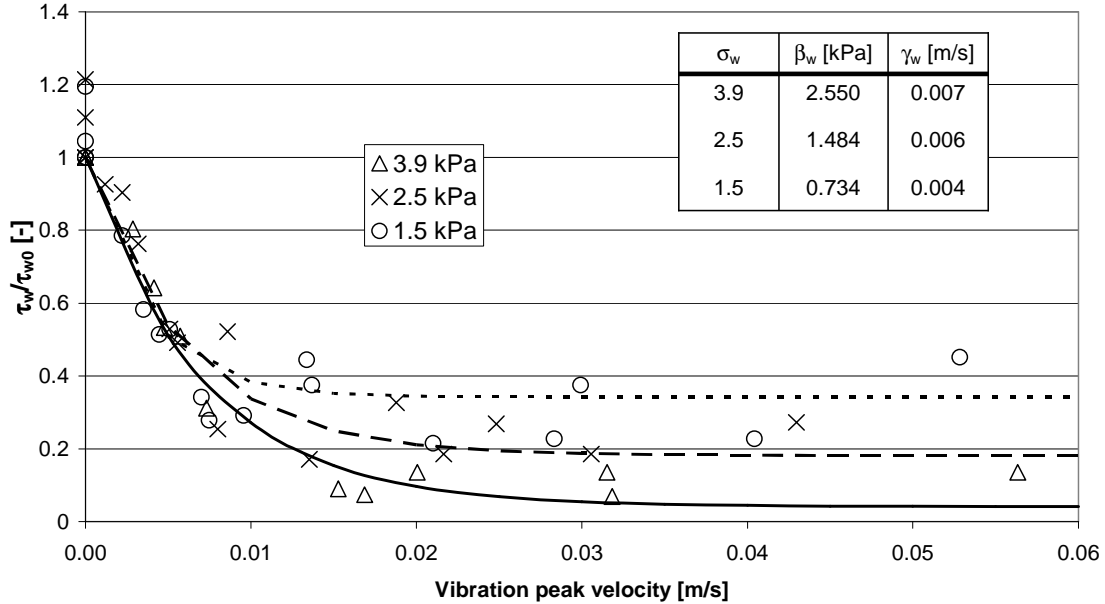


Figure 33: Wall shear stress ratio as a function of the peak vibration velocity, compared with the failure criterion, for small normal loads

To see an effect on the wall friction angle, the results are divided into velocity regions. For low vibration velocities, already an effect is seen. Figure 34 displays the results at low velocities graphically. The wall yield loci seem to have the same slope in the beginning, but are only shifted to the right compared to the previous.

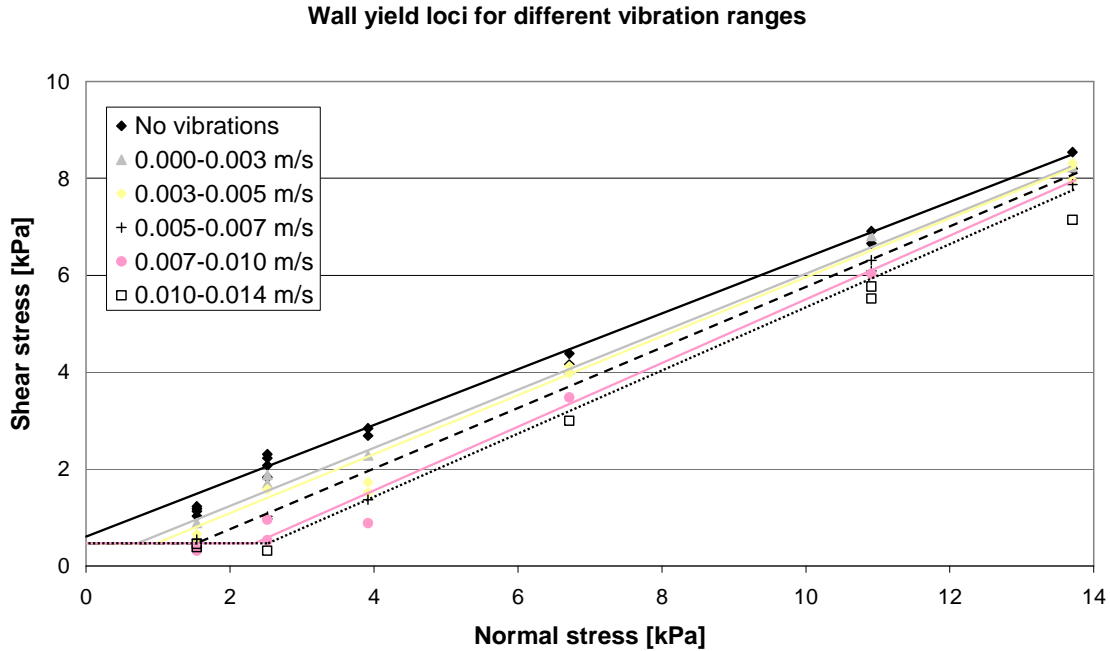


Figure 34: Wall yield loci for vibration ranges up to 0.01 m/s compared to the wall yield locus without vibration

For larger vibration peak velocities (>0.01 m/s) we see a similar effect, as displayed in Figure 35. For low normal stresses, the shear stress was found to be close to zero. Increasing vibration velocities therefore reduce the shear stress for increasing normal stresses. The wall friction angle can be seen to decrease as well.

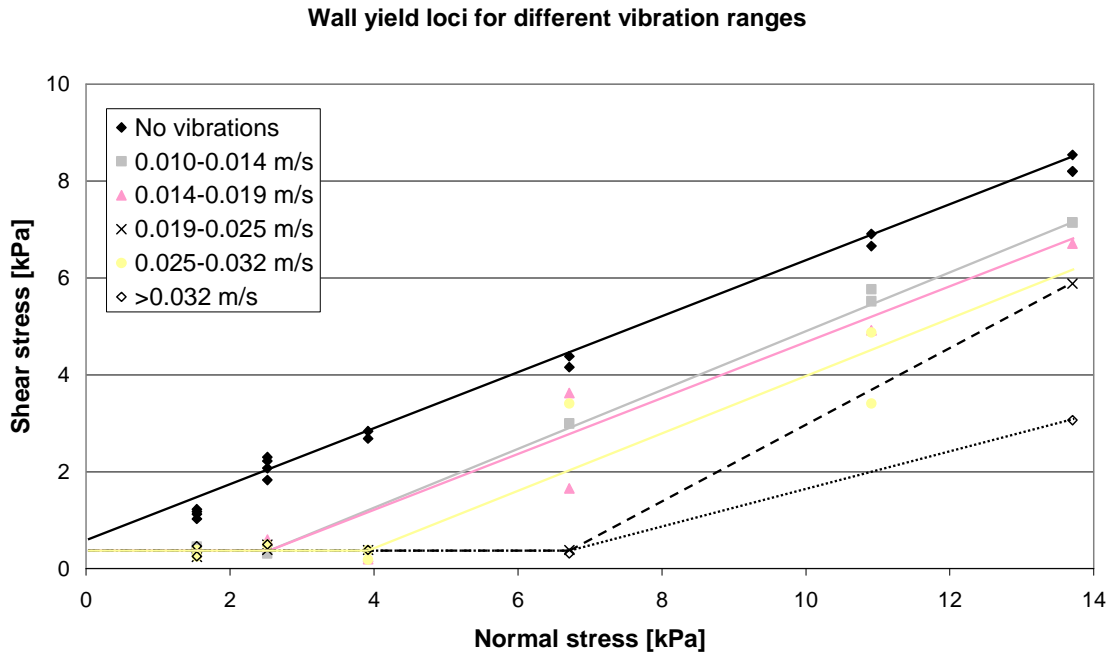


Figure 35: Wall yield loci for vibration ranges larger than 0.01 m/s compared to the wall yield locus without vibration

3.7 Conclusions

Vibrations show an interesting application to aid the flow behaviour of cohesive limestone powder. From the results of the vibrating shear cell, it can be concluded that vibrations decrease the unconfined yield strength σ_C , where a stronger effect is seen for higher bulk density. Only a small effect on the flow function was found; the flow classification is not changed by applying vibrations. A stronger effect was seen on the internal and effective friction angle, resp. φ_i and φ_e . These values both have shown a decrease with increasing vibration intensity.

In the case of the wall shear tests, for low normal stresses the behaviour can be fitted by the failure criterion of Roberts. This model is not valid for high normal stresses. However in both cases a strong decrease in wall shear stress was found with increasing vibration peak velocity. A strong effect was seen on the wall friction angle φ_w , as it drastically decreases with increasing vibration velocities. This offers interesting opportunities in increasing the hopper angle and decreasing the hopper outlet.

Although adding vibrations show a promising aid to increase powder flowability, only few tests have been performed in this project. More yield loci should be measured and higher vibration intensities should be applied to be able to draw clearer conclusions on the effect of vibrations on the flow behaviour of ultrafine cohesive limestone powder.

3.8 List of symbols and abbreviations

Symbols

Variable	Unit	Explanation
a	m/s ²	Acceleration
A	m ²	Cross sectional area
d	m	Particle diameter
f	Hz	Frequency
F	N	Force
ff	-	Flow factor
g	m/s ²	Gravitational velocity
m	kg	(reduced) mass
R	m	Roughness
t	s	Time
v	m/s	Velocity
V	m ³	Volume

Subscripts

Subscript	Explanation
0	Unvibrated
1	Major principal
2	Minor principal
a	Arithmetic
b	Bulk
c	Cohesion
cl	Consolidation lid
C	Unconfined yield
e	Effective
	Excitation
f	Friction
i	Internal
l	Shear lid
m	Shear mass
M	Mean
n	Normal
N	Normal
p	Particle
peak	Peak value
pre	Pre-shearing
r	Response
	Shear ring
R	Radius
S	Shear
sc	Shear cell
sf	Stationary flow
T	Total
w	Wall
y	Yoke
z	Largest peak-valley difference

Greek symbols

Variable	Unit	Explanation
α	°	Angle
β	Pa	Maximum shear stress reduction
γ	m/s	Vibration velocity constant
ε	-	Porosity
φ	°	Friction angle
μ	-	Friction coefficient
ρ	kg/m ³	Density
σ	Pa	Normal stress
τ	Pa	Shear stress

Superscripts

Superscript	Explanation
max	Maximum
min	Minimum

4 Discrete Element Model

For the two-dimensional simulations of the silo, the Discrete Element Method will be used. In this chapter, it will be explained what this method is and how the used program works. Multiple simulations will be done to understand several parameters, such as damping and friction. Complete understanding of these parameters is required so that the user knows what actually happens inside the software, so that comparisons with theory and other simulation software can be made.

During working with ITASCA PFC^{2D}, several mistakes have been made. Several times there has not been complete understanding between the user and the software and several common mistakes have been made. For people who are planning to work with ITASCA PFC^{2D}, Chapter 4.7 gives an overview and evaluation of these common mistakes. It is recommended to first read this chapter before starting to work with the software.

Simulations started getting importance in the 1980s. Before this time, computer processing speed and data storage were too limited for large systems of particles. As speed and capacity of computers increased, computer simulations started to become an effective and powerful tool. Importance of simulations lies in the fact that in simulations e.g. frictionless materials can be used and environments that can be difficultly observed can be modelled. Intermediate states can be easily visualized, and simulations can give valuable insight on how granular materials behave ^[16].

Most simulations that involve granular materials are Discrete Element Methods (DEM). Rigid particle molecular dynamics (MD) situations exist as well, where collisions are binary and instantaneous. However, in dense systems, particles have multiple contacts that take a certain time. This was the basic difference between MD and DEM. The Discrete Element Method (DEM) was introduced by Cundall ^[44] for the analysis of rock-mechanics problems, and later applied by Cundall and Strack ^[45] who applied it for soils. A more thorough description of the method is described in two papers, by Cundall ^[46] and Hart et al. ^[47]. According to the definition of Cundall and Hart ^[48], the used PFC^{2D} software from ITASCA is regarded as DEM software. They assume that particle contacts exist for a certain amount of time, and calculations are solving Newton's second law of motion and a force-displacement law. A more thorough description of the DEM method will be given in the following section.

4.1 Theoretical background

The Discrete (or Distinct) Element Method (DEM) is a numerical technique to model the motion of a large number of particles that are interacting with each other through collisions. This method considers each body separately, and it describes the path of each particle as time proceeds. The particles are treated to be independent, and (in the case of a two-dimensional system) they have a finite extent in 2 dimensions. The Discrete Element Method allows finite displacements and rotations of discrete particles and automatically recognizes new contacts. Interaction only occurs at contact among each other or with the interfaces ^[49].

The particles are treated as rigid bodies, and contacts only occur as point contacts. In reality, particles are allowed to deform. This is accounted for by the fact that particles are allowed to (virtually) overlap. The magnitude of the overlap is related to the contact force via a contact force model, and all overlaps are small in relation to particle sizes ^[49,50].

Even though it is a two-dimensional simulation, three-dimensional spherical particles exist in the PFC^{2D} software of ITASCA. The particles look circular but are treated as spheres by means of their mass. A two-dimensional assembly of circles can therefore be seen as a three-dimensional system where all (variable-radius) sphere centroids lie in the same plane. Because of only spherical particles, the PFC^{2D} software can be seen as a simplified version of DEM. Non-spherical particles can be formed by the clump logic, where spherical particles connect via contact bonds to form a clump.

The use of only spherical particles allows easy detection of overlaps and locations of contact points. Other shaped particles could cause interlocking, thus having a higher effective friction than spherical particles. When using irregular shaped particles, the resulting moment on a particle may cause it to rotate. This causes the particles to obtain a preferable orientation causing anisotropic behaviour of the complete system. In the case of spherical particles, this preference is absent. Furthermore, with irregular shapes more complicated numerical calculations need to be performed due to the irregular surface. One needs to use more intensive calculations to find when and where contacts have been formed and broken ^[16].

The PFC^{2D} software contains only balls and walls. The walls are not influenced by the equations of motion; a force on a wall does not cause it to move. The movement of the walls is supplied by the user and does not change, regardless of the forces on it. Only the force-displacement law applies, as it accounts for ball-wall contacts. This will be examined more closely in Chapter 4.5. First, we will take a look at how the calculation cycle looks like.

4.2 Calculation cycle

The calculations performed in PFC^{2D} consist of the application of Newton's second law of motion to the particles, based on a force-displacement law at the contacts. Newton's second law of motion is used to determine the motion of each particle arising from the contact and body forces acting upon it, while the force-displacement law is used to update the contact forces arising from the relative motion at each contact.

The calculation cycle is displayed in Figure 36. It consists of the repeated application of the law of motion to each particle, a force-displacement law to each contact, and a constant updating of wall positions. Ball-ball and ball-wall contacts are formed and broken automatically during the course of a simulation.

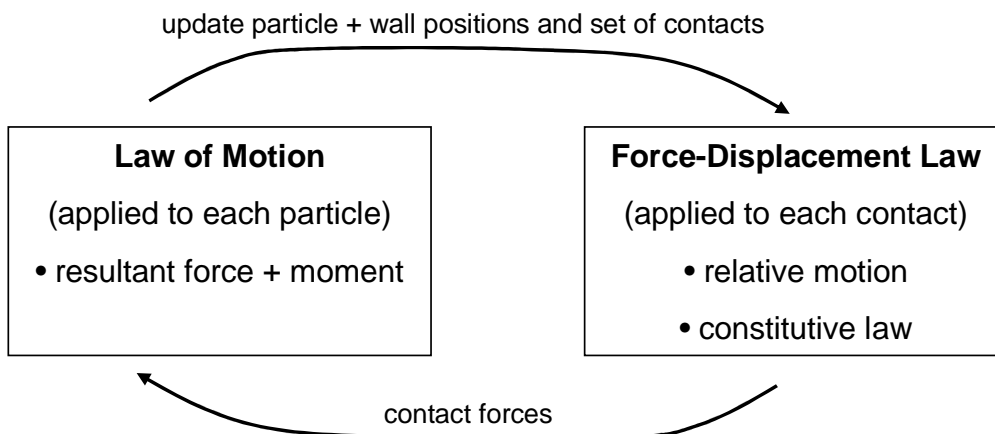


Figure 36: Calculation cycle in PFC^{2D} [49]

At the start of each time step, the set of contacts is updated from the known particle and wall positions. The force-displacement law is then applied to each contact to update the contact forces based on the relative motion between the two entities at the contact and the contact constitutive model. Next, the law of motion is applied to each particle to update its velocity and position based on the resultant force and moment arising from the contact forces and any body forces acting on the particle. Also, the wall positions are updated based on the specified wall velocities. After this, the cycle is repeated, until cycling encounters an ending condition. The calculations of the law of motion and the force-displacement law are done in parallel. A detailed outline of the calculations made each cycle is given in Appendix 6.

4.3 Integration time step

The integration time step is chosen to be so small that, during a single time step, disturbances cannot deviate from any particle further than its immediate neighbours. This means that the forces acting on any particle are determined solely by its interaction with the particles with which it is in contact. The time step for integration is crucial for numerical calculations. If the integration time step is too large, two particles may cross each other, and may cause numerical instability. When using a too small time step, on the other hand, unnecessary calculation time is consumed. It is therefore critical to have a good estimation for the optimal time step.

The time step that is used in PFC^{2D} can be found by a simplified procedure. Each cycle a critical time step is estimated, of which a certain fraction is taken. To calculate the critical time step, we see the system as a one-dimensional mass-spring system described by a point mass m [kg] and spring stiffness k_n [N/m] (explained in more detail in Chapter 4.5.2). The critical time step t_{crit} [s] can be calculated by:

$$t_{crit} = \sqrt{\frac{m}{k_n}} \quad (4.1)$$

Please note here that the particle mass and the particle stiffness are taken (and not the reduced mass and contact stiffness, which is the case in other definitions). If more than one particle is present in the simulation, the smallest mass is taken. The actual time step that is taken for the simulations is a fraction of this critical time step. This fraction is standard set as 0.8 and can be changed manually by the user.

The stability of this time step estimation is a point to discuss. This will be evaluated more closely in Chapter 4.5.3, where two-particle collisions will be examined.

4.4 Law of motion

If the particles are assumed to be completely rigid, and the behaviour of the contacts is described by a soft contact model, then the movement of the particles can be described in terms of Newton's law of motion. When all forces \vec{f}_i [N] acting on a particle are known, the problem is reduced to integration of Newton's second law of motion. This law describes fundamental relationship between the translational and rotational motion of a body and the forces on the body causing this motion.

For translational motion,

$$m_i \vec{a}_i = \vec{f}_i + m_i \vec{g} \quad (4.2)$$

Here m_i is the mass of particle i [kg], \vec{a}_i is the acceleration of the particle [m/s²], \vec{g} is the gravitational velocity [m/s²]

For rotational motion,

$$I_i \vec{\omega}_i = \vec{q}_i \quad (4.3)$$

Here I_i is the moment of inertia [kg m²] of a spherical particle, $\vec{\omega}_i$ is the angular acceleration of the particle [1/s²], \vec{q}_i is the total torque on the particle [N m]. This torque is defined as

$$\vec{q}_i = \vec{q}_i^{\text{fric}} + \vec{q}_i^{\text{roll}} \quad (4.4)$$

Since rolling is not considered,

$$\vec{q}_i = \vec{q}_i^{\text{fric}} \quad (4.5)$$

These forces can be calculated by solving the force-displacement law. This will be explained in the next subsection.

4.5 Force-displacement law

On the particles, both body forces and contact forces act. Body forces are forces that acts on all particles (e.g. gravitational forces and electromagnetic fields), whereas contact forces only occur when particles are in contact. The present simulations only include gravitational forces, and particle-particle and particle-wall forces.

The gravitational force acts on all the particles. The force on particle i due to gravity \vec{f}_{gi} acts at the particle centre and can be expressed by

$$\vec{f}_{gi} = m_i \vec{g} \quad (4.6)$$

where m_i is the mass of particle i [kg] and \vec{g} is the gravitational acceleration vector [m/s²].

Contact forces can be calculated from the force-displacement law. This law is separated into two parts:

- particle-particle contact model
- damping model

In the particle-particle contact model, the interaction force between particles is related to the overlap of two particles. Contact forces are typically decomposed into a normal and a shear component, with respect to the contact surface. In tangential direction, the forces depend on the tangential displacement as well, since the beginning of the contact ^[51,52]. Various models have been developed over the years, and the models that have been of interest in this project will be discussed in Chapter 4.5.2 and 4.5.5, for normal and tangential direction, respectively.

There are several models available to dissipate kinetic energy, and the viscous damping model is one of them. This model adds a normal and/or shear dashpot to each contact, which act in parallel with the contact model. The theory and how the viscous damping model works in the PFC^{2D} software will be under discussion in Chapter 4.5.3 and 4.5.6, for normal and tangential direction, respectively.

Apart from viscous damping at contacts, local damping can be used and acts on each particle (instead of particle-particle contacts). Chapter 4.5.7 discusses how local damping affects particle-particle collisions.

In principle, four surface deformation effects are essential when explaining force-displacement behaviour in case of particle-particle contacts. These effects have been characterized in Table 6.

Table 6: Deformation effects that can occur in particle-particle contacts ^[53]

Effect	Reversible	Dependent on		Example
		Consolidation time	Deformation rate	
Elastic	Yes	No	No	All particulate solids
Plastic	No	No	No	Mineral powders
Viscoelastic	Yes	Yes	Yes	Bio-particles
Viscoplastic	No	Yes	Yes	Nanoparticles fusion

Each contact model can be explained by these four terms: elastic, plastic, viscoelastic and viscoplastic. Particle-particle collisions can be placed in an elastic and a plastic region. In the elastic region, the deformation is reversible; after removing the normal force, the particle will go back to its original state. For a plastic deformation, the deformation is permanent; the particle is permanently deformed due to the overlap, even after removing the normal force. A consequence of plastic deformation is that energy is dissipated.

Viscoelastic and viscoplastic effects consider the time dependence on the force-displacement law. Deformation and adhesion might change over time, and this is taken into account in the contact model by viscous forces. It therefore gives a correction for slow deformations. Before any contact laws are discussed, first the effect of friction will be studied.

4.5.1 Friction

Friction plays a role when two surfaces slide over each other and thus in this case when a particle hits another particle or a wall. In the simulation software, it is possible to set both ball and wall friction. In this section, the influence of friction is investigated by dragging a non-spinning ball over a horizontal wall, while the energy caused by friction is measured. In order to understand what is happening, the theory about friction is briefly reviewed ^[54].

Friction is defined as the force that resists the relative motion of two surfaces that are in contact with each other, or a surface in contact with a fluid. The presence of friction can cause deformation and energy dissipation. Like any other force, frictional force causes "acceleration", but it acts to oppose motion.

The easiest and most known model for friction is the Coulomb friction. In this model, the friction force f_f [N] is proportional to the normal force f_n [N] acting perpendicular to the surfaces in contact:

$$f_f = \mu f_n \quad (4.7)$$

The proportionality constant μ is called the friction coefficient [-].

There are various types of friction.

- *Static friction* occurs when two surfaces are not moving. When a non-moving object is pushed or pulled but it does not move, the cause for it is static friction. As long as the frictional force is not overcome, the object does not move. This static friction is generally denoted by μ_s .
- *Dynamic (or kinetic) friction* occurs when two surfaces move relative to each other. In general, this friction is smaller than the static friction. Since this friction works in the opposite direction of the movement, it dissipates energy. Dynamic friction is denoted by μ_d . An example is shown in Figure 37.
- *Rolling friction* occurs when two surfaces are rolling relative to each other. This is caused by the deformation of either of the surfaces. Rolling friction is denoted by μ_r .

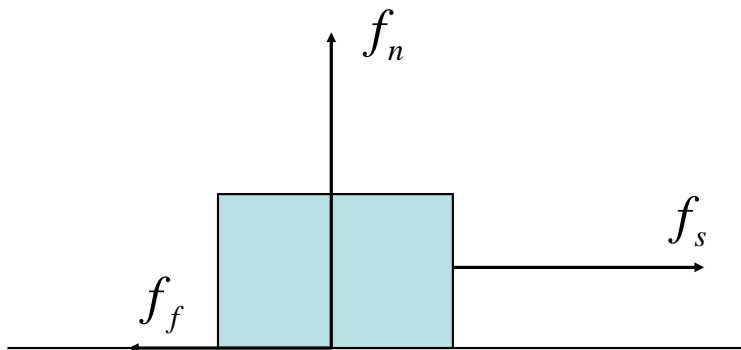


Figure 37: Schematic representation of the effect of dynamic (or kinetic) friction. A block is pulled over a horizontal surface with shear force f_s , while normal force f_n is working perpendicular to the pulling direction, and the frictional force f_f acts so as to counter the shear force

The energy dissipated by frictional sliding E_f [J] can be easily monitored in ITASCA [46]. It can be calculated from

$$E_f = f_f \Delta^{slip} = (\mu \cdot mg) \cdot \Delta^{slip} \quad (4.8)$$

Here Δ^{slip} is the total slip displacement [m], m is the mass of the object [kg] and g is the gravitational acceleration [m/s^2]. This equation will be used for the simulations to monitor the effect of the friction.

Example case 1:

We consider the following case:

One particle with fixed zero spin is moved over a horizontal wall with a constant velocity $v = 1m/s$. The maximum time step is chosen to be $10^{-4}s$, so that after 10^4 cycles, a total slip displacement of 1 m is obtained. The particle diameter is chosen to be $d = 1.24076m$, so

that the particle volume is $V_p = \frac{4}{3}\pi\left(\frac{d}{2}\right)^3 = 1m^3$. The particle density is $\rho = 1kg/m^3$ and the

gravity is set to $g = 10m/s^2$. The simulation script is given in Appendix 12.

The properties that are varied in this simulation are μ_p and μ_w , the particle and wall friction, respectively, and the monitored value is the frictional energy E_f .

There are multiple possibilities of combining individual friction coefficients to a system coefficient μ_{pw} . Consider the following options:

- 1) The minimum value of either is taken: $\mu_{pw} = \min(\mu_p, \mu_w)$
- 2) The linear average is taken: $\mu_{pw} = \frac{\mu_p + \mu_w}{2}$
- 3) Friction coefficients act in series: $\mu_{pw} = \frac{\mu_p \mu_w}{\mu_p + \mu_w}$
- 4) The geometric mean is taken: $\mu_{pw} = \sqrt{\mu_p \mu_w}$

The results of the simulations are shown in Figure 38.

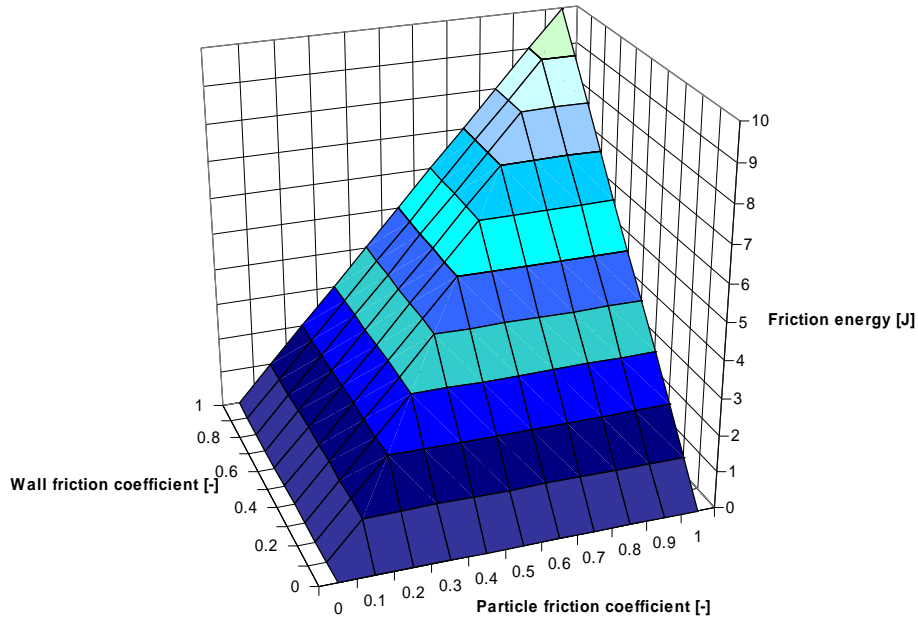


Figure 38: Effect of particle and wall friction on the frictional energy

From these results, we can see that the minimum value of the two friction factors is taken. This can be explained by the fact that, when two surfaces slide over each other, and only one surface has active friction, no frictional energy is dissipated. As a consequence, friction is only activated when the user specifies both particle and wall friction in the simulation. A friction factor above 1 is not shown in Figure 38, but is possible; it means that a shear force higher than the normal load is required to move the particle in a horizontal direction.

4.5.2 Normal force-displacement model

When two particles collide, in reality they are allowed to deform. To include this deformation in a contact model, a virtual particle-particle overlap δ is defined. A contact model relates the normal force acting on a contact to the particle-particle overlap. Such a particle-particle contact model has to be described in two directions: normal and shear direction. First, different models that are valid in the normal direction will be described. Among these are some standard models (by Hooke and Hertz) but also more advanced models (e.g. Tomas).

The first and most basic models for linear and non-linear elastic, reversible behaviour are based on laws developed by Hooke and Hertz, respectively. It is assumed that the overlap is small in comparison to the particle radius R , i.e. $\delta/R \ll 1$. But on the other hand, another assumption is that the overlap is large enough to have the contact area consist of multiple representative molecules^[55].

A schematic explanation of Hooke's model and Hertz' model is displayed in Figure 39.

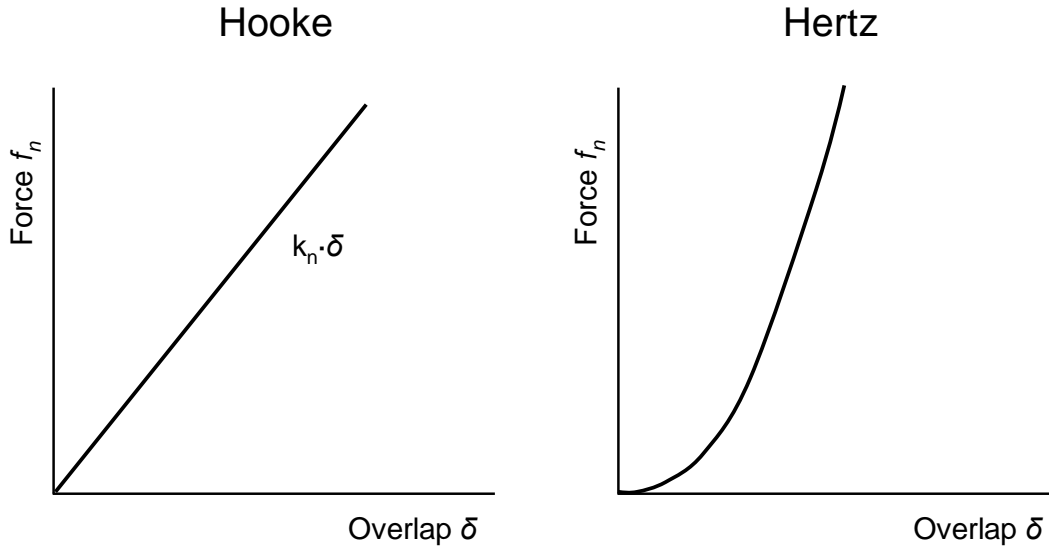


Figure 39: Schematic representation of the two basic particle-particle contact models. Left: Hooke's model, where the normal force is a linear function of the overlap with the normal stiffness of the contact as proportionality constant. Right: Hertz' model, which assumes an exponential relation between overlap and normal force

Hooke's model is a linear elastic contact model, where the normal force f_n [N] is a linear function of the particle-particle overlap, δ [m]:

$$f_n = k_n \cdot \delta \quad (4.9)$$

Here we define the overlap as

$$\delta = \frac{1}{2}(d_1 + d_2) - (\vec{r}_1 - \vec{r}_2) \cdot \hat{n} \quad (4.10)$$

Where \vec{r}_i is the position of particle i and \hat{n} is the unit-normal vector. This unit-normal vector points from particle 2 to particle 1

$$\hat{n} = \frac{\vec{r}_1 - \vec{r}_2}{|\vec{r}_1 - \vec{r}_2|} \quad (4.11)$$

The proportionality constant in Eq. (4.9) is the contact normal stiffness k_n [N/m]. In case of two particles with normal stiffnesses $k_n^{(1)}$ and $k_n^{(2)}$, they act in series to form the contact stiffness. If the particle stiffnesses are equal, the contact stiffness inherits half of either particle stiffness.

$$k_n = \frac{k_n^{(1)} + k_n^{(2)}}{\frac{1}{k_n^{(1)}} + \frac{1}{k_n^{(2)}}} \quad (4.12)$$

The behaviour in this model is elastic, meaning that the contact deformation is reversible. Any contact loading follows the line, whereas when the normal force is removed, the behaviour will still be on the line, and will finally reach the origin, where the contact ends.

The Hertz-Mindlin contact model consists of a nonlinear function of the overlap δ of the particles. The contact normal stiffness can be calculated by

$$k_n = \left(\frac{2\langle G \rangle \sqrt{2\tilde{R}}}{3(1-\langle \nu \rangle)} \right) \sqrt{\delta} \quad (4.13)$$

Here $\langle G \rangle$ is the average elastic shear modulus [Pa], \tilde{R} is the average particle radius [m] and $\langle \nu \rangle$ is the average Poisson's ratio [-]. For these three parameters we have:

$$\langle G \rangle = \frac{1}{2}(G_1 + G_2) \quad (4.14)$$

$$\tilde{R} = \frac{2R_1R_2}{R_1 + R_2} \quad (4.15)$$

$$\langle \nu \rangle = \frac{1}{2}(\nu_1 + \nu_2) \quad (4.16)$$

where the average values are a function of the parameters of the individual particles. We can see that there is already an overlap-dependence in the contact normal stiffness. It can be seen that instead of the normal and shear stiffness, the user is required to specify the shear modulus and Poisson's ratio. A similar style is used for Hertz' tangential force-displacement law (see p. 62).

The above mentioned models are standard implemented in the ITASCA PFC^{2D} software. A more complex model, based on the Hooke and Hertz model, has been developed by Tomas [12]. Tomas adjusted and generalized multiple contact models to implement elastic-plastic contact flattening, adhesion and dissipation. This model by Tomas is difficult to implement in simulation software, due to the large amount of non-linear equations and variables. To provide easier implementation, the model has been simplified to a piecewise linear model by Luding. A brief overview of both models is described in Appendix 1.

Apart from these models, there is a possibility for the user to write his/her own contact model and load it into the software. In this project, the option has been examined but due to limitation of time and programming knowledge, this has not been applied. More information can be found in Appendix 2 and 3, where also an example of a user-defined contact model can be found: the hysteretic damping model. This model was planned to be used due to easy implementation of cohesion.

4.5.3 Normal viscous damping

When viscous damping is present, normal and/or shear dashpots are added to each contact, which act in parallel with the present contact model. Viscous damping is modelled by a linear dashpot and forms a linear spring dashpot (LSD) system, according to Luding [56]. In the following, only normal viscous damping is derived. Shear damping can be derived analogously (see Chapter 4.5.6). To implement dissipation, one assumes velocity dependent viscous damping, so that

$$f^{(n)} = f_{el}^{(n)} + f_{diss}^{(n)} \quad (4.17)$$

Here $f_{el}^{(n)}$ is the elastic repulsive normal force from Eq. (4.9) and $f_{diss}^{(n)}$ is the damping force. This damping force is defined as

$$f_{diss}^{(n)} = \gamma_n \dot{\delta} \quad (4.18)$$

Here γ_n is the normal damping constant [kg/s] and $\dot{\delta} = \frac{d\delta}{dt}$ is the normal contact velocity [m/s]. This damping force acts to counter motion.

From Newton's second law of motion, we get:

$$f^{(n)} = -m_{12} \ddot{\delta} \quad (4.19)$$

Here $\ddot{\delta} = \frac{d^2\delta}{dt^2}$ is the contact acceleration [m/s²], and m_{12} is the reduced mass [kg], defined as:

$$m_{12} = \frac{m_1 m_2}{m_1 + m_2} \quad (4.20)$$

The total normal force now becomes:

$$f^{(n)} = m_{12} \ddot{\delta} = k_n \delta + \gamma_n \dot{\delta} \quad (4.21)$$

We define the oscillation frequency of an elastic oscillator $\omega_{0,n}$ [1/s] as

$$\omega_{0,n} = \sqrt{\frac{k_n}{m_{12}}} \quad (4.22)$$

and the effective viscosity η_n [1/s] is defined as

$$\eta_n = \frac{\gamma_n}{2m_{12}} \quad (4.23)$$

Now, we can reduce Eq. (4.17) to:

$$\ddot{\delta} + 2\eta_n \dot{\delta} + \omega_{0,n}^2 \delta = 0 \quad (4.24)$$

This is the famous equation for the damped harmonic oscillator.

We can solve this equation by looking for a solution in the form of $A \exp(\xi t)$. This means we find:

$$\xi^2 + 2\eta_n \xi + \omega_0^2 = 0 \quad (4.25)$$

Since $\eta_n > 0$ and $\omega_{0,n}^2 > 0$, and we define the oscillation frequency of the damped oscillator ω_n as

$$\omega_n = \sqrt{\omega_{0,n}^2 - \eta_n^2} \quad (4.26)$$

We get a complex solution for this equation:

$$\xi = -\eta_n \pm i\omega_n \quad (4.27)$$

The general solution of Eq. (4.25) is:

$$\delta(t) = \exp(-\eta_n t) \cdot [c_1 \sin(\omega_n t) + c_2 \cos(\omega_n t)] \quad (4.28)$$

For the boundary conditions we have:

$$\begin{aligned} \delta(t=0) &= x_0 = 0 \rightarrow c_2 = 0 \\ \dot{\delta}(t=0) &= v_0 \rightarrow c_1 = \frac{v_0}{\omega_n} \end{aligned} \quad (4.29)$$

This brings us to the equation for the particle-particle contact overlap:

$$\delta(t) = \frac{v_0}{\omega_n} \cdot \exp(-\eta_n t) \cdot \sin(\omega_n t) \quad (4.30)$$

And by differentiating, we get for the contact velocity:

$$\dot{\delta}(t) = \frac{v_0}{\omega_n} \cdot \exp(-\eta_n t) \cdot [-\eta_n \sin(\omega_n t) + \omega_n \cos(\omega_n t)] \quad (4.31)$$

The contact duration is defined as the time

$$t_c = \frac{\pi}{\omega_n} \quad (4.32)$$

as long as $\eta_n < \omega_{0,n}$. This contact time is only half period of the oscillation, since it is assumed that the contact ends when the overlap becomes negative.

We are interested in the effect of viscous damping on the restitution coefficient. In the direction parallel to the line connecting the centres of the two particles, the restitution coefficient e_n [-] describes the change in relative velocity in the centre of mass reference frame:

$$e_n = -\frac{v^{(n)}}{v^{(n)}} \quad (4.33)$$

This is the restitution coefficient in normal directions, and it can have values in the range of $0 \leq e_n \leq 1$, displaying the collision as completely inelastic ($e_n = 0$) and completely elastic ($e_n = 1$). The prime ` represents the velocity after collision.

We can now rewrite Eq. (4.33). For the velocity at $t = t_c$, we get from Eq. (4.31):

$$\dot{\delta}(t = t_c) = \frac{v_0}{\omega_n} \cdot \exp(-\eta_n t_c) \cdot [-\eta_n \sin(\omega_n t_c) + \omega_n \cos(\omega_n t_c)] \quad (4.34)$$

Since $t = t_c$,

$$-\eta_n \sin(\omega_n t_c) + \omega_n \cos(\omega_n t_c) = -\omega_n \quad (4.35)$$

because t_c is at half period. Eq. (4.34) is simplified to:

$$\dot{\delta}(t = t_c) = -v_0 \cdot \exp(-\eta_n t_c) \quad (4.36)$$

For the restitution coefficient, we rewrite Eq. (4.33) to:

$$e_n = -\frac{v^{(n)}}{v^{(n)}} = -\frac{\dot{\delta}(t = t_c)}{v_0} = \exp(-\eta_n t_c) \quad (4.37)$$

With the definition of t_c , we now have for the restitution coefficient:

$$e_n = \exp\left(-\frac{\pi \eta_n}{\omega_n}\right) \quad (4.38)$$

This equation can be used to calculate a theoretical value for the restitution coefficient, for a given particle system with masses m_1 and m_2 , and contact stiffness k_n .

In ITASCA, instead of normal damping constant γ_n , the damping forces are not specified directly, but in terms of a critical damping ratio β_n [-]:

$$\gamma_n = \beta_n \gamma_n^{crit} \quad (4.39)$$

Here γ_n^{crit} is defined as the critical damping constant, which can be calculated by setting the square root in Eq. (4.26) to zero:

$$\omega_{0,n}^2 = \eta_n^2 \quad (4.40)$$

$$\left(\sqrt{\frac{k_n}{m_{12}}}\right)^2 = \left(\frac{\gamma_n}{2m_{12}}\right)^2 \quad (4.41)$$

$$\gamma_n = \gamma_n^{crit} = 2\sqrt{m_{12}k_n} \quad (4.42)$$

Here the stiffness is the contact stiffness.

When $\beta_n = 1$, the system is said to be *critically damped*. Such a system goes back to the original position in the fastest time possible, compared to any other type without oscillation. When $\beta_n > 1$, the system is called *overdamped*. The system still approaches the original position, but even slower than in the critically damped case. The response is an exponential decaying response. In the case of $0 \leq \beta_n < 1$, the system is *underdamped*. The response in this case is oscillatory. When $\beta_n = 1$, it represents the critical transition from an oscillatory response to an exponentially decaying response.

In the simulations done in this section, the theoretical value of the restitution coefficient is calculated from Eq. (4.38). This value is compared to the restitution coefficient in the simulations, for various damping coefficients, where it is calculated by Eq. (4.33). A similar procedure is done with the contact time; the theoretical contact time can be calculated by Eq. (4.32). To determine the contact time in the simulations, during each cycle the contact force between the particles is measured. At the end of each simulation, the time-contact force data are stored in a file. For analysis of these data, for a certain amount of cycles, a contact force has been measured. The cycles in which a force is measured together determine the particle-particle contact time.

For each simulation, there is the possibility to turn tension on and off. In the manual it was not clear how this works. The effect and meaning of this tension has also been investigated.

In this case, we are only interested in the underdamped region. For the overdamped region, the contact force decays exponentially but never reaches zero. This means the contact would never end, since there is always a (very small) contact force.

If we fill in Eq. (4.39) and Eq. (4.40) into Eq. (4.26), we can obtain the following relation:

$$\omega_n = \omega_{0,n} \cdot \sqrt{1 - \beta^2} \quad (4.43)$$

This is a more direct way to calculate ω_n and thus the particle-particle contact time t_c becomes:

$$t_c = \frac{\pi}{\omega_n} = \frac{\pi}{\omega_{0,n} \cdot \sqrt{1 - \beta^2}} = \frac{\pi}{\sqrt{1 - \beta^2}} \cdot \sqrt{\frac{m_{12}}{k_n}} \quad (4.44)$$

$$t_c = \frac{\pi}{\sqrt{1 - \beta^2}} \cdot \sqrt{\frac{m_{12}}{k_n}} \quad (4.45)$$

Example case 2:

Two non-rotating particles undergo central collisions, while the normal viscous damping of the contact is varied. External forces such as gravity are neglected. The effect of damping on the contact time and the restitution coefficient is determined and compared with theory. In the simulations done here, we use particles with diameter $d = 1\text{ m}$, density $\rho = 1\text{ kg} / \text{m}^3$, and normal and shear particle stiffness $k_n = k_s = 10^8 \text{ N} / \text{m}$. The particles are placed in a horizontal separation of 2 m between the sphere centres, and both particles have a horizontal velocity of 50 m/s towards each other. The simulation script is given in Appendix 12.

Using the current values, Using Eq. (4.1) (p. 42) we can estimate the critical time step to be

$$t_{crit} = \sqrt{\frac{m}{k_n}} = \sqrt{\frac{\frac{4}{3}\pi \cdot (0.5)^3 \cdot 1}{10^8}} = 7.24 \cdot 10^{-5} s \quad (4.46)$$

In case of no damping, the contact time becomes

$$t_c (\beta_n = 0) = \pi \sqrt{\frac{m}{k_n}} = \pi \cdot t_{crit} = 2.27 \cdot 10^{-4} s \quad (4.47)$$

The integration time step is taken to be $\Delta t = 1 \cdot 10^{-6} s$, which is small enough to have multiple cycles during particle-particle contact.

The particle diameter is chosen to be $d = 1m$ because it is easy to make calculations with. The same accounts for the density. Particle stiffnesses are taken $10^8 N/m$ so that "normal" behaviour is observed; lower stiffnesses make the particles go through each other. The reason why $\Delta t = 1 \cdot 10^{-6} s$ is chosen is so that there are multiple time steps during the time the particles are in contact, and the particle velocity is taken high to decrease the amount of required cycles, but not too high to decrease the accuracy of the calculations. With the current time step, velocities and separation between the particles, it takes 10000 calculation cycles to bring the particles into contact. With the theoretical restitution coefficient, it can be estimated how many cycles are required to have the particles to be sufficiently separated from each other, so that there is no overlap any more. Due to the built-in tolerance, a particle-particle contact is formed when the particles have a small separation from each other. This means that after the collision, the particles may look separated, but it is not detected that they are separated. More cycles are required to have the particles in a sufficient distance from each other.

The effect of damping on the contact time is graphically displayed in Figure 40, for both tension allowed and disabled. These results are summarized in Appendix 9.

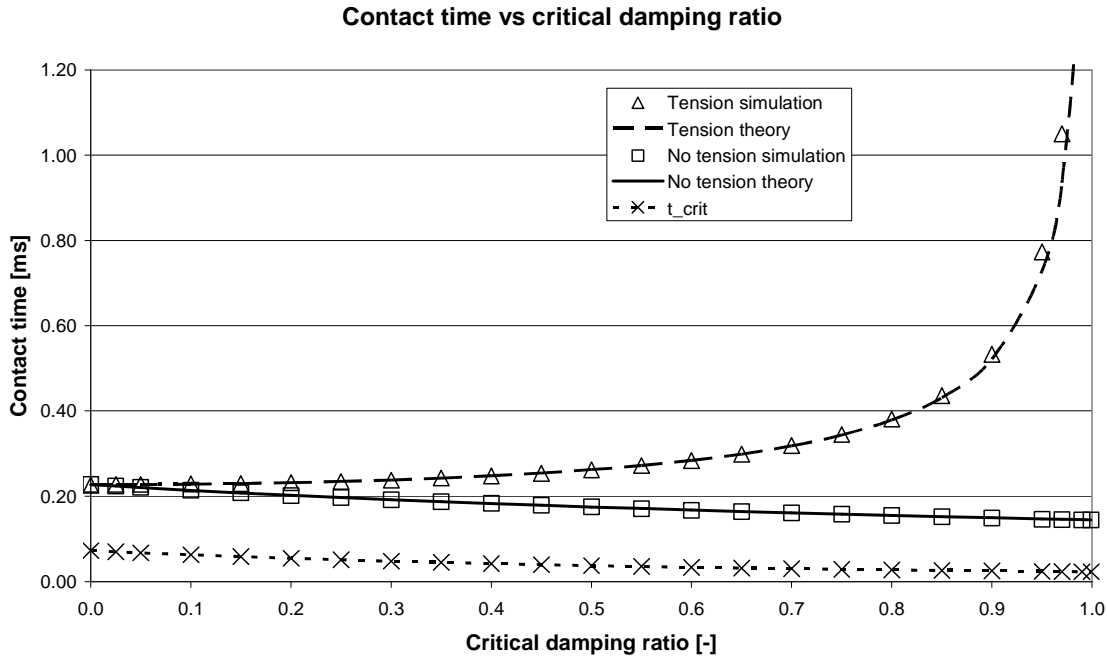


Figure 40: Effect of normal viscous damping on the particle-particle contact time, with and without tension force allowed. The theoretic lines follow Eq. (4.32) and Eq. (4.48), respectively. To compare, the critical time step t_{crit} as calculated by PFC^{2D} is plotted as well

It can be seen that the critical time step decreases with increasing values of β_n . ITASCA has implemented a standard time step reduction that accounts for viscous damping. As is mentioned in the manual, this is accompanied by a change in “apparent” stiffness; an increase in viscous damping means that the particles experience a higher stiffness. It is not clear from the manual how this stiffness is calculated.

With an increasing critical damping ratio, the contact time increases and decreases, for the case of tension and no tension, respectively. In the case of tension, it is expected that the particles have a longer contact time with increasing damping. The particles are attracted to each other, and due to the damping, it is less easy to separate the particles from each other. This is what can also be seen in Figure 40, and this line follows the theoretical expectations from Eq. (4.45). For high damping values, a small difference is found due to numerical errors.

In the case of no tension, increasing dissipation causes the contact time to decrease. In the case of no damping, the normal force is half period of a perfect sine function. In Figure 41 it can be seen that, in the case of damping, at the end of the contact, the normal force becomes negative.

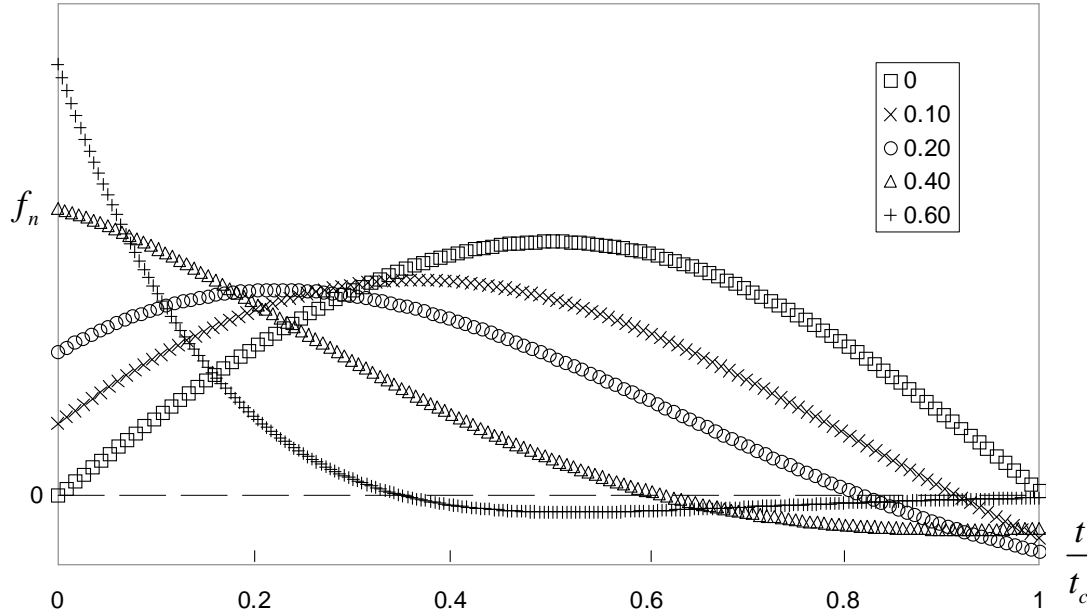


Figure 41: Normal force [arbitrary units] as function of dimensionless contact time, for various values of β_n shown as inlet ^[56]

Now, when there is no tension allowed, negative normal forces are forbidden, and the contact is said to end at the time where the normal force becomes zero, and thus the contact breaks. So for example, for $\beta_n=0.6$, the contact time is 60% of the contact time when tension would be allowed. This is confirmed by Figure 40. As equation, the contact time without tension allowed can be found by ^[56]

$$t_c = \frac{1}{\omega_n} \cdot \left(\pi - \arctan \frac{\eta_n}{\omega_n} \right) \quad (4.48)$$

This equation follows the simulated values smoothly.

The effect of normal viscous damping on the restitution coefficient has been studied as well. Figure 42 graphically displays the results of these simulations. These results are summarized in Appendix 9.

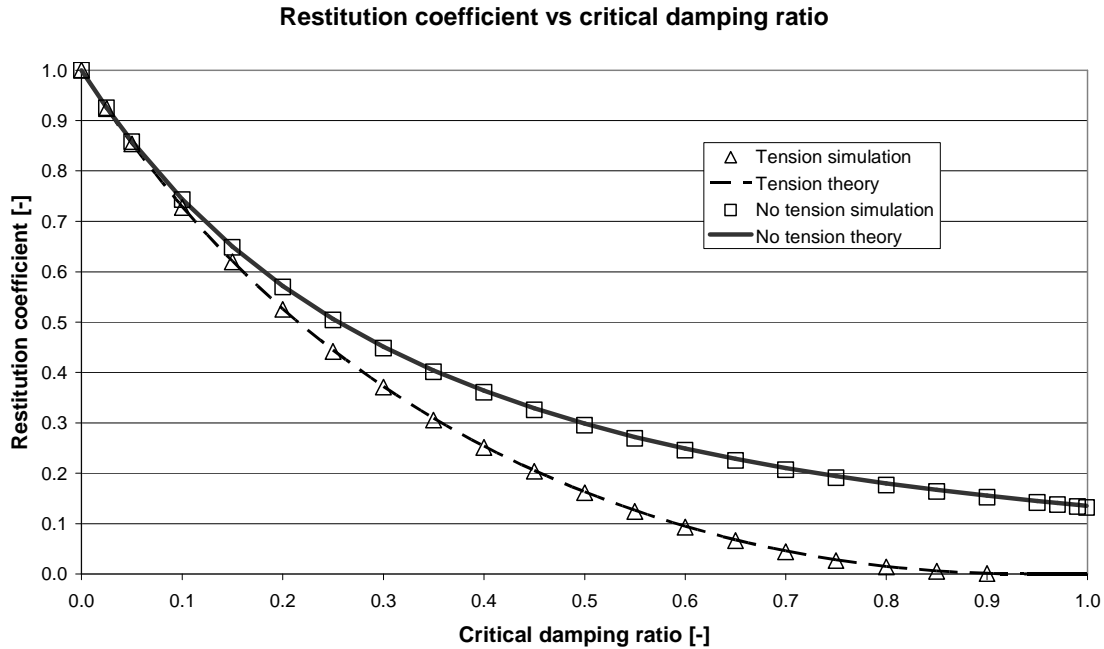


Figure 42: Effect of normal viscous damping on the restitution coefficient, with and without tension force allowed. The theoretic lines follow Eq. (4.37) with t_c from Eq. (4.32) and Eq. (4.48), respectively

For a higher critical damping ratio, the restitution coefficient decreases. This is what is expected, since a higher critical damping ratio means more damping, and thus more energy is dissipated, resulting in a larger velocity decrease after collision. The effect of allowed tension can also be clearly seen. The theoretic line is in agreement with the line with tension. When tension is allowed, there is more dissipation than when tension is disabled, because with tension towards the end of the contact the particles attract each other and it is more difficult to separate them.

In the case of tension disabled, the line follows exactly Eq. (4.37), when we use the calculated contact time for these collisions. The change between tension and no tension therefore only is due to a different particle-particle contact time while forces are active.

4.5.4 Classification of collisions

There are different approaches to model collisions of two particles. One approach is to study the particles' velocities before and after collision, while the collision itself is not of interest and can be assumed to be instantaneous. Another approach is to also track the velocities and forces on the particles during contact, which means the contact takes a certain time. This second approach will be followed in this section. In this model, the particles are "soft", i.e. they are allowed to deform upon impact.

In order to classify collisions, the tangential contact velocity before and after collision are compared. A typical diagram as shown Figure 43 can be derived for a number of collisions. The equations for such a diagram will be derived in this section.

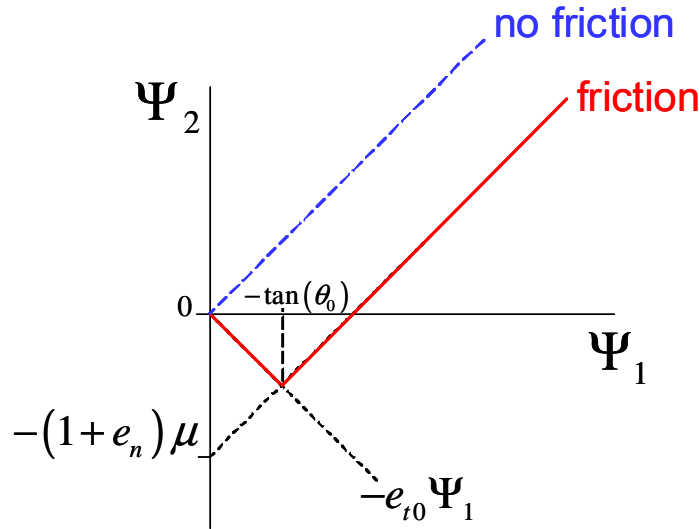


Figure 43: Example of Ψ_2 as a function of Ψ_1 [56]. The dotted line corresponds to perfectly smooth particles, and the solid line corresponds to particles with active friction

The system under consideration is displayed in Figure 44. Two spherical particles with diameter d_i [m] and velocity \vec{v}_i [m/s] collide under a certain angle θ .

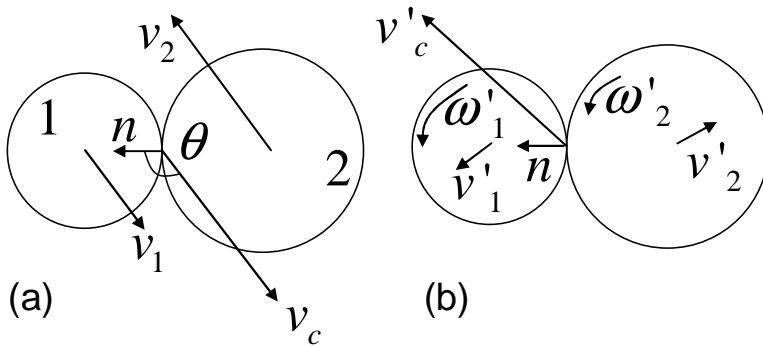


Figure 44: Schematic representation of the velocities before (a) and after (b) collision [53]

According to Luding [56], the contact velocity \vec{v}_c [m/s] is defined as:

$$\vec{v}_c = \vec{v}_1 - \vec{v}_2 - \left(\frac{d_1}{2} \omega_1 + \frac{d_2}{2} \omega_2 \right) \times \hat{n} \tag{4.49}$$

Where ω_i is the angular velocity of particle i [1/s] and \hat{n} is the unit-normal vector, which points from particle 2 to particle 1, as shown in Figure 44.

In the following, rotations of the particles will be disabled, which is done to simplify the equations. A similar thing is done in experiments, since in experimental setups it is difficult to measure the spin of the particles [57].

When we disable rotation of the particles, Eq. (4.49) can be simplified to:

$$\vec{v}_c = \vec{v}_1 - \vec{v}_2 \tag{4.50}$$

We are interested in the normal and tangential component of the contact velocity. The normal component is found by

$$\overline{v_c^{(n)}} = \hat{n}(\overline{v_c} \cdot \hat{n}) \quad (4.51)$$

This can be seen as a projection of $\overline{v_c}$ on the unit-normal vector. The tangential contact velocity can then be found by vector subtraction

$$\overline{v_c^{(t)}} = \overline{v_c} - \overline{v_c^{(n)}} \quad (4.52)$$

This vector $\overline{v_c^{(t)}}$ defines the unit-tangential vector as:

$$\hat{t} = \frac{\overline{v_c^{(t)}}}{\left| \overline{v_c^{(t)}} \right|} \quad (4.53)$$

It is thus obtained by rotating the unit-normal vector by 90° in the direction of the active velocity. Now that we have derived how to calculate $\overline{v_c^{(n)}}$ and $\overline{v_c^{(t)}}$, Ψ_1 and Ψ_2 can be defined:

$$\Psi_1 = \frac{v_c^{(t)}}{v_c^{(n)}} \quad (4.54)$$

$$\Psi_2 = \frac{v_c^{(t)}}{v_c^{(n)}} \quad (4.55)$$

The tangential contact velocity before and after collision is required for these equations, as well as the normal contact velocity before collision. The normal and tangential contact velocity before collision are both positive, since they are defined to be absolute values. This means Ψ_1 is always positive. But Ψ_2 can become negative, when the tangential contact velocity changes direction during collision.

From the change of momentum during collision, it can be derived that ^[56]:

$$\Psi_2 = \begin{cases} \Psi_1 - \frac{1+q}{q}(1+e_n)\mu & \text{for } \theta < \theta_0 \\ -e_{t0}\Psi_1 & \text{for } \theta \geq \theta_0 \end{cases} \quad (4.56)$$

Here e_{t0} is the cut-off value for the tangential restitution coefficient [-], and $q = 2/5$ for the case of spheres, where the ratio $\frac{1+q}{q}$ is taken into account for the change of angular momentum. If rotation is not allowed, and angular momentum is not taken into account, $q \rightarrow \infty$ (infinite inertia so no rotation) and therefore $\frac{1+q}{q} \rightarrow 1$.

Eq. (4.56) is used to distinguish two regimes of collisions. The first equation is valid for small θ (large Ψ_1), i.e. for Coulomb-type sticking collisions, whereas the second equation is valid for large θ , the so-called sliding (or grazing) collisions, which are highly tangential. For an almost central collision, the contact cannot slide, and there will be deformation described by the second equation. For highly non-central collisions, the surfaces slide, and the friction coefficient comes into play, as can be seen in the first equation.

In the case of $\theta < \theta_0$, we can describe Ψ_2 by

$$\Psi_2 = \Psi_1 - (1 + e_n) \mu \quad (4.57)$$

So for $\Psi_1 = 0$, we get

$$\Psi_2 = -(1 + e_n) \mu \quad (4.58)$$

This equation can be used to find the intersection with the y-axis.

For small Ψ_1 ,

$$\Psi_2 = -e_{t0} \Psi_1 \quad (4.59)$$

Here we can find e_{t0} by ^[53]:

$$e_{t0} = -\cos\left(\pi \sqrt{\frac{k_t}{k_n}}\right) \quad (4.60)$$

The equations above only describe the two extremes of the collisions. The section around θ_0 is in the region where neither/both equations are valid, meaning behaviour in this region may be poorly predicted.

Example case 3:

In the following simulations, we use particles with diameter $d = 1m$ and density is $\rho = 1kg / m^3$. The particles are placed in a horizontal separation of 2 m between the sphere centres, and both particles have a horizontal velocity of 50 m/s towards each other. The integration time step is taken to be $\Delta t = 1 \cdot 10^{-6} s$. The vertical position of ball 1 is varied between 0 and 0.99, whereas 0 means a sticking collision and 0.99 means a sliding collision. The unit-normal vector and the contact velocity after collision are determined, from which all other parameters can be calculated using the formulae described in Chapter 4.5.3. The simulation script is given in Appendix 12.

Instead of different starting positions, another approach to vary Ψ_1 is to vary the angular velocity ω_1 of particle 1, while maintaining $\omega_2 = 0s^{-1}$. However, this path has not been tested in this project, but it should lead to similar results, since Eq. (4.49) and Eq. (4.56) are still valid.

First, the effect of friction will be studied. The result of the simulations is shown in Figure 45. All results are listed in Appendix 10.

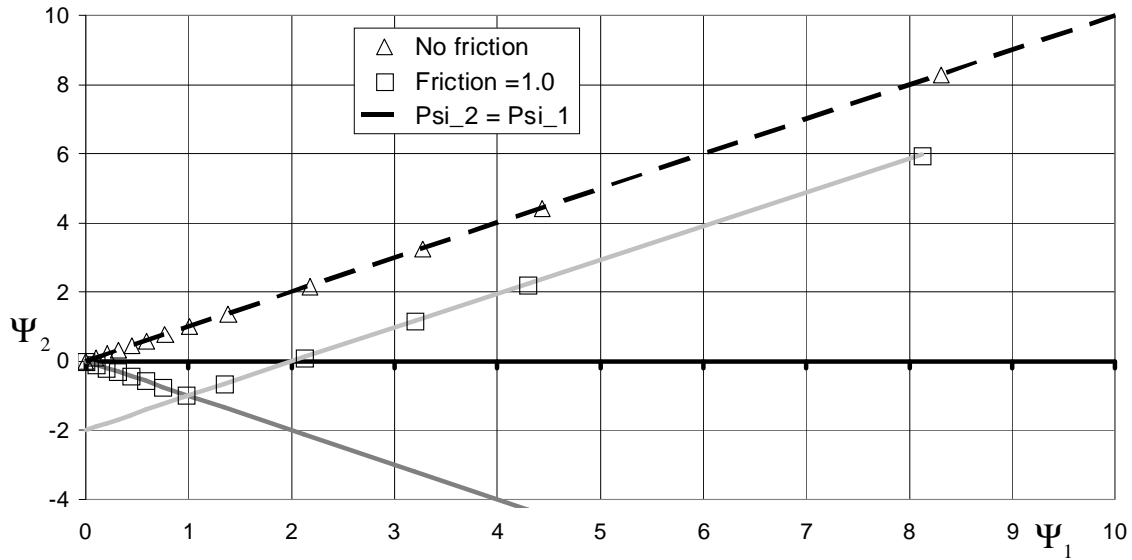


Figure 45: Effect of friction on Ψ_2 versus Ψ_1

In the case of no friction, the results display a linear relation between Ψ_1 and Ψ_2 . Due to the absence of friction, Eq. (4.57) can be reduced to

$$\Psi_2 = \Psi_1 \quad (4.61)$$

The line is an exact straight line through the origin with slope 1.

It can be clearly seen where the effect of friction “kicks in”. Since we define $\overline{v_c^{(n)}}$ and $\overline{v_c^{(t)}}$ as positive, Ψ_1 must always be positive. A negative value of Ψ_2 therefore has to be the result of a change in direction of the tangential contact velocity during collision. As can be seen in Eq. (4.56), this can only be a result of friction at low Ψ_1 (sticking collisions). Due to this inversion in tangential velocity, e_{t0} becomes positive. A straight line with slope e_{t0} (as described by Eq. (4.59)) is thus the result. The pink line is a fit of Eq. (4.59), for equal normal and tangential springs, and the slope (as found from Eq. (4.60)) is -1.

Next the effect of normal viscous damping on two-particle collisions is investigated. The results are shown in Figure 46. All results are listed in Appendix 10.

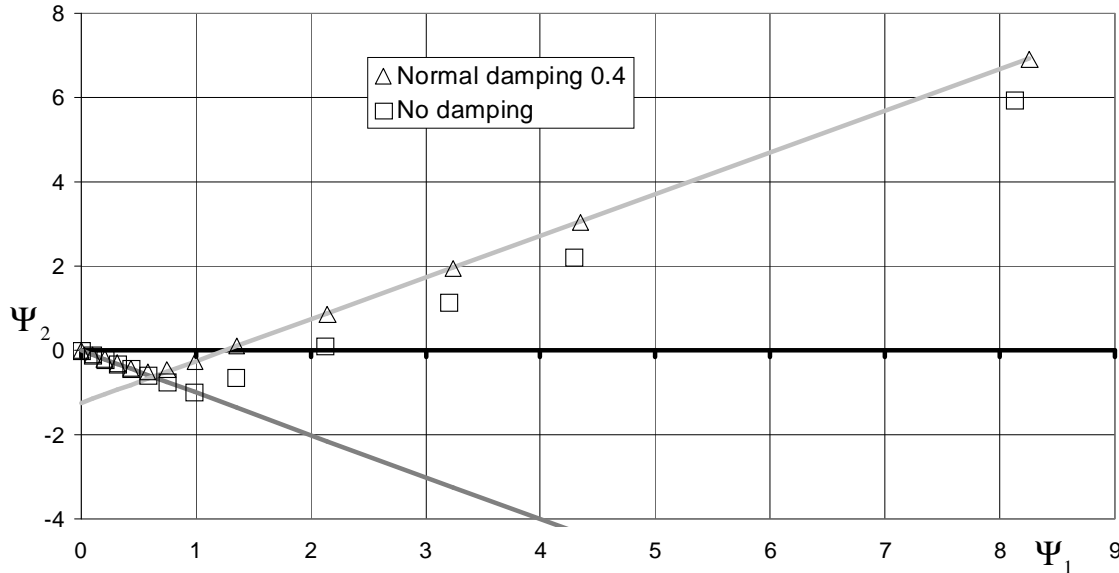


Figure 46: Effect of normal viscous damping on Ψ_2 versus Ψ_1

Normal viscous damping only affects sliding collisions. There is no effect on small Ψ_1 because the tangential velocity is very small and thus is unaffected by normal viscous damping. It can be seen that the slope for large Ψ_1 is unaltered, only the offset changes.

In Figure 42 on p. 57, $\beta_n = 0.4$ gives $e_n \approx 0.25$. With Eq. (4.58), the offset can be calculated to be approx. -1.25.

Foerster et al. ^[57] have performed experiments with particle-particle collisions, and they have found that the experimental results also follow the equations above.

4.5.5 Tangential force-displacement model

Apart from the normal force-displacement model, a tangential force-displacement model is required as well, which acts in the tangential direction, perpendicular to the particle-particle overlap. There are three different force- and torque-laws that can be implemented:

- friction
- rolling resistance

The rolling resistance is much less dominant than the friction force and is not implemented in the ITSACA software, and is furthermore beyond the scope of this project. This limits us to the presence of friction force only.

The simplest linear elastic tangential force-displacement relation is again Hooke's model; a linear dependence of the shear force f_s on the tangential displacement Δ . The scheme looks similar to that of the normal force-displacement relation, as shown in Figure 47.

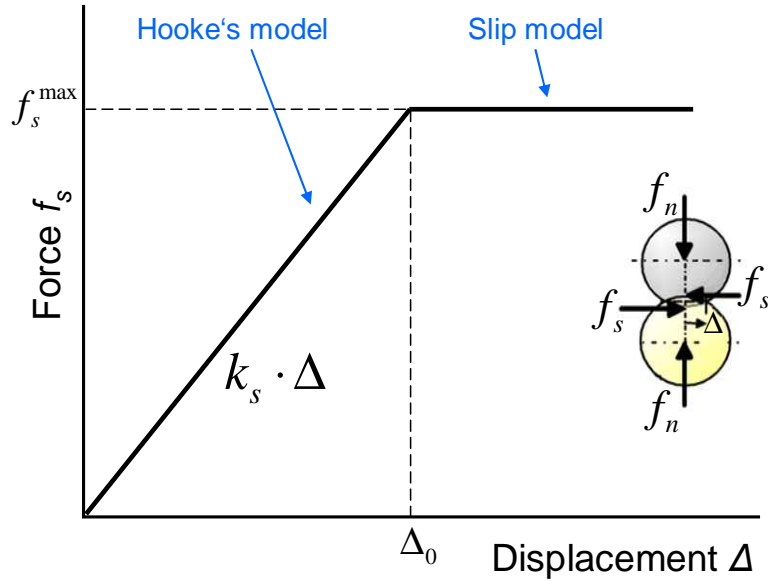


Figure 47: Linear elastic-plastic, frictional tangential particle-particle model, composed of Hooke's model and the slip model. In the region of Hooke's model, the normal force is linearly dependent on the tangential displacement. This model is valid up to Δ_0 , after which the slip model is active

The linear relation is only applicable up to a maximum shear force f_s^{\max} , after which Hooke's model is not valid anymore. This point corresponds to a limited displacement Δ_0 . From this point, the so-called slip model becomes active, where particles are allowed to slip over each other with force

$$f_s = \mu_i \cdot f_n \quad (4.62)$$

In this region, the shear force is a function of the normal load only and acts opposite to the velocity, and no more of the displacement. The proportionality constant is the internal friction coefficient μ_i [-].

Apart from Hooke's model, Hertz' model also has a shear component of the contact model. It is similar to the normal component, but with a different equation for the contact stiffness. In this case, the shear stiffness k_s is given by

$$k_s = \left(\frac{2 \left(\langle G \rangle^2 \cdot 3(1-\langle \nu \rangle) \tilde{R} \right)^{1/3}}{2-\langle \nu \rangle} \right) \cdot |f_n|^{1/3} \quad (4.63)$$

here $|f_n|$ is the magnitude of the normal force. If the maximum shear force f_s^{\max} is reached, again the slip model is activated.

The effect of Hooke's model on Ψ_2 versus Ψ_1 is displayed in Figure 48. The same system (Example case 3, p. 60) has been used. All results are listed in Appendix 10.

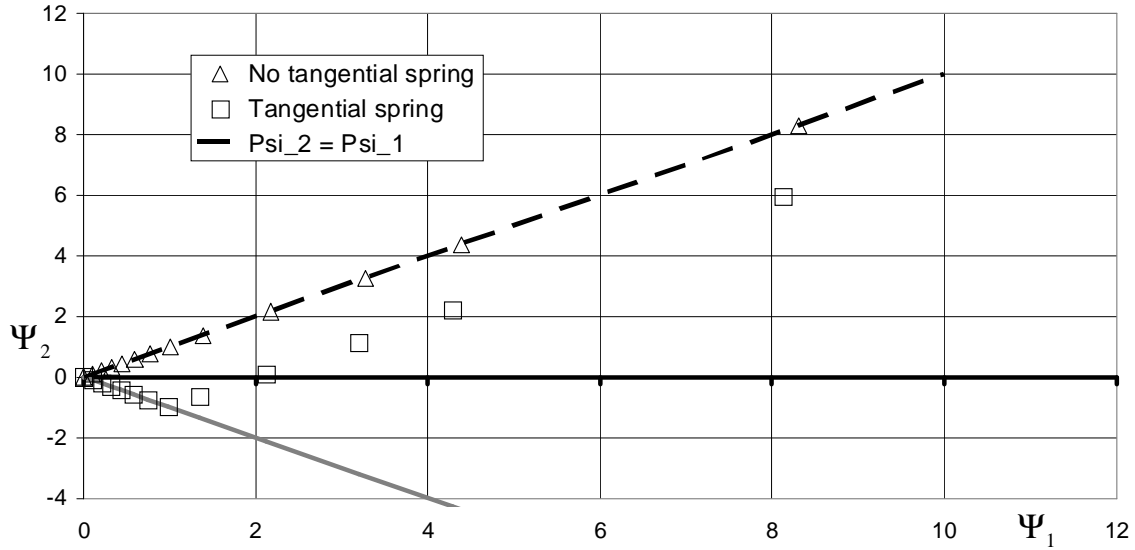


Figure 48: Effect of tangential spring on Ψ_2 versus Ψ_1

When the tangential spring is disabled, Hooke's model is disabled, and apparently the above laws are not valid. Even though the system should be affected by the friction coefficient, a straight line through the origin with slope 1 was observed, as if there were no friction.

4.5.6 Tangential viscous damping

Apart from the normal direction, it is also required to model the viscous force in tangential direction. Again a linear elastic model is applied, which allows inversion of the tangential velocity during collision, so that negative Ψ_2 values can be obtained and explained. Here the inversion is connected to the elasticity of the material. For this elasticity, a tangential spring is chosen to be appropriate, which is similar to the spring in normal direction.

For a viscous tangential force, Eq. (4.18) can be written for the tangential direction:

$$f_{diss}^{(t)} = \gamma_t \dot{\vartheta} \quad (4.64)$$

where $\dot{\vartheta}$ is the tangential component of the relative velocity [m/s], γ_t is the tangential viscosity [kg/s], and $f_{diss}^{(t)}$ is the tangential dissipation force [N]. It may be derived that ^[50]

$$\Psi_2 = \Psi_1 \cdot \exp(-2\eta_t t_c) \quad (4.65)$$

The effective tangential viscosity η_t [1/s] is defined analogously to Eq. (4.23) for the normal viscosity:

$$\eta_t = \frac{\gamma_t}{2m_{12}} \quad (4.66)$$

The contact time is found by Eq. (4.45) and the tangential damping coefficient γ_t [kg/s] is calculated analogously to Eq. (4.39) and Eq. (4.40):

$$\gamma_t = 2\beta_t \sqrt{m_{12}k_s} \quad (4.67)$$

This model can only reproduce negative tangential restitutions. A positive value should have to come from the tangential spring (in this case Hooke's model). The tangential restitution coefficient is defined as

$$e_t = -\frac{v^{(t)}}{v^{(t)}} \quad (4.68)$$

A positive tangential restitution coefficient is caused by an inversion of the direction of the tangential velocity. To see the effect of shear viscous damping on the development of Ψ_2 versus Ψ_1 , the same system as used in for normal viscous damping is used. The results are shown in Figure 49. All results are listed in Appendix 10.

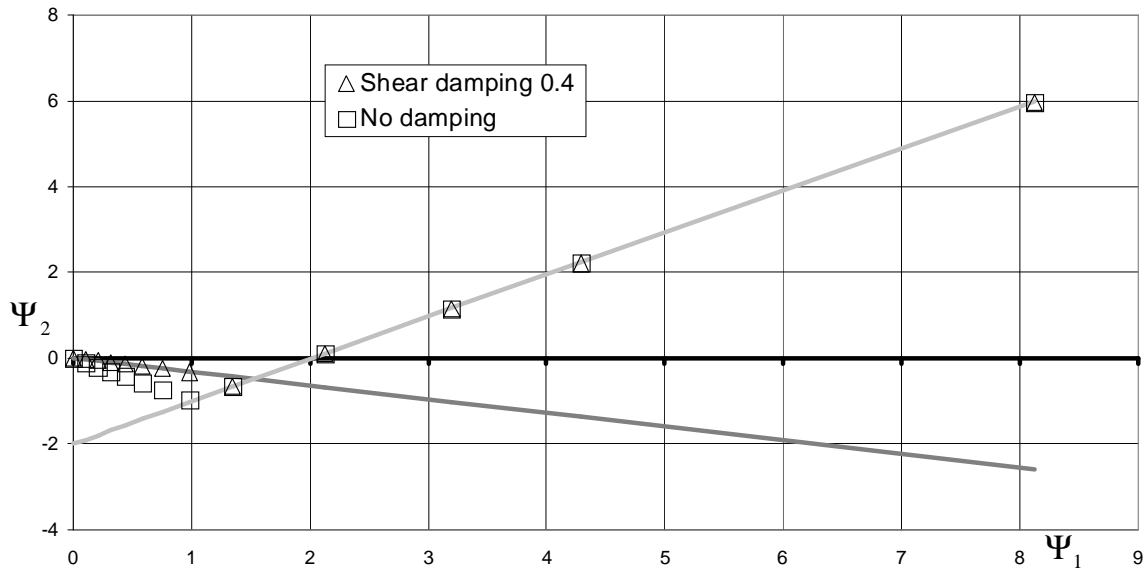


Figure 49: Effect of shear viscous damping on Ψ_2 versus Ψ_1

Apparently shear viscous damping only affects close to central collisions. Due to a shear viscous damping coefficient of 0.4, the tangential restitution coefficient is reduced to 0.4. Although there is no linear relation between β_t and e_t , a value of $e_t = 0.4$ was found to fit the equation. However, Eq. (4.59) alone is insufficient to describe the effect. Eq. (4.65) has to be added to account for the effect of shear viscous damping.

The case of friction, normal viscous damping and/or tangential viscous damping, but without tangential spring has also been investigated. Both simulation series show a similar result as Figure 48: a straight line through the origin with slope 1.

4.5.7 Local damping

Local damping is applied as a damping force that acts on each single particle. Local damping only affects accelerating motion. In the case of steady-state motion, no erroneous damping forces arise. A damping force \vec{f}^d is added to the equation of motion:

$$\vec{f}_i + \vec{f}_i^d = m_i \vec{a}_i \quad (4.69)$$

Here all acceleration forces are categorized together under \vec{a}_i [m/s]. Damping always acts to oppose motion, and local damping is scaled to the generalized force acting on the particle:

$$\vec{f}_i^d = -\alpha \cdot \vec{f}_i \quad (4.70)$$

Here α is the local damping coefficient [-]. We can simplify Eq. (4.69) to:

$$\vec{f}_i \cdot (1 - \alpha) = m_i \vec{a}_i \quad (4.71)$$

To see the effect of local damping on an accelerating particle, consider the following system:

Example case 4:

A single particle with diameter $d = 1m$ and density is $\rho = 1kg / m^3$ is placed in a system with gravitational acceleration $g = 10m / s^2$. With a time step of $\Delta t = 10^{-6}s$, the velocity of the particle is determined each cycle for 5000 cycles. The local damping coefficient is varied between 0 and 1. The simulation script is given in Appendix 12. The result is displayed in Figure 50.

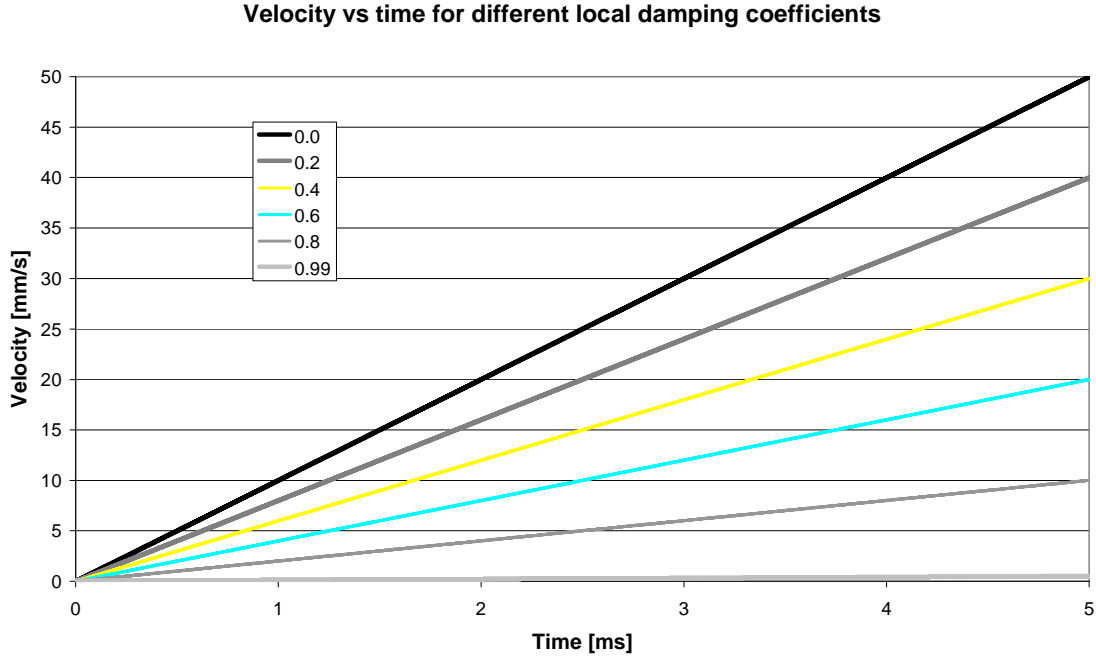


Figure 50: Effect of local damping on the velocity over time for different values of α (shown in the inlet)

In this figure the effect of local damping is clearly seen. In case of $\alpha = 0.2$, the particle has 80% of the velocity that it would have when there were no damping. This is exactly what is described by Eq. (4.71).

For two-particle collisions, local damping could have an impact as well. To verify this, similar simulations as for the case of normal viscous damping have been done:

Example case 5:

Two non-rotating particles undergo central collisions, while the local damping coefficient is varied. External forces such as gravity are neglected. The effect of damping on the contact time and the restitution coefficient is determined. In the simulations done here, we use particles with diameter $d = 1m$, density $\rho = 1kg / m^3$, and normal and shear particle stiffness $k_n = k_s = 10^8 N / m$. The particles are placed in a horizontal separation of 2 m between the sphere centres, and both particles have a horizontal velocity of 50 m/s towards each other. The integration time step is taken to be $\Delta t = 1 \cdot 10^{-6} s$. The simulation script is given in Appendix 12.

An attempt has been made to find an equation that describes the effect of this local damping. For this it was assumed that the local damping acts similar to the viscous damping force (Eq. (4.17)):

$$f^{(n)} = f_{el}^{(n)} + f_{diss}^{(n)} \quad (4.72)$$

The dissipative local damping force acts as to counter the normal load

$$f_{diss}^{(n)} = -\alpha k \delta \quad (4.73)$$

With Hooke's contact model we get

$$f^{(n)} = (1 - \alpha)k\delta \quad (4.74)$$

Analogously to viscous damping (Chapter 4.5.3) we can derive ω_n so that

$$\omega_{0,n} = \omega_n = \sqrt{\frac{k_n(1 - \alpha)}{m_{12}}} \quad (4.75)$$

For the contact time we thus get

$$t_c = \frac{\pi}{\omega_n} = \pi \sqrt{\frac{m_{12}}{k_n(1 - \alpha)}} \quad (4.76)$$

The results of the simulation are displayed in Figure 51, where Eq. (4.76) is displayed as well. These results are listed as well in Appendix 10.

Contact time vs local damping coefficient

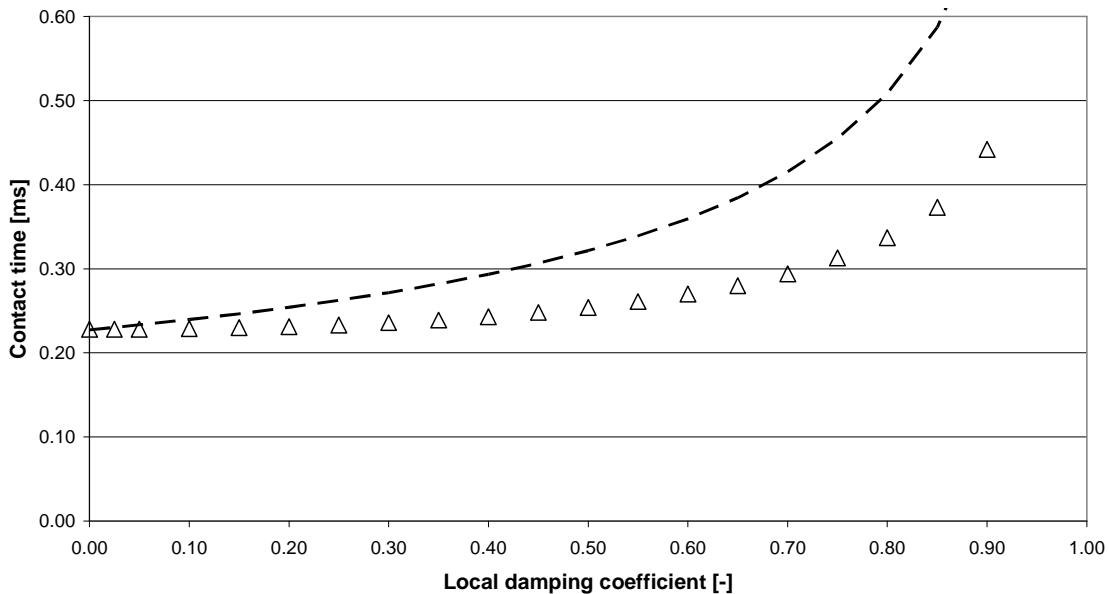


Figure 51: Effect of local damping on the particle-particle contact time. The theoretical line follows Eq. (4.76)

Eq. (4.76) does not quantitatively describe the effect of local damping, so apparently local damping affects the particle-particle contact time in a different way. However the qualitative description is agreed, as they both increase with increasing damping coefficient.

As can be seen, the effect of local damping is similar to that of normal viscous damping (Figure 40, p. 55) but lower. This can be understood by the fact that

$$\bar{a}_i = \frac{\bar{f}_i \cdot (1 - \alpha)}{m_i} \quad (4.77)$$

In case when there are forces present, acceleration occurs. This acceleration is damped by the local damping. A larger damping factor results in more energy dissipation, and therefore (comparable to normal viscous damping) the particles are in contact for a longer period of time.

The effect of local damping on the restitution coefficient is displayed in Figure 52. It seems that there is a linear relation between the local damping coefficient and the restitution coefficient, but after fitting this was found to be not entirely true.

The change in restitution coefficient is not due to a change in particle-particle contact time since there is no value for η and thus Eq. (4.37) cannot be used. These results are listed as well in Appendix 10.

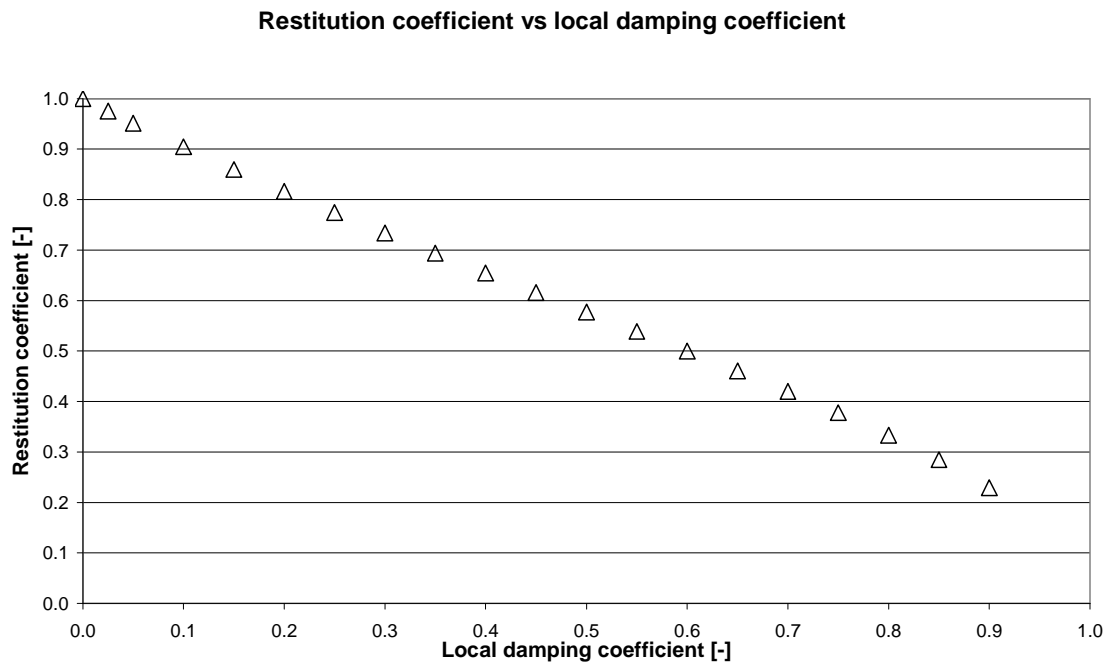


Figure 52: Effect of local damping on the restitution coefficient

The influence of local damping on the tangential velocity has also been studied. These results are given in the Ψ_2 versus Ψ_1 figure below. All results are listed in Appendix 10.

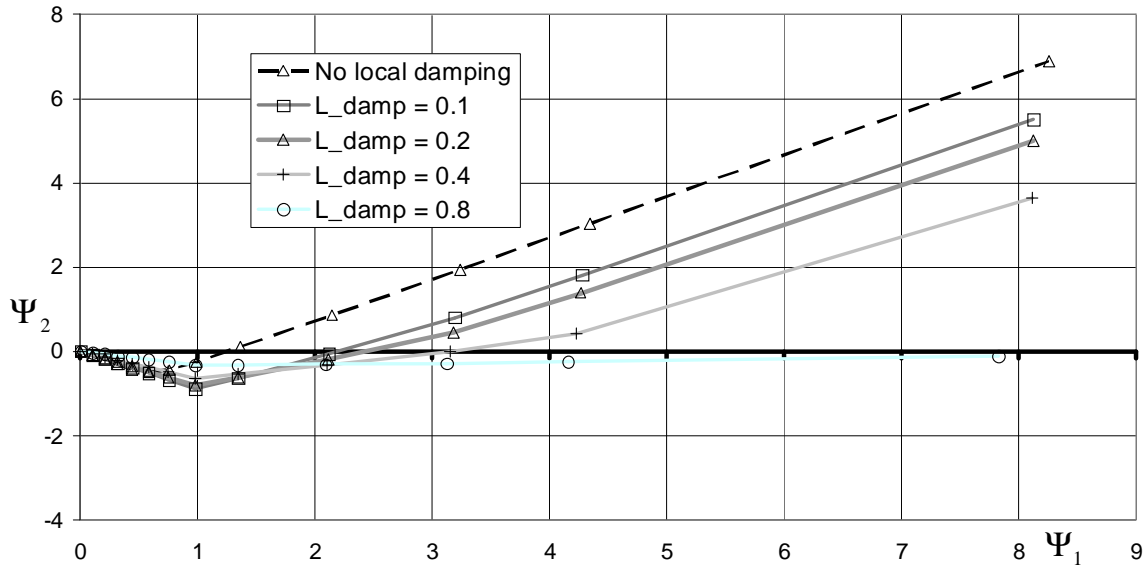


Figure 53: Effect of local damping on Ψ_2 versus Ψ_1

Local damping has an effect on both collision regions. For small values of local damping, the curve approaches the no-damping curve. For large local damping, apparently the tangential velocity after collision becomes very small, and values approach the horizontal axis. Unfortunately no equations could be derived that explain this behaviour.

4.6 DEM programming languages

There are four different levels of communicating with ITASCA PFC^{2D}. These will be discussed shortly in this subsection.

1. Command mode using PFC-code

The upper level of programming is typing the text in the PFC-command window. This is the most basic level, and only useful for the simplest simulations. If more difficult simulations are run, it is more convenient to store the commands in a file, which is then read by the program and executed in batch mode.

2. Batch mode using PFC-code

The second level of programming is operation in batch mode using the PFC-code. The PFC-code is the general code in the PFC^{2D} software. By writing commands in a data file, this data file can be loaded in the program, and the simulation is performed. This is more convenient than the command mode, since the user can reuse written commands, create a clear layout and may add comments.

3. FISH programming language using FISH- and PFC-code

The FISH programming language enables the user to define new variables and functions. It provides the possibility to write more advanced functions and gives the possibility to make simulations that are not possible with the PFC-code only. FISH-functions can be embedded in PFC-codes, but PFC-codes can also be called into FISH-functions.

4. C++ programming language (optional)

The C++ programming may be seen as a fourth level of programming, however this is optional. C++ can be used to write user-defined contact models, which is something for the more advanced programmer. ITASCA PFC^{2D} already provides some standard models (see Appendix 2 and 3). Additional C++ knowledge is required, which is not supported by the ITASCA manual. Generally mostly level 2 and 3 are used. Level 1 is considered to be inconvenient for large simulations, and level 4 requires additional C++ programming knowledge.

4.7 Common mistakes

The simulations with ITASCA did not go quite smooth, and some common mistakes have been made. These points will be listed in this chapter, and may be of importance to people who are planning to work with ITASCA in the future. For those people, it is recommended to read this section first.

A small observed source of confusion is the allowance (or disabling) of particle spin. To see the influence of friction, a ball was first moved along a horizontal wall, but there was no frictional energy observed, thus friction was presumably not active. After a closer look it was observed that it was because the particle was rotating. Since the particle spin could be fixed, the particle could be 'dragged' over the wall, and in this way, friction was observed. By default, rotation is allowed, and it can be turned off by **FIX SPIN <range>**.

One complication was the definition of damping. The difference between local damping and viscous damping was not clear from the manual. For a long time it was thought that with 'damping', viscous damping on the particle-particle contact was meant. However, after a while it became clear that there are various definitions of 'damping'. Local damping acts on each ball, whereas viscous damping acts on each contact. Due to these differences in definition (which we were not aware of), it was not possible for a long time to get agreement between theory and simulations, mainly caused by the outdated version of the manual

Another problem was that the value for local damping is standard set to 0.7. One should be aware of standard values that are nonzero, since these may crawl into the simulation as unwanted. It is therefore advised not to leave anything on default, since when you set the values yourself, you know what to expect from the program.

The automatic time step calculation is also not as stable as expected. For two-particle collisions, it was found that there is only one time step wherein the particles are in contact. This is far too low for the accuracy. The so-called safety factor, which is a fraction of the calculated critical time step, is standard set to 0.8. This is far too high to obtain a stable simulation. To set this value lower (**SET SAFETY_FAC** to e.g. 0.05), multiple cycles are obtained during collision. Each cycle the time step is recalculated. For more complex simulations, the time step therefore may vary widely between cycles, and one therefore does not have a clear overview of the elapsed real time. One advice therefore is to manually set a constant maximum time step, so that it is easier to calculate how much time has elapsed. This can be done by the command **SET DT MAX <value>**.

Later on, a closer look at the definitions made it clear that there were actually more time steps during collision, however there was only one time step recorded. The command **HISTORY NSTEP** can be used to change the amount of steps that the history is recorded. This number is standard set to 10, so that every 10 cycles is stored in the history database. Afterwards, when this number was changed to 1, more cycles have been observed where the particles were in contact.

A common mistake that is made is the definition of stiffness in theory and in simulations. In the viscous damping models, the values are associated with the contact, whereas in the force-displacement models, particle stiffnesses are used. This means in the viscous damping theory, the stiffness that is required is the stiffness of the particle-particle contact, and not of the individual particles. When two particles collide, the stiffnesses of both particles are assumed to act in series, so that the contact between these particles inherits half the stiffness of either particle (when we assume that both particles have the same stiffness). This was not known beforehand, since it was assumed that both stiffnesses were the same. This means a large discrepancy between the theoretic and simulated values was observed, before $k = k / 2$ was used in the equations.

During the two-particle simulations, each simulation was run 3 times. After changing the particle offset, the first run was somehow (for an unknown reason) done with the unit-normal vector of the previous run. When the simulation was done again, a new unit vector was found. A third run was done to confirm that the second run was good. Until now no solution has been found to this problem.

A disadvantage of the ITASCA software is that there is no built-in help function. Whenever one encounters a problem with a certain command, the only options left for the user is to search through the PFC^{2D} manual or observe how the command is used in examples. A hardcopy of the manual is available, as well as a digital version. In the beginning, only the hardcopy version was known to the user, which was rather outdated. The digital manual was found accidentally, and while reading the up-to-date manual, extra possibilities were discovered (such as viscous damping) ^[49].

4.8 Conclusions

DEM is a powerful tool to simulate individual particle movements and forces, by solving Newton's second law of motion based on a force-displacement law. The calculations itself are not complex, only the fact that each calculation has to be updated each cycle for each particle/contact makes it a computationally intensive method. Different programming levels are available in PFC^{2D}, and a mix of different levels will provide to be convenient to find the optimal result.

A stable integration time step is crucial for simulations. In this chapter, equations to estimate the critical time step and the particle-particle contact time have been derived. From this, the user can estimate an appropriate integration time step to be used in many-particle simulations.

The working of friction between particle and wall has been investigated. It has been found that, when both surfaces slide over each other, the friction value is the minimum of both surface friction values. Other quantities have found to be averaged in different ways.

In the case of particle-particle collisions, the effect of normal viscous damping on the restitution coefficient and on the contact time has been investigated. These results have shown satisfactory agreement with theory, in the case of both allowed and disabled tension.

It has been shown that the simulation software is able to reproduce the Ψ_2 versus Ψ_1 diagram, as it has been described in literature by Luding^[56] and references therein. Also the behaviour of the tangential spring and normal and shear viscous damping has been placed in this diagram, and the results satisfy the theory. For local damping, a similar effect on the particle-particle contact time and on the restitution coefficient has been found: contact time increases and restitution coefficient decreases with increasing damping. For large local damping, Ψ_2 approaches zero for all values of Ψ_1 , whereas for small damping, the values approach the $\Psi_2 - \Psi_1$ curve without local damping. Unfortunately no equations were found to support these results.

The goal of this chapter was to study the working of friction, normal/tangential springs, viscous and local damping, so that we can give them a meaning in the complete silo simulations. This has been successfully done, and the next chapter will describe the simulation setup and results of the silo simulations, with and without vibrations.

4.9 List of symbols and abbreviations

Symbols

Variable	Unit	Explanation
d	m	Particle diameter
e	-	Restitution coefficient
E	J	Energy
f	N	Force
g	m/s ²	Gravity acceleration
G	Pa	Shear modulus
I	kg m ²	Particle moment of inertia
k	N/m	Stiffness
m	kg	(reduced) mass
q	-	Pre-factor for moment of inertia
	N m	Torque
r	m	Position
R	m	Particle radius
t	s	Time
v	m/s	Velocity
V	m ³	Volume

Subscripts

Subscript	Explanation
0	No overlap
c	Contact
crit	Critical
d	Dynamic
diss	Dissipative
el	Elastic
f	Friction
g	Gravity
i	particle index
n	Normal
p	Particle
r	Rolling
s	Static
	Shear
t	Tangential
w	Wall

Greek symbols

Variable	Unit	Explanation
α	-	Local damping coefficient
β	-	Critical damping ratio
γ	kg/s	Damping constant
δ	m	Particle-particle overlap
Δ	m	Displacement
η	1/s	Effective viscosity
θ	-	Angle between unit-normal vector and contact velocity
μ	-	Friction coefficient
ν	-	Poisson's ratio
ρ	kg/m ³	Particle density
ψ	-	Velocity ratio (tangential/normal)
ω	1/s	Oscillation frequency
	1/s	Angular velocity

Superscripts

Superscript	Explanation
'	After collision
crit	Critical
fric	Friction
n	Normal
roll	Rolling
slip	Slip
t	Tangential
tors	Torsion

5 Silo simulations

This chapter contains the theory and simulations of the complete silo. The results that have been found in this chapter are used to be able to see how the silo functions with and without any vibrations. First the silo geometry and particle generation methodology shall be described, after which the setup and results of the simulations are given and discussed.

5.1 Silo geometry

A 3D-model and an inside photograph of the real vibrating hopper is shown in Figure 54, whereas a simplified 2D-model of the hopper as used in the simulations is shown in Figure 55. In Appendix 5 the complete design of the hopper is presented.

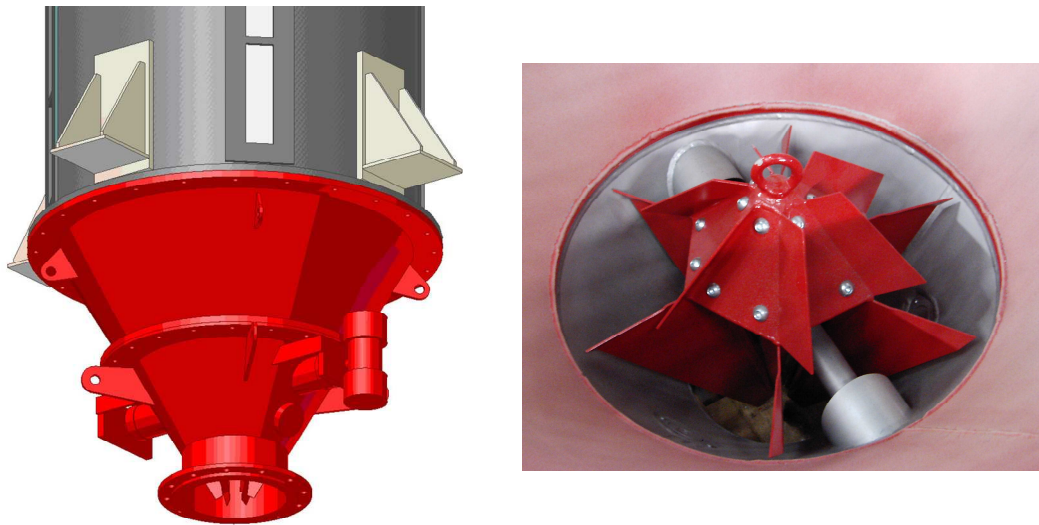


Figure 54: Left: 3D-model of the bottom view of the vibrating hopper. Right: inside photograph of the horizontally vibrating internal cone

Not the complete silo above the hopper is simulated, as this would require far too many particles and far too much time to simulate the movement of these particles. Therefore the silo shaft is cut off at 0.40 m (in reality the shaft would cover 3 m), which is considered to be enough to have the silo sufficiently filled.

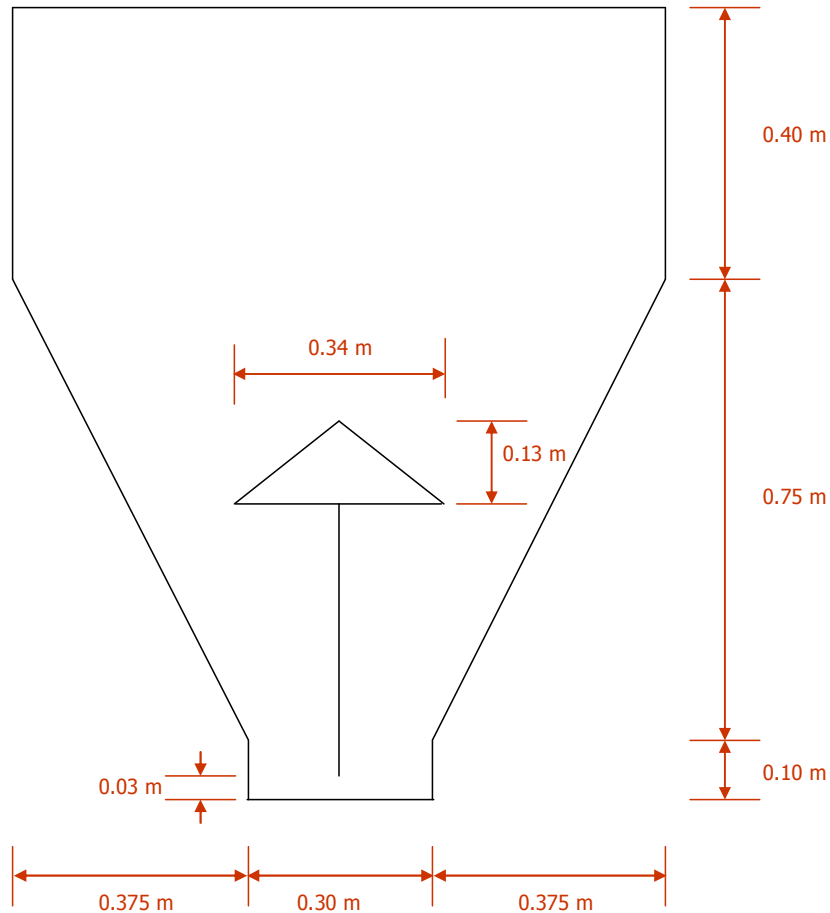


Figure 55: Simplified 2D-model of the hopper, which is used in the simulations. The hopper dimensions in the simulations match the real dimensions

The inner vibrating cone with baffles is simplified by a triangular area. The area below the cone is divided in six areas by other baffles. Dependent on how the cross section is taken, different views can be obtained. Here it is chosen to take a cross section so that the baffles do not have to be taken into account. In three dimensions, particles are able to flow between different areas by going over or past the baffles. In two dimensions, this is not the case, and these baffles are therefore not applied. It has been tested to apply these baffles in two dimensions by placing vibrating walls parallel along the hopper outer walls. However they created flow disturbances that would not be present in the real silo, and after some discussion it was decided to remove them. In the next section it will be explained how the particles are generated and how the silo is filled in a fast and easy way.

5.2 Particle generation

In ITASCA, there are two commands to generate the spherical particles: **BALL** and **GENERATE**. The **BALL** command generates a particle at a position, irrespective of whether there already is a ball present at that position; this means that particles may overlap each other. One advantage of this is that before cycling, it is easy to predefine present overlap forces in the system. The **GENERATE** command creates a specified amount of particles, but these particles are influenced by each other; particles cannot be placed on top of each other, so no particle-particle overlap is possible. Also particle positions are chosen randomly, whereas with the **BALL** command, coordinates for a certain particle must be supplied.

In this project the **GENERATE** command is used to generate an irregular packing of spherical particles. Since there is no allowed particle-particle overlap (but some may be created by radius expansion), it takes less time to cycle the system towards equilibrium. Particles with given small radii are generated and these radii are increased until a target porosity is reached. It is easy to create a system with very small particles since there is a lower chance of overlapping. Particle radii are taken at random from a uniform statistical distribution, or if desired, a Gaussian distribution may be chosen ^[49].

The walls have been placed before the generation of the particles. A FISH function is written that creates a particle assembly with a target porosity. The porosity n is defined as:

$$n = 1 - \frac{A_p}{A} \quad (5.1)$$

Here A_p is the sum of particle areas and A is the silo area. Since the particles are spherical, the area can be taken to be circular, and we can rearrange Eq. (5.1) to:

$$nA = A - \sum \pi R^2 \quad (5.2)$$

$$\sum R^2 = \frac{A(1-n)}{\pi} \quad (5.3)$$

Here the Σ denotes the sum over all particle radii R . If we define R_0 and R as the 'old' and 'new' radii, respectively, and n_0 and n as the 'old' and 'new' porosity, we can define

$$\frac{\sum R^2}{\sum R_0^2} = \frac{1-n}{1-n_0} \quad (5.4)$$

When we use the same multiplier M to increase the radius of all particles, then $R = M \cdot R_0$ and we can rewrite Eq. (5.4):

$$M^2 = \frac{1-n}{1-n_0} \quad (5.5)$$

$$M = \sqrt{\frac{1-n}{1-n_0}} \quad (5.6)$$

With Eq. (5.6) we can find the multiplier with which we must multiply all radii in order to increase the porosity from n_0 to n .

We can approximate the mean particle radius \bar{R} :

$$\bar{R} = \frac{R_{LO} \cdot (1+r)}{2} \quad (5.7)$$

Here R_{LO} is the lower particle radius of the distribution and r is the radius multiplier (so that $R_{HI} = rR_{LO}$).

At this point we do not know the amount of particles to be created. We can assume that

$$\sum R^2 = \sum \bar{R}^2 = N\bar{R}^2 \quad (5.8)$$

This is not correct but it is a good approximation for a uniform distribution. With this, we can rearrange Eq. (5.3) to approximate N :

$$N = \text{int} \left(\frac{A \cdot (1 - n_0)}{\pi \bar{R}^2} \right) \quad (5.9)$$

The integer is used since the amount of particles has to be an integer; no incomplete particles can be generated.

After having calculated the amount of particles to be used, the particles can be generated. The used particle size for the initial assembly will be $0.5 \cdot R_{LO}$ to assure that enough particles can be placed. The initial porosity of the system can be measured using Eq. (5.1), and one can calculate the radius multiplier using Eq. (5.6). This multiplier is then used to increase the radius of all particles, after which the target porosity is reached. Now the system can be cycled towards equilibrium and the assembly is ready to be used.

5.3 Simulation setup

5.3.1 Hopper loading

After placing the walls, the silo is filled according to the method described in Chapter 5.2. The system properties that are used are displayed in Table 7.

Table 7: Comparison of system properties between real limestone and simulated particles

		Limestone	Simulation
Lower particle radius	m	$5.0 \cdot 10^{-7}$	$4.0 \cdot 10^{-3}$
Mean particle radius	m	$1.6 \cdot 10^{-6}$	$5.0 \cdot 10^{-3}$
Upper particle radius	m	$4.0 \cdot 10^{-6}$	$6.0 \cdot 10^{-3}$
Material density	kg/m ³	2714	723.25
Bulk density	kg/m ³	579	579
Porosity	-	0.79	0.20
Normal stiffness	N/m	-	10^8
Shear stiffness	N/m	-	10^8
Wall stiffness	N/m	-	10^8
Integration time step	s	-	$2.5 \cdot 10^{-7}$

The system settings that are used have been tested in Chapter 4. They can be understood with the collision theory, so from the stiffness and the viscous damping we can calculate the minimum contact duration and the restitution coefficient.

The particle properties are chosen to resemble the realistic values of the limestone powder. The main problem is that the particle size of the real material is much smaller than what can be simulated in ITASCA. It is impossible to match the particle size of the material, which in turn results in no possibility to get a realistic simulation (not even close). Another problem is the porosity of the material. In reality limestone is as closely packed as only 21 vol% material. If this porosity is used in the two-dimensional simulation, this does not make much sense, since the large particles do not even touch each other. It is therefore chosen to use a more dense packing in these simulations. The bulk density of the material is chosen to be the same as the real limestone, with a porosity of 20 vol%. As a consequence, the material density has to be decreased.

A distribution of particle radii is used, to decrease the likeliness of regular packings. When only one particle size is chosen, the particles tend to cluster together to form regular structures, which move together in one piece. The implementation of a particle size distribution decreases the likeliness to form regular packings. The radii of the particles are randomly chosen from a normal distribution. A ratio of lower to higher radius of 1.5 is chosen here, where a large ratio would cause a less accurate hopper outflow calculation.

The normal and shear stiffness of the simulation particles are chosen so that the behaviour of the spheres looks realistic. A too low stiffness makes the particles disappear through the wall, while a too high stiffness gives rise to a lower critical time step (through Eq. (4.1), Chapter 4), which means a smaller time step and thus longer simulations. The same accounts for the wall stiffness: too low is unrealistic, however too high is not a problem. For the sake of simplicity, the same value as the particle stiffness is taken. For shear stiffnesses, the same value as normal stiffnesses is used, since there is no reason to change to a different value.

Using the current values, with Eq. (4.1) we can estimate the critical time step to be

$$t_{crit} = \sqrt{\frac{m}{k_n}} = \sqrt{\frac{\frac{4}{3}\pi \cdot R^3 \cdot \rho}{k_n}} = \sqrt{\frac{\frac{4}{3}\pi \cdot (3 \cdot 10^{-3})^3 \cdot 723.25}{10^8}} = 9 \cdot 10^{-7} \text{ s} \quad (5.10)$$

In Chapter 4, an equation for the particle-particle contact time has been derived (Eq. (4.45), p. 53)):

$$t_c = \frac{\pi}{\sqrt{1 - \beta_n^2}} \cdot \sqrt{\frac{m_{12}}{k_n}} \quad (5.11)$$

The main difference here with the critical time step is the definition of mass and stiffness: for the critical time step, these values are taken for the *particle*, whereas for the contact time, these values are defined for the *contact*. In case of equal masses and equal stiffnesses, there will be no difference between the critical time step and the contact time (since the factor 0.5 due to acting in series will cancel out), except for the pre-factor in Eq. (5.11). Since this pre-factor is larger than 1,

$$t_c \geq \pi \cdot t_{crit} \quad (5.12)$$

and depends on the viscous damping of the system.

Although there are (using standard settings in ITASCA) multiple cycles during contact, it has been chosen to take a user-defined integration time step, to avoid strange behaviour. It is therefore chosen to manually set the time step to $\Delta t = 2.5 \cdot 10^{-7} \text{ s}$. This also makes it easier to calculate the elapsed time after a number of cycles.

Some form of damping (either local or viscous) is required to slow down the particles. After particle generation, some overlaps are formed, meaning that the system is not in equilibrium. Either local damping or viscous damping is required to dissipate energy, otherwise no equilibrium state will be reached. The effect of both types of damping shall be evaluated here as well.

The loading is ended at the time when the system has cycled towards equilibrium using the **SOLVE** command. With this command the cycling automatically ends when either the maximum or average unbalanced-force ratio reaches a value of 10^{-2} . After solving, the simulation will be saved as it is and stored as a hardcopy file. This makes it easy to run subsequent emptying simulations many times without having to wait for the silo to load and with identical initial conditions, which will prove useful in the case of testing different vibration velocities.

Several parameters are to be varied, to see the relative effect on the number flow rate. In this chapter, the most important factor to be varied are damping, friction and vibration frequency and amplitude.

5.3.2 Hopper discharge

After the silo and hopper have been filled with the material, the bottom wall of the hopper can be removed, after which the powder flows out by gravity. Snapshots will be taken during the simulation and the number flow out of the hopper will be monitored over time. This is done by counting the particles that fall below the hopper outlet each 4000 cycles (10^{-3} s).

To save simulation time, it has been tested to delete particles that fall too far out of the silo. If this would not be done, these particles would keep on falling and their motion and forces will still be calculated, even though we are not interested in this. A border was placed 0.1 m below the hopper outlet, and particles that are below this line at the time a new cycle is started will be deleted.

However, when particles are being deleted, they are not added to the number flow rate. Keeping the particles there as they are and not deleting them means more calculation time, but they have to be monitored in order to obtain the number flow rate.

5.4 *Simulation results and discussion*

The influence of various parameters on the number flow rate has been investigated. First the effects of local and viscous damping are studied, after which friction is varied. Finally vibrations are applied, where the number flow rate was measured as well.

5.4.1 Effect of damping

Various starting parameters have been tested, and one of them is local damping. First, simulations without any local damping (only normal viscous damping) have been performed. However, some strange behaviour was observed at these simulations. Some snapshots are shown in Figure 56.

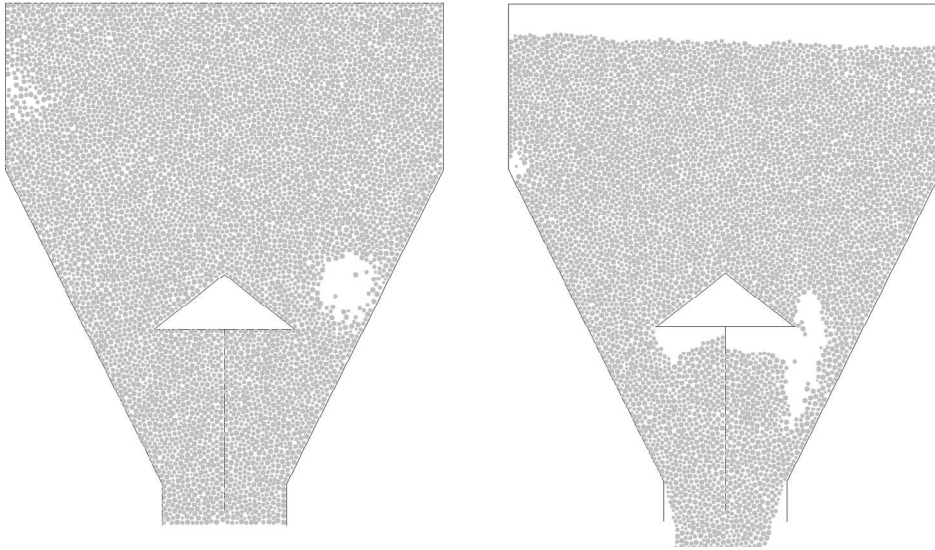


Figure 56: Loaded silo with $\beta_n = 0.7$ and $\alpha = 0$. Left: initial state. Right: state after 0.02 s

After $0.59 \cdot 10^{-3}$ sec the filling was ended as in the software a minimum unbalanced force has been reached. Large holes were formed in the loading state and during emptying, when a particle hits the section where the wall and hopper are connected, the particle gains energy and bounces back, creating larger holes. Also the particles in the silo seem to flow like a liquid; particles move in circles around the large holes. Somehow, without local damping, some numerical instability is created. From these simulations, it may be concluded that local damping is required to have realistic behaviour. However the exact reasoning behind this is not completely understood.

The hopper is loaded again with $\alpha = 0.7$, and immediately more realistic behaviour is observed. For the following simulations, $\alpha = 0.2$ has been tested, to decrease the energy loss due to local damping. Various values of β_n have been tested but all show more or less the same initial loading state.

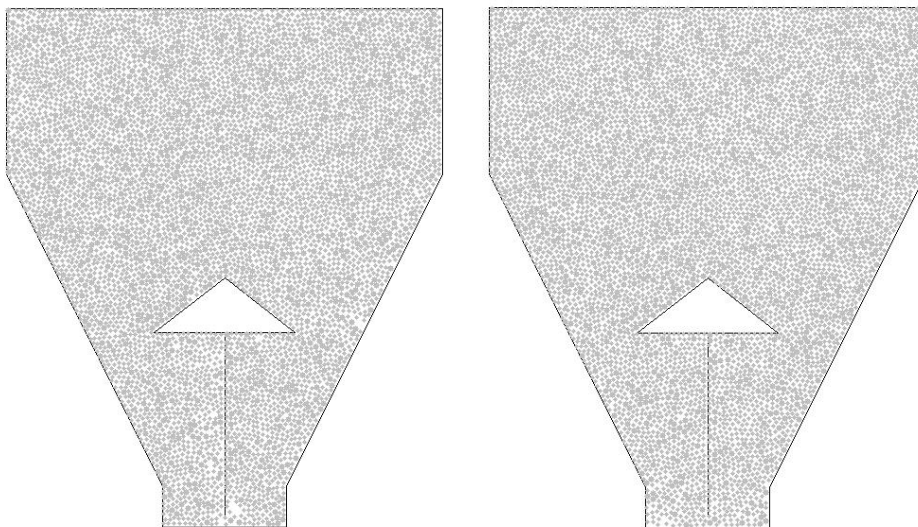


Figure 57: Initial loading states with $\alpha = 0.2$. Left: $\beta_n = 0.2$. Right: $\beta_n = 0$

An effect of viscous damping on the hopper out flow has been observed, however. A simulation with $\beta_n = 0.2$ has shown to give a faster silo discharge than when there is no normal viscous damping active (see Figure 58).

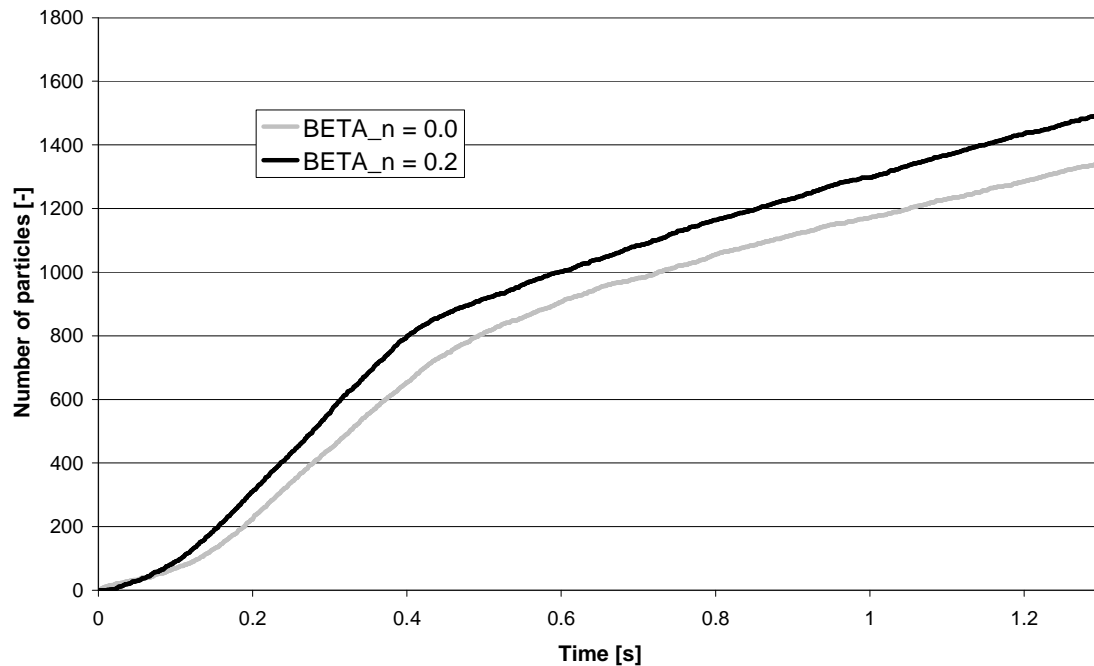


Figure 58: Amount of particles leaving the silo for $\beta_n = 0.2$ and disabled viscous damping

Snapshots of both simulations are compared as well. This is shown after 0.5 sec (Figure 59) and after 1 sec (Figure 60). Although a clear effect is seen, no explanation was found for this difference. Nevertheless, viscous damping will be kept active in the forthcoming simulations to stay as close to reality as possible.

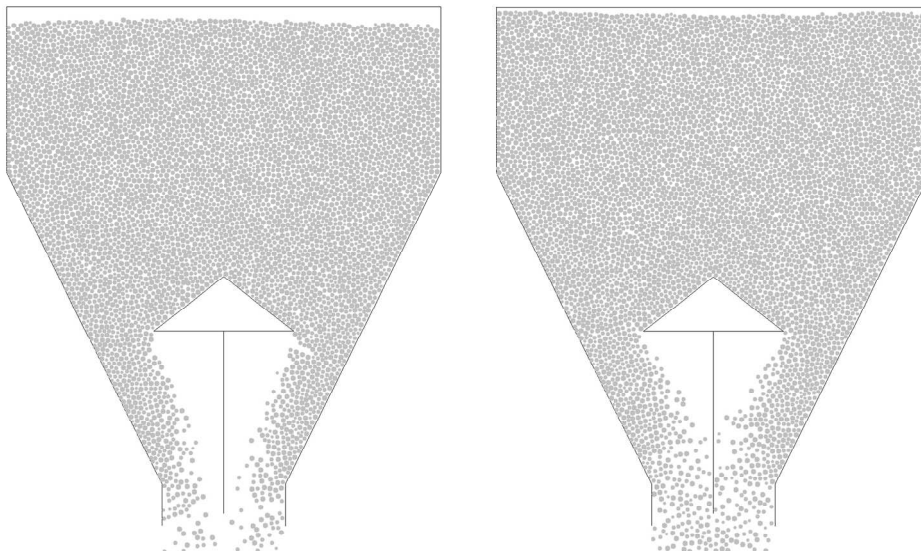


Figure 59: Simulation snapshots after 0.5 sec, $\alpha = 0.2$. Left: $\beta_n = 0.2$. Right: $\beta_n = 0$

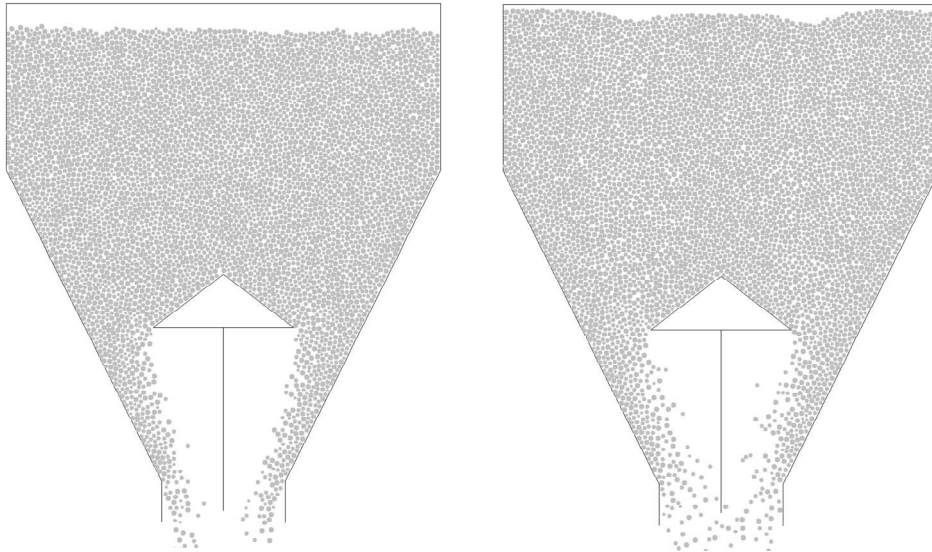


Figure 60: Simulation results after 1 sec, $\alpha = 0.2$. Left: $\beta_n = 0.2$. Right: $\beta_n = 0$

Continuing with the same simulations, in the right side of Figure 60 two small valleys may be observed. These valleys show the beginning of core flow behaviour; in the simulations it was found that the material flow was directed in two patterns around the deflector. This is shown more clearly in Figure 61. A stationary zone is visible directly on top of the deflector. A better visualisation would be obtained by dividing the material in horizontal sections of different colours.

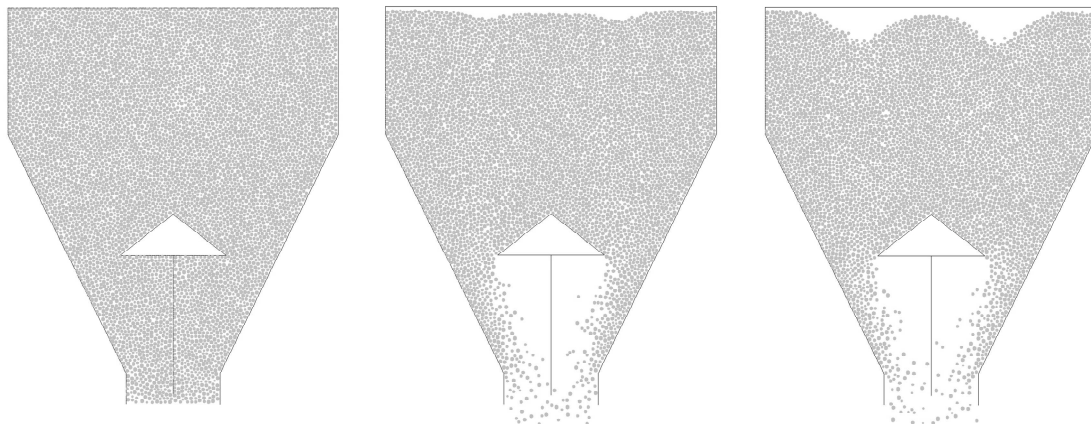


Figure 61: Simulation results for $\alpha = 0.2$ and $\beta_n = 0$. Left: Initial condition. Middle: after 1 sec. Right: after 1.6 sec

5.4.2 Effect of friction

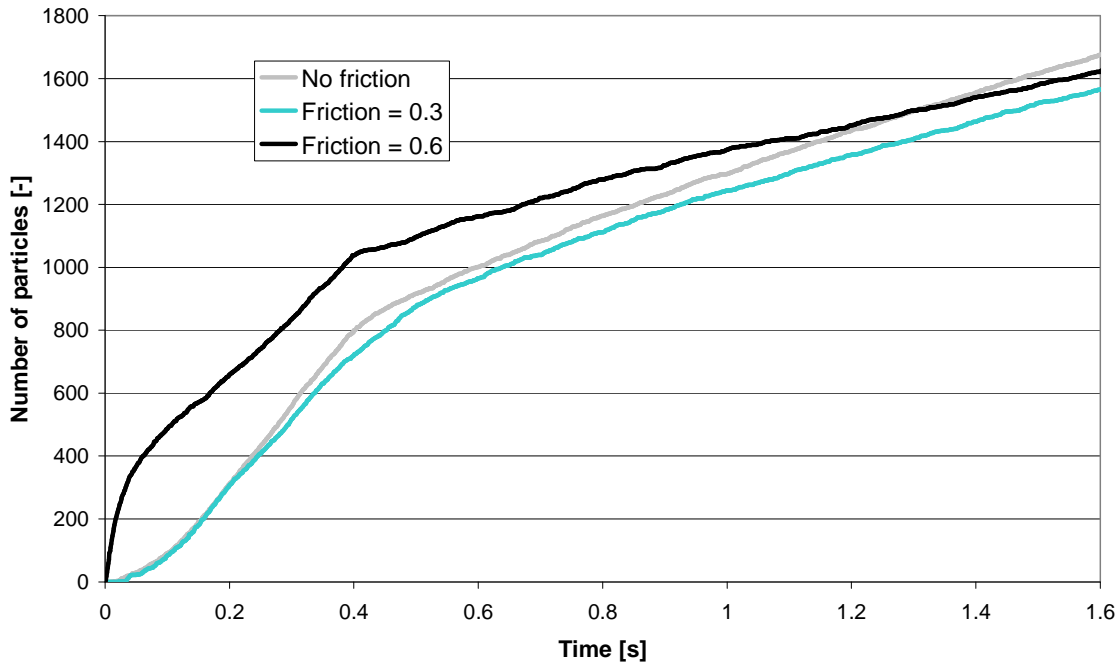


Figure 62: Amount of particles leaving the silo for various friction coefficients

Initially, high friction coefficients seem to have a high initial hopper outflow. However after analysis of the screenshots and study of the movie created from the screenshots, it was found that in the initial loading, particles were “pushed” out of the silo. It was found that there still was some particle-particle overlap present, even though the software had detected an ending condition.

It can be observed that there are two different steady-state values for the flow rate, both characterized by a constant mass flow region. Initially a high flow rate is observed, caused by the falling particles directly above the outlet. After approx. 0.5 s these particles have left the silo, and the flow rate decreases. This is caused by the fact that the particles now have to flow around the triangular discharge aid. The second steady state flow rate is clearly lower for higher friction values.

After 1.2 s, the advantage of the friction is already cancelled. In the long run, the simulations without friction show the highest number flow rate, although there is only a small difference.

5.4.3 Effect of vibrations

The number outflow of the hopper over time is shown in Figure 63. From this figure only a very small effect of the vibrations on the flow rate is seen. However, only a frequency of 200 Hz and vibration peak amplitude up to 5 mm/s have been tested, whereas the application range of both parameters is quite different (15-50 Hz, up to 6.3 m/s). Although these parameters are out of application range, they are chosen as starting values to see how the simulation would behave. Figure 63 shows no clear increase in flow rate, which is mainly thought to be due to the fact that cohesion is not active.

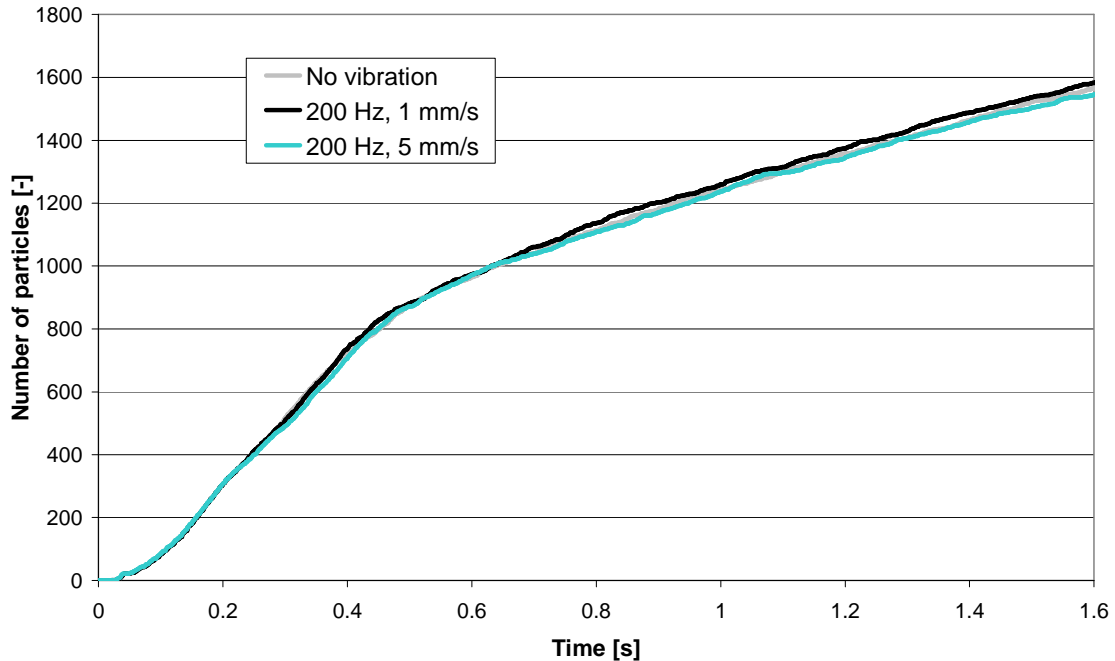


Figure 63: Effect of vibration on the amount of particles leaving the silo bottom

5.4.4 Effect of internals

One simulation has also been performed to see how fast discharge would be when there would be no discharge aid. The result is clearly visible in Figure 64; with the current parameters it would be advantageous to remove the discharge aids. Main reasons for this are that the simulation is two-dimensional and cohesion has been disabled.

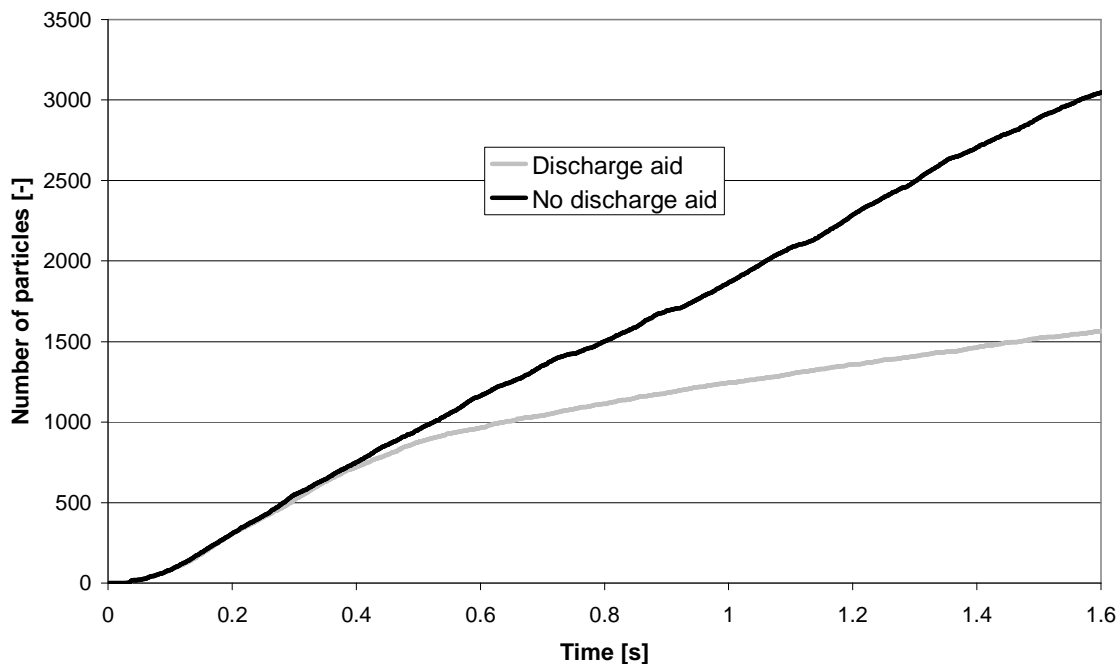


Figure 64: Effect of removing the discharge aid on the number of particles leaving the silo. Here $\alpha = 0.2$ and $\beta_n = 0$ and vibrations have been disabled

Cohesionless material easily flows out through the large central hopper outlet, and there is no chance for blocking of the silo. In case of active cohesion, it is expected that such behaviour is absent.

5.5 Conclusions

In this chapter the effect of damping, friction and vibrations on the hopper mass flow rate has been investigated by means of two-dimensional DEM simulations. It was found that local damping is required in order to have "real" silo simulations. Without local damping active there was found to be instability, whereas this problem was solved when local damping was applied.

The ending conditions of the filling procedure were found to give questionable solutions. In case of no local damping, unusual ending conditions were obtained. In case of active friction, sometimes clearly no minimum force was obtained.

Friction has a negligible effect on the hopper out flow. Initially higher friction seemed to increase the flow rate, but after 1.6 sec almost no difference was found; frictionless material flows out slightly easier than when the material would have friction.

Vibrations have shown to have only a negligible effect on the flow rate. The main reason is thought to be that cohesion is not active. With active cohesion, however, such vibrating devices could provide interesting discharge aids.

When no internals are placed within the silo, the number flow rate is much higher than in the case of discharge aid. The main reason is that the particle properties are not matched with reality.

5.6 List of symbols and abbreviations

Symbols

Variable	Unit	Explanation
A	m ²	Area
k	N/m	Stiffness
m	kg	(reduced) mass
M	-	Multiplier
n	-	Porosity
N	-	Number of particles
r	-	Ratio of upper to lower radius
R	m	Particle radius
t	s	Time

Subscripts

Subscript	Explanation
0	Initial
c	Contact
crit	Critical
HI	Upper
LO	Lower
n	Normal
p	Particle

Greek symbols

Variable	Unit	Explanation
α	-	Local damping coefficient
β	-	Critical damping ratio
ρ	kg/m ³	Particle density

Superscripts

Superscript	Explanation
-	Average

6 Summary, conclusions and recommendations

This chapter contains a review of the obtained goals, which refers back to the introduction. Furthermore the work is summarized and concluded, and finally several recommendations for continued research are given.

6.1 Review of obtained results

The goal of the project was to study the effect of vibrations on the particle flow behaviour

- by doing shear test experiments with a vibrating Jenike shear cell
- by performing 2D DEM simulations of a vibrating hopper

During the project, it was found necessary to start with two-particle simulations to get a better understanding of the used simulation software. This means the project target was extended and an additional goal was added. The three targeted goals have been successfully reached. To get a good overview, a schematic representation of the research and its results is displayed in Figure 65.

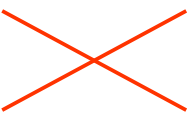
	Two particles	Shear test	Silo
Experiments			
Simulations			

Figure 65: Schematic display of the obtained results

The sections with a cross have been studied. New results include experiments involving two-particle simulations, which have found to give agreement with the analytical solution. Cohesion forces between two particles can be measured using Atomic Force Microscopy ^[55-57]. To be able to compare experiments with the performed simulations, more realistic contact models are required. This mainly includes the implementation of cohesion forces and matching particle properties. But on the other hand, not all the details are known, which are needed to model the contact of fine powder particles.

In case of shear tests involving the vibrating Jenike shear cell, results comparable to that in literature have been obtained ^[3-7]: vibrations decrease the stresses in the shear cell. Clear simulations considering the vibrating Jenike shear cell have not been reported yet.

The 2D DEM simulations on the complete vibrating hopper have shown interesting results, comparable with those in literature ^[16,18], even though no realistic contact model has been applied. The next step in simulating such systems is the addition of cohesion. When two particle simulations have been successfully tested with a contact model including cohesion, this contact model can also be applied to the two-dimensional silo simulations.

6.2 Summary and conclusions

Ultrafine particles often show cohesive behaviour, caused by molecular based van der Waals forces. Due to these interparticle cohesion forces often flow disturbances (e.g. arching and ratholing) occur when such powders are stored in a silo.

Bulk shear tests have been performed to study the effect of horizontal vibrations on the flow characteristics of limestone powder. From the experiments done, it can be concluded that vibrations decrease the unconfined yield strength σ_c , where a stronger effect is seen for higher bulk density. A clear trend was observed, however the flowability classification according to Jenike^[29,42] remains in the same regime of "very cohesive" material. A stronger effect was seen on the internal and effective friction angle, resp. φ_i and φ_e . These values both have shown a decrease with increasing vibration intensity.

In the case of the wall shear tests, for low normal stresses the behaviour can be fitted by the failure criterion of Roberts. This model is not valid for high normal stresses. However in both cases a strong decrease in wall shear stress was found with increasing vibration peak velocity. A strong effect was seen on the wall friction angle φ_w , as it drastically decreases with increasing vibration velocities. This offers interesting opportunities in increasing the hopper angle and decreasing the hopper outlet.

Various simulations of two colliding particles have been done using the PFC^{2D} software from ITASCA. It has been found that, when both surfaces slide over each other, the friction value is the minimum of both surface friction values. The effect of normal viscous damping on the restitution coefficient and on the contact time has been investigated. These results have shown satisfactory agreement with theory, in the case of both allowed and disabled tensile normal forces.

A quantitative classification of collisions has been made by plotting the scaled tangential velocity before and after collision, as described in literature by Luding^[56] and references therein. The behaviour of the tangential spring and normal and shear viscous damping has been placed in this diagram, and the results satisfy the theory. For local damping, a similar result has been found, although no equations satisfying the results could be derived so far.

Friction was found to have a negligible effect on the hopper out flow. In the long run, frictionless material flows out slightly easier than materials with friction. Local damping is required in order to have "realistic" silo simulations. Without local damping active there was found to be instability, whereas this problem was not observed when local damping was activated.

Vibrations have shown to have a negligible effect on the hopper flow rate. While effects clearly have been observed in the shear test experiments, the main reason for no observed effect in the simulations is thought to be because of inactive cohesion. With active cohesion, however, such vibrating devices could provide interesting discharge aids.

The main reason that the simulations have not shown satisfactory results are caused by the fact that too many assumptions had to be made, rendering the simulated system far from the real system. The simulation is two-dimensional, used particle sizes are 10^3 times higher than the real limestone and no cohesion has been implemented in the model. This means only relative and qualitative results could be obtained. Nevertheless vibrations show a promising trend for a discharge aid, as the shear test results have shown.

6.3 Recommendations

Unfortunately not all the ideas could be examined, due to the limited time span available. The most important recommendations for continued research are therefore listed in this section. The following recommendations are sorted by priority and personal preference:

- apply contact model that includes cohesion
- apply wider range of vibration frequencies and amplitudes in silo simulations
- simplify hopper geometry by symmetry
- study effect of pulsed vibrations
- measure more yield loci for bulk shear tests
- application of Janssen pressure in silo simulations
- investigate effect of moisture
- test different wall material for wall shear tests
- look for software different than PFC^{2D}

One must-have implementation to simulate materials such as limestone is the feature to add cohesion. Without cohesion it is not possible to create a flow disturbance such as arching. To implement a new contact model including cohesion, additional C++ programming knowledge would be required, or one could implement a user-defined contact model, depending on the C++ knowledge of the user.

To get a better understanding of the effect of vibrations, it is recommended to apply a wider range of frequencies and amplitudes and determine the hopper flow rates. Due to time limitation this has not been done in this project.

One idea was to simulate only one half of the silo (left or right). This would allow the use of more and smaller particles, hence coming closer to the real powder. However the implementation of only one half would give rise to new problems (such as boundary conditions). It still remains an interesting option to evaluate more closely. Especially in three dimensions (for conical silos) one could profit from the cylindrical geometry, and model only small fractions of the silo (like "pieces of cake").

In practise often pulsed operation of vibrating discharge aids is applied, where a period of vibration is followed by an idle time. Operators of such devices find this style advantageous for the flow behaviour. Although no guidelines have been developed yet for pulsed operation, it might be interesting to test this effect using DEM simulations.

Considering the shear tests, far too little experimental work has been done to draw conclusions with respect to applicability in industry. It is therefore recommended to perform shear tests with higher normal loads so that (at least) two more yield loci are measured. Tests at higher vibration intensities (0.02-0.05 m/s) are interesting as well to investigate so that the applicability can be tested over a wider range.

During the project, it has been discussed that instead of filling the complete silo with powder, the silo could be filled partly, and a horizontal wall could be placed on top of the powder. This wall exerts a vertical pressure on the powder that represents the pressure of the powder that would be present in the real case. As idea, the pressure that this wall exerts could be estimated by Janssen's equation for a conical hopper ^[1]. Due to the limited time, this has not been evaluated.

It has been noted that the moisture content of the limestone powder is on its equilibrium value and therefore has a negligible effect on the flow behaviour. One interesting parameter to add to the shear tests is an increased moisture content, to see if a higher moisture percentage has a substantial effect on the cohesive behaviour. In addition, vibrations could be applied to cancel the effect caused by this moisture.

Concerning the wall friction angle, one might consider testing other wall materials as well. Although the general idea remains the same (increasing vibrations reduce the wall friction angle), quantitative results should lead to a better understanding of the effect of vibrations.

A final personal recommendation is to look for a different software package that allows similar options as PFC^{2D}, but with a better help database and/or easy cohesion implementation. During the work on this project, it was found that the PFC^{2D} software from ITASCA is not the ideal software to work with. An advantage is that it does not take a lot of time to learn how to program the simulation scripts and to run them. Particle and wall properties are easily assigned, graphs are easily made, and the graphical output of the program looks fancy.

However, there are also some disadvantages as well. It takes a lot of time and energy to understand what is actually happening inside the software and how the program calculates certain values. It is also difficult to set the right properties to the materials that you are simulating, since different properties may lead to strange results. There is no built-in help function, so the only thing to do after getting some error is to search through all the details in the books that were delivered together with the software.

Acknowledgements

As I would not be able to do this project on my own, there are some people that I would like to thank.

First of all I would like to thank Jürgen Tomas, for providing me this project and giving me the opportunity to do my master thesis in Germany. Without his hospitality I would have never had the possibility to do this project in Magdeburg.

Special thanks go out to Guido Kache, for his availability to be my daily supervisor and for his help and insight in the project, and for letting me feel comfortable in this new environment. He has helped me a lot with non-project related arrangements, and assisted me where my German knowledge was insufficient.

My best appreciations go out to Stefan Luding, for his experience and insight in DEM modelling regarding bulk materials, and for his major help during my project. Whenever things did not work out very well, he gave me the help and explanations that made me continue my project. I would also like to thank him for his hospitality regarding the meetings in Enschede.

I would like to thank Andreas Schmidt-Ott for his time and interest in the project, and for his availability to be my supervisor.

Further appreciations go out to Ruud van Ommen, for his time to be my third reviewer, and for his interest in the project.

I want to thank all my friends and colleagues in Magdeburg, for making my stay here one that I will never forget. Outside working hours there have been enough time spending activities and travels to fill in my free time in a very enjoyable way.

I would like to thank my family for their continuous support and trust in my capacities and courage. Contact with the home front made me feel comfortable, and they supported me in every possible way.

And last but not least, most of all I would like to thank my girlfriend Kaewta Jetsrisuparb. I cannot possibly express in words the support, help and love she has given me throughout my time in Magdeburg. She gave me the impulse and motivation for doing my master thesis abroad and gave her full support in this. Furthermore, she has always supported my personal development and without her encouragements I would have never been able to accomplish this step in my life.

References

- [1] Nedderman, R.M., *Statics and Kinematics of Granular Materials*, Cambridge University Press, Cambridge **1992**, ISBN 0-521-40435-5
- [2] Bates, L.; Dhodapkar, S.; Klinzing, G., *Discharge aids*, SHAPA Technical Bulletin No. 12, **August 2007**
- [3] Roberts, A.W., *Vibration of Powders and its Application*, in: Fayed, M.E.; Otten, L., *Handbook on Powder Science and Technology*, Van Nostrand, 181-229, **1984**, ISBN 0-4422-2610-1
- [4] Roberts A.W.; Scott, O.J., *An Investigation into the Effect of Sinusoidal and Random Vibrations on the Strength and Flow Properties of Bulk Solids*, *Powder Technology*, 21, 45-53, **1978**
- [5] Arnold, P.C.; Kaaden, A.S., *Reducing Hopper Wall Friction by Mechanical Vibration*, *Powder Techn.*, 16, 63-66, **1977**
- [6] Kollmann, T.; Tomas, J., *Effect of Applied Vibration on Silo Hopper Design*, Presentation, Fine Powder Processing, Pennsylvania State University, State College **2001**
- [7] Kollmann, T.; Tomas, J., *The Influence of Vibrations on Flow Properties of Cohesive Powders*, *Conf. Bulk Materials Storage, Handling and Transportation*, 1, 417-427, Newcastle, **2001**
- [8] Tykhoniuk, R.; Luding, S.; Tomas, J., *Simulation der Scherdynamik kohäsiver Pulver*, *Chem. Ing. Tech.*, 76 (1-2), 59-62, **2004**
- [9] Tykhoniuk, R.; Tomas, J.; Luding, S.; Kappl, M.; Heim, L.; Butt, H.-J., *Adhesion, inelastic contact behavior and simulation of shear dynamics of ultrafine cohesive powder*, in: Garcia-Rojo, R.; Herrmann, H.J.; McNamara, S., *Powders and Grains 2005* Balkema, Leiden, Netherlands, 499-503, **2005**
- [10] Thornton, C.; Zhang, L., *Numerical Simulations of the Direct Shear Test*, *Chem. Eng. Technol.*, 26 (2), 153-156, **2003**
- [11] Härtl, J.; Ooi, J.Y., *Experiments and simulations of direct shear tests: porosity, contact friction and bulk friction*, *Granular Matter*, 263-273, **2008**
- [12] Chladni, E.F.F., *Entdeckungen über die Theorie des Klanges*, Leipzig **1787** (cited by Wassgren^[16])
- [13] Faraday, M., *On a Peculiar Class of Acoustical Figures; and on Certain Forms Assumed by Groups of Particles upon Vibrating Elastic Surfaces*, *Phil. Trans. R. Soc. London*, vol. 52, 299-340, **1831**
- [14] Bachmann, D., *ZVDI, Beiheft Verfahrenstechnik*, 2 (43), **1940** (cited by Wassgren^[16])
- [15] Kroll, W., *Fliesserscheinungen an Haufwerken in schwingenden Gefäßen*, *Chemie Ing. Techn.*, 27 (1), 33-38, **1954** (cited by Wassgren^[16])

- [16] Wassgren, C.R., *Vibration of Granular Materials*, Dissertation, California Institute of Technology, Pasadena, **1997**
- [17] Takahashi, H.; Suzuki, A.; Tanaka, T., *Behavior of a particle bed in the field of vibration*, Powder Techn., 2, 65-77, **1968** (cited by Wassgren ^[16])
- [18] Wassgren, C.R.; Brennen, C.E.; Hunt, M.L., *Granular flow in a vertically vibrating hopper*, Proceedings of the 10th ASCE Engineering Mechanics Specialty Conference, Boulder, CO, **1995** (cited by Wassgren ^[16])
- [19] Böhrnsen, J.-U.; Antes, H.; Ostendorf, M.; Schwedes, J., *Silo Discharge: Measurement and Simulation of Dynamic Behavior in Bulk Solids*, Chem. Eng. Technol., 21 (1), 71-76, **2004**
- [20] Wassgren, C.R.; Hunt, M.L.; Freese, P.J.; Palamara, J.; Brennen, C.E., *Effects of vertical vibration on hopper flows of granular material*, Phys. Fluids, 14 (10), 3439-3458, **2002**
- [21] Suzuki, A.; Tanaka, T., *Behaviour of a Particle Bed in the Field of Vibration. IV. Flow of Cohesive Solids from Vibrating Hopper*, Powder Technol., 6, 301-308, **1972**
- [22] Marring, E.; Hoffmann, A.C.; Janssen, L.P.B.M., *A Study of the Discharge of Cohesive Powders under Simultaneous Aeration and Vibration*, Part. Sci. Technol., 13 (1), 7-21, **1995**
- [23] Limestone, <http://en.wikipedia.org/wiki/Limestone>
- [24] Rhodes, M., *Introduction to Particle Technology*, John Wiley & Sons, New York, **2005**, ISBN 0-471-98483-3
- [25] Tomas, J., *Mechanics of Particle Adhesion*, conference proceeding, CHISA, Prague **2004**
- [26] Alexander, A.W.; Chaudhuri, B.; Faqih, A.; Muzzio, F.J.; Davies, C.; Tomassone, M.S., *Avalanching flow of cohesive powders*, Powder Technology (164), **2006**, 13-21
- [27] Schulze, D., *Flow Properties of Powders and Bulk Solids and Silo Design For Flow*, **2002**, <http://www.dietmar-schulze.de/>
- [28] Jacob, K., *Bin and Hopper Design*, Presentation Dow Chemical Company, Solids Processing Lab, **2000**
- [29] Jenike, A.W., *Storage and Flow of Solids*, Bulletin No. 123, Utah Engineering Experiment Station, University of Utah, Salt Lake City, 53 (26), **1964**
- [30] Mouraille, O.; Herbst, O.; Luding, S., *Sound propagation in isotropically and uniaxially compressed cohesive, frictional granular solids*, submitted to Engineering Fracture Mechanics, **2008**
- [31] Mouraille, O.; Luding, S., *Sound wave propagation in weakly polydisperse granular materials*, submitted to Ultrasonics, **2007**

- [32] Mouraille, O.; Luding, S., *Acoustic waves in granular materials*, Proceedings, Paper #1752, Int. Conf. on Ultrasonics, Vienna, April 9-13, **2007**
- [33] Mouraille, O.; Luding, S., *Mechanic waves in sand: Effect of polydispersity*, PARTEC **2007**, Nuremberg, Germany, pp. 1-4, CD Proceedings
- [34] Mouraille, O.; Mulder, W.A.; Luding, S., *Sound wave acceleration in granular materials*, *J. Stat. Mech.*, P07023, 15 pages, **2006**
- [35] Mouraille, O.; Luding, S., *Mechanic waves in sand, 3d simulations*, World Congress Particle Technology, Florida, 8 pages, CD-Proceedings, AIChE, **April 2006**, ISBN 0-8169-1005-7
- [36] Mouraille, O.; Luding, S., *Sound propagation in dense, frictional granular materials*, in: *Powders and Grains 2005*, Stuttgart, **July 2005**, Garcia-Rojo, R.; Herrmann, H.J.; McNamara, S., Balkema, Leiden, Netherlands, 319-322
- [37] Janssen, H.A., *Versuche über Getreidedruck in Silozellen*, *Zeitschrift des Vereines deutscher Ingenieure*, 35, 1045-1049, **1895**
- [38] Roberts, A.W., *100 Years of Janssen*, *Bulk Solids Handling*, 15 (3), **1995**
- [39] Schwedes, J., *Review on testers for measuring flow properties of bulk solids*, *Granular Matter* 5, 1-43, **2003**
- [40] Schulze, D., *Pulver und Schüttgüter; Fließeigenschaften und Handhabung*, Springer, Berlin **2006**, ISBN 3-540-34082-3
- [41] Feise, H.J., *A review of induced anisotropy and steady-state flow in powders*, *Powder Techn.* 98, 191-200, **1998**
- [42] Tomas, J., *Zur Produktgestaltung kohäsiver Pulver – mechanische Eigenschaften, Kompressions- und Fließverhalten*, *Chem.- Ing.- Technik*, 75 (6), 651-661, **2003**
- [43] *Flow of Solids from Bins and Hoppers – Benefits of TIVAR 88 Lining Systems*, System Tivar Engineering, **2005**
- [44] Cundall, P.A., *A Computer Model for Simulating Progressive Large Scale Movements in Blocky Rock Systems*, Proc. Symp. Int. Soc. Rock Mech., Nancy, France, 1971, 1, Paper No. II-8, **1971** (cited by ITASCA Manual ^[49])
- [45] Cundall, P.A.; Strack, O.D.L., *A discrete numerical model for granular assemblies*, *Geotechnique*, 29, 47-65, **1979** (cited by Cundall ^[46])
- [46] Cundall, P.A., *Formulation of a Three-Dimensional Distinct Element Model – Part I. A Scheme to Detect and Represent Contacts in a System Composed of Many Polyhedral Blocks*, *Int. J. Rock Mech., Min. Sci. & Geomech. Abstr.*, 25(3), 107-116, **1988**
- [47] Hart, R.; Cundall, P.A.; Lemos, J., *Formulation of a Three-Dimensional Distinct Element Model – Part II. Mechanical Calculations for Motion and Interaction of a System Composed of Many Polyhedral Blocks*, *Int. J. Rock Mech., Min. Sci. & Geomech. Abstr.*, 25(3), 117-125, **1988**

- [48] Cundall, P.A.; Hart, R., *Numerical Modeling of Discontinua*, J. Engr. Comp, 9, 101-113, **1992**
- [49] ITASCA PFC^{2D} Manual. Hardcopy: PFC^{2D} version 2.0, 1st edition, **June 1999**, Digital: PFC^{2D} version 3.1, 3rd edition, **November 2004**
- [50] Tijssens, E.; Ramon, H.; De Baerdemaeker, J., *Discrete element modeling for process simulation in agriculture*, Journal of Sound and Vibration, 266, 493-514, **2003**
- [51] Luding, S., *About contact force-laws for cohesive frictional materials in 2D and 3D*, In: Walzel, P.; Linz, S.; Krülle, C.; Grochowski, R., *Behavior of Granular Media*, Band 9, Schriftenreihe Mechanische Verfahrenstechnik, Shaker Verlag, Aachen, 137-147, **2006**, ISBN 3-8322-5524-9
- [52] Luding, S., *Cohesive frictional powders: Contact models for tension*, Granular Matter 10(4), in press, **2008**
- [53] Tomas, J., *Assessment of mechanical properties of cohesive particulate solids – part 1: particle contact constitutive model*, Particulate Sci. & Technol. 19, 95-110, **2001**
- [54] Friction, <http://en.wikipedia.org/wiki/Friction>
- [55] Luding, S.; Herrmann, H. J., *Micro-Macro Transition for Cohesive Granular Media*, In: Zur Beschreibung komplexen Materialverhaltens, Institut für Mechanik, S. Diebels (Ed.), Stuttgart, 121-134, **2001**, ISBN 3-9373-9907-0
- [56] Luding, S., *Collisions & Contacts between Two Particles*, In: Herrmann, H.J.; Hovi, J.-P.; Luding, S., *Physics of dry granular media*, NATO ASI Series E350, page 285, Dordrecht, Kluwer Academic Publishers, **1998**, ISBN 0-7923-5102-9
- [57] Foerster, S.F.; Louge, M.Y.; Chang, H.; Allia, K., *Measurements of the collision properties of small spheres*, Phys. Fluids, 6 (3), **March 1994**
- [58] Tykhoniuk, R.; Tomas, J.; Luding, S.; Kappl, M.; Heim, L.; Butt, H.-J., *Ultrafine cohesive powders: From interparticle contacts to continuum behaviour*, Chemical Engineering Science, 62, 2843-2864, **2007**
- [59] Kappl, M.; Butt, H.-J., *The Colloidal Probe Technique and its Application to Adhesion Force Measurements*, Part. Part. Syst. Charact., 19, 129-143, **2002**
- [60] Farshchi-Tabrizi, M.; Kappl, M.; Cheng, Y.; Gutmann, J.; Butt, H.-J., *On the Adhesion between Fine Particles and Nanocontacts: An Atomic Force Microscopy Study*, Langmuir, 22, 2171-2184, **2006**
- [61] Tomas, J., *Fundamentals of Cohesive Powder Consolidation and Flow*, Granular Matter, 6, 75-86, **2004**
- [62] User-defined models for Itasca code, <http://www.itasca-udm.com/>
- [63] sh minerals GmbH, <http://www.sh-minerals.eu/>

- [64] Schubert, W., *Simulation of Particle Dynamics with the Discrete Element Method (DEM)*, Lecture notes, Otto-von-Guericke-University Magdeburg, **2007**

Appendices

Appendix 1: Particle-particle contact models

Appendix 2: User-defined contact model: hysteretic damping

Appendix 3: Hysteretic damping model from ITASCA Manual

Appendix 4: Limestone production and sources (German)

Appendix 5: Silo design by Schäffer

Appendix 6: Equations of calculation cycle

Appendix 7: Results of shear tests

Appendix 8: Results of wall shear tests

Appendix 9: Results of e_n and t_c simulations

Appendix 10: Results of Ψ_1 - Ψ_2 simulations

Appendix 11: Test charts of the vibrating shear cell

Appendix 12: Used scripts for simulations

- After unloading (beginning at point U along curve U-A), the contact recovers elastically in the compression mode and remains with a plastic deformation δ_A . It is assumed that this unloading occurs following a Hertz-type curve until point E (the zero force point) is reached. For unloading below the δ -axis, a tension force is required, whereas a too large tension causes the contact to break. Along curve A-U the contact may be reloaded. The area between the two curves provides a measure for the energy dissipation during one cycle.
- d) At point A the adhesion boundary is reached, and the contact plates are detaching with increasing distance.

A more detailed description of this model can be found in [25,53].

The particles in this model are considered to be rigid and therefore do not deform. In reality particles do deform when they collide. This is accounted for assuming that the contacts are soft. The softer the particle contacts, the larger are the differences between friction angles and the more cohesive is the powder response. Since the scale of the overlap is much smaller than the particle radius, the assumption of rigid particles is reasonable.

Normal contact model by Luding

The Tomas model has been simplified by Luding [51,52] to a piecewise linear model, as this would allow an easier implementation, as well as more efficient and less intensive numerical calculations. The model is shown in Figure A2.

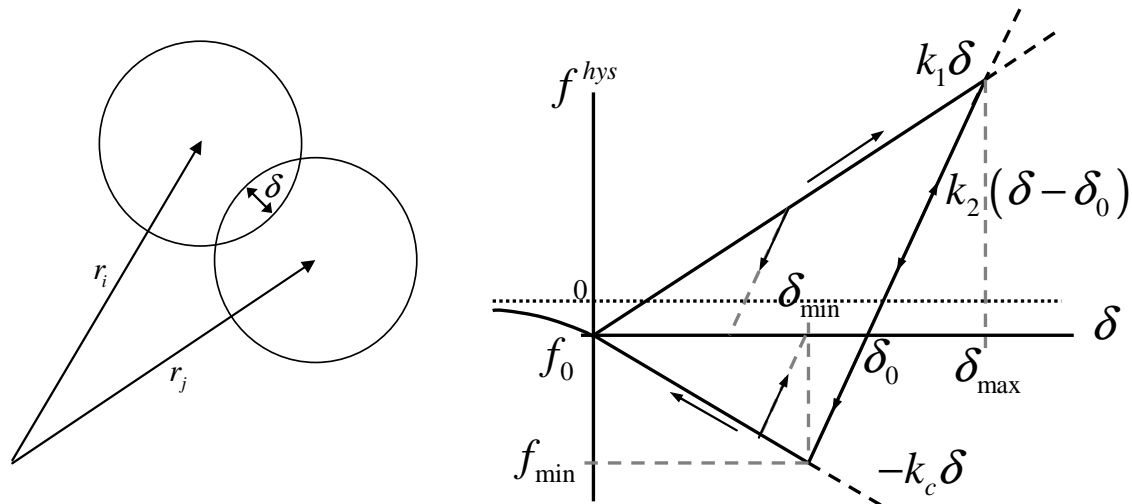


Figure A2: Particle-particle contact model for adhesive elastic-plastic contacts, as described by Luding. Left: Two-particle contact with overlap δ in normal direction. Right: Simplified linearized contact model in normal direction [51,52]

For small deformations, the Hertz region is neglected. Instead, the limiting plastic yield and maximum adhesion-limit lines are kept. The hysteretic unloading/reloading curves are replaced by a linear, elastic, reversible line. To account for energy losses, a simple velocity-dependent dashpot is implemented.

During initial loading, the normal force increases linearly with the overlap δ , with slope k_1 . When the maximum overlap δ^{max} is reached, the contact is being unloaded with slope k_2 , until the point of zero overlap δ_0 :

$$\delta_0 = \left(1 - \frac{k_1}{k_2}\right) \cdot \delta_{\max}$$

This point δ_0 resembles the plastic contact deformation. Reloading at any time will occur along the same line with slope k_2 , until the maximum force is reached.

Unloading below δ_0 leads to attractive forces, until the minimum force $-k_c h_k$ is reached, at the point of minimum overlap δ_{\min} :

$$\delta_{\min} = \frac{k_2 - k_1}{k_2 + k_c} \cdot \delta_{\max}$$

Further unloading leads to attractive forces with slope $-k_c$, until the particles are separated at $\delta = 0$ [51,52].

During loading the normal force increases with stiffness k_1 , which accounts for perfect plastic (so no elastic) repulsion. A linear spring with stiffness k_2 (where $k_2 > k_1$) accounts for unloading and reloading, so that the stiffness is increased due to plastic contact deformation/flattening. The adhesion force comes into play via the adhesion stiffness k_c . This k_c gives the slope of the adhesion limit. Adhesion is allowed up to a maximum pull-off force f_{\min} .

This particle-particle contact model by Luding can be summarized by the following equations:

$$f_n = \begin{cases} k_1 \delta - f_0 & \text{for loading} \\ k_2 (\delta - \delta_0) - f_0 & \text{for un - /reloading} \\ -k_c \delta - f_0 & \text{for unloading} \end{cases}$$

As can be seen, this model can be implemented quite easily, as the system is only a set of linear equations. However, due to the lack of C++ knowledge of the user, this model could not be compiled.

Tangential contact model by Tomas

Tomas [53,61] has developed an elastic-plastic, frictional, dissipative, adhesive model for the tangential force-displacement, which is shown in Figure A3. The linear elastic region can be expressed by Hooke's law, until the limited displacement Δ_0 is reached, which increases with increasing normal load. At the yield point, the elastic behaviour is transmitted into the frictional, sliding behaviour, described by Coulomb friction. The maximum tangential force is reached, where maximum contact deformation occurs, after which the deformation enters the plastic region. Unloading the contact means that the direction of the tangential force is changed. At the end of a shear test, this is necessary to remove the stress from the material. Unloading occurs over a line with slope $-k_s$ until the maximum tangential force in reversed direction is reached, where the behaviour enters the Coulomb friction region. Reloading is similar to unloading, however the direction is reversed.

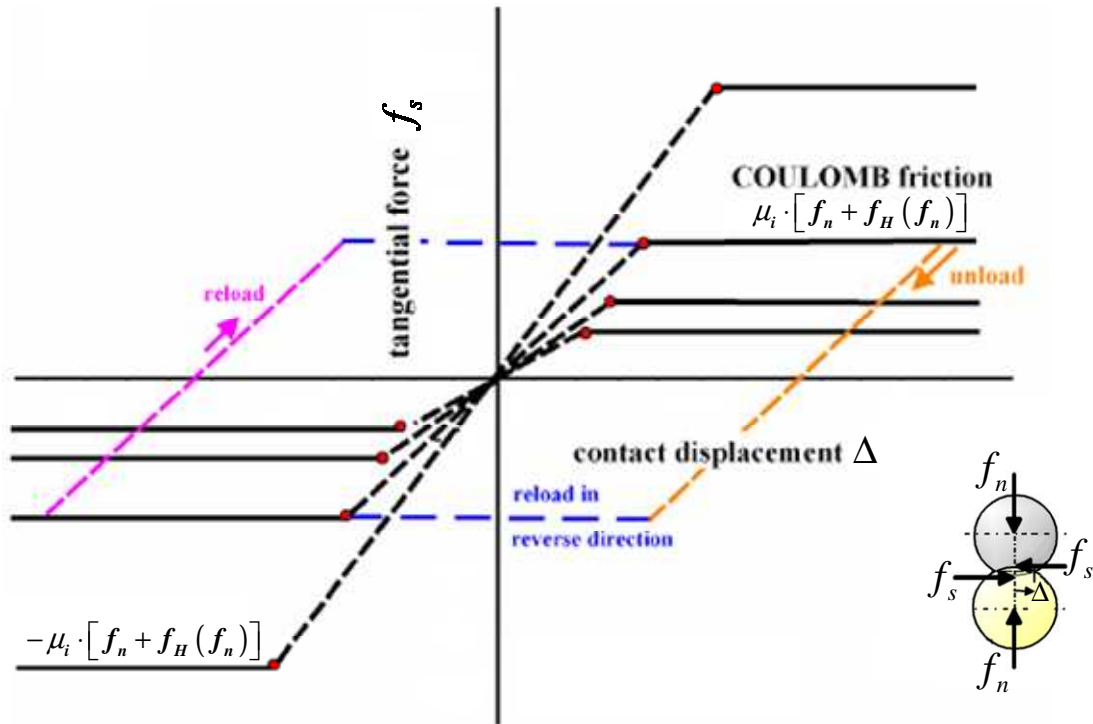


Figure A3: Linear elastic-plastic, frictional, dissipative, adhesive tangential force-displacement model as described by Tomas ^[53,61]

We can see that this model is similar to Hooke's model plus the slip model, except for the case of dissipation and adhesion. The Coulomb friction force is described by the normal force and the adhesion force $f_H(f_n)$, which in turn depends on the normal load as well.

$$f_s = \mu_i \cdot [f_n + f_H(f_n)]$$

In this case, a larger normal load increases the slope of the linear elastic region and increases the level of the Coulomb friction. A more detailed description of this model can be found in ^[25,53,61].

Appendix 2: User-defined contact model: hysteretic damping

In ITASCA PFC^{2D}, the user has the ability program his/her own contact model and load it into the software. Such user-defined models are written in the C++ language using Microsoft Visual C++, and then compiled as a DLL (Dynamic Link Library) file. The option for user-defined models is activated by the command **CONFIG CPPUDM**, after which the command **MODEL LOAD <filename>** is applied to load the model. The model is now loaded and recognised by PFC^{2D}, however it has not yet been activated. This is done by the command **MODEL <modelname>**. At this point, contact properties are modified to the new model. Properties that are associated with the user-defined contact model are assigned by the **PROPERTY** command, however the values now apply to the contact and not to the particles. Even though C++ programming is beyond the scope of the project and the language is not known to the writer of this report, the option is there to modify models to the user's preference and therefore provides a very interesting tool for the more experienced programmer. An example of a user-defined contact model is the hysteretic damping model [62].

As the model of Luding was of interest for this research, but could not be programmed manually, a search was done to find a similar model that is already compiled. A good alternative for the Luding model would be the hysteretic damping model. The hysteretic response is shown in Figure A4.

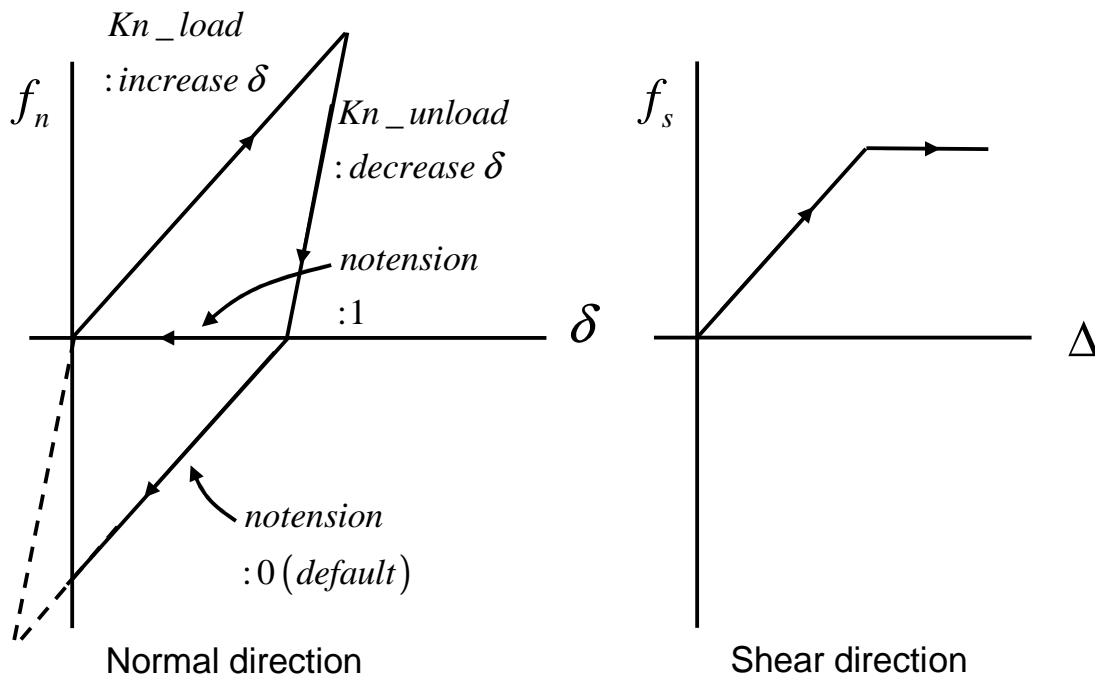


Figure A4: Hysteretic particle-particle contact model [62]

This model explains linear elastic-plastic dissipative behaviour of a particle-particle contact. The normal contact model is similar to that of Luding (Appendix 1). The tangential contact model is similar to Hooke's model plus slip model.

In this model, the kn_load and kn_unload are calculated from hys_knm and hys_dampn .

$$kn_load = \frac{2 \cdot hys_dampn \cdot hys_knm}{(1 + hys_dampn)}$$

$$kn_unload = \frac{2 \cdot hys_knm}{(1 + hys_dampn)}$$

Since we are not interested in these two parameters, we rewrite these equations so that we can input kn_load and kn_unload as parameters into the model.

$$hys_dampn = \frac{kn_load}{kn_unload}$$

$$hys_knm = \frac{kn_unload}{2} \cdot \left(1 + \frac{kn_load}{kn_unload} \right)$$

From these equations, we can specify the kn_load and kn_unload that we want to have in our model.

If we compare to the Luding model:

$$kn_load = k_1$$

$$kn_unload = k_2$$

In this model it is possible to have tension activated. This tension works similar to the **NOTENSION** switch of the viscous damping model.

Other user-defined contact models are already available. Some examples are the Burger's model (to simulate creep mechanisms), and modified viscoelastic and ductile models. More information can be found in ^[49,62].

Appendix 3: Hysteretic damping model from ITASCA Manual ^[62]

The contact model **hysdamp** is intended to introduce energy dissipation by hysteretic damping to a linear contact model with frictional slip.

The model has the following properties.

hys_knm	normal stiffness, the average of the normal stiffness on loading, kn_load , and on unloading, kn_unload
hys_dampn	the ratio of normal stiffness on loading, kn_load , to that on unloading, kn_unload , ($0.4 \leq \mathbf{hys_dampn} \leq 1.0$ (with tensile force); $0.05 \leq \mathbf{hys_dampn} \leq 1.0$ (without tensile force); default 0.8)
hys_ks	shear stiffness
hys_fric	friction coefficient
hys_nstr	contact bond normal strength [force]
hys_sstr	contact bond shear strength [force]
hys_notension	switch (0: tensile force allowed (default); 1: no tension allowed)
hys_inheritprop	switch (0: the model does not inherit properties from <i>PFC^{2D}</i> , (default); 1: the model inherits the properties)

The normal stiffness on loading, **kn_load**, and on unloading, **kn_unload**, used in this model are calculated using **hys_dampn** and **hys_knm**.

$$kn_load = \frac{2 \cdot hys_dampn \cdot hys_knm}{(1 + hys_dampn)}$$

$$kn_unload = \frac{2 \cdot hys_knm}{(1 + hys_dampn)}$$

where **hys_knm** is taken as the average of **kn_load** and **kn_unload**.

Note that if **hys_inheritprop** is set to 1, the model sets the parameters, **hys_knm**, **hys_ks**, **hys_fric**, **hys_nstr** and **hys_sstr** to the values of normal stiffness, shear stiffness, friction coefficient, contact bond normal strength and contact bond shear strength to those values associated with contacts before cycling, even though these parameters are specified explicitly. If **hys_inheritprop** is set to 0 (default), users must specify these values (**hys_knm** at minimum). Otherwise, *PFC^{2D}* posts an error message before cycling.

In the hysteretic damping model, normal stiffness on unloading is greater than that on loading (see Figure A5). The hysteretic damping is independent of the relative velocity before and after contact between two entities. It is suggested that the ratio between the two stiffnesses, **hys_dampn**, should be determined with a parametric pretest to obtain a measurable quantity, such as the restitution coefficient (see Figure A6), which illustrates the results of drop tests. Also, the local-damping coefficient should be set to zero in advance by the command **PROP damp** or the *FISH* function **b_damp(bp)** (see the **zero_damp** function in the Example). The data file used for the drop tests is shown in the Example.

This damping model is applicable to impact problems in which there is large relative particle movement, but it should not be used for problems of compact particle assemblies.

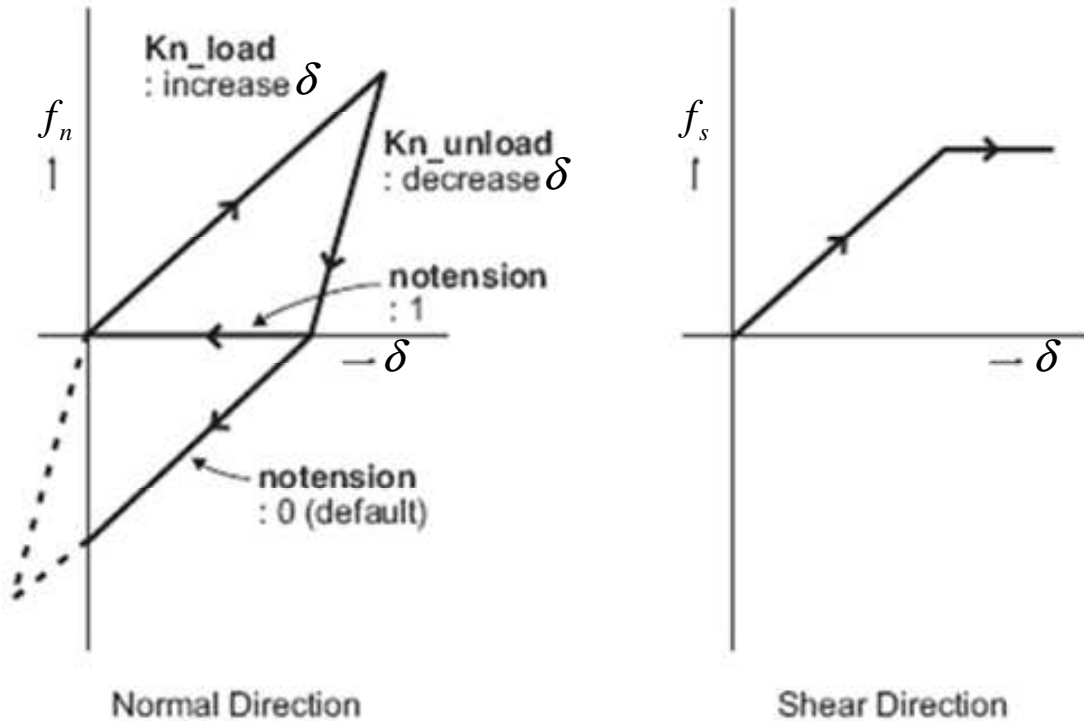


Figure A5: Hysteretic response

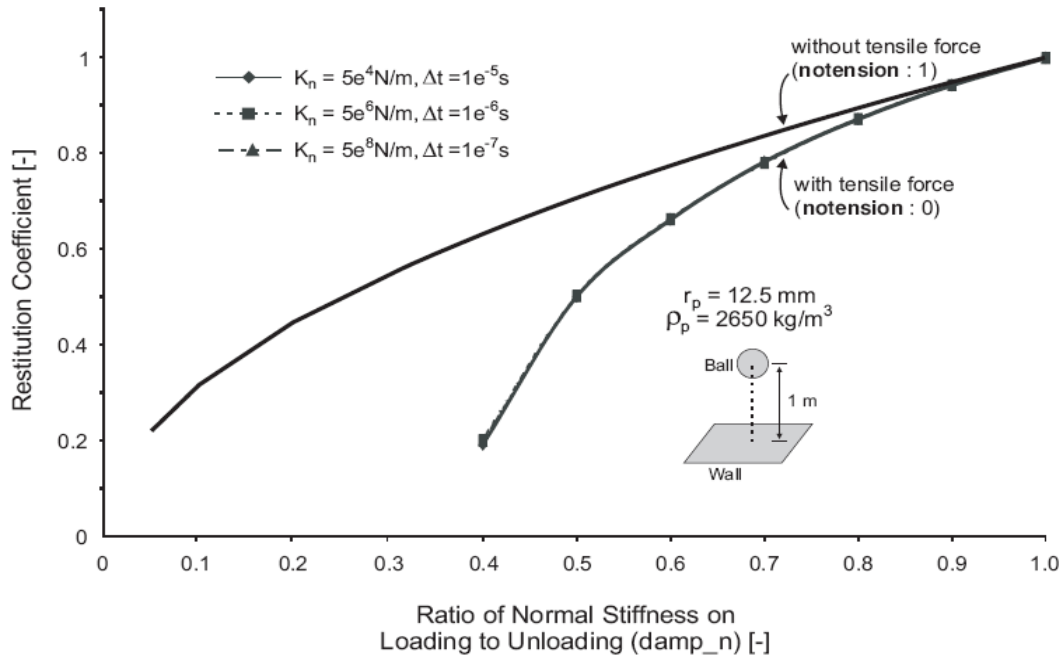


Figure A6: Relation between restitution coefficient and ratio of normal stiffness on loading to unloading, *hys_dampn*

Example: Data file for drop tests

```

; fname: drop2dhys.DAT
new
set dt max 1.0e-4
set pinterval 200
config cppudm
model load hys2wrv.dll
;-----
def make_ball
  command
    ball id = 1 rad = 0.04 x = 0.0 y = 1.0 ;0.03 ; 1.0
    prop dens = 2600 kn = 1.0e6 ks = 1.0e6 fric = 0.0
  end_command
end
;-----
def zero_damp
  bp = ball_head
  loop while bp # null
    b_damp(bp) = 0.0
    bp = b_next(bp)
  end_loop
end
;-----
def catch_contact_hys
  cp = fc_arg(0);
  c_model(cp) = 'hysdamp'
  c_prop(cp,'hys_dampn')= setv
  c_prop(cp,'hys_notension')= 1 ; 0 if you want tensile force
  c_prop(cp,'hys_inheritprop')= 1

```

```
end
;-----
def plot_view
  command
  title 'Drop Tests with Hysteretic Damping (damp_n: 1.0, 0.8, 0.5)'
  plot create 1
  plot add axes black
  plot add ball yellow
  plot add wall lblue
  plot add cf white
  end_command
end

model hysdamp
set fishcall 6 catch_contact_hys
plot_view

wall id = 1 kn = 1.0e6 ks = 1.0e6 fric = 0.0 &
  nodes (-0.5,0.0) (0.5,0.0)
set grav 0 -9.8

; ----- case damp_n = 1.0 -----
make_ball
zero_damp
set setv = 1.0
plot show
cycle 30000
del ball 1
; ----- case damp_n = 0.8 -----
make_ball
zero_damp
set setv = 0.8
cycle 70000
del ball 1
; ----- case damp_n = 0.5 -----
make_ball
zero_damp
set setv = 0.5
cycle 20000
return
```

Appendix 4: Limestone production and sources (German) ^[63]

Standard-Lieferprogramm CALCIT Calciumcarbonat-Füllstoffe

Charakteristik: Die **CALCIT-Füllstoffe** von Schön + Hippelein sind feinkristalline, *natürliche Calciumcarbonate* mit rhomboedrischer Kristallstruktur, die wir nach modernsten Trockenmahlverfahren und Sichtprozessen herstellen. *Den weißen Rohstein*, der sich durch *sehr hohe chemische Reinheit* auszeichnet, gewinnen wir *im eigenen Vorkommen* aus der Malm-Epsilon-Schichtung des oberen Weißjura.

Chemische Analyse:

CaCO ₃	99,5 %
MgCO ₃	0,3 %
Fe ₂ O ₃	0,05 %
HCl-Unlösliches	0,3 %

Feuchtigkeit ab Werk (ISO 787/2) max. 0,2 %

pH-Wert (ISO 787/9) 9

Physikalische Kennwerte: Farbmaßzahlen CIE - L* a* b*

(DIN 5033 Teil 3 LUCI 100, Dr. Lange

d/8° Normlichtart D65, Normbeobachter 10°)

L* (Helligkeitswert) min. 91

a* (Rot-Grün-Buntheit) max. 0,6

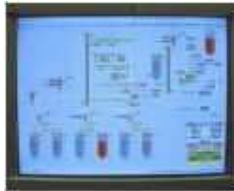
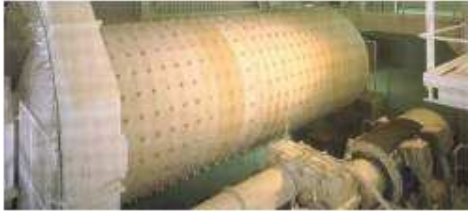
b* (Gelb-Blau-Buntheit) max. 7

Helligkeit (Ry, C/2°, DIN 53163) min. 87

Type	Korngößen- verteilung (µm)	mittl. Teilchen- durchmesser D 50% (µm)	Farbmaßzahlen CIE- L*a*b*		
			L*	a*	b*
CALCIT MX 10	0 - 10	2,0	92	0,4	6
CALCIT MX 20	0 - 15	2,5	92	0,4	6
CALCIT MX 30	0 - 23	3,0	92	0,4	6
CALCIT MS 70 F	0 - 60	4,5	> 91	0,6	7
CALCIT MS 12	0 - 70	5,0	91	0,6	7
CALCIT MS 70	0 - 70	5,0	> 91	< 0,6	< 7
CALCIT FA 14	0 - 135	8,0	88	1,5	9
CALCIT FN 13	0 - 260	12	88	1,5	9
CALCIT MW 240	0 - 210	35	90	0,7	8

Production

Spitzenprodukte durch modernste Anlagentechnik!



Die Bearbeitungsstufen, die das Rohgestein bis hin zum hochwertigen Endprodukt durchläuft, sind vielfältig und technisch sehr anspruchsvoll. Die daraus produzierten Füllstoffe und Körnungen sind in Korngrößenverteilung und Farbe exakt definiert. Modernste rechnergesteuerte Trockenmahlverfahren und Sichtprozesse ermöglichen eine konstante Produktqualität zu einem vorteilhaften Preis-/Leistungsverhältnis. Durch die Großinvestitionen in neueste Anlagentechnik haben wir in den letzten Jahren unsere Produktionskapazitäten beträchtlich erweitert. Wir stellen heute eine breite Palette an verschiedenen Füllstoffen her - mikrofeine Qualitäten mit einem oberen Schnitt von weniger als 10 μm bis hin zu Mehlen um 300 μm . Ergänzt wird unser Produktsortiment durch getrocknete, staubfreie Körnungen in Absiebungen von 0,1 bis 6 mm sowie diverse Splittsorten.

Durch großzügige Silokapazitäten und einen 3-Schichtbetrieb in Produktion und LKW-Beladung gewährleisten wir ein hohes Maß an Flexibilität und Liefersicherheit. Neben loser Ware, die den größten Teil der Verladungen darstellt, bieten wir unsere Produkte auch in verschiedenen Sackvarianten und Big-Bags an.

Hochwertiger Rohstoff in Hülle und Fülle!

Appearance



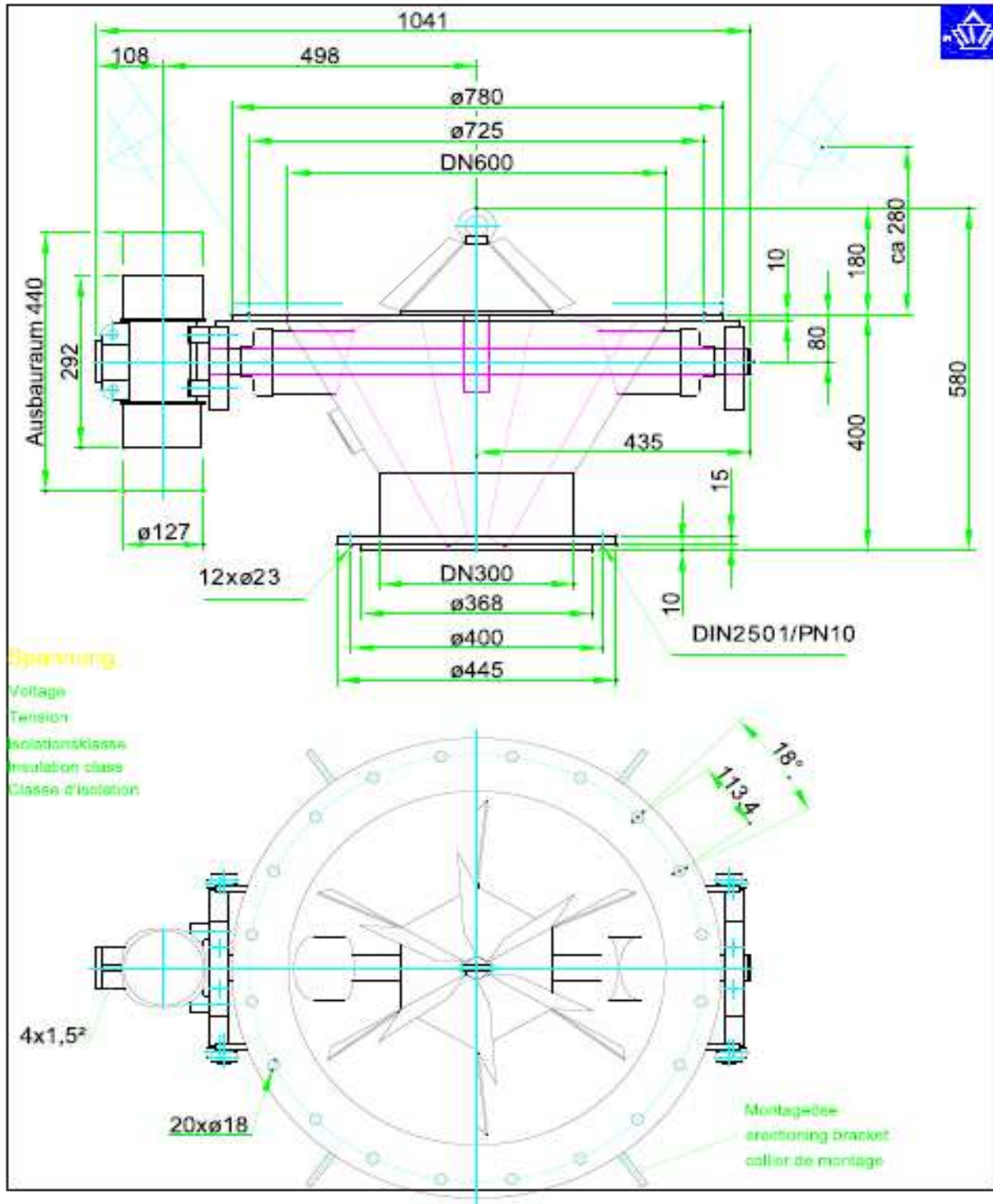
Unser Vorkommen an sehr hellem, feinkristallinem Calcit entstammt der Malm-Epsilon-Schichtung der schwäbisch-en Alb. Diese vor ca. 150 Mio. Jahren entstandene Jura-Formation ist Garant für unser chemisch hochreines Gestein mit einem Calciumcarbonatgehalt von ca. 99%.

Hieraus bauen wir die Rohstoffe für unsere hochwertigen Füllstoffqualitäten und Körnungen ab.

Das firmeneigene Vorkommen stellt die Versorgung für viele Generationen sicher.

Unsere Produktionsstätte liegt verkehrstechnisch sehr günstig an der Autobahn A7, ca. 60 km nördlich von Ulm.

Appendix 5: Silo design by Schäffer



Copyright by Schäffer-PD: 10-000201

Änderungen vorbehalten • Details are not binding • Sous réserve de modifications

SCHÄFFER - Verfahrenstechnik GmbH & Co. KG Postfach 1152 D-86670 Thierhaupten

Tel 08271/8015-6

Fax 08271/8015-89

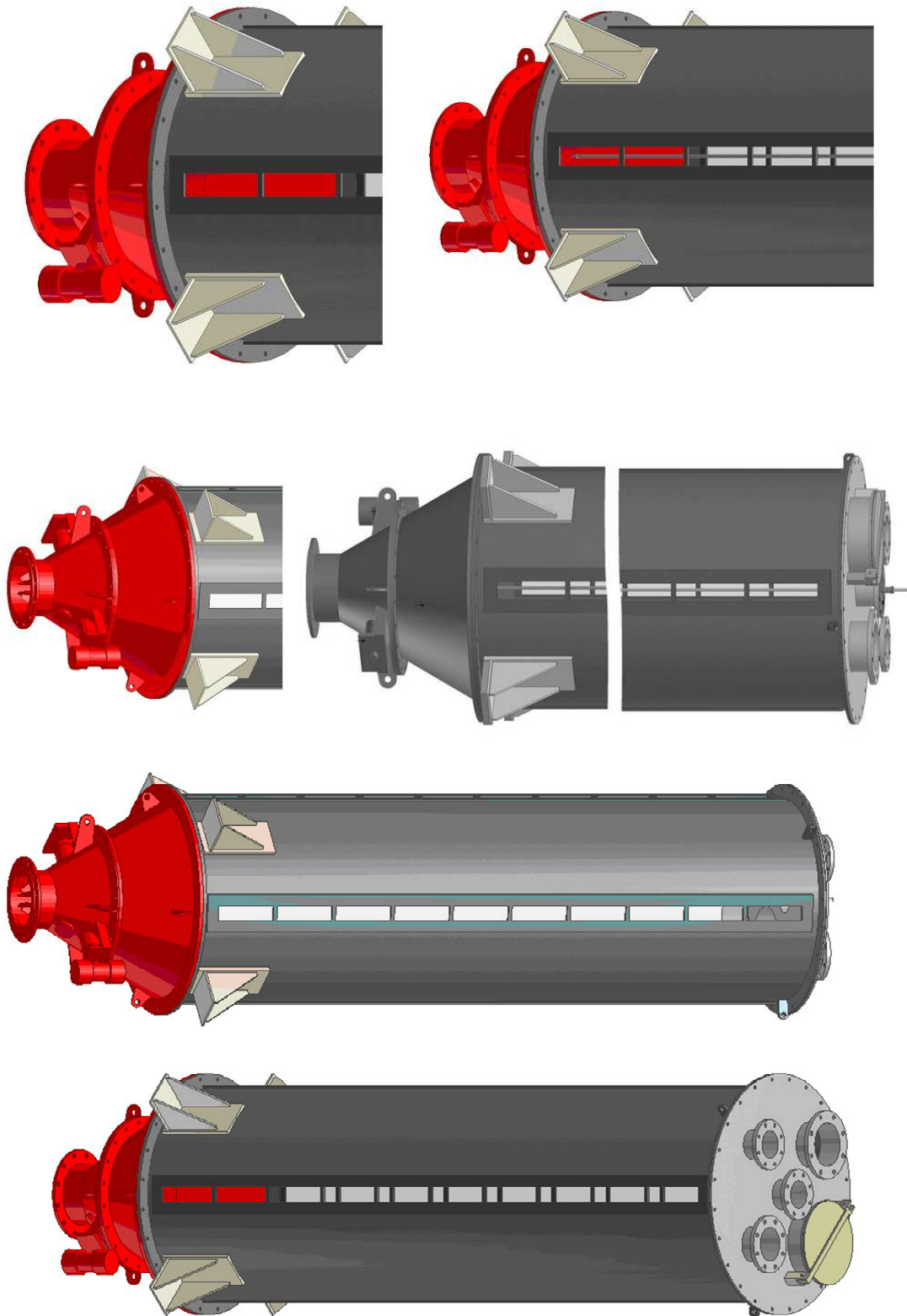


Figure A7: Design pictures of the silo plus vibrating hopper

Appendix 6: Equations of calculation cycle

This appendix contains the calculations that are made within the ITASCA PFC^{2D} software during one calculation cycle ^[47,49,64].

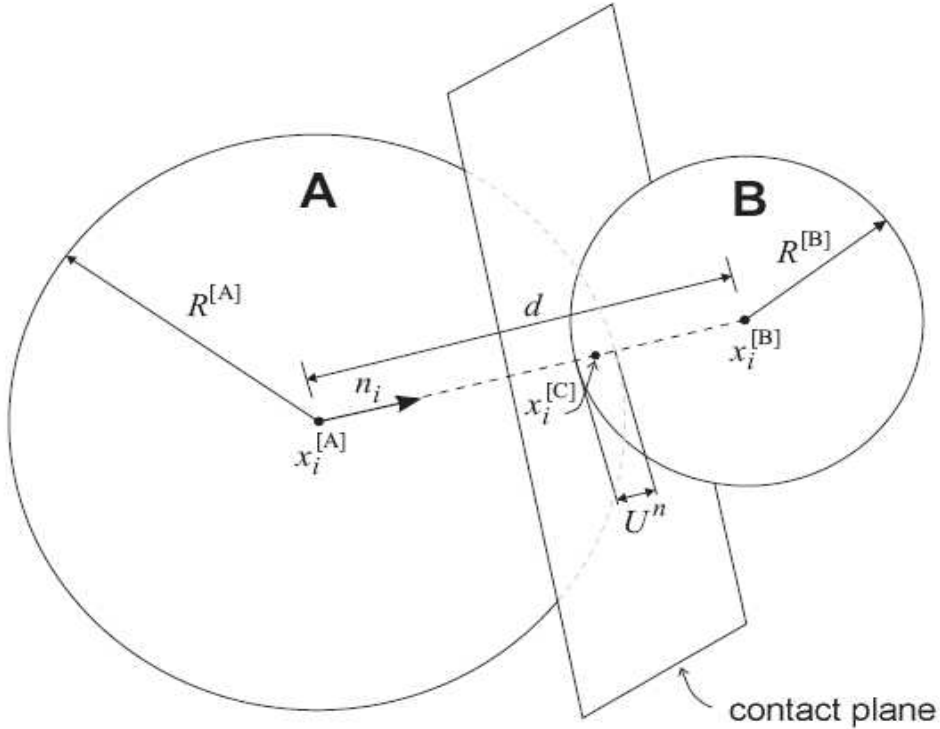


Figure A8: Notations used to describe particle-particle contact ^[49]

0 After ball creation, the following properties are defined:

- positions of the balls $r_i^{[A]}$ and $r_i^{[B]}$,
- radii $R^{[A]}$ and $R^{[B]}$,
- density ρ
- normal stiffness k^n and shear stiffness k^s .

i .. 1, 2-index of a vector (x, y-direction)

1. Given values at cycle start

$$v_i^{(t-\Delta t/2)}, r_i^{(t)}, f_i^{(t)}, m, g_i$$

2 Calculation of the geometry at cycle start

The distance d between the ball centres is defined as:

$$d = r_i^{[B]} - r_i^{[A]}$$

The particle-particle overlap δ is defined as the relative contact displacement in the normal direction:

$$\delta = R^{[A]} + R^{[B]} - d$$

The location of the contact point $r_i^{[C]}$ is given by

$$r_i^{[C]} = r_i^{[A]} + R^{[A]} - \frac{1}{2} \delta$$

3 Calculation of the forces at cycle start

The contact force vector f_i can be resolved into normal and shear components:

$$f_i = f_i^{(n)} + f_i^{(s)}$$

The normal contact force is calculated by

$$f_i^{(n)} = k^n \delta$$

The new shear contact force is found by summing the old shear force existing at the start of the time step with the shear force-increment $\Delta f_i^{(s)}$. If the slip model is active the shear force will be corrected below $f_{\max}^{(s)}$ when it is above:

$$f_i^{(s)} \leftarrow f_i^{(s)} + \Delta f_i^{(s)} \leq \mu f_i^{(n)}$$

The shear force-increment $\Delta f_i^{(s)}$ will be found by the following equations:

$$V_i = \left(v_i^{[C]} \right)_{[B]} - \left(v_i^{[C]} \right)_{[A]}$$

The contact velocity V_i (relative motion at the contact) can be resolved into normal and shear components:

$$V_i = V_i^{(n)} + V_i^{(s)}$$

We can get the shear displacement-increment $\Delta \delta_i^{(s)}$ over a time step of Δt from

$$\Delta \delta_i^{(s)} = V_i^{(s)} \Delta t$$

The shear force-increment then becomes:

$$\Delta f_i^{(s)} = -k^s \Delta \delta_i^{(s)}$$

The contribution of the final contact force to the resultant force on the two balls in contact is given:

$$\begin{aligned} f_i^{[A]} &\leftarrow f_i^{[A]} - f_i \\ f_i^{[B]} &\leftarrow f_i^{[B]} + f_i \end{aligned}$$

$f_i^{[A]}$ and $f_i^{[B]}$ are the resultant force, the sum of all externally applied forces acting on the two particles.

4 Calculation at the middle (velocity) and end (position) of the time interval

v_i is calculated at the mid-intervals $t \pm n\Delta t/2$, while r_i , a_i and f_i are computed at the primary intervals of $t \pm n\Delta t$.

$$f_i = m(a_i - g_i)$$

$$a_i^{(t)} = \frac{1}{\Delta t} \left(v_i^{(t+\Delta t/2)} - v_i^{(t-\Delta t/2)} \right)$$

Insert the equation for the force and solving for the velocities at time $(t + \Delta t/2)$ results in

$$v_i^{(t+\Delta t/2)} = v_i^{(t-\Delta t/2)} + \left(\frac{f_i^{(t)}}{m} + g_i \right) \Delta t$$

Finally, the velocities are used to update the position of the particle centre as

$$r_i^{(t+\Delta t)} = r_i^{(t)} + v_i^{(t+\Delta t/2)} \Delta t$$

List of symbols and abbreviations

Symbols

Variable	Unit	Explanation
a	m/s ²	Acceleration
d	m	Distance
f	N	Force
g	m/s ²	Gravity acceleration
k	N/m	Stiffness
m	kg	Mass
r	m	Position
R	m	Particle radius
t	s	Time
v	m/s	Velocity
V	m/s	Contact velocity

Subscripts

Subscript	Explanation
i	Direction index
A	Ball A
B	Ball B

Greek symbols

Variable	Unit	Explanation
δ	m	Particle-particle overlap
Δ	-	Increment
	m	Displacement
μ	-	Friction coefficient
ν	-	Poisson's ratio
ρ	kg/m ³	Density
ω	1/s	Angular velocity

Superscripts

Superscript	Explanation
A	Ball A
B	Ball B
C	Contact
n	Normal
s	Shear
t	Time
Δ	Increment

Appendix 7: Results of shear tests

Table A1: Summarized shear test results

		0 mm/s		10 mm/s		20 mm/s	
		YL1	YL2	YL1	YL2	YL1	YL2
T_{room}	°C	22	24	23	24	23	24
rel. humidity	%	73	60	80	59	68	63
moisture	%	0.81	0.21	0.31	0.21	0.27	0.24
σ_M	kPa	3.009	4.417	2.919	4.290	3.170	4.218
σ_R	kPa	2.443	3.410	2.322	3.158	2.240	2.936
σ_C	kPa	3.588	5.139	3.298	4.707	3.460	4.323
σ_{RC}	kPa	1.794	2.570	1.649	2.353	1.730	2.162
σ_1	kPa	5.452	7.827	5.240	7.448	5.410	7.155
σ_2	kPa	0.565	1.006	0.597	1.132	0.931	1.282
τ_c	kPa	0.988	1.572	0.914	1.512	1.195	1.455
ff_c	-	1.5	1.5	1.6	1.6	1.6	1.7
φ_e	rad	0.948	0.882	0.920	0.827	0.785	0.770
	°	54.3	50.5	52.7	47.4	44.9	44.1
φ_i	rad	0.564	0.473	0.558	0.429	0.362	0.386
	°	32.3	27.1	32.0	24.6	20.7	22.1

Table A2: Shear test results of 0 mm/s, YL 1

	pre-shear		shear		bulk density	porosity	acceleration	
	σ_{an}	τ_{an}	σ	τ	ρ_b	ϵ	a_e	a_r
	kPa	kPa	kPa	kPa	kg/m ³	--	m/s ²	m/s ²
	2.654	2.565	2.234	2.495	980	0.64	0	0
	2.651	2.425	2.231	2.355	964	0.64	0	0
	2.651	2.495	1.812	2.147	963	0.65	0	0
	2.648	2.287	1.808	2.009	942	0.65	0	0
	2.649	2.495	1.390	1.869	950	0.65	0	0
	2.649	2.355	1.390	1.938	948	0.65	0	0
	2.651	2.495	1.112	1.650	962	0.65	0	0
	2.649	2.217	1.110	1.719	950	0.65	0	0
average	2.650	2.417			957	0.65	0	0
deviation	0.0019	0.1201			12	0.00	0	0

Table A 3: Shear test results of 0 mm/s, YL 2

	Pre-shear		shear		Bulk density	porosity	acceleration	
	σ_{an}	τ_{an}	σ	τ	ρ_b	ϵ	a_e	a_r
	kPa	kPa	kPa	kPa	kg/m ³	--	m/s ²	m/s ²
	4.050	3.462	3.351	3.363	965	0.64	0	0
	4.052	3.346	3.353	3.201	978	0.64	0	0
	4.051	3.428	2.513	2.809	973	0.64	0	0
	4.055	3.388	2.516	2.921	997	0.63	0	0
	4.050	3.271	1.813	2.495	969	0.64	0	0
	4.051	3.410	1.813	2.495	970	0.64	0	0
	4.052	3.341	1.534	2.287	977	0.64	0	0
	4.051	3.480	1.533	2.425	970	0.64	0	0
average	4.051	3.391			975	0.64	0	0
deviation	0.0016	0.0694			10	0.00	0	0

Table A4: Shear test results of 10 mm/s, YL 1

	Pre-shear		shear		Bulk density	porosity	acceleration	
	σ_{an}	τ_{an}	σ	τ	ρ_b	ϵ	a_e	a_r
	kPa	kPa	kPa	kPa	kg/m ³	--	m/s ²	m/s ²
	2.654	2.565	2.234	2.495	966	0.64	3.25	3.23
	2.651	2.425	2.231	2.355	944	0.65	3.10	3.15
	2.651	2.495	1.812	2.147	977	0.64	3.16	3.19
	2.648	2.287	1.808	2.009	956	0.65	3.19	3.25
	2.649	2.495	1.390	1.869	962	0.65	2.94	3.15
	2.649	2.355	1.390	1.938	943	0.65	3.35	3.41
	2.651	2.495	1.112	1.650	969	0.64	3.13	3.17
	2.649	2.217	1.110	1.719	948	0.65	3.40	3.36
average	2.650	2.417			958	0.65	3.19	3.24
deviation	0.0019	0.1201			12	0.00	0.1456	0.0979

Table A5: Shear test results of 10 mm/s, YL 2

	Pre-shear		shear		bulk density	porosity	acceleration	
	σ_{an}	τ_{an}	σ	τ	ρ_b	ϵ	a_e	a_r
	kPa	kPa	kPa	kPa	kg/m ³	--	m/s ²	m/s ²
	4.053	3.271	3.354	3.122	987	0.64	2.70	2.73
	4.050	3.132	3.350	3.063	965	0.64	2.84	2.87
	4.051	2.993	2.512	2.565	970	0.64	3.21	3.29
	4.050	2.993	2.511	2.565	964	0.65	3.11	3.13
	4.053	3.132	1.815	2.422	985	0.64	3.39	3.36
	4.054	3.063	1.816	2.287	990	0.64	3.27	3.32
	4.055	3.409	1.537	2.277	996	0.63	3.33	3.45
	4.053	3.201	1.536	2.217	988	0.64	3.50	3.21
average	4.052	3.149			981	0.64	3.17	3.17
deviation	0.0020	0.1424			12	0.00	0.2746	0.2502

Table A6: Shear test results of 20 mm/s, YL 1

	Pre-shear		shear		bulk density	porosity	acceleration	
	σ_{an}	τ_{an}	σ	τ	ρ_b	ϵ	a_e	a_r
	kPa	kPa	kPa	kPa	kg/m ³	--	m/s ²	m/s ²
	2.650	2.107	2.230	2.040	958	0.65	6.08	6.56
	2.648	2.124	2.229	2.007	946	0.65	6.49	6.70
	2.649	2.290	1.810	1.969	954	0.65	6.27	6.38
	2.651	2.123	1.812	1.815	967	0.64	6.45	6.61
	2.651	2.134	1.392	1.734	964	0.64	6.53	6.69
	2.650	2.291	1.392	1.772	961	0.65	6.34	6.67
	2.648	2.231	1.109	1.690	943	0.65	6.75	6.65
	2.649	2.126	1.111	1.486	954	0.65	6.45	6.53
average	2.650	2.178			956	0.65	6.42	6.60
deviation	0.0013	0.0790			8	0.00	0.1972	0.1072

Table A7: Shear test results of 20 mm/s, YL 2

	Pre-shear		shear		bulk density	porosity	acceleration	
	σ_{an}	τ_{an}	σ	τ	ρ_b	ε	a_e	a_r
	kPa	kPa	kPa	kPa	kg/m ³	--	m/s ²	m/s ²
	4.050	2.993	3.351	2.843	968	0.64	6.65	6.53
	4.052	2.934	3.352	2.906	976	0.64	6.25	6.25
	4.052	2.923	2.513	2.355	978	0.64	5.94	6.20
	4.051	2.923	2.512	2.357	972	0.64	6.32	6.44
	4.055	3.063	1.817	2.294	997	0.63	6.50	6.67
	4.051	2.775	1.814	2.190	975	0.64	6.33	6.31
	4.051	2.994	1.534	2.096	975	0.64	6.11	6.15
	4.050	2.849	1.532	2.087	963	0.65	6.10	6.38
average	4.052	2.932			976	0.64	6.28	6.37
deviation	0.0015	0.0898			10	0.00	0.2290	0.1756

Appendix 8: Results of wall shear tests

Table A 8: Wall shear test results. Left: for $m_m=9.0\text{kg}$ ($\sigma=13.706\text{ kPa}$). Right: for $m_m=7.0\text{kg}$ ($\sigma=10.909\text{ kPa}$)

pre-shear		shear		a	pre-shear		shear		a
σ_{an}	τ_{an}	τ_{min}	τ_{max}		σ_{an}	τ_{an}	τ_{min}	τ_{max}	
kPa	kPa	kPa	kPa	m/s^2	kPa	kPa	kPa	kPa	m/s^2
19.301	10.109	8.198	7.785	0	19.301	11.934	6.908	6.487	0
	11.812	8.205	7.799	0		11.705	6.658	6.288	0
		8.540	8.070	0			6.088	6.088	0.8
		8.234	7.941	0.5			6.309	6.202	2.1
		8.312	8.256	0.8			6.031	5.945	2.2
		7.956	7.813	1.3			5.767	5.717	3.0
		7.877	7.770	1.5			5.518	5.518	3.9
		7.143	7.086	4.2			4.919	4.905	5.2
		6.708	6.672	5.2			3.408	3.408	8.4
		5.881	5.774	7.4			4.876	4.876	8.6
		3.065	3.065	15.6					

Table A9: Wall shear test results. Left: for $m_m=4.0\text{kg}$ ($\sigma=6.713\text{ kPa}$). Right: for $m_m=2.0\text{kg}$ ($\sigma=3.915\text{ kPa}$)

pre-shear		shear		a	pre-shear		shear		a
σ_{an}	τ_{an}	τ_{min}	τ_{max}		σ_{an}	τ_{an}	τ_{min}	τ_{max}	
kPa	kPa	kPa	kPa	m/s^2	kPa	kPa	kPa	kPa	m/s^2
19.301	11.670	4.156	3.978	0	19.301	11.827	2.688	2.609	0
	11.976	4.384	4.235	0		12.140	2.837	2.752	0
		4.049	3.978	0.8			2.281	2.281	0.9
		4.120	4.120	1.0			1.725	1.725	1.3
		3.978	3.978	1.1			1.511	1.511	1.5
		3.479	3.479	3.0			1.369	1.369	1.8
		2.994	2.994	3.4			0.884	0.884	2.3
		3.621	3.621	4.5			0.242	0.242	4.8
		1.654	1.654	5.5			0.200	0.200	5.3
		0.385	0.385	6.3			0.385	0.385	6.3
		3.408	3.408	9.5			0.385	0.385	9.9
		0.314	0.314	11.0			0.185	0.185	10.0
							0.385	0.385	17.7

Table A10: Wall shear test results. Left: for $m_m=1.0\text{kg}$ ($\sigma=2.517\text{ kPa}$). Right: for $m_m=0.3\text{kg}$ ($\sigma=1.538\text{ kPa}$)

pre-shear		shear		a	pre-shear		shear		a
σ_{an}	τ_{an}	τ_{min}	τ_{max}		σ_{an}	τ_{an}	τ_{min}	τ_{max}	
kPa	kPa	kPa	kPa	m/s ²	kPa	kPa	kPa	kPa	m/s ²
19.301	11.677	1.832	1.725	0	19.301	11.734	1.126	1.098	0
	11.912	2.224	2.224	0		11.898	1.176	1.126	0
		2.074	2.039	0			1.027	1.027	0
		2.303	2.253	0			1.226	1.226	0
		1.697	1.697	0.4			0.884	0.884	0.7
		1.875	1.853	0.7			0.526	0.526	1.1
		1.583	1.583	1.0			0.656	0.656	1.4
		0.970	0.970	1.6			0.542	0.542	1.6
		1.019	0.970	1.8			0.385	0.385	2.2
		0.528	0.499	2.5			0.314	0.314	2.4
		0.955	0.955	2.7			0.328	0.328	3.0
		0.314	0.314	2.8			0.456	0.456	4.2
		0.599	0.599	4.3			0.385	0.385	4.3
		0.385	0.385	5.9			0.242	0.242	6.6
		0.492	0.485	6.8			0.385	0.385	8.9
		0.492	0.485	7.8			0.257	0.257	9.4
		0.499	0.499	13.5			0.463	0.442	12.7
							0.257	0.257	16.6

Appendix 9: Results of e_n and t_c simulations

Table A11: Simulation results of e_n and t_c for various values of α , compared with the analytical results

α [-]	<i>RESTITUTION COEFFICIENT e_n [-]</i>	<i>CONTACT TIME t_c [ms]</i>	
	Simulations	Theory	Simulations
0.000	1.000	0.227	0.228
0.025	0.975	0.230	0.228
0.050	0.951	0.233	0.228
0.100	0.905	0.240	0.229
0.150	0.860	0.247	0.230
0.200	0.817	0.254	0.231
0.250	0.775	0.262	0.233
0.300	0.734	0.272	0.236
0.350	0.694	0.282	0.239
0.400	0.655	0.293	0.243
0.450	0.616	0.307	0.248
0.500	0.577	0.321	0.254
0.550	0.539	0.339	0.261
0.600	0.500	0.359	0.270
0.650	0.461	0.384	0.280
0.700	0.420	0.415	0.294
0.750	0.378	0.455	0.313
0.800	0.333	0.508	0.337
0.850	0.285	0.587	0.373
0.900	0.229	0.719	0.442

Table A12: Simulation results of e_n and t_c for various values of β_n for both disabled and allowed tension, compared with the analytical results and with t_{crit}

$\beta_n [-]$	$\eta_n [-]$	$\omega_n [-]$	<i>RESTITUTION COEFFICIENT $e_n [-]$</i>				<i>CONTACT TIME $t_c [ms]$</i>				$t_{crit} [ms]$
			Tension allowed		Tension disabled		Tension allowed		Tension disabled		
			Theory	Simulations	Theory	Simulations	Theory	Simulations	Theory	Simulations	
0.000	0.00	13819.77	1.000	1.000	1.000	1.000	0.227	0.226	0.227	0.228	0.072
0.025	345.49	13815.45	0.924	0.924	0.926	0.925	0.227	0.228	0.224	0.224	0.070
0.050	690.99	13802.48	0.854	0.854	0.859	0.858	0.228	0.228	0.220	0.221	0.067
0.100	1381.98	13750.49	0.729	0.728	0.744	0.743	0.228	0.229	0.214	0.214	0.063
0.150	2072.96	13663.41	0.621	0.620	0.650	0.648	0.230	0.230	0.208	0.208	0.059
0.200	2763.95	13540.55	0.527	0.525	0.572	0.570	0.232	0.232	0.202	0.202	0.055
0.250	3454.94	13380.93	0.444	0.442	0.506	0.504	0.235	0.235	0.197	0.197	0.051
0.300	4145.93	13183.22	0.372	0.371	0.451	0.448	0.238	0.238	0.192	0.192	0.048
0.350	4836.92	12945.66	0.309	0.306	0.404	0.401	0.243	0.243	0.187	0.187	0.045
0.400	5527.91	12666.02	0.254	0.251	0.364	0.361	0.248	0.248	0.183	0.183	0.042
0.450	6218.89	12341.45	0.205	0.204	0.329	0.326	0.255	0.254	0.179	0.179	0.040
0.500	6909.88	11968.27	0.163	0.161	0.298	0.295	0.262	0.262	0.175	0.175	0.037
0.550	7600.87	11541.78	0.126	0.124	0.272	0.269	0.272	0.272	0.171	0.171	0.035
0.600	8291.86	11055.81	0.095	0.093	0.249	0.246	0.284	0.284	0.168	0.167	0.034
0.650	8982.85	10502.11	0.068	0.066	0.228	0.225	0.299	0.299	0.164	0.164	0.032
0.700	9673.84	9869.29	0.046	0.044	0.210	0.207	0.318	0.319	0.161	0.161	0.030
0.750	10364.82	9140.92	0.028	0.027	0.194	0.191	0.344	0.345	0.158	0.158	0.029
0.800	11055.81	8291.86	0.015	0.014	0.180	0.177	0.379	0.381	0.155	0.155	0.027
0.850	11746.80	7280.01	0.006	0.006	0.167	0.164	0.432	0.436	0.152	0.152	0.026
0.900	12437.79	6023.90	0.002	0.001	0.155	0.152	0.522	0.533	0.150	0.149	0.025
0.950	13128.78	4315.22	0.000	-----	0.145	0.142	0.728	0.773	0.147	0.146	0.024
0.970	13405.17	3359.65	0.000	-----	0.141	0.138	0.935	1.050	0.146	0.145	0.024
0.990	13681.57	1949.52	0.000	-----	0.137	0.134	1.611	-----	0.145	0.144	0.023
0.999	13805.95	617.88	0.000	-----	0.136	0.132	5.084	-----	0.145	0.144	0.023

Appendix 10: Results of Ψ_1 - Ψ_2 simulations

Table A13: Starting positions and velocities of particle 1 and 2

x_1	0
xvel_1	50
yvel_1	0
x_2	2
y_2	0
xvel_2	-50
yvel_2	0

y_1 is varied from 0 to 0.99

Table A14: Simulation results: No friction, tangential spring, no damping

y_1	BEFORE COLLISION												
	n_x	n_y	$v_{c,x}$	$v_{c,y}$	$v_{c,x}^{(n)}$	$v_{c,y}^{(n)}$	$v_{c,x}^{(t)}$	$v_{c,y}^{(t)}$	t_x	t_y	$v_c^{(n)}$	$v_c^{(t)}$	Ψ_1
0.00	-1.00000	0.00000	100.00	0.00	100.00000	0.00000	0.00000	0.00000	-----	-----	100.000000	0.00000	0.00000
0.10	-0.99476	0.10228	100.00	0.00	98.95392	-10.17417	1.04608	10.17417	0.10228	0.99476	99.4755853	10.22780	0.10282
0.20	-0.97887	0.20449	100.00	0.00	95.81855	-20.01650	4.18145	20.01650	0.20449	0.97887	97.8869512	20.44859	0.20890
0.30	-0.95186	0.30653	100.00	0.00	90.60397	-29.17735	9.39603	29.17735	0.30653	0.95186	95.1861187	30.65294	0.32203
0.40	-0.91283	0.40834	100.00	0.00	83.32545	-37.27485	16.67455	37.27485	0.40834	0.91283	91.2827735	40.83449	0.44734
0.50	-0.86027	0.50984	100.00	0.00	74.00599	-43.86015	25.99401	43.86015	0.50984	0.86027	86.0267338	50.98432	0.59266
0.60	-0.79173	0.61087	100.00	0.00	62.68351	-48.36454	37.31649	48.36454	0.61087	0.79173	79.1729194	61.08722	0.77157
0.70	-0.70288	0.71130	100.00	0.00	49.40463	-49.99646	50.59537	49.99646	0.71130	0.70288	70.2884279	71.13042	1.01198
0.80	-0.58536	0.81078	100.00	0.00	34.26438	-47.45935	65.73562	47.45935	0.81078	0.58536	58.5357801	81.07751	1.38509
0.90	-0.41751	0.90867	100.00	0.00	17.43160	-37.93810	82.56840	37.93810	0.90867	0.41751	41.7511683	90.86716	2.17640
0.95	-0.29195	0.95643	100.00	0.00	8.52363	-27.92331	91.47637	27.92331	0.95643	0.29195	29.1952617	95.64328	3.27599
0.97	-0.22017	0.97504	100.00	0.00	4.84739	-21.46732	95.15261	21.46732	0.97548	0.22008	21.9988006	97.54417	4.43407
0.99	-0.11948	0.99284	100.00	0.00	1.42751	-11.86228	98.57249	11.86228	0.99284	0.11948	11.9478643	99.28368	8.30974
y_1	AFTER COLLISION												
	n'_x	n'_y	$v'_{c,x}$	$v'_{c,y}$	$v_{c,x}^{(n)}$	$v_{c,y}^{(n)}$	$v_{c,x}^{(t)}$	$v_{c,y}^{(t)}$	e_n	$v_c^{(n)}$	$v_c^{(t)}$	Ψ_2	
0.00	-1.00000	0.00000	-100.00209	0.00000	-100.00209	0.00000	0.00000	0.00000	1.00002	-100.00209	0.00000	0.00000	
0.10	-0.99476	0.10228	-97.95538	20.12466	-98.97820	10.17666	1.02282	9.94799	1.00025	-99.499996	10.00044	0.10053	
0.20	-0.97887	0.20449	-91.82090	39.61377	-95.91075	20.03576	4.08985	19.57801	1.00096	-97.981135	20.00063	0.20432	
0.30	-0.95186	0.30653	-81.60359	57.79864	-90.80020	29.24054	9.19661	28.55810	1.00217	-95.392275	30.00238	0.31520	
0.40	-0.91283	0.40834	-67.32441	73.94078	-83.65968	37.42437	16.33527	36.51641	1.00401	-91.648925	40.00362	0.43824	
0.50	-0.86027	0.50984	-49.00579	87.16892	-74.49963	44.15271	25.49385	43.01621	1.00667	-86.600558	50.00331	0.58125	
0.60	-0.79173	0.61087	-26.68189	96.37549	-63.33671	48.86852	36.65482	47.50697	1.01042	-79.997945	60.00406	0.75789	
0.70	-0.70288	0.71130	-0.40300	99.98678	-50.18895	50.79017	49.78595	49.19661	1.01588	-71.40428	69.99248	0.99579	
0.80	-0.58536	0.81078	29.74151	95.47540	-35.12126	48.64622	64.86277	46.82917	1.02501	-59.999649	80.00094	1.36670	
0.90	-0.41751	0.90867	63.58448	77.18206	-18.19761	39.60525	81.78210	37.57681	1.04394	-43.585879	90.00182	2.15567	
0.95	-0.29195	0.95643	81.74925	57.59379	-9.11408	29.85761	90.86334	27.73618	1.06927	-31.217682	95.00232	3.25403	
0.97	-0.22017	0.97504	89.18267	45.23788	-5.38833	23.86290	94.57099	21.37497	1.11159	-24.45369	96.95649	4.40735	
0.99	-0.11948	0.99284	96.60632	25.83060	-1.68503	14.00215	98.29135	11.82845	1.18039	-14.103177	99.00051	8.28604	

Table A15: Simulation results: Friction=0.5, tangential spring, no damping

y_1	BEFORE COLLISION												
	n_x	n_y	$v_{c,x}$	$v_{c,y}$	$v_{c,x}^{(n)}$	$v_{c,y}^{(n)}$	$v_{c,x}^{(t)}$	$v_{c,y}^{(t)}$	t_x	t_y	$v_c^{(n)}$	$v_c^{(t)}$	Ψ_1
0.00	-1.00000	0.00000	100.00	0.00	100.00000	0.00000	0.00000	0.00000	-----	-----	100.00000	0.00000	0.00000
0.10	-0.99499	0.10001	100.00	0.00	98.99989	-9.95041	1.00011	9.95041	0.10001	0.99499	99.49869	10.00055	0.10051
0.20	-0.97979	0.20001	100.00	0.00	95.99951	-19.59708	4.00049	19.59708	0.20001	0.97979	97.97934	20.00123	0.20414
0.30	-0.95393	0.30002	100.00	0.00	90.99862	-28.62015	9.00138	28.62015	0.30002	0.95393	95.39320	30.00230	0.31451
0.40	-0.91651	0.40002	100.00	0.00	83.99867	-36.66184	16.00133	36.66184	0.40002	0.91651	91.65079	40.00166	0.43646
0.50	-0.86521	0.50142	100.00	0.00	74.85830	-43.38277	25.14170	43.38277	0.50142	0.86521	86.52069	50.14150	0.57953
0.60	-0.79720	0.60371	100.00	0.00	63.55327	-48.12805	36.44673	48.12805	0.60371	0.79720	79.72030	60.37113	0.75729
0.70	-0.70858	0.70563	100.00	0.00	50.20917	-49.99956	49.79083	49.99956	0.70563	0.70858	70.85843	70.56261	0.99583
0.80	-0.59079	0.80683	100.00	0.00	34.90321	-47.66641	65.09679	47.66641	0.80683	0.59079	59.07894	80.68258	1.36567
0.90	-0.42183	0.90668	100.00	0.00	17.79398	-38.24620	82.20602	38.24620	0.90668	0.42183	42.18291	90.66754	2.14939
0.95	-0.29512	0.95546	100.00	0.00	8.70933	-28.19718	91.29067	28.19718	0.95546	0.29512	29.51158	95.54615	3.23758
0.97	-0.22448	0.97448	100.00	0.00	5.03902	-21.87488	94.96098	21.87488	0.97448	0.22448	22.44776	97.44792	4.34110
0.99	-0.12081	0.99268	100.00	0.00	1.45962	-11.99297	98.54038	11.99297	0.99268	0.12081	12.08147	99.26751	8.21651
y_1	AFTER COLLISION												
	n'_x	n'_y	$v'_{c,x}$	$v'_{c,y}$	$v'^{(n)}_{c,x}$	$v'^{(n)}_{c,y}$	$v'^{(t)}_{c,x}$	$v'^{(t)}_{c,y}$	e_n	$v_c'^{(n)}$	$v_c'^{(t)}$	Ψ_2	
0.00	-1.00000	0.00000	-100.00209	0.00000	-100.00209	0.00000	0.00000	0.00000	1.00002	-100.00209	0.00000	0.00000	
0.10	-0.99499	0.10001	-100.00132	-0.00004	-99.00119	9.95054	-1.00013	-9.95059	1.00001	-99.49997	-10.00072	-0.10051	
0.20	-0.97979	0.20001	-100.00182	0.00012	-96.00128	19.59744	-4.00054	-19.59731	1.00002	-97.981146	-20.00148	-0.20414	
0.30	-0.95393	0.30002	-99.99848	0.00025	-90.99731	28.61974	-9.00117	-28.61950	0.99999	-95.391824	-30.00161	-0.31450	
0.40	-0.91651	0.40002	-99.98096	0.00417	-83.98421	36.65552	-15.99675	-36.65135	0.99983	-91.635006	-39.99022	-0.43633	
0.50	-0.86521	0.50142	-92.93528	12.21099	-74.86724	43.38796	-18.06805	-31.17696	1.00012	-86.531023	-36.03411	-0.41648	
0.60	-0.79720	0.60371	-75.34802	32.71299	-63.63025	48.18635	-11.71777	-15.47336	1.00121	-79.816873	-19.40956	-0.24347	
0.70	-0.70858	0.70563	-50.95402	49.64281	-50.40478	50.19435	-0.54924	-0.55154	1.00390	-71.134486	-0.77837	-0.01098	
0.80	-0.59079	0.80683	-18.53588	60.37209	-35.24682	48.13568	16.71095	12.23641	1.00984	-59.660558	20.71196	0.35058	
0.90	-0.42183	0.90668	24.58762	59.14856	-18.24696	39.21985	42.83459	19.92871	1.02546	-43.256773	47.24358	1.11997	
0.95	-0.29512	0.95546	52.68295	48.66560	-9.13399	29.57205	61.81694	19.09355	1.04876	-30.950536	64.69852	2.19231	
0.97	-0.22448	0.97448	66.37118	40.00792	-5.40723	23.47330	71.77841	16.53462	1.07307	-24.088044	73.65822	3.28132	
0.99	-0.12081	0.99268	83.60035	24.23077	-1.68574	13.85092	85.28609	10.37984	1.15492	-13.95313	85.91541	7.11134	

Table A16: Simulation results: Friction=1.0, tangential spring, no damping

y_1	BEFORE COLLISION												
	n_x	n_y	$v_{c,x}$	$v_{c,y}$	$v_{c,x}^{(n)}$	$v_{c,y}^{(n)}$	$v_{c,x}^{(t)}$	$v_{c,y}^{(t)}$	t_x	t_y	$v_c^{(n)}$	$v_c^{(t)}$	Ψ_1
0.00	-1.00000	0.00000	100.00	0.00	100.00000	0.00000	0.00000	0.00000	-----	-----	100.00000	0.00000	0.00000
0.10	-0.99499	0.10001	100.00	0.00	98.99989	-9.95041	1.00011	9.95041	0.10001	0.99499	99.49869	10.00055	0.10051
0.20	-0.97979	0.20001	100.00	0.00	95.99951	-19.59708	4.00049	19.59708	0.20001	0.97979	97.97934	20.00123	0.20414
0.30	-0.95394	0.30000	100.00	0.00	90.99992	-28.61829	9.00008	28.61829	0.30000	0.95394	95.39388	30.00013	0.31449
0.40	-0.91651	0.40000	100.00	0.00	83.99970	-36.66089	16.00030	36.66089	0.40000	0.91651	91.65135	40.00038	0.43644
0.50	0.86600	-0.50004	100.00	0.00	74.99566	-43.30378	25.00434	43.30378	0.50004	0.86600	86.60003	50.00434	0.57742
0.60	-0.79998	0.60003	100.00	0.00	63.99651	-48.00102	36.00349	48.00102	0.60003	0.79998	79.99782	60.00291	0.75006
0.70	-0.71409	0.70006	100.00	0.00	50.99203	-49.99016	49.00797	49.99016	0.70006	0.71409	71.40870	70.00569	0.98035
0.80	-0.59624	0.80281	100.00	0.00	35.54975	-47.86638	64.45025	47.86638	0.80281	0.59624	59.62361	80.28091	1.34646
0.90	-0.42623	0.90461	100.00	0.00	18.16726	-38.55744	81.83274	38.55744	0.90461	0.42623	42.62307	90.46145	2.12236
0.95	-0.29834	0.95446	100.00	0.00	8.90094	-28.47574	91.09906	28.47574	0.95446	0.29834	29.83445	95.44583	3.19918
0.97	-0.22704	0.97389	100.00	0.00	5.15474	-22.11114	94.84526	22.11114	0.97389	0.22704	22.70405	97.38853	4.28948
0.99	-0.12218	0.99251	100.00	0.00	1.49284	-12.12664	98.50716	12.12664	0.99251	0.12218	12.21818	99.25077	8.12320
y_1	AFTER COLLISION												
	n'_x	n'_y	$v'_{c,x}$	$v'_{c,y}$	$v_{c,x}^{(n)}$	$v_{c,y}^{(n)}$	$v_{c,x}^{(t)}$	$v_{c,y}^{(t)}$	e_n	$v_c^{(n)}$	$v_c^{(t)}$	Ψ_2	
0.00	-1.00000	0.00000	-100.00209	0.00000	-100.00209	0.00000	0.00000	0.00000	1.00002	-100.00209	0.00000	0.00000	
0.10	-0.99499	0.10001	-100.00132	-0.00004	-99.00119	9.95054	-1.00013	-9.95059	1.00001	-99.499997	-10.00072	-0.10051	
0.20	-0.97979	0.20001	-100.00181	0.00012	-96.00127	19.59744	-4.00054	-19.59731	1.00002	-97.981138	-20.00147	-0.20414	
0.30	-0.95394	0.30000	-99.99891	-0.00187	-90.99839	28.61781	-9.00052	-28.61968	0.99998	-95.392278	-30.00159	-0.31450	
0.40	-0.91651	0.40000	-99.99603	0.00025	-83.99645	36.65947	-15.99958	-36.65922	0.99996	-91.647808	-39.99856	-0.43642	
0.50	0.86600	-0.50004	99.99774	-0.00134	74.99454	-43.30313	25.00319	43.30179	0.99999	-86.598747	-50.00205	-0.57739	
0.60	-0.79998	0.60003	-99.99868	0.00440	-63.99777	48.00197	-36.00091	-47.99757	1.00002	-79.999403	-59.99860	-0.75000	
0.70	-0.71409	0.70006	-99.94306	0.05896	-50.99246	49.99058	-48.95059	-49.93163	1.00001	-71.409312	-69.92373	-0.97920	
0.80	-0.59624	0.80281	-66.77134	24.80026	-35.60803	47.94485	-31.16330	-23.14459	1.00164	-59.721361	-38.81782	-0.65105	
0.90	-0.42623	0.90461	-14.57944	40.80910	-18.38363	39.01667	3.80419	1.79244	1.01191	-43.130711	4.20532	0.09866	
0.95	-0.29834	0.95446	23.41024	39.56771	-9.18347	29.37958	32.59370	10.18814	1.03174	-30.781415	34.14891	1.14461	
0.97	-0.22704	0.97389	43.37091	34.67473	-5.43132	23.29753	48.80223	11.37719	1.05366	-23.922256	50.11086	2.20713	
0.99	-0.12218	0.99251	70.47215	22.63880	-1.69329	13.75494	72.16544	8.88387	1.13427	-13.858771	72.71020	5.95098	

Table A17: Simulation results: Friction=1.0, no tangential spring, no damping

y_1	BEFORE COLLISION												
	n_x	n_y	$v_{c,x}$	$v_{c,y}$	$v_{c,x}^{(n)}$	$v_{c,y}^{(n)}$	$v_{c,x}^{(t)}$	$v_{c,y}^{(t)}$	t_x	t_y	$v_c^{(n)}$	$v_c^{(t)}$	Ψ_1
0.00	-1.00000	0.00000	100.00	0.00	100.00000	0.00000	0.00000	0.00000	-----	-----	100.00000	0.00000	0.00000
0.10	-0.99476	0.10228	100.00	0.00	98.95392	-10.17417	1.04608	10.17417	0.10228	0.99476	99.47559	10.22780	0.10282
0.20	-0.97887	0.20449	100.00	0.00	95.81855	-20.01650	4.18145	20.01650	0.20449	0.97887	97.88695	20.44859	0.20890
0.30	-0.95186	0.30653	100.00	0.00	90.60397	-29.17735	9.39603	29.17735	0.30653	0.95186	95.18612	30.65294	0.32203
0.40	-0.91283	0.40834	100.00	0.00	83.32545	-37.27485	16.67455	37.27485	0.40834	0.91283	91.28277	40.83449	0.44734
0.50	-0.86027	0.50984	100.00	0.00	74.00599	-43.86015	25.99401	43.86015	0.50984	0.86027	86.02673	50.98432	0.59266
0.60	-0.79173	0.61087	100.00	0.00	62.68351	-48.36454	37.31649	48.36454	0.61087	0.79173	79.17292	61.08722	0.77157
0.70	-0.70288	0.71130	100.00	0.00	49.40463	-49.99646	50.59537	49.99646	0.71130	0.70288	70.28843	71.13042	1.01198
0.80	-0.58536	0.81078	100.00	0.00	34.26438	-47.45935	65.73562	47.45935	0.81078	0.58536	58.53578	81.07751	1.38509
0.90	-0.41751	0.90867	100.00	0.00	17.43160	-37.93810	82.56840	37.93810	0.90867	0.41751	41.75117	90.86716	2.17640
0.95	-0.29195	0.95643	100.00	0.00	8.52363	-27.92331	91.47637	27.92331	0.95643	0.29195	29.19526	95.64328	3.27599
0.97	-0.22202	0.97504	100.00	0.00	4.92915	-21.64759	95.07085	21.64759	0.97504	0.22202	22.20168	97.50428	4.39175
0.99	-0.11948	0.99284	100.00	0.00	1.42751	-11.86228	98.57249	11.86228	0.99284	0.11948	11.94786	99.28368	8.30974
y_1	AFTER COLLISION												
	n'_x	n'_y	$v'_{c,x}$	$v'_{c,y}$	$v'^{(n)}_{c,x}$	$v'^{(n)}_{c,y}$	$v'^{(t)}_{c,x}$	$v'^{(t)}_{c,y}$	e_n	$v_c'^{(n)}$	$v_c'^{(t)}$	Ψ_2	
0.00	-1.00000	0.00000	-100.00209	0.00000	-100.00209	0.00000	0.00000	0.00000	1.00002	-100.00209	0.00000	0.00000	
0.10	-0.99476	0.10228	-97.95538	20.12466	-98.97820	10.17666	1.02282	9.94799	1.00025	-99.499996	10.00044	0.10053	
0.20	-0.97887	0.20449	-91.82090	39.61377	-95.91075	20.03576	4.08985	19.57801	1.00096	-97.981135	20.00063	0.20432	
0.30	-0.95186	0.30653	-81.60359	57.79864	-90.80020	29.24054	9.19661	28.55810	1.00217	-95.392275	30.00238	0.31520	
0.40	-0.91283	0.40834	-67.32440	73.94078	-83.65968	37.42437	16.33527	36.51641	1.00401	-91.648921	40.00362	0.43824	
0.50	-0.86027	0.50984	-49.00579	87.16892	-74.49963	44.15271	25.49385	43.01621	1.00667	-86.600558	50.00331	0.58125	
0.60	-0.79173	0.61087	-26.68189	96.37549	-63.33671	48.86852	36.65482	47.50697	1.01042	-79.997945	60.00406	0.75789	
0.70	-0.70288	0.71130	-0.40300	99.99868	-50.19490	50.79619	49.79189	49.20249	1.01600	-71.412744	70.00084	0.99591	
0.80	-0.58536	0.81078	29.74151	95.47540	-35.12126	48.64622	64.86277	46.82917	1.02501	-59.999649	80.00094	1.36670	
0.90	-0.41751	0.90867	63.58448	77.18206	-18.19761	39.60525	81.78210	37.57681	1.04394	-43.585879	90.00182	2.15567	
0.95	-0.29195	0.95643	81.74925	57.59379	-9.11408	29.85761	90.86334	27.73618	1.06927	-31.217682	95.00232	3.25403	
0.97	-0.22202	0.97504	89.18267	45.23788	-5.39697	23.70214	94.57963	21.53574	1.09491	-24.308817	97.00049	4.36906	
0.99	-0.11948	0.99284	96.60632	25.83060	-1.68503	14.00215	98.29135	11.82845	1.18039	-14.103177	99.00051	8.28604	

Table A18: Simulation results: Friction=1.0, tangential spring, normal viscous damping = 0.4

y_1	BEFORE COLLISION												
	n_x	n_y	$v_{c,x}$	$v_{c,y}$	$v_{c,x}^{(n)}$	$v_{c,y}^{(n)}$	$v_{c,x}^{(t)}$	$v_{c,y}^{(t)}$	t_x	t_y	$v_c^{(n)}$	$v_c^{(t)}$	Ψ_1
0.00	-1.00000	0.00000	100.00	0.00	100.00000	0.00000	0.00000	0.00000	-----	-----	100.00000	0.00000	0.00000
0.10	-0.99501	0.09981	100.00	0.00	99.00385	-9.93089	0.99615	9.93089	0.09981	0.99501	99.50068	9.98072	0.10031
0.20	-0.97987	0.19962	100.00	0.00	96.01513	-19.56036	3.98487	19.56036	0.19962	0.97987	97.98731	19.96214	0.20372
0.30	-0.95412	0.29943	100.00	0.00	91.03417	-28.56917	8.96583	28.56917	0.29943	0.95412	95.41183	29.94300	0.31383
0.40	-0.91683	0.39927	100.00	0.00	84.05825	-36.60649	15.94175	36.60649	0.39927	0.91683	91.68329	39.92712	0.43549
0.50	-0.86626	0.49959	100.00	0.00	75.04094	-43.27761	24.95906	43.27761	0.49959	0.86626	86.62618	49.95904	0.57672
0.60	-0.79912	0.60118	100.00	0.00	63.85862	-48.04101	36.14138	48.04101	0.60118	0.79912	79.91159	60.11770	0.75230
0.70	-0.71062	0.70358	100.00	0.00	50.49785	-49.99752	49.50215	49.99752	0.70358	0.71062	71.06184	70.35776	0.99009
0.80	-0.59236	0.80568	100.00	0.00	35.08851	-47.72470	64.91149	47.72470	0.80568	0.59236	59.23555	80.56767	1.36012
0.90	-0.42262	0.90631	100.00	0.00	17.86063	-38.30223	82.13937	38.30223	0.90631	0.42262	42.26183	90.63077	2.14451
0.95	-0.29516	0.95545	100.00	0.00	8.71221	-28.20139	91.28779	28.20139	0.95545	0.29516	29.51645	95.54465	3.23700
0.97	-0.22421	0.97454	100.00	0.00	5.02703	-21.85022	94.97297	21.85022	0.97454	0.22421	22.42105	97.45407	4.34654
0.99	-0.12021	0.99275	100.00	0.00	1.44500	-11.93364	98.55500	11.93364	0.99275	0.12021	12.02080	99.27487	8.25859
y_1	AFTER COLLISION												
	n'_x	n'_y	$v'_{c,x}$	$v'_{c,y}$	$v_{c,x}^{(n)}$	$v_{c,y}^{(n)}$	$v_{c,x}^{(t)}$	$v_{c,y}^{(t)}$	e_n	$v_c^{(n)}$	$v_c^{(t)}$	Ψ_2	
0.00	-1.00000	0.00000	-25.12130	0.00000	-25.12130	0.00000	0.00000	0.00000	0.25121	-25.121296	0.00000	0.00000	
0.10	-0.99501	0.09981	-26.12173	-7.16084	-25.15038	2.52279	-0.97135	-9.68362	0.25403	-25.276592	-9.73222	-0.09781	
0.20	-0.97987	0.19962	-28.30686	-14.22701	-24.39602	4.97000	-3.91085	-19.19701	0.25409	-24.897119	-19.59132	-0.19994	
0.30	-0.95412	0.29943	-31.96428	-20.86667	-23.13699	7.26106	-8.82730	-28.12772	0.25416	-24.2496	-29.48033	-0.30898	
0.40	-0.91683	0.39927	-36.89481	-26.97204	-21.13962	9.20608	-15.75519	-36.17812	0.25149	-23.057221	-39.45988	-0.43039	
0.50	-0.86626	0.49959	-40.69098	-26.46468	-19.08162	11.00475	-21.60936	-37.46943	0.25428	-22.027541	-43.25416	-0.49932	
0.60	-0.79912	0.60118	-37.35037	-16.24934	-16.04508	12.07076	-21.30528	-28.32009	0.25126	-20.078543	-35.43928	-0.44348	
0.70	-0.71062	0.70358	-25.69964	-0.30704	-12.82425	12.69719	-12.87539	-13.00423	0.25396	-18.046609	-18.29988	-0.25752	
0.80	-0.59236	0.80568	-3.76765	15.94681	-8.93258	12.14942	5.16493	3.79740	0.25457	-15.079768	6.41067	0.10822	
0.90	-0.42262	0.90631	28.34058	25.49682	-4.70405	10.08786	33.04462	15.40897	0.26338	-11.130722	36.46071	0.86273	
0.95	-0.29516	0.95545	52.36610	24.67261	-2.39577	7.75512	54.76187	16.91749	0.27499	-8.1167448	57.31548	1.94181	
0.97	-0.22421	0.97454	65.01259	21.56851	-1.44456	6.27885	66.45715	15.28965	0.28736	-6.4428855	68.19330	3.04149	
0.99	-0.12021	0.99275	81.76964	13.94346	-0.48239	3.98388	82.25204	9.95958	0.33384	-4.0129832	82.85283	6.89245	

Table A19: Simulation results: Friction=1.0, tangential spring, shear viscous damping = 0.4

y_1	BEFORE COLLISION												
	n_x	n_y	$v_{c,x}$	$v_{c,y}$	$v_{c,x}^{(n)}$	$v_{c,y}^{(n)}$	$v_{c,x}^{(t)}$	$v_{c,y}^{(t)}$	t_x	t_y	$v_c^{(n)}$	$v_c^{(t)}$	Ψ_1
0.00	-1.00000	0.00000	100.00	0.00	100.00000	0.00000	0.00000	0.00000	-----	-----	100.00000	0.00000	0.00000
0.10	-0.99498	0.10006	100.00	0.00	98.99886	-9.95547	1.00114	9.95547	0.10006	0.99498	99.49817	10.00568	0.10056
0.20	-0.97977	0.20011	100.00	0.00	95.99546	-19.60657	4.00454	19.60657	0.20011	0.97977	97.97727	20.01135	0.20424
0.30	-0.95389	0.30015	100.00	0.00	90.99105	-28.63100	9.00895	28.63100	0.30015	0.95389	95.38923	30.01492	0.31466
0.40	-0.91643	0.40020	100.00	0.00	83.98376	-36.67566	16.01624	36.67566	0.40020	0.91643	91.64265	40.02030	0.43670
0.50	-0.86589	0.50024	100.00	0.00	74.97619	-43.31501	25.02381	43.31501	0.50024	0.86589	86.58879	50.02380	0.57772
0.60	-0.79979	0.60028	100.00	0.00	63.96675	-48.00968	36.03325	48.00968	0.60028	0.79979	79.97922	60.02770	0.75054
0.70	-0.71385	0.70030	100.00	0.00	50.95859	-49.99081	49.04141	49.99081	0.70030	0.71385	71.38529	70.02957	0.98101
0.80	-0.59624	0.80281	100.00	0.00	35.54975	-47.86638	64.45025	47.86638	0.80281	0.59624	59.62361	80.28091	1.34646
0.90	-0.42623	0.90461	100.00	0.00	18.16726	-38.55744	81.83274	38.55744	0.90461	0.42623	42.62307	90.46145	2.12236
0.95	-0.29834	0.95446	100.00	0.00	8.90094	-28.47574	91.09906	28.47574	0.95446	0.29834	29.83445	95.44583	3.19918
0.97	-0.22704	0.97388	100.00	0.00	5.15474	-22.11110	94.84526	22.11110	0.97389	0.22704	22.70397	97.38852	4.28949
0.99	-0.12218	0.99251	100.00	0.00	1.49284	-12.12664	98.50716	12.12664	0.99251	0.12218	12.21818	99.25077	8.12320
y_1	AFTER COLLISION												
	n'_x	n'_y	$v'_{c,x}$	$v'_{c,y}$	$v'^{(n)}_{c,x}$	$v'^{(n)}_{c,y}$	$v'^{(t)}_{c,x}$	$v'^{(t)}_{c,y}$	e_n	$v_c'^{(n)}$	$v_c'^{(t)}$	Ψ_2	
0.00	-1.00000	0.00000	-100.00209	0.00000	-100.00209	0.00000	0.00000	0.00000	1.00002	-100.00209	0.00000	0.00000	
0.10	-0.99498	0.10006	-99.30824	6.87904	-98.99887	9.95547	-0.30937	-3.07642	1.00000	-99.498181	-3.09194	-0.03108	
0.20	-0.97977	0.20011	-97.22755	13.55717	-95.99213	19.60589	-1.23542	-6.04872	0.99997	-97.973877	-6.17360	-0.06301	
0.30	-0.95389	0.30015	-93.79058	19.68964	-90.97837	28.62701	-2.81221	-8.93737	0.99986	-95.375937	-9.36937	-0.09822	
0.40	-0.91643	0.40020	-89.00291	25.12960	-83.96443	36.66722	-5.03848	-11.53763	0.99977	-91.621564	-12.58980	-0.13738	
0.50	-0.86589	0.50024	-82.97771	29.39605	-74.94643	43.29781	-8.03128	-13.90176	0.99960	-86.554423	-16.05492	-0.18542	
0.60	-0.79979	0.60028	-75.58198	32.45870	-63.93066	47.98259	-11.65132	-15.52390	0.99944	-79.934087	-19.40991	-0.24269	
0.70	-0.71385	0.70030	-67.22747	33.31512	-50.91267	49.94576	-16.31480	-16.63064	0.99910	-71.320954	-23.29701	-0.32636	
0.80	-0.59624	0.80281	-66.77134	24.80026	-35.60803	47.94485	-31.16330	-23.14459	1.00164	-59.721361	-38.81782	-0.65105	
0.90	-0.42623	0.90461	-14.57944	40.80910	-18.38363	39.01667	3.80419	1.79244	1.01191	-43.130711	4.20532	0.09866	
0.95	-0.29834	0.95446	23.41024	39.56771	-9.18347	29.37958	32.59370	10.18814	1.03174	-30.781415	34.14891	1.14461	
0.97	-0.22704	0.97388	43.37090	34.67473	-5.43131	23.29743	48.80221	11.37729	1.05365	-23.922111	50.11086	2.20714	
0.99	-0.12218	0.99251	70.47215	22.63880	-1.69329	13.75494	72.16544	8.88387	1.13427	-13.858771	72.71020	5.95098	

Table A20: Simulation results: Friction=1.0, tangential spring, normal and shear viscous damping = 0.4

y_1	BEFORE COLLISION												
	n_x	n_y	$v_{c,x}$	$v_{c,y}$	$v_{c,x}^{(n)}$	$v_{c,y}^{(n)}$	$v_{c,x}^{(t)}$	$v_{c,y}^{(t)}$	t_x	t_y	$v_c^{(n)}$	$v_c^{(t)}$	Ψ_1
0.00	-1.00000	0.00000	100.00	0.00	100.00000	0.00000	0.00000	0.00000	-----	-----	100.00000	0.00000	0.00000
0.10	-0.99499	0.10000	100.00	0.00	98.99999	-9.94993	1.00001	9.94993	0.10000	0.99499	99.49874	10.00006	0.10050
0.20	-0.97980	0.20000	100.00	0.00	95.99989	-19.59618	4.00011	19.59618	0.20000	0.97980	97.97953	20.00028	0.20413
0.30	-0.95395	0.29998	100.00	0.00	91.00117	-28.61650	8.99883	28.61650	0.29998	0.95395	95.39453	29.99805	0.31446
0.40	-0.91652	0.40000	100.00	0.00	84.00030	-36.66033	15.99970	36.66033	0.40000	0.91652	91.65168	39.99962	0.43643
0.50	-0.86603	0.49999	100.00	0.00	75.00052	-43.30097	24.99948	43.30097	0.49999	0.86603	86.60284	49.99948	0.57734
0.60	-0.79999	0.60001	100.00	0.00	63.99900	-48.00029	36.00100	48.00029	0.60001	0.79999	79.99938	60.00083	0.75002
0.70	-0.71413	0.70001	100.00	0.00	50.99874	-49.99002	49.00126	49.99002	0.70001	0.71413	71.41341	70.00090	0.98022
0.80	-0.59236	0.80568	100.00	0.00	35.08851	-47.72470	64.91149	47.72470	0.80568	0.59236	59.23555	80.56767	1.36012
0.90	-0.42262	0.90631	100.00	0.00	17.86063	-38.30223	82.13937	38.30223	0.90631	0.42262	42.26183	90.63077	2.14451
0.95	-0.29516	0.95545	100.00	0.00	8.71221	-28.20139	91.28779	28.20139	0.95545	0.29516	29.51645	95.54465	3.23700
0.97	-0.22421	0.97454	100.00	0.00	5.02703	-21.85022	94.97297	21.85022	0.97454	0.22421	22.42105	97.45407	4.34654
0.99	-0.12021	0.99275	100.00	0.00	1.44500	-11.93364	98.55500	11.93364	0.99275	0.12021	12.02080	99.27487	8.25859
y_1	AFTER COLLISION												
	n'_x	n'_y	$v'_{c,x}$	$v'_{c,y}$	$v'^{(n)}_{c,x}$	$v'^{(n)}_{c,y}$	$v'^{(t)}_{c,x}$	$v'^{(t)}_{c,y}$	e_n	$v_c'^{(n)}$	$v_c'^{(t)}$	Ψ_2	
0.00	-1.00000	0.00000	-25.12130	0.00000	-25.12130	0.00000	0.00000	0.00000	0.25121	-25.121296	0.00000	0.00000	
0.10	-0.99499	0.10000	-25.40185	-0.00488	-25.14734	2.52742	-0.25451	-2.53230	0.25401	-25.274032	-2.54505	-0.02558	
0.20	-0.97980	0.20000	-25.40204	-0.00971	-24.38403	4.97744	-1.01801	-4.98715	0.25400	-24.886861	-5.08999	-0.05195	
0.30	-0.95395	0.29998	-25.14555	-0.09506	-22.85554	7.18722	-2.29001	-7.28229	0.25116	-23.958962	-7.63386	-0.08002	
0.40	-0.91652	0.40000	-25.16569	-0.12225	-21.09444	9.20626	-4.07125	-9.32851	0.25112	-23.015876	-10.17822	-0.11105	
0.50	-0.86603	0.49999	-25.26171	-0.26897	-18.82995	10.87132	-6.43176	-11.14030	0.25106	-21.742876	-12.86366	-0.14854	
0.60	-0.79999	0.60001	-25.32421	-0.29966	-16.06341	12.04782	-9.26080	-12.34747	0.25099	-20.079418	-15.43446	-0.19293	
0.70	-0.71413	0.70001	-25.63349	-0.27117	-12.93720	12.68131	-12.69629	-12.95248	0.25368	-18.115929	-18.13732	-0.25398	
0.80	-0.59236	0.80568	-3.76765	15.94681	-8.93258	12.14942	5.16493	3.79740	0.25457	-15.079768	6.41067	0.10822	
0.90	-0.42262	0.90631	28.34058	25.49682	-4.70405	10.08786	33.04462	15.40897	0.26338	-11.130722	36.46071	0.86273	
0.95	-0.29516	0.95545	52.36610	24.67261	-2.39577	7.75512	54.76187	16.91749	0.27499	-8.1167448	57.31548	1.94181	
0.97	-0.22421	0.97454	65.01259	21.56851	-1.44456	6.27885	66.45715	15.28965	0.28736	-6.4428855	68.19330	3.04149	
0.99	-0.12021	0.99275	81.76964	13.94346	-0.48239	3.98388	82.25204	9.95958	0.33384	-4.0129832	82.85283	6.89245	

Table A21: Simulation results: Friction=1.0, no tangential spring, normal viscous damping = 0.4

y_1	BEFORE COLLISION												
	n_x	n_y	$v_{c,x}$	$v_{c,y}$	$v_{c,x}^{(n)}$	$v_{c,y}^{(n)}$	$v_{c,x}^{(t)}$	$v_{c,y}^{(t)}$	t_x	t_y	$v_c^{(n)}$	$v_c^{(t)}$	Ψ_1
0.00	-1.00000	0.00000	100.00	0.00	100.00000	0.00000	0.00000	0.00000	-----	-----	100.00000	0.00000	0.00000
0.10	-0.99474	0.10247	100.00	0.00	98.95001	-10.19297	1.04999	10.19297	0.10247	0.99474	99.47362	10.24691	0.10301
0.20	-0.97879	0.20486	100.00	0.00	95.80315	-20.05172	4.19685	20.05172	0.20486	0.97879	97.87908	20.48622	0.20930
0.30	-0.95168	0.30708	100.00	0.00	90.57027	-29.22419	9.42973	29.22419	0.30708	0.95168	95.16841	30.70786	0.32267
0.40	-0.91251	0.40905	100.00	0.00	83.26797	-37.32616	16.73203	37.32616	0.40905	0.91251	91.25128	40.90481	0.44827
0.50	-0.85977	0.51067	100.00	0.00	73.92127	-43.90641	26.07873	43.90641	0.51067	0.85977	85.97748	51.06734	0.59396
0.60	-0.79102	0.61179	100.00	0.00	62.57113	-48.39387	37.42887	48.39387	0.61179	0.79102	79.10192	61.17914	0.77342
0.70	-0.70197	0.71221	100.00	0.00	49.27562	-49.99475	50.72438	49.99475	0.71221	0.70197	70.19659	71.22105	1.01459
0.80	-0.58422	0.81159	100.00	0.00	34.13139	-47.41505	65.86861	47.41505	0.81159	0.58422	58.42208	81.15948	1.38919
0.90	-0.41615	0.90930	100.00	0.00	17.31797	-37.84026	82.68203	37.84026	0.90930	0.41615	41.61487	90.92966	2.18503
0.95	-0.29052	0.95687	100.00	0.00	8.44022	-27.79900	91.55978	27.79900	0.95687	0.29052	29.05205	95.68688	3.29364
0.97	-0.22071	0.97534	100.00	0.00	4.87131	-21.52675	95.12869	21.52675	0.97534	0.22071	22.07104	97.53394	4.41909
0.99	-0.11841	0.99297	100.00	0.00	1.40204	-11.75748	98.59796	11.75748	0.99297	0.11841	11.84077	99.29651	8.38598
y_1	AFTER COLLISION												
	n'_x	n'_y	$v'_{c,x}$	$v'_{c,y}$	$v'^{(n)}_{c,x}$	$v'^{(n)}_{c,y}$	$v'^{(t)}_{c,x}$	$v'^{(t)}_{c,y}$	e_n	$v_c^{(n)}$	$v_c^{(t)}$	Ψ_2	
0.00	-1.00000	0.00000	-25.12130	0.00000	-25.12130	0.00000	0.00000	0.00000	0.25121	-25.121296	0.00000	0.00000	
0.10	-0.99474	0.10247	-24.11669	12.53736	-25.14140	2.58985	1.02471	9.94751	0.25408	-25.274439	10.00015	0.10053	
0.20	-0.97879	0.20486	-20.26340	24.67473	-24.36068	5.09872	4.09728	19.57601	0.25428	-24.888544	20.00019	0.20434	
0.30	-0.95168	0.30708	-13.84692	35.99167	-23.05946	7.44057	9.21255	28.55110	0.25460	-24.230162	30.00061	0.31524	
0.40	-0.91251	0.40905	-4.87987	46.02336	-21.24212	9.52211	16.36225	36.50125	0.25511	-23.278712	40.00081	0.43836	
0.50	-0.85977	0.51067	6.62240	54.22191	-18.91153	11.23273	25.53393	42.98918	0.25583	-21.995914	50.00051	0.58155	
0.60	-0.79102	0.61179	20.63575	59.89184	-16.07195	12.43040	36.70771	47.46144	0.25686	-20.318031	60.00037	0.75852	
0.70	-0.70197	0.71221	36.98281	62.19789	-12.87217	13.06003	49.85498	49.13786	0.26123	-18.33732	70.00035	0.99720	
0.80	-0.58422	0.81159	55.83118	59.37585	-9.09713	12.63766	64.92831	46.73818	0.26653	-15.571393	80.00090	1.36936	
0.90	-0.41615	0.90930	76.97584	48.07669	-4.86169	10.62293	81.83753	37.45377	0.28073	-11.682578	90.00092	2.16271	
0.95	-0.29052	0.95687	88.42167	35.77258	-2.48144	8.17295	90.90311	27.59963	0.29400	-8.541352	95.00060	3.27001	
0.97	-0.22071	0.97534	93.11143	28.02449	-1.49702	6.61546	94.60845	21.40902	0.30731	-6.7827309	97.00054	4.39492	
0.99	-0.11841	0.99297	97.80431	15.91008	-0.49937	4.18769	98.30368	11.72238	0.35617	-4.2173629	99.00014	8.36095	

Table A22: Simulation results: Friction=1.0, no tangential spring, shear viscous damping = 0.4

y_1	BEFORE COLLISION												
	n_x	n_y	$v_{c,x}$	$v_{c,y}$	$v_{c,x}^{(n)}$	$v_{c,y}^{(n)}$	$v_{c,x}^{(t)}$	$v_{c,y}^{(t)}$	t_x	t_y	$v_c^{(n)}$	$v_c^{(t)}$	Ψ_1
0.00	-1.00000	0.00000	100.00	0.00	100.00000	0.00000	0.00000	0.00000	-----	-----	100.00000	0.00000	0.00000
0.10	-0.99476	0.10228	100.00	0.00	98.95392	-10.17417	1.04608	10.17417	0.10228	0.99476	99.47559	10.22780	0.10282
0.20	-0.97887	0.20449	100.00	0.00	95.81855	-20.01650	4.18145	20.01650	0.20449	0.97887	97.88695	20.44859	0.20890
0.30	-0.95186	0.30653	100.00	0.00	90.60397	-29.17735	9.39603	29.17735	0.30653	0.95186	95.18612	30.65294	0.32203
0.40	-0.91283	0.40834	100.00	0.00	83.32545	-37.27485	16.67455	37.27485	0.40834	0.91283	91.28277	40.83449	0.44734
0.50	-0.86027	0.50984	100.00	0.00	74.00599	-43.86015	25.99401	43.86015	0.50984	0.86027	86.02673	50.98432	0.59266
0.60	-0.79173	0.61087	100.00	0.00	62.68351	-48.36454	37.31649	48.36454	0.61087	0.79173	79.17292	61.08722	0.77157
0.70	-0.70288	0.71130	100.00	0.00	49.40463	-49.99646	50.59537	49.99646	0.71130	0.70288	70.28843	71.13042	1.01198
0.80	-0.58536	0.81078	100.00	0.00	34.26438	-47.45935	65.73562	47.45935	0.81078	0.58536	58.53578	81.07751	1.38509
0.90	-0.41751	0.90867	100.00	0.00	17.43160	-37.93810	82.56840	37.93810	0.90867	0.41751	41.75117	90.86716	2.17640
0.95	-0.29195	0.95643	100.00	0.00	8.52363	-27.92331	91.47637	27.92331	0.95643	0.29195	29.19526	95.64328	3.27599
0.97	-0.22202	0.97504	100.00	0.00	4.92915	-21.64759	95.07085	21.64759	0.97504	0.22202	22.20168	97.50428	4.39175
0.99	-0.11948	0.99284	100.00	0.00	1.42751	-11.86228	98.57249	11.86228	0.99284	0.11948	11.94786	99.28368	8.30974
y_1	AFTER COLLISION												
	n'_x	n'_y	$v'_{c,x}$	$v'_{c,y}$	$v'^{(n)}_{c,x}$	$v'^{(n)}_{c,y}$	$v'^{(t)}_{c,x}$	$v'^{(t)}_{c,y}$	e_n	$v_c'^{(n)}$	$v_c'^{(t)}$	Ψ_2	
0.00	-1.00000	0.00000	-100.00209	0.00000	-100.00209	0.00000	0.00000	0.00000	1.00002	-100.00209	0.00000	0.00000	
0.10	-0.99476	0.10228	-97.95538	20.12466	-98.97820	10.17666	1.02282	9.94799	1.00025	-99.499996	10.00044	0.10053	
0.20	-0.97887	0.20449	-91.82090	39.61377	-95.91075	20.03576	4.08985	19.57801	1.00096	-97.981135	20.00063	0.20432	
0.30	-0.95186	0.30653	-81.60359	57.79864	-90.80020	29.24054	9.19661	28.55810	1.00217	-95.392275	30.00238	0.31520	
0.40	-0.91283	0.40834	-67.32440	73.94078	-83.65968	37.42437	16.33527	36.51641	1.00401	-91.648921	40.00362	0.43824	
0.50	-0.86027	0.50984	-49.00579	87.16892	-74.49963	44.15271	25.49385	43.01621	1.00667	-86.600558	50.00331	0.58125	
0.60	-0.79173	0.61087	-26.68189	96.37549	-63.33671	48.86852	36.65482	47.50697	1.01042	-79.997945	60.00406	0.75789	
0.70	-0.70288	0.71130	-0.40300	99.99868	-50.19490	50.79619	49.79189	49.20249	1.01600	-71.412744	70.00084	0.99591	
0.80	-0.58536	0.81078	29.74151	95.47540	-35.12126	48.64622	64.86277	46.82917	1.02501	-59.999649	80.00094	1.36670	
0.90	-0.41751	0.90867	63.58448	77.18206	-18.19761	39.60525	81.78210	37.57681	1.04394	-43.585879	90.00182	2.15567	
0.95	-0.29195	0.95643	81.74925	57.59379	-9.11408	29.85761	90.86334	27.73618	1.06927	-31.217682	95.00232	3.25403	
0.97	-0.22202	0.97504	89.18267	45.23788	-5.39697	23.70214	94.57963	21.53574	1.09491	-24.308817	97.00049	4.36906	
0.99	-0.11948	0.99284	96.60632	25.83060	-1.68503	14.00215	98.29135	11.82845	1.18039	-14.103177	99.00051	8.28604	

Table A23: Simulation results: Friction=1.0, no tangential spring, normal and shear damping = 0.4

y_1	BEFORE COLLISION												
	n_x	n_y	$v_{c,x}$	$v_{c,y}$	$v_{c,x}^{(n)}$	$v_{c,y}^{(n)}$	$v_{c,x}^{(t)}$	$v_{c,y}^{(t)}$	t_x	t_y	$v_c^{(n)}$	$v_c^{(t)}$	Ψ_1
0.00	-1.00000	0.00000	100.00	0.00	100.00000	0.00000	0.00000	0.00000	-----	-----	100.00000	0.00000	0.00000
0.10	-0.99474	0.10247	100.00	0.00	98.94999	-10.19297	1.05001	10.19297	0.10247	0.99474	99.47359	10.24691	0.10301
0.20	-0.97879	0.20486	100.00	0.00	95.80315	-20.05172	4.19685	20.05172	0.20486	0.97879	97.87908	20.48622	0.20930
0.30	-0.95168	0.30708	100.00	0.00	90.57027	-29.22419	9.42973	29.22419	0.30708	0.95168	95.16841	30.70786	0.32267
0.40	-0.91251	0.40905	100.00	0.00	83.26797	-37.32616	16.73203	37.32616	0.40905	0.91251	91.25128	40.90481	0.44827
0.50	-0.85977	0.51067	100.00	0.00	73.92127	-43.90641	26.07873	43.90641	0.51067	0.85977	85.97748	51.06734	0.59396
0.60	-0.79102	0.61179	100.00	0.00	62.57113	-48.39387	37.42887	48.39387	0.61179	0.79102	79.10192	61.17914	0.77342
0.70	-0.70197	0.71221	100.00	0.00	49.27562	-49.99475	50.72438	49.99475	0.71221	0.70197	70.19659	71.22105	1.01459
0.80	-0.58422	0.81159	100.00	0.00	34.13139	-47.41505	65.86861	47.41505	0.81159	0.58422	58.42208	81.15948	1.38919
0.90	-0.41615	0.90930	100.00	0.00	17.31797	-37.84026	82.68203	37.84026	0.90930	0.41615	41.61487	90.92966	2.18503
0.95	-0.29052	0.95687	100.00	0.00	8.44022	-27.79900	91.55978	27.79900	0.95687	0.29052	29.05205	95.68688	3.29364
0.97	-0.22071	0.97534	100.00	0.00	4.87131	-21.52675	95.12869	21.52675	0.97534	0.22071	22.07104	97.53394	4.41909
0.99	-0.11841	0.99297	100.00	0.00	1.40204	-11.75748	98.59796	11.75748	0.99297	0.11841	11.84077	99.29651	8.38598
y_1	AFTER COLLISION												
	n'_x	n'_y	$v'_{c,x}$	$v'_{c,y}$	$v'^{(n)}_{c,x}$	$v'^{(n)}_{c,y}$	$v'^{(t)}_{c,x}$	$v'^{(t)}_{c,y}$	e_n	$v_c^{(n)}$	$v_c^{(t)}$	Ψ_2	
0.00	-1.00000	0.00000	25.12130	0.00000	25.12130	0.00000	0.00000	0.00000	0.25121	-25.121296	0.00000	0.00000	
0.10	-0.99474	0.10247	-24.11669	12.53736	-25.14139	2.58985	1.02470	9.94751	0.25408	-25.274431	10.00014	0.10053	
0.20	-0.97879	0.20486	-20.48622	24.67473	-24.57415	5.14340	4.08793	19.53133	0.25651	-25.106642	19.95454	0.20387	
0.30	-0.95168	0.30708	-13.84692	35.99167	-23.05946	7.44057	9.21255	28.55110	0.25460	-24.230162	30.00061	0.31524	
0.40	-0.91251	0.40905	-4.87987	46.02336	-21.24212	9.52211	16.36225	36.50125	0.25511	-23.278712	40.00081	0.43836	
0.50	-0.85977	0.51067	6.62240	54.22191	-18.91153	11.23273	25.53393	42.98918	0.25583	-21.995914	50.00051	0.58155	
0.60	-0.79102	0.61179	20.63575	59.89184	-16.07195	12.43040	36.70771	47.46144	0.25686	-20.318031	60.00037	0.75852	
0.70	-0.70197	0.71221	36.98281	62.19789	-12.87217	13.06003	49.85498	49.13786	0.26123	-18.33732	70.00035	0.99720	
0.80	-0.58422	0.81159	55.83118	59.37585	-9.09713	12.63766	64.92831	46.73818	0.26653	-15.571393	80.00090	1.36936	
0.90	-0.41615	0.90930	76.97584	48.07669	-4.86169	10.62293	81.83753	37.45377	0.28073	-11.682578	90.00092	2.16271	
0.95	-0.29052	0.95687	88.42167	35.77258	-2.48144	8.17295	90.90311	27.59963	0.29400	-8.541352	95.00060	3.27001	
0.97	-0.22071	0.97534	93.11143	28.02449	-1.49702	6.61546	94.60845	21.40902	0.30731	-6.7827309	97.00054	4.39492	
0.99	-0.11841	0.99297	97.80431	15.91008	-0.49937	4.18769	98.30368	11.72238	0.35617	-4.2173629	99.00014	8.36095	

Table A24: Simulation results: Friction=1.0, tangential spring, local damping = 0.1

y_1	BEFORE COLLISION												
	n_x	n_y	$v_{c,x}$	$v_{c,y}$	$v_{c,x}^{(n)}$	$v_{c,y}^{(n)}$	$v_{c,x}^{(t)}$	$v_{c,y}^{(t)}$	t_x	t_y	$v_c^{(n)}$	$v_c^{(t)}$	Ψ_1
0.00	-1.00000	0.00000	100.00	0.00	100.00000	0.00000	0.00000	0.00000	-----	-----	100.00000	0.00000	0.00000
0.10	-0.99499	0.10000	100.00	0.00	98.99993	-9.95021	1.00007	9.95021	0.10000	0.99499	99.49871	10.00034	0.10051
0.20	-0.97979	0.20001	100.00	0.00	95.99969	-19.59665	4.00031	19.59665	0.20001	0.97979	97.97943	20.00078	0.20413
0.30	-0.95394	0.30000	100.00	0.00	91.00029	-28.61776	8.99971	28.61776	0.30000	0.95394	95.39407	29.99951	0.31448
0.40	-0.91652	0.40000	100.00	0.00	84.00008	-36.66053	15.99992	36.66053	0.40000	0.91652	91.65156	39.99990	0.43643
0.50	-0.86601	0.50003	100.00	0.00	74.99670	-43.30318	25.00330	43.30318	0.50003	0.86601	86.60063	50.00330	0.57740
0.60	-0.79998	0.60002	100.00	0.00	63.99725	-48.00080	36.00275	48.00080	0.60002	0.79998	79.99828	60.00229	0.75004
0.70	-0.71410	0.70004	100.00	0.00	50.99390	-49.99012	49.00610	49.99012	0.70004	0.71410	71.41001	70.00436	0.98032
0.80	-0.59667	0.80248	100.00	0.00	35.60183	-47.88207	64.39817	47.88207	0.80248	0.59667	59.66727	80.24847	1.34493
0.90	-0.42724	0.90414	100.00	0.00	18.25380	-38.62873	81.74620	38.62873	0.90414	0.42724	42.72446	90.41361	2.11620
0.95	-0.29928	0.95417	100.00	0.00	8.95680	-28.55619	91.04320	28.55619	0.95417	0.29928	29.92791	95.41656	3.18821
0.97	-0.22761	0.97375	100.00	0.00	5.18069	-22.16369	94.81931	22.16369	0.97375	0.22761	22.76112	97.37521	4.27814
0.99	-0.12211	0.99252	100.00	0.00	1.49119	-12.12006	98.50881	12.12006	0.99252	0.12211	12.21145	99.25160	8.12775
y_1	AFTER COLLISION												
	n'_x	n'_y	$v'_{c,x}$	$v'_{c,y}$	$v'_{c,x}{}^{(n)}$	$v'_{c,y}{}^{(n)}$	$v'_{c,x}{}^{(t)}$	$v'_{c,y}{}^{(t)}$	e_n	$v_c^{(n)}$	$v_c^{(t)}$	Ψ_2	
0.00	-1.00000	0.00000	-90.45565	0.00000	-90.45565	0.00000	0.00000	0.00000	0.90456	-90.455645	0.00000	0.00000	
0.10	-0.99499	0.10000	-90.45575	-0.00342	-89.55079	9.00050	-0.90496	-9.00391	0.90455	-90.00196	-9.04928	-0.09095	
0.20	-0.97979	0.20001	-90.45602	-0.00573	-86.83637	17.72612	-3.61965	-17.73185	0.90455	-88.627144	-18.09753	-0.18471	
0.30	-0.95394	0.30000	-90.45328	-0.01085	-82.30965	25.88473	-8.14364	-25.89557	0.90450	-86.283818	-27.14589	-0.28457	
0.40	-0.91652	0.40000	-90.45244	-0.01281	-75.97542	33.15830	-14.47702	-33.17111	0.90447	-82.895944	-36.19263	-0.39489	
0.50	-0.86601	0.50003	-90.45256	-0.01622	-67.82941	39.16478	-22.62315	-39.18099	0.90443	-78.324376	-45.24331	-0.52244	
0.60	-0.79998	0.60002	-90.45307	-0.01273	-57.88137	43.41362	-32.57171	-43.42635	0.90444	-72.353264	-54.28410	-0.67857	
0.70	-0.71410	0.70004	-90.41326	-0.02821	-46.09115	45.18387	-44.32211	-45.21208	0.90386	-64.544374	-63.31337	-0.88662	
0.80	-0.59667	0.80248	-63.21531	21.53140	-32.81549	44.13463	-30.39982	-22.60323	0.92174	-54.997473	-37.88212	-0.63489	
0.90	-0.42724	0.90414	-20.35402	36.34848	-17.75634	37.57600	-2.59768	-1.22752	0.97275	-41.560116	-2.87311	-0.06725	
0.95	-0.29928	0.95417	13.66955	36.47494	-9.19150	29.30445	22.86105	7.17049	1.02620	-30.712125	23.95920	0.80056	
0.97	-0.22761	0.97375	34.85701	32.63324	-5.42690	23.21701	40.28391	9.41623	1.04752	-23.842835	41.36978	1.81756	
0.99	-0.12211	0.99252	65.10170	21.90190	-1.68373	13.68493	66.78543	8.21696	1.12911	-13.788123	67.28902	5.51032	

Table A25: Simulation results: Friction=1.0, tangential spring, local damping = 0.2

y_1	BEFORE COLLISION												
	n_x	n_y	$v_{c,x}$	$v_{c,y}$	$v_{c,x}^{(n)}$	$v_{c,y}^{(n)}$	$v_{c,x}^{(t)}$	$v_{c,y}^{(t)}$	t_x	t_y	$v_c^{(n)}$	$v_c^{(t)}$	Ψ_1
0.00	-1.00000	0.00000	100.00	0.00	100.00000	0.00000	0.00000	0.00000	-----	-----	100.00000	0.00000	0.00000
0.10	-0.99499	0.10001	100.00	0.00	98.99985	-9.95063	1.00015	9.95063	0.10001	0.99499	99.49867	10.00076	0.10051
0.20	-0.97979	0.20002	100.00	0.00	95.99937	-19.59740	4.00063	19.59740	0.20002	0.97979	97.97927	20.00158	0.20414
0.30	-0.95394	0.29999	100.00	0.00	91.00065	-28.61727	8.99935	28.61727	0.29999	0.95394	95.39428	29.99894	0.31447
0.40	-0.91651	0.40001	100.00	0.00	83.99919	-36.66136	16.00081	36.66136	0.40001	0.91651	91.65107	40.00102	0.43645
0.50	-0.86602	0.50002	100.00	0.00	74.99848	-43.30215	25.00152	43.30215	0.50002	0.86602	86.60166	50.00152	0.57737
0.60	-0.79997	0.60004	100.00	0.00	63.99548	-48.00132	36.00452	48.00132	0.60004	0.79997	79.99718	60.00376	0.75007
0.70	-0.71411	0.70003	100.00	0.00	50.99557	-49.99009	49.00443	49.99009	0.70003	0.71411	71.41118	70.00316	0.98028
0.80	-0.59705	0.80220	100.00	0.00	35.64719	-47.89569	64.35281	47.89569	0.80220	0.59705	59.70526	80.22021	1.34360
0.90	-0.42812	0.90372	100.00	0.00	18.32832	-38.68985	81.67168	38.68985	0.90372	0.42812	42.81158	90.37239	2.11093
0.95	-0.30030	0.95385	100.00	0.00	9.01784	-28.64371	90.98216	28.64371	0.95385	0.30030	30.02971	95.38457	3.17634
0.97	-0.22836	0.97358	100.00	0.00	5.21466	-22.23226	94.78534	22.23226	0.97358	0.22836	22.83564	97.35776	4.26341
0.99	-0.12211	0.99252	100.00	0.00	1.49116	-12.11991	98.50884	12.11991	0.99252	0.12211	12.21130	99.25162	8.12785
y_1	AFTER COLLISION												
	n'_x	n'_y	$v'_{c,x}$	$v'_{c,y}$	$v'_{c,x}{}^{(n)}$	$v'_{c,y}{}^{(n)}$	$v'_{c,x}{}^{(t)}$	$v'_{c,y}{}^{(t)}$	e_n	$v_c^{(n)}$	$v_c^{(t)}$	Ψ_2	
0.00	-1.00000	0.00000	-81.65198	0.00000	-81.65198	0.00000	0.00000	0.00000	0.81652	-81.651978	0.00000	0.00000	
0.10	-0.99499	0.10001	-81.65003	-0.00501	-80.83291	8.12464	-0.81712	-8.12965	0.81650	-81.240189	-8.17061	-0.08212	
0.20	-0.97979	0.20002	-81.65134	-0.00824	-78.38316	16.00121	-3.26818	-16.00945	0.81650	-79.999738	-16.33963	-0.16677	
0.30	-0.95394	0.29999	-81.65032	-0.01817	-74.29712	23.36446	-7.35320	-23.38263	0.81645	-77.884282	-24.51157	-0.25695	
0.40	-0.91651	0.40001	-81.65144	-0.02057	-68.57901	29.93124	-13.07243	-29.95180	0.81642	-74.826191	-32.68026	-0.35657	
0.50	-0.86602	0.50002	-81.65238	-0.02580	-61.22688	35.35078	-20.42551	-35.37659	0.81637	-70.699423	-40.84978	-0.47170	
0.60	-0.79997	0.60004	-81.65090	-0.02175	-52.24245	39.18567	-29.40845	-39.20743	0.81635	-65.305361	-49.01101	-0.61266	
0.70	-0.71411	0.70003	-81.62166	0.00159	-41.62423	40.80352	-39.99743	-40.80193	0.81623	-58.288106	-57.13661	-0.80011	
0.80	-0.59705	0.80220	-59.36109	18.64038	-30.08850	40.42701	-29.27259	-21.78663	0.84406	-50.395049	-36.49030	-0.61117	
0.90	-0.42812	0.90372	-23.98231	32.18367	-16.84737	35.56366	-7.13495	-3.38000	0.91920	-39.352357	-7.89505	-0.18441	
0.95	-0.30030	0.95385	3.44510	33.22422	-9.20598	29.24131	12.65108	3.98291	1.02086	-30.65623	13.26323	0.44167	
0.97	-0.22836	0.97358	25.52423	30.39589	-5.42669	23.13623	30.95092	7.25966	1.04066	-23.764139	31.79091	1.39216	
0.99	-0.12211	0.99252	58.85386	21.05132	-1.67380	13.60438	60.52765	7.44694	1.12248	-13.514633	44.65268	4.99407	

Table A26: Simulation results: Friction=1.0, tangential spring, local damping = 0.4

y_1	BEFORE COLLISION												
	n_x	n_y	$v_{c,x}$	$v_{c,y}$	$v_{c,x}^{(n)}$	$v_{c,y}^{(n)}$	$v_{c,x}^{(t)}$	$v_{c,y}^{(t)}$	t_x	t_y	$v_c^{(n)}$	$v_c^{(t)}$	Ψ_1
0.00	-1.00000	0.00000	100.00	0.00	100.00000	0.00000	0.00000	0.00000	-----	-----	100.00000	0.00000	0.00000
0.10	-0.99499	0.10000	100.00	0.00	98.99998	-9.94998	1.00002	9.94998	0.10000	0.99499	99.49873	10.00010	0.10050
0.20	-0.97979	0.20001	100.00	0.00	95.99941	-19.59729	4.00059	19.59729	0.20001	0.97979	97.97929	20.00147	0.20414
0.30	-0.95394	0.29999	100.00	0.00	91.00044	-28.61754	8.99956	28.61754	0.29999	0.95394	95.39415	29.99926	0.31448
0.40	-0.91651	0.40001	100.00	0.00	83.99943	-36.66114	16.00057	36.66114	0.40001	0.91651	91.65120	40.00071	0.43645
0.50	-0.86602	0.50000	100.00	0.00	74.99990	-43.30133	25.00010	43.30133	0.50000	0.86602	86.60248	50.00010	0.57735
0.60	-0.79997	0.60003	100.00	0.00	63.99586	-48.00121	36.00414	48.00121	0.60003	0.79997	79.99741	60.00345	0.75007
0.70	-0.71411	0.70003	100.00	0.00	50.99519	-49.99010	49.00481	49.99010	0.70003	0.71411	71.41092	70.00344	0.98029
0.80	-0.59766	0.80175	100.00	0.00	35.72028	-47.91753	64.27972	47.91753	0.80175	0.59766	59.76644	80.17464	1.34147
0.90	-0.42952	0.90306	100.00	0.00	18.44842	-38.78786	81.55158	38.78786	0.90306	0.42952	42.95162	90.30591	2.10250
0.95	-0.30222	0.95324	100.00	0.00	9.13349	-28.80848	90.86651	28.80848	0.95324	0.30222	30.22167	95.32393	3.15416
0.97	-0.23025	0.97313	100.00	0.00	5.30152	-22.40637	94.69848	22.40637	0.97313	0.23025	23.02502	97.31315	4.22641
0.99	-0.12237	0.99248	100.00	0.00	1.49740	-12.14485	98.50260	12.14485	0.99248	0.12237	12.23681	99.24848	8.11065
y_1	AFTER COLLISION												
	n'_x	n'_y	$v'_{c,x}$	$v'_{c,y}$	$v'_{c,x}{}^{(n)}$	$v'_{c,y}{}^{(n)}$	$v'_{c,x}{}^{(t)}$	$v'_{c,y}{}^{(t)}$	e_n	$v_c^{(n)}$	$v_c^{(t)}$	Ψ_2	
0.00	-1.00000	0.00000	-65.46705	0.00000	-65.46705	0.00000	0.00000	0.00000	0.65467	-65.467053	0.00000	0.00000	
0.10	-0.99499	0.10000	-65.46660	-0.00608	-64.81132	6.51385	-0.65528	-6.51993	0.65466	-65.137831	-6.55278	-0.06586	
0.20	-0.97979	0.20001	-65.46649	-0.00950	-62.84559	12.82928	-2.62090	-12.83878	0.65465	-64.141704	-13.10356	-0.13374	
0.30	-0.95394	0.29999	-65.46684	-0.03246	-59.56582	18.73208	-5.90101	-18.76454	0.65457	-62.441796	-19.67053	-0.20620	
0.40	-0.91651	0.40001	-65.46643	-0.02563	-54.98203	23.99664	-10.48440	-24.02227	0.65455	-59.990519	-26.21053	-0.28598	
0.50	-0.86602	0.50000	-65.46585	-0.03156	-49.08565	28.33969	-16.38019	-28.37125	0.65448	-56.679268	-32.76032	-0.37828	
0.60	-0.79997	0.60003	-65.46668	-0.02648	-41.88325	31.41526	-23.58343	-31.44174	0.65447	-52.355762	-39.30345	-0.49131	
0.70	-0.71411	0.70003	-65.45340	-0.01769	-33.36924	32.71155	-32.08416	-32.72924	0.65436	-46.728488	-45.83226	-0.64181	
0.80	-0.59766	0.80175	-50.63669	13.77608	-24.68872	33.11908	-25.94797	-19.34300	0.69117	-41.308672	-32.36431	-0.54151	
0.90	-0.42952	0.90306	-26.66671	24.64614	-14.47930	30.44276	-12.18741	-5.79662	0.78485	-33.710706	-13.49570	-0.31421	
0.95	-0.30222	0.95324	-8.43524	26.44364	-8.38844	26.45848	-0.04680	-0.01484	0.91843	-27.75639	-0.04909	-0.00162	
0.97	-0.23025	0.97313	3.88952	25.20563	-5.44146	22.99785	9.33098	2.20778	1.02640	-23.632831	9.58862	0.41644	
0.99	-0.12237	0.99248	42.66334	18.87713	-1.65376	13.41307	44.31710	5.46406	1.10442	-13.514633	44.65268	3.64904	

Table A27: Simulation results: Friction=1.0, tangential spring, local damping = 0.8

y_1	BEFORE COLLISION												
	n_x	n_y	$v_{c,x}$	$v_{c,y}$	$v_{c,x}^{(n)}$	$v_{c,y}^{(n)}$	$v_{c,x}^{(t)}$	$v_{c,y}^{(t)}$	t_x	t_y	$v_c^{(n)}$	$v_c^{(t)}$	Ψ_1
0.00	-1.00000	0.00000	100.00	0.00	100.00000	0.00000	0.00000	0.00000	-----	-----	100.00000	0.00000	0.00000
0.10	-0.99499	0.10000	100.00	0.00	98.99996	-9.95008	1.00004	9.95008	0.10000	0.99499	99.49872	10.00021	0.10051
0.20	-0.97979	0.20001	100.00	0.00	95.99971	-19.59659	4.00029	19.59659	0.20001	0.97979	97.97944	20.00071	0.20413
0.30	-0.95394	0.29998	100.00	0.00	91.00092	-28.61685	8.99908	28.61685	0.29998	0.95394	95.39440	29.99846	0.31447
0.40	-0.91651	0.40001	100.00	0.00	83.99950	-36.66107	16.00050	36.66107	0.40001	0.91651	91.65124	40.00062	0.43644
0.50	-0.86602	0.50001	100.00	0.00	74.99925	-43.30170	25.00075	43.30170	0.50001	0.86602	86.60211	50.00075	0.57736
0.60	-0.79999	0.60001	100.00	0.00	63.99842	-48.00046	36.00158	48.00046	0.60001	0.79999	79.99901	60.00132	0.75003
0.70	-0.71413	0.70001	100.00	0.00	50.99794	-49.99004	49.00206	49.99004	0.70001	0.71413	71.41284	70.00147	0.98024
0.80	-0.59853	0.80110	100.00	0.00	35.82394	-47.94830	64.17606	47.94830	0.80110	0.59853	59.85311	80.10996	1.33844
0.90	-0.43165	0.90204	100.00	0.00	18.63184	-38.93634	81.36816	38.93634	0.90204	0.43165	43.16461	90.20430	2.08977
0.95	-0.30518	0.95229	100.00	0.00	9.31371	-29.06245	90.68629	29.06245	0.95229	0.30518	30.51838	95.22935	3.12039
0.97	-0.23393	0.97225	100.00	0.00	5.47210	-22.74349	94.52790	22.74349	0.97225	0.23393	23.39253	97.22546	4.15626
0.99	-0.12674	0.99194	100.00	0.00	1.60628	-12.57171	98.39372	12.57171	0.99194	0.12674	12.67391	99.19361	7.82660
y_1	AFTER COLLISION												
	n'_x	n'_y	$v'_{c,x}$	$v'_{c,y}$	$v'_{c,x}{}^{(n)}$	$v'_{c,y}{}^{(n)}$	$v'_{c,x}{}^{(t)}$	$v'_{c,y}{}^{(t)}$	e_n	$v_c^{(n)}$	$v_c^{(t)}$	Ψ_2	
0.00	-1.00000	0.00000	-33.33840	0.00000	-33.33840	0.00000	0.00000	0.00000	0.33338	-33.338396	0.00000	0.00000	
0.10	-0.99499	0.10000	-33.33524	-0.00433	-33.00144	3.31684	-0.33380	-3.32117	0.33335	-33.167706	-3.33790	-0.03355	
0.20	-0.97979	0.20001	-33.33710	-0.00506	-32.00252	6.53273	-1.33457	-6.53779	0.33336	-32.662488	-6.67262	-0.06810	
0.30	-0.95394	0.29998	-33.33961	-0.04470	-30.32656	9.53673	-3.01305	-9.58143	0.33326	-31.790716	-10.04401	-0.10529	
0.40	-0.91651	0.40001	-33.34367	-0.02754	-27.99842	12.21974	-5.34525	-12.24728	0.33332	-30.548874	-13.36292	-0.14580	
0.50	-0.86602	0.50001	-33.33760	-0.02876	-24.99049	14.42856	-8.34711	-14.45732	0.33321	-28.856683	-16.69396	-0.19277	
0.60	-0.79999	0.60001	-33.33829	-0.01342	-21.32954	15.99770	-12.00875	-16.01112	0.33328	-26.66225	-20.01415	-0.25018	
0.70	-0.71413	0.70001	-33.33721	-0.01388	-16.99435	16.65848	-16.34286	-16.67237	0.33324	-23.797334	-23.34645	-0.32692	
0.80	-0.59853	0.80110	-28.40248	5.77821	-12.94544	17.32673	-15.45703	-11.54852	0.36136	-21.628688	-19.29477	-0.32237	
0.90	-0.43165	0.90204	-20.06536	10.96602	-8.00831	16.73556	-12.05705	-5.76955	0.42982	-18.552956	-13.36638	-0.30966	
0.95	-0.30518	0.95229	-13.16729	12.48101	-4.85365	15.14531	-8.31364	-2.66429	0.52113	-15.904033	-8.73013	-0.28606	
0.97	-0.23393	0.97225	-9.14949	12.37174	-3.31444	13.77566	-5.83505	-1.40392	0.60570	-14.168776	-6.00157	-0.25656	
0.99	-0.12674	0.99194	-2.88341	10.62209	-1.38169	10.81396	-1.50171	-0.19187	0.86018	-10.901876	-1.51392	-0.11945	

Table A28: Simulation results: Friction=1.0, tangential spring, time step = 10^{-7} s

y_1	BEFORE COLLISION												
	n_x	n_y	$v_{c,x}$	$v_{c,y}$	$v_{c,x}^{(n)}$	$v_{c,y}^{(n)}$	$v_{c,x}^{(t)}$	$v_{c,y}^{(t)}$	t_x	t_y	$v_c^{(n)}$	$v_c^{(t)}$	Ψ_1
0.00	-1.00000	0.00000	100.00	0.00	100.00000	0.00000	0.00000	0.00000	-----	-----	100.00000	0.00000	0.00000
0.10	-0.99499	0.10000	100.00	0.00	98.99993	-9.95022	1.00007	9.95022	0.10000	0.99499	99.49871	10.00035	0.10051
0.20	-0.97979	0.20001	100.00	0.00	95.99974	-19.59653	4.00026	19.59653	0.20001	0.97979	97.97946	20.00065	0.20413
0.30	-0.95394	0.30001	100.00	0.00	90.99939	-28.61905	9.00061	28.61905	0.30001	0.95394	95.39360	30.00102	0.31450
0.40	-0.91651	0.40001	100.00	0.00	83.99912	-36.66142	16.00088	36.66142	0.40001	0.91651	91.65103	40.00110	0.43645
0.50	-0.86602	0.50002	100.00	0.00	74.99827	-43.30227	25.00173	43.30227	0.50002	0.86602	86.60154	50.00173	0.57738
0.60	-0.79998	0.60002	100.00	0.00	63.99707	-48.00085	36.00293	48.00085	0.60002	0.79998	79.99817	60.00244	0.75005
0.70	-0.71412	0.70003	100.00	0.00	50.99609	-49.99008	49.00391	49.99008	0.70003	0.71412	71.41155	70.00279	0.98027
0.80	-0.59624	0.80281	100.00	0.00	35.54974	-47.86638	64.45026	47.86638	0.80281	0.59624	59.62360	80.28092	1.34646
0.90	-0.42623	0.90462	100.00	0.00	18.16703	-38.55725	81.83297	38.55725	0.90462	0.42623	42.62279	90.46158	2.12238
0.95	-0.29833	0.95446	100.00	0.00	8.90036	-28.47489	91.09964	28.47489	0.95446	0.29833	29.83347	95.44613	3.19930
0.97	-0.22700	0.97389	100.00	0.00	5.15296	-22.10754	94.84704	22.10754	0.97389	0.22700	22.70014	97.38944	4.29026
0.99	-0.12218	0.99251	100.00	0.00	1.49284	-12.12664	98.50716	12.12664	0.99251	0.12218	12.21818	99.25077	8.12320
y_1	AFTER COLLISION												
	n'_x	n'_y	$v'_{c,x}$	$v'_{c,y}$	$v'^{(n)}_{c,x}$	$v'^{(n)}_{c,y}$	$v'^{(t)}_{c,x}$	$v'^{(t)}_{c,y}$	e_n	$v_c'^{(n)}$	$v_c'^{(t)}$	Ψ_2	
0.00	-1.00000	0.00000	-100.00002	0.00000	-100.00002	0.00000	0.00000	0.00000	1.00000	-100.00002	0.00000	0.00000	
0.10	-0.99499	0.10000	-100.00000	0.00020	-98.99995	9.95022	-1.00005	-9.95002	1.00000	-99.498724	-10.00015	-0.10051	
0.20	-0.97979	0.20001	-99.99995	0.00042	-95.99978	19.59653	-4.00018	-19.59612	1.00000	-97.979495	-20.00023	-0.20413	
0.30	-0.95394	0.30001	-99.99983	0.00088	-90.99949	28.61908	-9.00034	-28.61820	1.00000	-95.393701	-30.00012	-0.31449	
0.40	-0.91651	0.40001	-99.99968	0.00108	-83.99925	36.66148	-16.00044	-36.66040	1.00000	-91.651175	-39.99999	-0.43644	
0.50	-0.86602	0.50002	-99.99924	0.00185	-74.99851	43.30240	-25.00073	-43.30055	1.00000	-86.601815	-49.99974	-0.57735	
0.60	-0.79998	0.60002	-99.99737	0.00442	-63.99751	48.00118	-35.99986	-47.99677	1.00001	-79.998716	-59.99733	-0.74998	
0.70	-0.71412	0.70003	-99.94133	0.06094	-50.99664	49.99061	-48.94469	-49.92967	1.00001	-71.41231	-69.91820	-0.97909	
0.80	-0.59624	0.80281	-66.77106	24.80020	-35.60790	47.94468	-31.16316	-23.14448	1.00164	-59.721141	-38.81764	-0.65104	
0.90	-0.42623	0.90462	-14.57888	40.80890	-18.38334	39.01636	3.80446	1.79255	1.01191	-43.130305	4.20561	0.09867	
0.95	-0.29833	0.95446	23.41012	39.56778	-9.18330	29.38011	32.59342	10.18768	1.03179	-30.781871	34.14849	1.14464	
0.97	-0.22700	0.97389	43.37116	34.67457	-5.43079	23.29950	48.80196	11.37506	1.05392	-23.924055	50.11011	2.20748	
0.99	-0.12218	0.99251	70.47195	22.63896	-1.69331	13.75512	72.16526	8.88384	1.13429	-13.858953	72.71002	5.95097	

Appendix 11: Test charts of the vibrating shear cell

This appendix lists the used test charts that have been used to measure all bulk yield loci and wall yield loci.

Test Chart Vibrational Shear Cell				editor: J. Knijnenburg				Date:						
Material: Calcit MX10				Origin of material: sh minerals, Heidenheim				Material moisture (%):						
Room temperature (°C):				rel. Humidity (%):				Storage time (h):						
Vibrational velocity of exciter (mm/s): 0				Vibrational acceleration of exciter (m/s ²): 0.0										
				Pre-Shearing					Shearing					
Trial No.	YL No.	n	m _N	m _{pre}	F _{S,pre}	f _{pre}	a ₁ (base)	a ₂ (ring)	m	F _S	f	a ₁ (base)	a ₂ (ring)	m _{total}
--	--	--	kg	kg	N	Hz	m/s ²	m/s ²	kg	N	Hz	m/s ²	m/s ²	g
	1	20	3	1.1		50			0.8		50			
	1	20	3	1.1		50			0.8		50			
	1	20	3	1.1		50			0.5		50			
	1	20	3	1.1		50			0.5		50			
	1	20	3	1.1		50			0.2		50			
	1	20	3	1.1		50			0.2		50			
	1	20	3	1.1		50			0		50			
	1	20	3	1.1		50			0		50			

Test Chart Vibrational Shear Cell				editor: J. Knijnenburg				Date:						
Material: Calcit MX10				Origin of material: sh minerals, Heidenheim				Material moisture (%):						
Room temperature (°C):				rel. Humidity (%):				Storage time (h):						
Vibrational velocity of exciter (mm/s): 10				Vibrational acceleration of exciter (m/s ²): 3.1										
				Pre-Shearing					Shearing					
Trial No.	YL No.	n	m _N	m _{pre}	F _{S,pre}	f _{pre}	a ₁ (base)	a ₂ (ring)	m	F _S	f	a ₁ (base)	a ₂ (ring)	m _{total}
--	--	--	kg	kg	N	Hz	m/s ²	m/s ²	kg	N	Hz	m/s ²	m/s ²	g
	2	20	4	2.1		50			1.6		50			
	2	20	4	2.1		50			1.6		50			
	2	20	4	2.1		50			1		50			
	2	20	4	2.1		50			1		50			
	2	20	4	2.1		50			0.5		50			
	2	20	4	2.1		50			0.5		50			
	2	20	4	2.1		50			0.3		50			
	2	20	4	2.1		50			0.3		50			

Test Chart Vibrational Shear Cell				editor: J. Knijnenburg					Date:					
Material: Calcit MX10				Origin of material: sh minerals, Heidenheim					Material moisture (%):					
Room temperature (°C):				rel. Humidity (%):					Storage time (h):					
Vibrational velocity of exciter (mm/s): 0-50				Vibrational acceleration of exciter (m/s ²):										
				Pre-Shearing					Shearing					
Trial No.	YL No.	n	m _N	m _{pre}	F _{S,pre} max	F _{S,pre} min	f _{pre}	a (ring)	m	F _{S,0} max	F _{S,0} min	f	a (ring)	F _S
--	--	--	kg	kg	N	N	Hz	m/s ²	kg	N	N	Hz	m/s ²	N
	WYL	20	13	13			0	0	4.0			50		
									4.0			50		
									4.0			50		
									4.0			50		
	WYL	20	13	13		0	0	0	4.0			50		
									4.0			50		
									4.0			50		
									4.0			50		
	WYL	20	13	13		0	0	0	2.0			50		
									2.0			50		
									2.0			50		
									2.0			50		
	WYL	20	13	13		0	0	0	2.0			50		
									2.0			50		
									2.0			50		
									2.0			50		

Test Chart Vibrational Shear Cell				editor: J. Knijnenburg					Date:					
Material: Calcit MX10				Origin of material: sh minerals, Heidenheim				Material moisture (%):						
Room temperature (°C):				rel. Humidity (%):				Storage time (h):						
Vibrational velocity of exciter (mm/s): 0-50				Vibrational acceleration of exciter (m/s ²):										
				Pre-Shearing					Shearing					
Trial No.	YL No.	n	m _N	m _{pre}	F _{S,pre} max	F _{S,pre} min	f _{pre}	a (ring)	m	F _{S,0} max	F _{S,0} min	f	a (ring)	F _S
--	--	--	kg	kg	N	N	Hz	m/s ²	kg	N	N	Hz	m/s ²	N
	WYL	20	13	13			0	0	1.0			50		
									1.0			50		
									1.0			50		
									1.0			50		
	WYL	20	13	13		0	0	0	1.0			50		
									1.0			50		
									1.0			50		
									1.0			50		
	WYL	20	13	13		0	0	0	1.0			50		
									1.0			50		
									1.0			50		
	WYL	20	13	13		0	0	0	1.0			50		
									1.0			50		
									1.0			50		
									1.0			50		

Appendix 12: Used scripts for simulations

File: singleball.DAT Used for: particle-wall friction

Example case: 1

```
; FNAME: singleball.DAT

new
set random
set disk off

trace energy ON

wall id=1 friction=1.0 kn=1e8 ks=1e8 nodes=(0,0) (30,0)

ball id=1 radius=0.62038 x=0.5 y=0.62038
property kn=1e8 ks=1e8 friction=1.0 density=1.0

SET gravity 0 -10

plot create ball_wall_setup
  plot ball lblue outline off
  plot add wall black
plot show ball_wall_setup

cycle 1000

set dt max 1e-4      ; constant timestep to fix displacement (displacement = velocity * timestep)

fix spin range id=1

fix x              range id=1
property xvelocity=1 range id=1

history id=1 energy frictional

plot create frictional_energy
plot set back white
plot add history 1
plot set title text 'Frictional energy'
;plot show frictional_energy

cycle 10000

print energy
return
```

File: l_damp.DAT Used for: particle local damping

Example case: 4

```
;l_damp.dat
new

SET random
SET disk off

TRACE energy ON

call FISHCALL.FIS

DEF ball_size
```

```
r1 = 0.5
END
```

```
ball_size
```

```
DEF yvelocity_
  bp = find_ball(1)
  yvelocity_ = -b_yvel(bp)
END
```

```
DEF starting_positions
  x_1 = 0
  y_1 = 0
END
```

```
starting_positions
```

```
DEF damping_
  l_damp = 0.0           ; local damping
  n_damp = 0.0         ; viscous damping, normal direction
  s_damp = 0.0         ; viscous damping, shear direction
END
```

```
damping_
```

```
DAMP default local l_damp
DAMP default viscous normal n_damp
DAMP default viscous shear s_damp
DAMP default viscous notension OFF
```

```
DEF time_
  time_ = time
END
```

```
ball id=1 radius=r1 x=x_1 y=y_1
```

```
property kn=1e8 ks=1e8 friction=0.0 density=1.0
```

```
SET dt max 1e-6 ; max timestep is fixed
```

```
history nstep=1
history id=1 time_
history id=2 yvelocity_
```

```
SET gravity 0 -10
```

```
cycle 5000
```

```
history write 1,2 file velocity.HIS
return
```

File: TwoBalls4.DAT Used for: all two-particle simulations Example case: 2, 3, 5

```
;TwoBalls4.dat
new
```

```
SET random
SET disk off
```

TRACE energy ON

call FISHCALL.FIS

```
DEF init_veloc
  xvel_1 = 50
  yvel_1 = 0
```

```
  xvel_2 = -50
  yvel_2 = 0
```

END

```
DEF ball_size
```

```
  r1 = 0.5
```

```
  r2 = 0.5
```

END

ball_size

```
DEF starting_positions
```

```
  x_1 = 0
```

```
  y_1 = 0
```

```
  x_2 = 2
```

```
  y_2 = 0
```

END

starting_positions

```
DEF damping_
```

```
  l_damp = 0.0
```

```
; local damping
```

```
  n_damp = 0.0
```

```
; viscous damping, normal direction
```

```
  s_damp = 0.0
```

```
; viscous damping, shear direction
```

END

damping_

DAMP default local l_damp

DAMP default viscous normal n_damp

DAMP default viscous shear s_damp

DAMP default viscous notension ON

```
DEF veloc_before
```

```
  cp = fc_arg(0)
```

```
; contact address
```

```
  bp2 = c_ball1(cp)
```

```
; position of ball 1
```

```
  bp1 = c_ball2(cp)
```

```
; position of ball 2
```

```
  n_x = c_xun(cp)
```

```
; unit-normal vector (x-position)
```

```
  n_y = c_yun(cp)
```

```
; unit-normal vector (y-position)
```

```
  v1_x = b_xvel(bp1)
```

```
; x-velocity of ball 1
```

```
  v1_y = b_yvel(bp1)
```

```
; y-velocity of ball 1
```

```
  v2_x = b_xvel(bp2)
```

```
; x-velocity of ball 2
```

```
  v2_y = b_yvel(bp2)
```

```
; y-velocity of ball 2
```

```
  omega1 = b_rvel(bp1)
```

```
; rotational velocity of ball 1
```

```
  omega2 = b_rvel(bp2)
```

```
; rotational velocity of ball 2
```

```

vc_x = v1_x - v2_x ; velocity of contact (x-direction)
vc_y = v1_y - v2_y ; velocity of contact (y-direction)
vc = sqrt((vc_x)^2 + (vc_y)^2) ; velocity of contact

vc_nx = n_x*(vc_x*n_x + vc_y*n_y) ; normal velocity of contact (x-direction)
vc_ny = n_y*(vc_x*n_x + vc_y*n_y) ; normal velocity of contact (y-direction)
vc_n = sqrt((vc_nx)^2 + (vc_ny)^2) ; normal velocity of contact

vc_tx = vc_x - vc_nx ; tangential velocity of contact (x-direction)
vc_ty = vc_y - vc_ny ; tangential velocity of contact (y-direction)
vc_t = vc - vc_n ; tangential velocity of contact
END

DEF veloc_after
cp = fc_arg(0) ; contact address

bp1_ = c_ball1(cp) ; position of ball 1
bp2_ = c_ball2(cp) ; position of ball 2

n_x_ = c_xun(cp) ; unit-normal vector (x-position)
n_y_ = c_yun(cp) ; unit-normal vector (y-position)

v1_x_ = b_xvel(bp1_) ; x-velocity of ball 1
v1_y_ = b_yvel(bp1_) ; y-velocity of ball 1

v2_x_ = b_xvel(bp2_) ; x-velocity of ball 2
v2_y_ = b_yvel(bp2_) ; y-velocity of ball 2

omega1_ = b_rvel(bp1_) ; rotational velocity of ball 1
omega2_ = b_rvel(bp2_) ; rotational velocity of ball 2

vc_x_ = - (v1_x_ - v2_x_) ; velocity of contact (x-direction) (MINUS due to
change in direction!!!)
vc_y_ = - (v1_y_ - v2_y_) ; velocity of contact (y-direction) (MINUS due to
change in direction!!!)
vc_ = sqrt((vc_x_)^2 + (vc_y_)^2) ; velocity of contact

vc_nx_ = n_x_*(vc_x_*n_x_ + vc_y_*n_y_) ; normal velocity of contact (x-direction)
vc_ny_ = n_y_*(vc_x_*n_x_ + vc_y_*n_y_) ; normal velocity of contact (y-direction)
vc_n_ = sqrt((vc_nx_)^2 + (vc_ny_)^2) ; normal velocity of contact

vc_tx_ = vc_x_ - vc_nx_ ; tangential velocity of contact (x-direction)
vc_ty_ = vc_y_ - vc_ny_ ; tangential velocity of contact (y-direction)
vc_t_ = vc_ - vc_n_ ; normal velocity of contact

r_ = vc_n_ / vc_n ; restitution coefficient
psi_1 = vc_t_ / vc_n
psi_2 = vc_t_ / vc_n
END

DEF time_
time_ = time
END

ball id=1 radius=r1 x=x_1 y=y_1
ball id=2 radius=r2 x=x_2 y=y_2

property kn=1e8 ks=1e8 friction=1.0 density=1.0

```

```

init_veloc

;plot create ball_wall_setup
; plot ball lblue outline off
; plot add wall black
;plot show ball_wall_setup

SET dt max 1e-6                ; max timestep is fixed

fix spin                        ; spin is fixed, so no rotation allowed

property xvelocity=xvel_1 yvelocity=yvel_1    range id=1
property xvelocity=xvel_2 yvelocity=yvel_2    range id=2

SET FISHCALL FC_CONT_CREATE veloc_before      ; calculate velocities BEFORE collision
SET FISHCALL FC_CONT_DEL veloc_after          ; calculate velocities AFTER collision

;--- history ---
history nstep=1
history id=1 time_
history id=2 diagnostic mcf                    ; mean contact force
;--- END history ---

cycle 45000

print x_1 y_1 xvel_1 yvel_1 x_2 y_2 xvel_2 yvel_2
print n_x n_y
print n_x_ n_y_ vc_x_ vc_y_
print r_ psi_1 psi_2

;history write 1,2,11,12,21,22,31,32,41,42 file ZWEIBALLS.HIS
history write 1,2 file ZWEIBALLS.HIS
return

; can be added to the HISTORY to monitor positions to determine the overlap
history id=11 ball xposition id=1
history id=12 ball xposition id=2
history id=21 ball yposition id=1
history id=22 ball yposition id=2
history id=31 ball xposition id=1
history id=32 ball xposition id=2
history id=41 ball yposition id=1
history id=42 ball yposition id=2

File: 0load.DAT      Used for: loading the silo

; fname: 0load.DAT
; loading of the silo using the STANDARD DAMPING MODEL

new

SET random
SET gen_error off

call fishcall.FIS

DEF create_hopper
;--- create outer wall coordinates ---

```

```

x_ptA = -h_bot_width * 0.5
y_ptA = 0.0
x_ptB = -h_bot_width * 0.5
y_ptB = h_bot_height
x_ptC = -h_upp_width * 0.5
y_ptC = h_bot_height + h_height
x_ptD = -h_upp_width * 0.5
y_ptD = h_bot_height + h_height + h_upp_height
x_ptE = h_bot_width * 0.5
y_ptE = 0.0
x_ptF = h_bot_width * 0.5
y_ptF = h_bot_height
x_ptG = h_upp_width * 0.5
y_ptG = h_bot_height + h_height
x_ptH = h_upp_width * 0.5
y_ptH = h_bot_height + h_height + h_upp_height

;--- create flow-promoting triangle coordinates ---
x_ptM = 0.0
y_ptM = 0.03
x_ptN = -br_width * 0.5
y_ptN = br_bot_height
x_ptO = br_width * 0.5
y_ptO = br_bot_height
x_ptP = 0.0
y_ptP = br_bot_height + br_upp_height
x_ptQ = 0.0
y_ptQ = br_bot_height

command
  wall id=1 nodes (x_ptM,y_ptM) (x_ptQ,y_ptQ)
  wall id=2 nodes (x_ptQ,y_ptQ) (x_ptM,y_ptM)
  wall id=3 nodes (x_ptN,y_ptN) (x_ptP,y_ptP) (x_ptO,y_ptO) (x_ptN,y_ptN)
  wall id=4 nodes (x_ptD,y_ptD) (x_ptC,y_ptC) (x_ptB,y_ptB) (x_ptA,y_ptA)
  wall id=5 nodes (x_ptE,y_ptE) (x_ptF,y_ptF) (x_ptG,y_ptG) (x_ptH,y_ptH)
  wall id=6 nodes (x_ptH,y_ptH) (x_ptD,y_ptD)
  wall id=7 nodes (x_ptA,y_ptA) (x_ptE,y_ptE)
; moving wall

  wall property kn=wall_kn ks=wall_ks friction=wall_fric
end_command

_area1 = h_upp_height * h_upp_width
_area2 = 0.5 * (h_upp_width - h_bot_width) * h_height
_area3 = h_bot_width * (h_height + h_bot_height)
_area4 = 0.5 * br_width * br_upp_height
tot_area = _area1 + _area2 + _area3 - _area4

END

;--- parameters and variables ----

DEF hopper_variables
;--- create the variables for the hopper ---

h_bot_height = 0.10 ; meter
h_height = 0.75 ; meter
h_upp_height = 0.4 ; meter
h_upp_width = 1.05 ; meter
h_bot_width = 0.30 ; meter

```

```

br_upp_height = 0.13                ; meter
br_bot_height = 0.47                ; meter
br_width      = 0.34                ; meter

wall_kn = 1.0e8                     ; N/m
wall_ks = 1.0e8                     ; N/m
wall_fric = 0.3                     ; -
END

DEF ball_variables
;--- here the ball properties are set ---

ball_dens = 723.75                  ; kg/m^3
r_lo = 0.004                       ; meter
r_rat = 1.5                         ; -
poros = 0.20                       ; -
END

DEF std_model_parameters
;--- parameters that are used for the STANDARD ITASCA MODEL ---
ball_kn = 1.0e8                    ; N/m
ball_ks = 1.0e8                    ; N/m
ball_fric = 0.3                    ; -
END

;--- END parameters and variables ---

DEF get_porosity
;--- calculate the real porosity ---
sum = 0.0
bp = ball_head
loop while bp # null
  if b_id(bp) >= _start_id then
    sum = sum + pi * b_rad(bp)^2.0
  endif
  bp = b_next(bp)
end_loop
pmeas = 1.0 - (sum / tot_area)      ; -
END

DEF filter_for_ball_creation
;--- create filter for ball creation ---
;--- balls cannot be formed within the triangle ---
;--- and also not outside the hopper ---

;--- 0 means: accept the ball ---
;--- 1 means: DO NOT accept the ball ---

_xpos = fc_arg(1)
_ypos = fc_arg(2)
_xlim = 0.5 * (h_bot_width + (_ypos - h_bot_height) * (h_upp_width - h_bot_width) / h_height)
_xlim2 = -0.5 * (_ypos - br_upp_height - br_bot_height) * (br_width / br_upp_height)

if abs(_xpos) <= _xlim
  if abs(_xpos) <= _xlim2

```

```

    if _ypos >= y_ptQ
        filter_for_ball_creation = 1
    else
        filter_for_ball_creation = 0
    end_if
else
    filter_for_ball_creation = 0
end_if
else
    filter_for_ball_creation = 1
end_if
END

```

```

DEF create_balls
; variables needed to target porosity
mult = 1.5
r_ave = 0.5 * (r_lo * (1 + r))
num = int(tot_area * (1 - poros) / (pi * r_ave^2.0))
r_hi = r_lo * r_rat
r_lo0 = r_lo / mult
r_hi0 = r_hi / mult
; variables related to the generation process
_start_id = 1
_end_id = _start_id + num -1
_xr = x_ptG
_xl = x_ptC
_yb = y_ptA
_yt = y_ptD

command
gen id _start_id _end_id rad r_lo0 r_hi0 x _xl _xr y _yb _yt &
    FILTER filter_for_ball_creation
property kn=ball_kn ks=ball_ks density=ball_dens friction=ball_fric
end_command

get_porosity
mult = sqrt((1.0-poros)/(1.0-pmeas))

command
property radius multiply mult
cycle 100
endcommand

END

```

;--- damping parameters ---

```

DEF damping_
    l_damp = 0.2 ; local damping
    n_damp = 0.2 ; viscous damping, normal direction
    s_damp = 0.0 ; viscous damping, shear direction
END

```

damping_

```

DAMP default local l_damp
DAMP default viscous normal n_damp
DAMP default viscous shear s_damp
DAMP default viscous notension OFF

```

```
;--- END damping parameters ---
```

```
;--- create plot ---
plot create hopper_model
plot set back white
plot add wall black
plot add ball lgray outline off
;plot add velocity red
plot set win size 0.7 0.7 pos 0.0 0.0
plot set title text 'Initial compact state (file 0load.DAT)'
;--- END create plot ---
```

```
SET gravity 0.0 -9.81
hopper_variables
```

```
create_hopper
```

```
plot show hopper_model
```

```
ball_variables
std_model_parameters           ; load the model parameters
create_balls
SET dt max = 2.5e-7             ; maximum constant time step
```

```
solve
save 0load.SAV
```

```
print pmeas
```

```
return
```

File: 2empty.DAT Used for: emptying the silo

```
; FNAME: 2empty.DAT
new
rest 0load.SAV                 ; restore the saved situation
```

```
DEF time_
  time_ = time
END
```

```
DEF y_pos
  y_pos_ = 0                   ; the line below which the mass flow rate and average
yvelocity are determined
END
```

```
DEF remove_balls
; balls are removed
; NOT used when flow rate has to be determined !!!
count_ = count_ + 1
if count_ > 100
  count_ = 0
  bp = ball_head
  loop while bp # null
    next_ = b_next(bp)
    if b_y(bp) < -0.1         ; y-level below which balls are deleted
      ii = b_delete(bp)
```

```

        end_if
        bp = next_
    end_loop
end_if
END

```

```

DEF empty_and_print
; emptying of the silo and making a hardcopy of the snapshots
command
delete wall 7
plot show hopper_model
plot set title text 'Flow after deletion of the lower wall (file 2empty.DAT)'
SET plot jpg qual 2 size 1536 1152
; SET fishcall FC_CYC_TOP remove_balls ; remove balls
SET fishcall FC_CYC_TOP count_the_balls
end_command
ToNextFile = 16000 ; make a snapshot every x cycles
CycleEnd = 10000000
ImgNr=0
loop n(0,CycleEnd) ;
    ImgNr = ImgNr + 1
    fileName = 'img'+string(ImgNr)+'.jpg' ; filenames are img1.jpg, img2.jpg, etc.
    command
        plot hardcopy file = fileName
        history write 1,2 file MASSFLOW.HIS ; save number flow rate as hardcopy file
        cycle ToNextFile
    endcommand
    n = n + ToNextFile
end_loop
END

```

```

DEF count_the_balls
ballnum_ = 0
bp = ball_head
loop while bp # null
    if b_y(bp) < y_pos_
        ballnum_ = ballnum_+1
    end_if
    bp = b_next(bp)
end_loop
END

```

;--- this section is related to the vibrating walls ---

```

DEF vibration_parameters
oldtime_ = time
frequency_ = 50 ; 1/s
amplitude_ = 0.01 ; m
gravity_ = 9.81 ; m/s^2
omega_ = 2.0*pi*frequency_ ; 1/s
END

```

```

DEF vibrate_hopper
while_stepping
realtime_ = time - oldtime_
vel_ = amplitude_ * cos(omega_ * realtime_)
wp = wall_head
loop n(1,3) ; which walls vibrate?
    w_xvel(wp) = vel_

```

```
    wp = w_next(wp)
  endloop
END
;--- END vibrating walls ---

vibration_parameters

set pint 20 ; update plots every this many cycles

SET hist_rep = 4000
history id=1 time_
history id=2 ballnum_

empty_and_print
```